
Cluster through the cosmic time: detection, characterization and evolution

Seyed Mohammad Mirkazemi



München, 2014

Cluster through the cosmic time: detection, characterization and evolution

Seyed Mohammad Mirkazemi

Dissertation
an der Fakultät für Physik
der Ludwig–Maximilians–Universität
München

vorgelegt von
Seyed Mohammad Mirkazemi
aus dem Iran

München, den June 2014

Erstgutachter: Prof. Dr. Kirpal Nandra

Zweitgutachter: Prof. Dr. Joseph Mohr

Tag der mündlichen Prüfung: 23. July 2014

Contents

Summary	xv
Zusammenfassung	xvii
1 Introduction	1
1.1 The cosmological framework	1
1.1.1 The Hubble Expansion	1
1.1.2 Concordance cosmology	2
1.2 Galaxy clusters	5
1.2.1 Formation of galaxy clusters	7
1.2.2 Definition of cluster mass	9
1.2.3 Abundance of galaxy cluster	11
1.2.4 Methods of detection and mass measurement	12
1.3 Galaxies	19
1.3.1 Classification	19
1.3.2 Luminosity and stellar mass functions	22
1.3.3 Environmental dependence of galaxy properties	23
2 Brightest X-ray clusters of galaxies in the CFHTLS wide fields: Catalog and optical mass estimator	29
2.1 Abstract	29
2.2 Introduction	30
2.3 Data	31
2.3.1 X-ray data	31
2.3.2 Optical, photometric redshift and spectroscopic data	33
2.4 Optical counterparts for X-ray sources	34
2.4.1 Red sequence method	34
2.4.2 Applying the red sequence finder to identify XMM-Newton extended sources	40
2.4.3 Velocity dispersion	41
2.4.4 Stellar luminosity as a L_X estimator	44
2.4.5 Applying the red sequence finder to identify RASS sources	47
2.5 RASS-CFHTLS and XMM-CFHTLS catalogs of X-ray selected clusters	52

2.6	Summary	55
2.7	acknowledgments	60
2.8	Appendix: Color variation of early-type galaxies as a function of redshift	61
2.9	Appendix: Correction for Eddington Bias	62
3	Dependence of galaxy stellar mass function on halo mass of clusters	63
3.1	Introduction	63
3.2	Data	67
3.2.1	COSMOS	67
3.2.2	CFHTLS	70
3.2.3	Stellar mass computation	71
3.3	Error analysis	73
3.3.1	Completeness in stellar mass measurement	73
3.3.2	Photometric redshift error	75
3.3.3	Uncertainty in stellar mass induced by error in redshift	76
3.3.4	Uncertainty in stellar mass induced by error in photometry and absence of NIR data	78
3.3.5	Total uncertainty in stellar mass	80
3.4	The group and cluster membership	81
3.4.1	The individual and composite GSMF	85
3.4.2	Robustness of the method	87
3.5	Group and cluster sample	90
3.6	GSMF of X-ray selected clusters	90
3.6.1	Central galaxies	90
3.6.2	Satellite galaxies	98
3.6.3	GSMF of member galaxies vs field	101
3.7	Conclusion	102
4	Morphological properties of galaxies in an X-ray detected group at redshift $z = 1.6$	105
4.1	Introduction	105
4.2	Data	106
4.2.1	Chandra and XMM-Newton X-ray data	106
4.2.2	Optical and IR Data	107
4.3	X-ray selected group catalog in CDFS and a group at $z=1.6$	108
4.4	Properties of member galaxies	111
4.4.1	Stellar mass of member galaxies	111
4.4.2	Morphology of member galaxies	112
4.4.3	Structural properties	118
4.4.4	Summary and conclusion	121

5 Conclusion	123
5.1 Technical results	123
5.1.1 Red sequence technique	123
5.1.2 Computing the stellar mass and the stellar mass error	123
5.1.3 Testing the method of mass function computation on mock catalog	124
5.2 Scientific results	124
5.2.1 X-ray selected clusters in CFHTLS	124
5.2.2 Scaling relations	125
5.2.3 GSMF of X-ray selected clusters	125
5.2.4 Morphology of group galaxies at redshift 1.6	125
Bibliography	127
Acknowledgement	139
Cirriculum Vitae	140

List of Figures

1.1	Multi-wavelength images off El Gordo cluster.	6
1.2	Simulation of a dark matter density field evolution through the time. . . .	10
1.3	Number density of the halos more massive than M derived from Press-Schechter model.	12
1.4	X-ray image of Coma cluster observed by ROSAT.	13
1.5	Planck y -map of Coma on a $\sim 3 \text{ deg} \times 3 \text{ deg}$ patch with the <i>ROSAT-PSPC</i> iso-luminosity contours overlaid (Planck Collaboration et al., 2011). . . .	15
1.6	Mass as a function of redshift for three major cluster samples.	17
1.7	Example of gravitational lensing features in Abell 2218.	18
1.8	Geometry of a gravitational lens system.	19
1.9	Hubble sequence.	20
1.10	Sérsic profile, where r_e is held fixed.	21
1.11	Star formation rate versus stellar mass for different redshift ranges.	22
1.12	Morphology-density relation (Dressler, 1980).	24
1.13	Luminosity and mass functions of galaxies in the local Universe.	25
1.14	Stellar mass function of galaxies in different environments.	27
2.1	Distribution of the u^* , g' , r' , i' and z' magnitudes in W1, W2, and W4 fields.	34
2.2	Characteristic magnitude $m_*(z)$ for different filters as a function of redshift.	37
2.3	Model colors for ETGs as a function of redshift.	38
2.4	Magnitude errors in g' , r' , i' and z' band versus redshift for galaxies brighter than $m_{*(z)}+1$	39
2.5	Color – magnitude diagrams for three clusters with high detection level in X-ray.	40
2.6	Illustration of the red sequence finder using XMM cluster XCC J0224.0-0835 at a red sequence redshift of 0.28.	42
2.7	Examples of clusters with different visual flags.	43
2.8	Red sequence redshifts versus spectroscopic redshifts for 81 clusters with spectroscopic counterparts.	44
2.9	X-ray luminosity versus the velocity dispersion for XMM clusters with more than ten spectroscopic members from gapper estimator method.	45
2.10	Convergence test for calculating L_S	46

2.11	Integrated stellar luminosity in z' band versus L_X for clusters with X-ray detection level above 4.6 and $0.1 < z < 0.6$	47
2.12	Integrated stellar luminosity in z' band versus L_X for clusters with visual flag=1 and at $0.1 < z < 0.6$	48
2.13	Stellar luminosity versus X-ray luminosity of clusters for low redshift and high redshift subsamples.	49
2.14	redMaPPer richness parameter λ (calculated using SDSS data) versus stellar luminosity within r_{200c} , L_S	50
2.15	As in Figure 2.6 but for a RASS cluster at the redshift of 0.2.	51
2.16	RGB images of two RASS X-ray sources produced using CFHTLS broadband images in g' as blue, r' as green and i' as red.	52
2.17	Red sequence significance, α , versus redshift and offset between optical and X-ray cluster centers for RASS X-ray sources.	53
2.18	X-ray mass and X-ray luminosity as functions of redshift.	55
2.19	RASS X-ray flux versus XMM-Newton X-ray flux for 16 clusters in overlap between the RASS and XMM cluster samples.	59
2.20	Magnitude–redshift distribution of the ETGs brighter than $z'=20$ and $m_*(z)$	61
2.21	Colors evolution of ETGs as functions of redshifts.	62
3.1	Stellar mass function of elliptical galaxies from Ilbert et al. (2010).	64
3.2	Stellar mass function of quiescent, high star-forming and intermediate star-formation activities galaxies from Ilbert et al. (2010).	65
3.3	Fraction of star-forming galaxies to the total galaxies in all environments and its evolution through the redshift (Giodini et al., 2012).	67
3.4	SED templates used for photometric redshift of galaxies in COSMOS survey Ilbert et al. (2009).	69
3.5	M_{200c} as a function of redshift for COSMOS clusters (blue dots) and CFHTLS clusters (red dots).	71
3.6	Response function of MegaCam and WIRCAM filters.	72
3.7	Results of SED fitting method for galaxies in CFHTLS.	74
3.8	Completeness mass threshold for star-forming and passive galaxies as a function of redshift.	75
3.9	Distribution of photometric redshift deviation from spectroscopic redshift for different magnitude brightness ranges.	77
3.10	Error in photometric redshift as a function of i band magnitude for CFHTLS.	78
3.11	Error in photometric redshift as a function of i band magnitude for COSMOS.	79
3.12	Variation of stellar mass induced by uncertainty in the photometric redshift as a function of i band magnitude for different redshift ranges.	80
3.13	Mass derived using u, g, r, i, z filters in W1 versus the mass calculated using D1 u, g, r, i, z, J, H, K bands.	81
3.14	Deviation of the stellar mass computed with W1 data from the mass computed using D1 data as a function of galaxy brightness.	82
3.15	Total error in estimating stellar mass in redshift-magnitude space.	83

3.16	Magnitude–redshift distribution of all galaxies within r_{200c} of a mock cluster at redshift 0.25.	84
3.17	Galaxy stellar mass function of the whole population of galaxies at $0.3 < z < 0.4$	86
3.18	Mass versus redshift of clusters in mock catalog.	87
3.19	Simulated photometric redshift versus the spectroscopic redshift in the mock catalog.	88
3.20	Simulated measured stellar mass versus the true stellar mass in the mock catalog.	89
3.21	Composite GSMF for mock clusters with the mass of $6 \times 10^{13} \leq M_{200c} \leq 2 \times 10^{14} M_{\odot}$ at different redshift ranges.	91
3.22	Composite GSMF for mock clusters with the mass $6 \times 10^{13} \leq M_{200c} \leq 2 \times 10^{14} M_{\odot}$ at different redshifts.	92
3.23	Composite GSMF for mock clusters with total mass of $6 \times 10^{13} \leq M_{200c} \leq 2 \times 10^{14} M_{\odot}$ at different redshift ranges.	93
3.24	Composite GSMF for mock clusters with total mass of $6 \times 10^{13} \leq M_{200c} \leq 2 \times 10^{14} M_{\odot}$ at different redshift ranges.	94
3.25	Mass versus the redshift for the final cluster sample.	95
3.26	Stellar mass distributions for central galaxies of the cluster with the masses of $2 \times 10^{14} < M_{200} < 6 \times 10^{14} M_{\odot}$ and $6 \times 10^{13} < M_{200} < 2 \times 10^{14} M_{\odot}$ at redshift $0.2 < z < 0.4$ and $0.4 < z < 0.6$	96
3.27	Mean central galaxy stellar mass as a function of redshift for different halo masses.	97
3.28	Mean central galaxy stellar mass as a function of cluster total mass, M_{200} , for different redshift ranges.	97
3.29	Composite GSMF for clusters of different mass and redshift.	99
3.30	Similar to Figure 3.29 for different subsamples.	100
3.31	Characteristics mass of satellite galaxies as a function of redshift for different halo masses.	101
3.32	Comparison between the GSMF of field galaxies and member galaxies.	103
3.33	Characteristics mass of satellite galaxies as a function of redshift for different halo masses.	104
4.1	RGB image of $z=1.6$ galaxy group	109
4.2	Color–magnitude diagrams using CANDELS I , J , and H bands.	110
4.3	Best-fitted model and the photometry of object–A (BGG).	111
4.4	Group image in WFC3 F160W band.	113
4.5	Image of an unsaturated star used as a PSF image.	114
4.6	Input, model, residual, and mask images of galaxies.	115
4.7	As in Figure 4.6 but for object–E to h.	116
4.8	Simulated image of the group in WFC3 F160W band.	117
4.9	Sérsic index and half-light radius plotted against stellar mass.	119

List of Tables

2.1	The completeness magnitude limits for each field.	35
2.2	The maximum redshift at which galaxies with luminosity of $0.2L_*$, $0.4L_*$ and $1.0L_*$ are detectable in each filter.	36
2.3	Fitting parameters of $\log(L_X)$ - $\log(L_S)$ relation. The Eddington bias correction is considered in fitting procedure (see §2.9). Col.(1) indicates the type of selection of red galaxies; col.(2) is the radius within which L_X is calculated. The fitting procedure is listed in col.(3). The cols. (4-5) present the intercept and slope of fittings respectively. The scatter in $\log L_X$ and $\log L_S$ direction are in cols. (6-7).	49
2.4	Fitting parameters of $\log(L_X - \log(L_S))$ relation for high redshift and low redshift samples.	50
2.5	Catalog of XMM-CFHTLS X-ray Selected Galaxy Clusters	56
2.4	Continued from previous page.	57
2.4	Continued from previous page.	58
2.5	Catalog of RASS-CFHTLS X-ray Selected Galaxy Clusters	59
3.1	Parameters used to generate the SED templates.	73
3.2	Mean and the dispersion of the central galaxies within each bin of mass and redshift derived from Gaussian fitting.	96
3.3	Mean and the dispersion of the central galaxies within each bin of mass and redshift.	96
3.4	Parameters of Schechter fitting on mass function of satellite galaxies. . . .	98
3.5	Number of halos within a given mass range at the volume between various redshift ranges.	102
4.1	Results of SED fitting on the member galaxies photometry.	112
4.2	Structural properties of galaxies.	118

Summary

Galaxy clusters have a twofold importance. They are used to constraint with high accuracy the cosmological parameters and they are also commonly defined as "laboratories" of galaxy formation and evolution due to their particular mix of galaxy types with respect to other environments. Optical galaxy cluster searches are often hindered by galaxy projection effects. Several algorithms have been applied to solve this problem including red sequence method.

We have initiated an XMM-CFHTLS project to provide X-ray observations of the brightest X-ray clusters within the wide CFHTLS area. We solve for the problem of identification of the unresolved X-ray sources in the ROSAT All-Sky survey (RASS) through a novel red sequence finder, which uses the multi-color space. We provide the calibration of the red sequence observed in the CFHT filters and compare the results with the traditional single color red sequence. We test the identification algorithm on the subset of high Signal to noise XMM clusters and identify a 100% of the sample. We find that the integrated z-band luminosity of the red sequence galaxies correlates well with the X-ray luminosity with a surprisingly small scatter of 0.22 dex. We further use the multi-color red sequence to reduce spurious detections in the full XMM and RASS data sets, resulting in catalogs of 196 and 27 clusters, respectively. We made follow-up observations of some of these systems with HECTOSPEC and in combination with BOSS DR9 data we confirm spectroscopically 71 clusters. We also describe the modifications to be applied to the source detection algorithm in order to reduce the contamination by spurious sources when creating an extended source catalog with relatively shallow X-ray data. For clusters with more than ten spectroscopic members, we present the scaling relation between X-ray luminosity and velocity dispersion.

We use the clean cluster sample created on the basis of the multi-color space red sequence finder, in addition to the X-ray detected group sample of Finoguenov et al. (2009) of the COSMOS field, to analyze the galaxy stellar mass function (GSMF) as a function of the host halo mass. This is done to understand how the mass segregation is evolving with time and what is the role of massive halos in the mass assembly history of the Universe. The cluster and group sample of CFHTLS and COSMOS, respectively, allow us study the dependence of the characteristic magnitude of the satellite and central galaxy as a function of the host halo mass and as a function of redshift to check if and how the stellar mass accretion of galaxies is related to the mass accretion of their host halo. Indeed, the full sample spans a halo mass range of two order of magnitude from 6×10^{12} to 6×10^{14} solar

masses and a redshift window from $z \sim 0.2$ to $z \sim 1$. In addition, we use the photometric information and the available photometric redshift of the CFHTLS and the COSMOS galaxy sample to estimate the stellar mass of each galaxy and to assign the group and cluster membership. In particular we carefully analyse the uncertainties in cluster GSMF estimation induced by errors in photometric redshift and stellar mass. We extensively test our method on mock a catalog. We find that the GSMF in massive halos is well modeled by a combination of a Schechter function for the satellite galaxies and a Gaussian function for the central galaxies, in agreement with the findings of Yang et al. (2007). Our results show that the characteristic mass of satellite galaxies in groups and clusters is independent on the host halo mass. In addition, it increases by a factor of 0.25-0.3 dex from redshift 0.9 to 0.3. We show that there is an impressive consistency between the mass evolution of satellite galaxies and their mass growth caused by star-formation history. This would suggest that star formation is the main mechanism for satellite galaxies to accrete their mass. Differently from satellite galaxies, the mass of central galaxies is correlated with host halo mass. We do not find any redshift evolution in relation between the mean central galaxy stellar mass and the host halo mass. This indicates that the mass growth of central galaxy is controlled by hierarchical mass growth of the host halo. Thus likely merger events play a more important role in mass accretion history of central galaxies with respect to the star formation activity.

We finally compare the GSMF in the massive halos with the global population GSMF. We show that all massive galaxies with masses above $10^{11} M_{\odot}$ reside in clusters but only a low fraction of low mass ones are in such environments. The density of cluster galaxies with stellar masses above $10^{11.5} M_{\odot}$, which is described by Gaussian component, is comparable to the density of galaxies with similar mass in the field. This means that strong mass segregation in massive halos is mostly caused by central galaxies.

We also study the properties of member galaxies in a very high redshift X-ray selected group. This $z = 1.6$ group with the mass of $\sim 3 \times 10^{13} M_{\odot}$ is the lowest mass X-ray group discovered above redshift 1.5. We use the WFC3 F160W image from CANDELS, which probes the rest frame r-band at $z = 1.6$ to compute the structural parameters of member galaxies and find that they are morphologically early-type. The uncertainties in structural parameters are derived by extensive Monte-Carlo simulations. The comparison with mass – Sersic and mass – radius relation of early-type galaxies in local Universe shows that the group is dominated by quiescent early-type galaxies, and it appears quite evolved and similar to groups in the local Universe.

Zusammenfassung

Die Bedeutung von Galaxienhaufen ist vielfältig. Sie werden verwendet, um kosmologische Parameter mit hoher Präzision zu bestimmen und werden wegen ihrem speziellen Mix von Galaxientypen im Vergleich zu anderen Umgebungen häufig als "Labore" für Galaxienentstehung und -entwicklung bezeichnet. Die Suche nach Galaxienhaufen im optischen Bereich wird oft durch Projektionseffekte von Galaxien beeinträchtigt. Verschiedene Algorithmen wurden angewandt, um dieses Problem zu lösen, darunter auch die "Red Sequence" Methode.

Wir haben ein XMM-CFHTLS Projekt begonnen, um Röntgenbeobachtungen der hellsten Galaxienhaufen innerhalb der großen CFHTLS Region zu bekommen. Wir lösen das Problem der Identifikation von nicht aufgelösten Röntgenquellen in der ROSAT All-Sky survey (RASS) durch einen neuen Red Sequence Finder, der mehrere Farbfilter verwendet (multi-color space Red Sequence). Wir zeigen die Kalibrierung der Red Sequence, die in den CFHT Filtern beobachtet wurde, und vergleichen die Ergebnisse mit der traditionellen Red Sequence, die durch eine Farbe bestimmt wird. Wir testen den Identifikationsalgorithmus an einer Teilmenge der XMM-Galaxienhaufen mit hohem Signal-Geräusch-Verhältnis und identifizieren 100% dieser Stichprobe. Wir beobachten, dass die integrierte z-Band Leuchtkraft der Red Sequence Galaxien gut und mit einer überraschend kleinen Streuung von 0.22 dex mit der Röntgenleuchtkraft korreliert. Weiters benutzen wir die multi-color Red Sequence, um falsche Detektionen im gesamten XMM und RASS Datensatz zu reduzieren. Dies führt zu einem Katalog von 196 bzw. 27 Galaxienhaufen. Wir haben Nachfolgebeobachtungen von einigen dieser Systeme mit HECTOSPEC durchgeführt und konnten in Kombination mit BOSS DR9 Daten 71 Galaxienhaufen spektroskopisch bestätigen. Wir beschreiben auch die Modifizierungen, die am Quellendetektionsalgorithmus durchgeführt werden müssen, um die Kontamination durch unechte Quellen bei der Erstellung eines Katalogs von ausgedehnten Quellen mit relativ schwachen Röntgendaten zu reduzieren. Für Galaxienhaufen mit mehr als zehn spektroskopischen Mitgliedern präsentieren wir Scaling Relations zwischen der Röntgenleuchtkraft und der Geschwindigkeitsdispersion.

Wir verwenden eine gesäuberte Stichprobe, welche auf Basis des multi-color space Red Sequence Finders erstellt wurde, als Ergänzung zu der Stichprobe von Finoguenov et al. (2009) von Galaxiengruppen, die im Röntgenbereich im COSMOS Feld detektiert wurde, um die stellare Massenfunktion der Galaxien (GSMF) als Funktion der Halomasse des Hosts zu analysieren. Diese Untersuchung soll klären, wie die sich die Massensegregation zeitlich entwickelt und welche Rolle massereiche Halos beim Anwachsen von Massen im Universum

spielen. Die Haufen- bzw. Gruppenstichprobe von CFHTLS bzw. COSMOS erlauben es, die Abhängigkeit der charakteristischen Magnitude der Satelliten- und zentralen Galaxie als Funktion der Halomasse des Hosts und als Funktion der Rotverschiebung zu studieren, um zu sehen, ob und wie das stellare Massenwachstum von Galaxien mit dem Massenwachstum des Hosthalos zusammenhängt. Die gesamte Stichprobe überspannt einen Massenbereich des Halos von zwei Größenordnungen ($6 \times 10^{12} - 6 \times 10^{14} M_{\odot}$) und einen Rotverschiebungsbereich von $z \sim 0.2-1$. Außerdem benutzen wir die photometrischen Informationen und die verfügbaren photometrischen Rotverschiebungen der CFHTLS und der COSMOS Galaxienstichprobe, um die stellare Masse jeder Galaxie abzuschätzen und um die Gruppen- und Haufenmitgliedschaft zu bestimmen. Im Speziellen analysieren wir sorgfältig die Unsicherheit in der Bestimmung der Haufen-GSMF durch Fehler in der photometrischen Rotverschiebung und der stellaren Masse. Wir testen unsere Methode ausgiebig mithilfe von simulierten Katalogen. Wir beobachten in Übereinstimmung mit Yang et al. (2007), dass die GSMF in massereichen Halos gut durch eine Kombination einer Schechterfunktion für die Satellitengalaxien und einer Gaußfunktion für die zentralen Galaxien modelliert werden kann. Unsere Ergebnisse zeigen, dass die charakteristische Masse der Satellitengalaxien in Gruppen und Haufen unabhängig von der Halomasse des Hosts ist. Weiters steigt sie mit einem Faktor von 0.25-0.3 dex von Rotverschiebung 0.9 bis 0.3. Im Gegensatz zu Satellitengalaxien, korreliert die Masse der zentralen Galaxien mit der Halomasse des Hosts. Wir finden keine Entwicklung mit der Rotverschiebung in der Beziehung zwischen der mittleren stellaren Masse der Zentralgalaxie und der Halomasse des Hosts. Dies deutet an, dass das Massenwachstum der Zentralgalaxie durch hierarchisches Massenwachstum des Hosthalos kontrolliert wird. Daher spielen Verschmelzungsprozesse wahrscheinlich eine wichtigere Rolle in der Geschichte des Massenzuwachs von zentralen Galaxien als die Sternentstehungsaktivität. Zum Schluß vergleichen wir die GSMF in massereichen Halos mit der GSMF der Gesamtpopulation. Wir zeigen, dass alle massereichen Galaxien mit $M > 10^{11} M_{\odot}$ in Haufen liegen, aber wir finden nur einen kleinen Teil von massearmen Galaxien in dieser Umgebung. Die Dichte an Haufengalaxien mit stellaren Massen über $10^{11.5} M_{\odot}$, welche durch eine Gaußkomponente beschrieben wird, ist vergleichbar mit der Dichte an Feldgalaxien mit ähnlicher Masse. Das heißt, dass starke Massensegregation in massereichen Halos hauptsächlich durch die zentralen Galaxien verursacht wird.

Wir untersuchen auch die Eigenschaften der Mitgliedsgalaxien in einer hochrotverschobenen Galaxie, die im Röntgenbereich gefunden wurde. Diese $z=1.6$ Gruppe hat eine Masse von $\sim 3 \times 10^{13} M_{\odot}$ und ist die massenärmste Röntgengruppe, die über $z=1.5$ gefunden wurde. Wir verwenden das WFC3 F160W Bild von CANDELS, welches das rest frame r-Band bei $z=1.6$ untersucht, um die Strukturparameter der Mitgliedsgalaxien zu bestimmen und finden, dass es sich um morphologisch frühe Galaxien handelt. Die Unsicherheit bei den Strukturparametern wurde mithilfe von umfangreichen Monte-Carlo Simulationen bestimmt. Der Vergleich mit der Masse-Serie und der Masse-Radius Beziehung von frühen Galaxien im lokalen Universum zeigt, dass die Gruppe von inaktiven frühen Galaxien dominiert wird. Sie erscheint relativ entwickelt und ähnlich zu Gruppen im lokalen Universum.

Chapter 1

Introduction

1.1 The cosmological framework

According to the standard cosmological model (Peebles, 1980), the Universe started from a hot state, then, during an inflationary phase, the volume of the Universe expanded by a factor of $\sim 10^{78}$. The fluctuations in primordial density were formed during the inflationary phase (Guth & Pi, 1982). The self-gravity of the peaks in the density fluctuations gradually led to decoupling of the peaks from the Hubble flow and inverting the local expansion of matter. Increasing the abundance of matter at the peaks of fluctuations caused the formation of galaxies and galaxy clusters. The most important aspects of of this scenario and some related observable cosmological effects are explained in this section.

1.1.1 The Hubble Expansion

By measurement on the Doppler shift of spectral lines, one can measure the radial velocity of galaxies. The redshift z of a galaxy is defined as a relative change in the wavelength of observed photons to the wavelength of emitted photons:

$$z := \frac{\lambda_{obs} - \lambda_0}{\lambda_0} \quad (1.1)$$

where λ_{obs} and λ_0 are the wavelength of the observed and emitted photons, respectively. For an object with a radial velocity much smaller than speed of light c :

$$v \approx zc. \quad (1.2)$$

For almost all galaxies this radial velocity is positive which means that the galaxies are moving away from the Milky Way. In 1928, Edwin Hubble discovered that the radial velocity v of a galaxy is proportional to its distance. The following relation between distance D of a galaxy and its radial velocity v is called Hubble law:

$$v = H_0 D \quad (1.3)$$

where H_0 is Hubble constant.

The dynamics of the Universe is described by a dimensionless scale factor $a(t)$ where t is the cosmic time. This scale factor is proportional to the mean distance between the galaxies in the Universe and normalized to $a(t_0) = 1$ for present time t_0 . Using the scale factor, one can define the Hubble parameter as:

$$H(t) = \frac{\dot{a}(t)}{a(t)} \quad (1.4)$$

where $\dot{a}(t)$ is time derivative of the scale factor. The Hubble parameter at present time has been precisely constrained by Type Ia supernovae to $H(t_0) = H_0 = 73.8 \pm 2.4 \text{ km s}^{-1} \text{ Mpc}^{-1}$ (Riess et al., 2011).

Lets assume a photon that have been emitted by an object at time t_e and reaches to us today. We parametrize the photon path by cosmic time t . We also consider two imaginary comoving observers along the photon path with a small separation dr from each other. Thus, it takes $dt = dr/c$ for a photon to travel between two observers. Their relative velocity due to cosmic expansion is dv . According to relation 1.2, the difference between the observed redshift of the photo by two observers is $dz = d\lambda/\lambda = dv/c$. By combination of relation 1.4 and the relation between $d\lambda$ and dv , we find:

$$\frac{d\lambda}{\lambda} = Hdt = \frac{da}{a}. \quad (1.5)$$

The above equation has a solution of $\lambda \propto a$. Since for $a = 1$, λ should equals to λ_{obs} , we can write:

$$\lambda(a) = a\lambda_{obs}. \quad (1.6)$$

If we replace the wavelength with redshift, we can achieve an important relation between the scale factor a and the redshift:

$$1 + z = \frac{1}{a}. \quad (1.7)$$

If the scale factor is a monotonic function of time, the redshift should also be a monotonic function of time.

1.1.2 Concordance cosmology

The modern Λ CDM cosmology, known as concordance cosmology, is founded on two main assumptions. The first one is that the matter dynamical evolution in the Universe can be explained by general relativity. Based on the second assumption, the Universe is “homogeneous“ and ”isotropic“ which means that there is no observable irregularity on sufficiently large scales ($> 100 \text{ Mpc}$) of the Universe (Peebles, 1980). The Robertson-Walker metric (Robertson, 1935) can express two assumptions for distribution of the matter in the Universe in mathematical language:

$$ds^2 = -c^2 dt^2 + a^2(t) \left[\frac{dr^2}{1 - \kappa r^2} + r^2 (d\theta^2 + \sin^2(\theta) d\phi^2) \right], \quad (1.8)$$

where (r, ϕ, θ) are comoving spherical coordinates, t is the cosmic time, and s is proper time. In this metric, the symmetric space can have positive, negative, or zero (flat space) curvatures κ .

Friedmann equations and cosmological constant

According to the field equation of General Relativity, the distribution of the mass and energy leads to a space-time curvature. By inserting the Roberston-Walker metric into the General Relativity field equation, one can derive the Friedmann equations (Friedmann, 1922) for scale factor $a(t)$:

$$\left(\frac{\dot{a}}{a}\right)^2 = \frac{8\pi G}{3}\rho - \frac{\kappa c^2}{a^2} + \frac{\Lambda}{3} \quad (1.9)$$

$$\frac{\ddot{a}}{a} = -\frac{4\pi G}{3}\left(\rho + \frac{3P}{c^2}\right) + \frac{\Lambda c^2}{3} \quad (1.10)$$

where Λ is the cosmological constant introduced by Einstein to obtain a static solution for the resulting equation. Once the equation of state $P(\rho)$ is specified, the Friedmann equations can be solved for $a(t)$. The equation of state have the form of $p = w\rho c^2$ where w value depends on the component which P and ρ belong to.

Vacuum energy

According to quantum mechanics, a vacuum space has a finite energy density. For physical measurements, not affected by gravity, the difference between energy levels are important so the vacuum energy can be discarded (e.g. energy of a photon emitted by an electron transition between two states). For explaining the behavior of vacuum energy and deriving w in equation of state of dark energy, we need to explain the first law of thermodynamics.

When gas is compressed, its temperature increases and accordingly so does the thermal energy of the gas. According to the first law of thermodynamics, the change in internal energy, dU , of a gas with pressure P through an (adiabatic) variation in volume dV equals the work $dU = -PdV$. For a homogeneous isotropic universe:

$$\frac{d}{dt}(c^2\rho a^3) = -P\frac{da^3}{dt}. \quad (1.11)$$

Because the energy density ρ_v of the vacuum is constant in space and time, the w in the equation of state has value of -1 and the equation can be written in following form:

$$P_v = -\rho_v c^2. \quad (1.12)$$

According to the relation 1.12 the vacuum energy has a negative pressure. Assuming a change in volume V that only contains vacuum, an increase of dV in volume leads to a growth in U because the internal energy U is proportional to V .

Matter component

Besides vacuum energy, there are two important components of the Universe in Equations 1.9 and 1.10: pressure-free matter and radiation. The molecules of air in a room (with room temperature) have a speed similar to the speed of sound ($c_s \sim 300m/s$). Thus for the air at room temperature, $P \sim \rho c_s^2 \ll \rho c^2$ and the pressure term is gravitationally negligible. Since the speed of light c is much larger than the speed of matter particle, the pressure term is negligible in comparison to the density term and one can assume that $P_m = 0$ (m stands for matter). A matter component with $P^2 \ll \rho c^2$ is called pressure-free matter or dust by cosmologists. For such a *matter dominant* universe with equation of state of $P = 0$ ($w = 0$), one can show that the Friedmann equations lead to $\rho \propto a^{-3}$.

Radiation component

If the thermal velocities are comparable with the speed of light, then the condition of $P^2 \ll \rho c^2$ is no longer satisfied. A component with thermal velocity equal to the speed of light is denoted as “radiation”. All electromagnetic radiations including CMB photons are examples of radiation. Particles with a finite mass and a thermal velocity close to the speed of light are the other examples for radiation. For these particles, the rest mass is much smaller than the thermal energy, $mc^2 \ll k_b T$. The parameter of w equals to 1/3 for a universe with only radiation component and equation of state is:

$$P_r = \frac{1}{3} \rho_r c^2. \quad (1.13)$$

By inserting above equation of state in the Friedmann equations one can show that, for a *radiation dominant* universe, $\rho \propto a^{-4}$.

Density parameter

Considering the Friedmann equations for the case of $\kappa = 0$, one can define a critical density as a boundary between the universes that expand forever (open models) and those ones that collapse after a finite cosmic time (closed models). For a universe with critical density, the Hubble expansion stops after infinite time has elapsed. The critical density is:

$$\rho_c := \frac{3H_0^2}{8\pi G} = 1.88 \times 10^{-29} h^2 g cm^{-3}. \quad (1.14)$$

As the ρ_m and ρ_r are proportional to $a(t)^{-3}$ and $a(t)^{-4}$ respectively, the first Friedmann equation can be written in terms of present time densities:

$$H^2(t) = \left(\frac{\dot{a}}{a}\right) = \frac{8\pi G}{3} [\rho_{m,0} a^{-3} + \rho_{r,0} a^{-4} + \rho_{\Lambda,0}] - \frac{\kappa c^2}{a^2}. \quad (1.15)$$

where $\rho_{m,0}$, $\rho_{r,0}$, and $\rho_{\Lambda,0}$ are matter, radiation, and vacuum densities in present time. Using the definition of critical density, one can define dimensionless densities for the Universe

components and rewrite the equation 1.15 in this form:

$$H^2(t) = H_0^2 \left[\Omega_r a^{-4} + \Omega_m a^{-3} + \Omega_\Lambda - \frac{\kappa c^2}{a^2} \right]. \quad (1.16)$$

where Ω_i terms are the ratio of each components density to the critical density. If $\kappa = 0$ or -1 and if $\Lambda \geq 0$, the right hand side of equation 1.17 is positive. Thus $\dot{a}(t)$ also have positive value and $a(t)$ increases with time. But for a universe with $\kappa = +1$ and $\Lambda = 0$, the right hand side equals to zero in the future when the curvature term is as large as the sum of radiation and matter terms. After this time $a(t)$ decreases with time and the Universe contracts until $a = 0$. If $\Lambda \leq 0$ or if $\kappa = +1$ and $\Lambda = 0$ the expansion will finally halt and the universe will recollapse.

Because at the present time $\Omega_m + \Omega_r + \Omega_\Lambda - \kappa c^2/(H_0 a^2) = 1$, one can rewrite the equation 1.17 in following form:

$$H^2(t) = H_0^2 E(z) = H_0^2 \left[\Omega_r a^{-4} + \Omega_m a^{-3} + (1 - \Omega_m - \Omega_r - \Omega_\Lambda) a^{-2} + \Omega_\Lambda \right]. \quad (1.17)$$

According to seven year data from *WMAP* the density of the Universe components are, $\Omega_\Lambda = 0.725 \pm 0.016$, $\Omega_m = 0.270 \pm 0.007$, and $H_0 = 70.2 \pm 1.4 \text{ km s}^{-1} \text{ Mpc}^{-1}$. The values of Ω_r and κ are close to the zero (Komatsu et al., 2011).

1.2 Galaxy clusters

Galaxies are not uniformly distributed in the Universe but instead show a tendency to gather together in galaxy groups and clusters. Clusters are the most massive gravitationally bound systems in the Universe. Historically, measuring the velocities of the galaxies in the clusters and assuming the virial equilibrium was the first method for computing the mass of clusters (Hubble & Humason, 1931; Zwicky, 1933; Smith, 1936; Zwicky, 1937). The measured gravitational mass of clusters had the values of few hundred times the total stellar masses in the clusters. This point leads to suggestion of dark matter (DM) by Zwicky.

The existence of dark matter was a matter of debate for few decades. Finally in 1970s, it was confirmed by detection of X-ray emission from hot intracluster medium (ICM) for Coma, Virgo, and Perseus cluster (Cavaliere, Gursky & Tucker, 1971; Gursky et al., 1971; Meekins et al., 1971; Forman et al., 1972; Kellogg et al., 1972). Measuring the temperature of ICM and subsequent measurement on the gravitational potential of clusters implied that an additional missed component (called dark matter) in clusters is still inevitable.

Besides of providing part of missing mass in clusters, the ICM facilitated discovery of clusters at high redshifts (Rosati, Borgani & Norman, 2002). In addition to the mentioned remarkable properties, ICM can change the spectrum of cosmic microwave background (CMB) by inverse Compton scatter between hot electrons in ICM and CMB's photons. This effect, known as Sunyaev–Zel'dovich (SZ) effect, leads to variations of $\sim 10^{-5}$ in black body temperature of CMB's photons (Sunyaev & Zeldovich, 1970, 1972). Beside X-ray emission, SZ effect is also a robust tool for finding galaxy clusters (Planck Collaboration

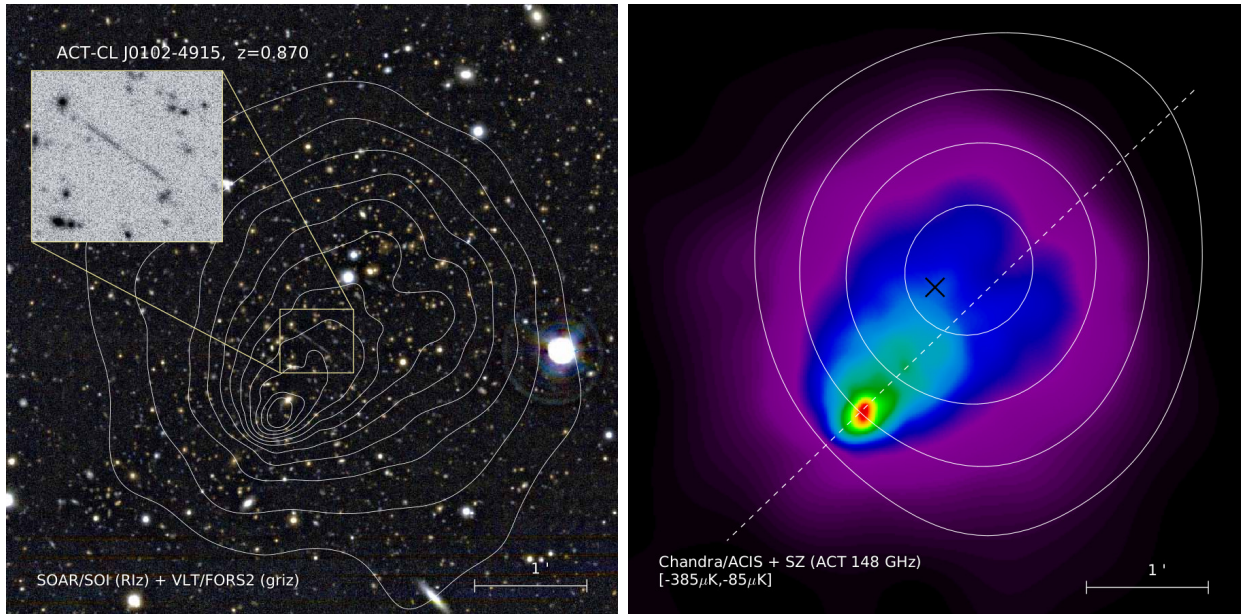


Figure 1.1: Multi-wavelength images off El Gordo cluster. The left panel shows the combined optical imaging. The white contours illustrate different X-ray flux level observed by Chanrda X-ray telescope. An overplotted image shows a noticeable strong lensing arc. The right panel is Chandra images overplotted with the contours of SZ signal at 148 GHz.

et al., 2013; Williamson et al., 2011). The SZ effect and X-ray emission of clusters will be explained with more details in following.

To provide an example of a cluster with multi-wavelength data and to show which kind of information can derived by study on a cluster, here we introduce a well studied cluster. Figure 1.1 shows the massive El Gordo cluster at $z = 0.87$ at different wavelengths. The optical observation of this cluster was done in *griz* bands by SOAR/SOI and *Riz* bands by (VLT/FORS2). In addition, the observations with Chandra Spitzer IRAC and ACT (Atacama Cosmology Telescope) respectively provided the X-ray, infra-red and SZ data (Menanteau et al., 2012). The spectroscopic redshifts of member galaxies were measured by VLT/FORS2. Menanteau et al. (2012) measured the velocity dispersion of $\sigma_v = 1321 \pm 106$ km s⁻¹ with the X-ray temperature of $T_X = 14.5 \pm 0.1$ keV and X-ray luminosity of $L_X = (2.19 \pm 0.11) \times 10^{45} h_{70}^{-2}$ erg s⁻¹ in 0.5-2.0 keV band. With a combination of measurements on X-ray temperature, SZ distortion and velocity dispersion, they derived the mass of $M_{200c} = (2.16 \pm 0.32) \times 10^{15} h_{70}^{-1} M_{\odot}$. They also put a constrain of less than 1% on total stellar content of this cluster. In following, the methods of mass estimation will be explained.

In past decades, numerous studies have been done on processes that have role in formation of observed properties of clusters (see the review of Allen, Evrard & Mantz 2011). According to the hierarchical scenario of structure formation, small systems collapse at higher redshifts when the universe was denser and then merge hierarchically to form larger haloes. Galaxy clusters are at the top of this hierarchy: they represent the most massive virialized structures in the present-day universe and may host thousands of galaxies.

The models based on hierarchical scenario reproduce well the abundance and clustering properties of galaxy clusters. In the following, we shortly explain the theory of structure formation.

1.2.1 Formation of galaxy clusters

According to the standard hierarchical structure formation scenario, objects are thought to form via gravitational collapse of peaks in the initial primordial density field characterized by the density contrast (or overdensity) field: $\delta(x) = (\rho(x) - \rho_m)/\rho_m$, where ρ_m is the mean mass density of the Universe. Properties of the field depend on specific details of the processes occurring during the earliest inflationary stage of the Universe evolution (Guth & Pi, 1982; Bardeen, Steinhardt & Turner, 1983) and the subsequent stages prior to recombination (Peebles, 1982; Bond & Efstathiou, 1984; Eisenstein & Hu, 1999). Here we suppose that the $\delta(x)$ is homogeneous and isotropic random field (Kravtsov & Borgani (2012)). Thus the properties of such a field can be fully characterized by its power spectrum, $P(k)$, where k is wave vector modulus. The variance of the overdensity field on a scale R is:

$$\langle \delta_R^2 \rangle = \frac{1}{(2\pi)^3} \int P(k) |\check{W}(k, R)|^2 d^3k, \quad (1.18)$$

where $\check{W}(k, R)$ is the Fourier transform of the filter $W(k, R)$ so $\delta_r(k) = \delta(k)\check{W}(k, R)$ (Mo, van den Bosch & White, 2010). For narrow range of k the power spectrum $P(k)$ is proportional to k^n , and the variance of overdensity is $\delta_R^2 \propto R^{-n-3}$. Since the enclosed mass within R is $M = 4\pi/3\rho_m(z)R^3$, one can replace R by M . In other words, one can define $\langle \delta_M \rangle$ instead of $\langle \delta_R \rangle$. The probability distribution function (PDF) for such density field is:

$$p(\delta_M) = \frac{1}{\sqrt{2\pi\langle \delta_M^2 \rangle}} \exp\left(\frac{-\delta_M^2}{2\langle \delta_M^2 \rangle}\right). \quad (1.19)$$

In the standard scenario of structure formation, the Gaussianity of the $\delta(x)$ is retained during early linear epochs since different modes of $\delta(k)$ grow at the same rate. The growth factor of structure $D_+(a)$ (Heath, 1977) for Λ CDM cosmology is given by the following relation:

$$D_+(a) = \frac{5}{2}\Omega_m E(z) \int_0^a \frac{da'}{[a'E(a')]^3}, \quad (1.20)$$

where $a = (1+z)^{-1}$ is the expansion factor. If the contribution from relativistic species, such as radiation or neutrinos, to the energy density is neglected and, the normalized expansion rate, $E(a)$, defined as following (similar to 1.17):

$$E(a) \equiv \frac{h(a)}{H_0} = [\Omega_m a^{-3} + (1 - \Omega_m - \Omega_\Lambda) a^{-2} + \Omega_\Lambda]^{1/2}. \quad (1.21)$$

In the models with dark energy clustering (Alimi et al., 2010) or modified gravity, the growth factor depends on the scale. When the root mean square of fluctuations approaches the value of one, the linear approximation is not valid. Later evolution can be investigated by means of nonlinear models or numerical simulations.

Nonlinear growth of fluctuations

The simplest model for nonlinear collapse is to assume a constant overdensity within a radius R . Although a real density is much complicated, such a simple top-hat model gives a comprehension about overall timescale and properties of a nonlinear collapse. In spite of its simplicity and limitations, the model provides useful insight into general features and timing of nonlinear collapse.

In this model, a spherically symmetric overdensity with initial radius R_i and initial fluctuation amplitude $\delta_i > 0$ is considered. Consequently, the mass of overdensity is $M = (4/3)\pi(1 + \delta_i)\bar{\rho}R^3$ where $\bar{\rho}$ is the mean density of the Universe at the initial time. Given the symmetry, the collapse of such perturbation is a one-dimensional problem and is fully specified by evolution of the top-hat radius $R(t)$ (Gunn & Gott, 1972; Lahav et al., 1991). Due to the gravitational force, the sphere will expand slightly more slowly than the Universe as a whole, which again will lead to an increase in its density contrast. This then decelerates the expansion rate even further, relative to the cosmic expansion rate. The equations of motion for the sphere radius are identical to the Friedmann equations for the cosmic expansion, only with the sphere having a higher value of Ω_m (Schneider, 2006). If the initial density is sufficiently large, the expansion of the sphere will come to a halt, i.e., $R(t)$ will reach a maximum t_{ta} (turnaround time). Then $R(t)$ starts to decrease and reaches the final value R_f at $t = t_{coll}$. Physically, R_f is set by the virial relation between potential and kinetic energy and is $R_f = t_{ta}/2$ in cosmologies with $\Omega_\Lambda = 0$. The turnaround epoch and the epoch of collapse and virialization are defined by initial conditions.

The final mean internal density of a collapsed object can be estimated by noting the time interval $t_{coll} - t_{ta} = t_a$ should be equal to the free-fall time of a uniform sphere (Kravtsov & Borgani, 2012). For a cosmology with $\Omega_m = 1$ and $\Omega_\Lambda = 0$ and the concordance cosmology with $\Omega_m = 0.27$ and $\Omega_\Lambda = 0.73$ (Komatsu et al., 2011) the density contrasts are:

$$\Delta_{vir} \approx \begin{cases} 178 & \text{for } \Omega_m = 1 \ \& \ \Omega_\Lambda = 0; \\ 358 & \text{for } \Omega_m = 0.27 \ \& \ \Omega_\Lambda = 0.73. \end{cases}$$

In comparison to linear growth, the density contrast of the nonlinear growth at t_{coll} is more than one hundred times larger.

The mentioned spherical collapse model provides a helpful approximation for collapse but it misses many details of halo formation from real density fluctuations. More complicated scenarios are traced using numerical cosmological simulations (Bertschinger, 1998; Dolag, Bykov & Diaferio, 2008; Norman, 2010; Borgani & Kravtsov, 2011). Figure 1.2 illustrates dark matter density field evolution in a cosmological simulation within a box of a comoving size $15h^{-1}Mpc$ on side (Kravtsov & Borgani, 2012). There are some important

differences between the top-hat collapse and the modeled collapse in cosmological simulation. First, real peaks in the primordial density field do not have the constant density or sharp boundary of the top-hat, but have a certain radial profile and curvature (Bardeen et al., 1986; Dalal et al., 2008). Thus, different regions of a peak collapse at different epochs so that the overall collapse is extended in time and the peak does not have a single collapse time (Prada et al., 2006; Kravtsov & Borgani, 2012). This point leads to some difficulties in definition of halo mass. Different type of mass definition will be discussed in following.

The second difference is that in the top-hat model, the density peaks are isolated while in reality peaks are encompassed into other density inhomogeneities. The tidal forces from the most massive and rarest peaks in the primordial density field shepherd the surrounding matter into massive filamentary structures that connect them (Bond, Kofman & Pogosyan, 1996). These filaments look like bridges between two density field peaks (Figure 1.2). The later mass growth of clusters proceeds by matter accretion along these filaments.

Finally, the density is not smoothly distributed in the space around a peak but the it has fluctuations on all scales. The matter collapse can occur simultaneously on different scales. Figure 1.2 shows that some small size collapsed regions formed at high redshift. These proto-clusters merge together and form larger and more massive virialized systems. Nonlinear interactions between smaller-scale peaks within a cluster-scale peak during mergers lead to relaxation processes and energy exchange on different scales, and mass redistribution (Kravtsov & Borgani, 2012).

1.2.2 Definition of cluster mass

The absence of a well-defined boundary for collapsed objects makes the definition of the halo boundary and the associated enclosed mass ambiguous. There are several definitions in the literature for boundaries of a cluster or more precisely boundaries of a halo. Here we explain two most useful ones: spherical overdensity and friend-of-friend (FoF). In the analyses of cosmological simulation mostly FoF mass is used but the spherical overdensity is employed in both simulation and observational studies. There are other definition of halo mass in the literature but some of them are not applicable to observations. For example, in simulation works, one can define the halo mass as a mass that will ever collapse (Cuesta et al., 2008; Anderhalden & Diemand, 2013) but measuring such a mass is not feasible in observation.

Friend-of-friend mass

Historically, the FoF algorithm was used to identify clusters of galaxies in observations (Huchra & Geller, 1982; Press & Davis, 1982; Einasto et al., 1984). After a while, it was adopted to define collapsed objects in simulations of structure formation (Einasto et al., 1984; Davis et al., 1985). This algorithm considers two particles to be members of the same group (i.e., friends) if they are separated by a distance that is less than a given linking length. The linking length, is commonly defined in units of the mean interparticle separation. Then the total mass of the linked objects is considered as the mass of halo.

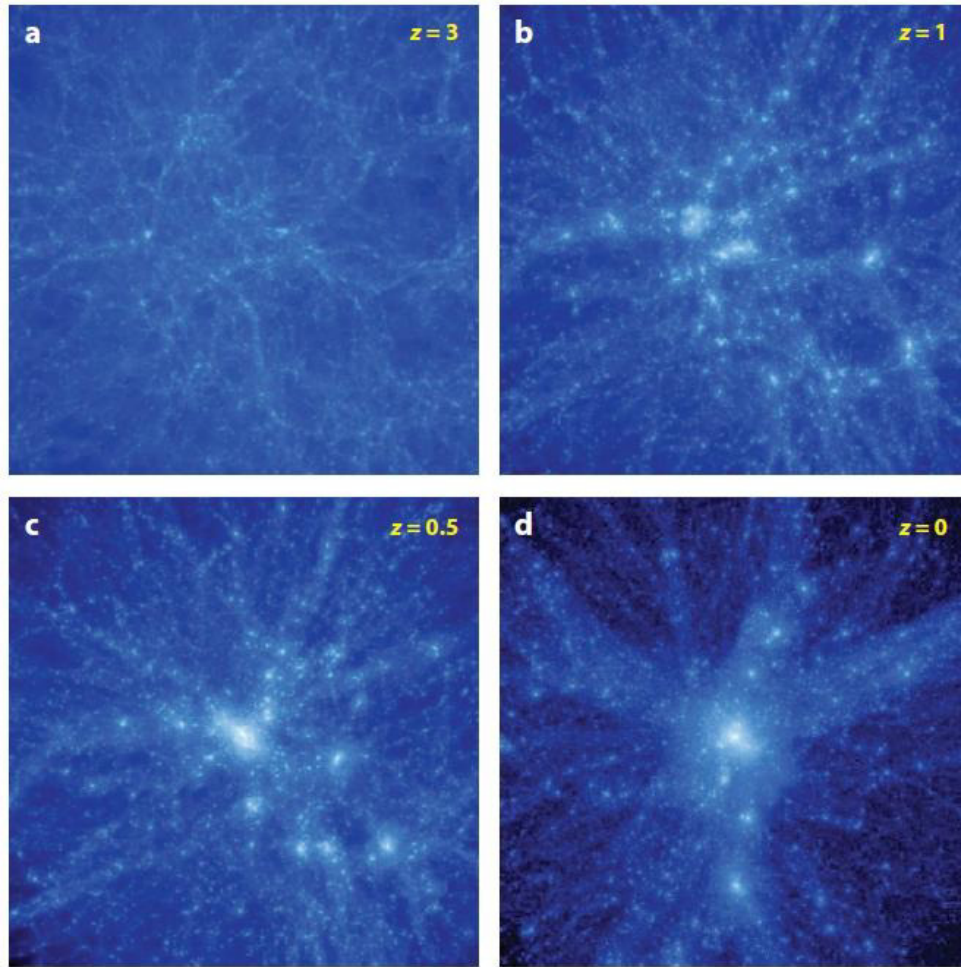


Figure 1.2: Simulation of a dark matter density field evolution through the time. The panels a, b, c, and d respectively belongs to redshifts of 3, 1 0.5 and 0. The comoving size of simulation box is $15h^{-1}Mpc$ (Kravtsov & Borgani, 2012).

The advantages of FoF method are that there is no assumption about the centre of a halo and it is applicable to the halos with different shapes. In contrast, the results of FoF are sensitive to the resolution of the data (e.g. uncertainties in spectroscopic redshifts). Another disadvantage of this method is that it may join two different halos with volume overlap between them. Since the concentration of the forming halos depends on three items of mass, redshift and cosmology, the enclosed overdensity is also a dependent of these three items.

Spherical overdensity mass

According to the spherical overdensity algorithm, the boundary of a halo is defined as a sphere of radius enclosing a given density contrast Δ with respect to the reference density

ρ . In contrast to the FoF algorithm, the definition of an SO halo also needs a definition of the halo center. In theoretical analyses, the natural choices for the center are the peak of density, the minimum of the potential, the position of the most bound particle, or, more rarely, the center of mass. Given that the center and the boundary need to be found simultaneously, an iterative scheme is used to identify the SO boundary around a given peak. The radius of the halo boundary, R_Δ , is defined by solving the equation

$$M(< R) = \frac{4}{3}\Delta\pi\rho(z)R^3. \quad (1.22)$$

where ρ is the reference physical density at redshift z , $\Omega_m \neq 1$ is the total mass profile, and r is in physical (not comoving) radius.

The choice of Δ and the reference ρ may be motivated by theoretical or by observational considerations. Note that for a Universe with $\Omega_m \neq 1$, there is a choice for reference density to be either the critical density $\rho_{cr}(z)$ or the mean matter density $\rho_m(z)$, and both are in common use. In observations, the choice may simply be determined by the extent of the measured mass profile. Thus, masses derived from X-ray data under the assumption of hydrostatic equilibrium are limited by the extent of the measured gas density and temperature profiles and are therefore often defined for the high values of overdensity: $\Delta_c = 200$ or 500 .

The important difference from the FoF algorithm is the fact that the SO definition forces a spherical boundary on the generally nonspherical mass definition. Furthermore, spheres corresponding to different halos may overlap, which means that a certain fraction of mass may be double counted. However, this amount of mass is practically small in comparison to the halos mass (Tinker et al., 2008).

The noteworthy advantage of the SO algorithm is that the SO-defined mass can be measured both in simulations and in observational studies of clusters. In the observational analyses, the SO mass can be estimated from the total mass profile derived from the hydrostatic and Jeans equilibrium analysis for the ICM gas and galaxies, respectively (see § 1.2.4) or gravitational lensing analyses (see § 1.8). In addition, suitable observables that correlate with the SO mass with scatter of less than 10% can be defined. Therefore, making this mass definition preferable in the cosmological interpretation of observed cluster populations. The small scatter indicates that the effects of triaxiality are quite small in practice. Note, however, that the definition of the halo center in simulations and observations may not necessarily be identical, since in observations the cluster center is usually defined at the position of the peak or the centroid of X-ray emission or SZ signal, or at the position of the BCG.

1.2.3 Abundance of galaxy cluster

Usually galaxy clusters are characterized by properties, such as X-ray luminosity, which are derived almost directly from observables. But these properties are less sensitive in theoretical models and they are also affected by some processes in intracluster gas which are not fully understood. Thus, the prediction of halo abundance are usually characterized as

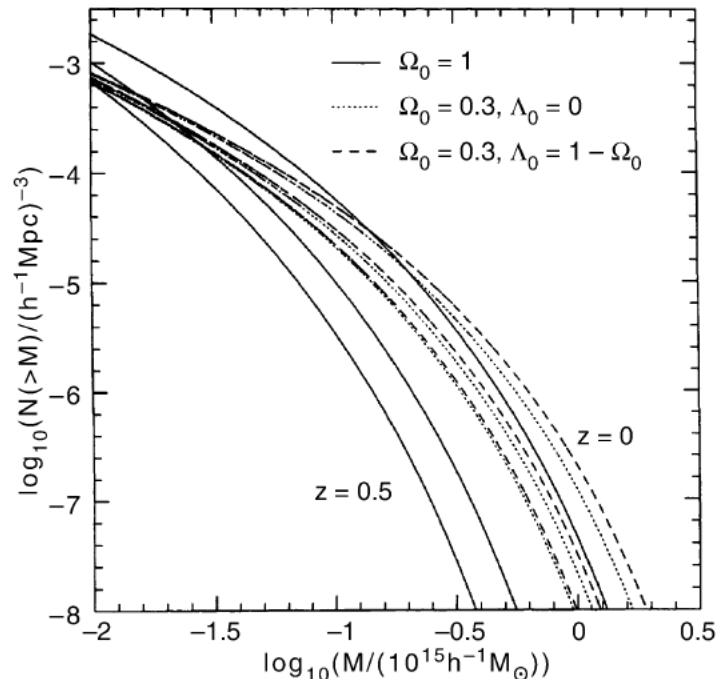


Figure 1.3: Number density of the halos more massive than M derived from Press-Schechter model. Three sets of curves illustrate the comoving number density at redshifts $z = 0$ (upper), $z = 0.33$ (middle), and $z = 0.5$ (lower). Three line types represent three different cosmological models: the Einstein–de Sitter universe (solid line), an open model with $\Omega_m = 0.3$ and $\Omega_\Lambda = 0$, and a universe with $\Omega_m = 1 - \Omega_\Lambda$ and $\Omega_\Lambda = 0.7$ (Schneider, 2006).

a function of mass. The mass function $dn(M, z)$ is the volume number density of the halos with mass between M and $M + dM$ at a redshift z . Then, using scaling relations between halo mass and observables, the prediction of mass function is linked to the observed cluster abundance. Press & Schechter (1974) presented the first statistical model for prediction of halo mass abundance. According to *Press-schechter model*, the mass function of collapsed objects directly determined by the properties of initial spectrum of fluctuations.

Figure 1.3 illustrates the halo mass function for different cosmologies and redshifts. $n(M, z)$ is exponentially decreasing at large M because for large smoothing length, high peaks are very rare. So, there are very few clusters with $M > 2 \times 10^{15} M_\odot$.

1.2.4 Methods of detection and mass measurement

There are several methods for detecting and mass measurement of galaxy clusters: detection of overdensity of red galaxies in optical data using the red-sequence method (e.g. Gladders & Yee 2000; Koester et al. 2007), detection of X-ray emission from hot gas in the clusters (e.g. Finoguenov et al. 2009), measurement of weak gravitational lensing signal (e.g. Miyazaki et al. 2007), and spectroscopic selection of cluster (e.g. Gerke et al. 2012;

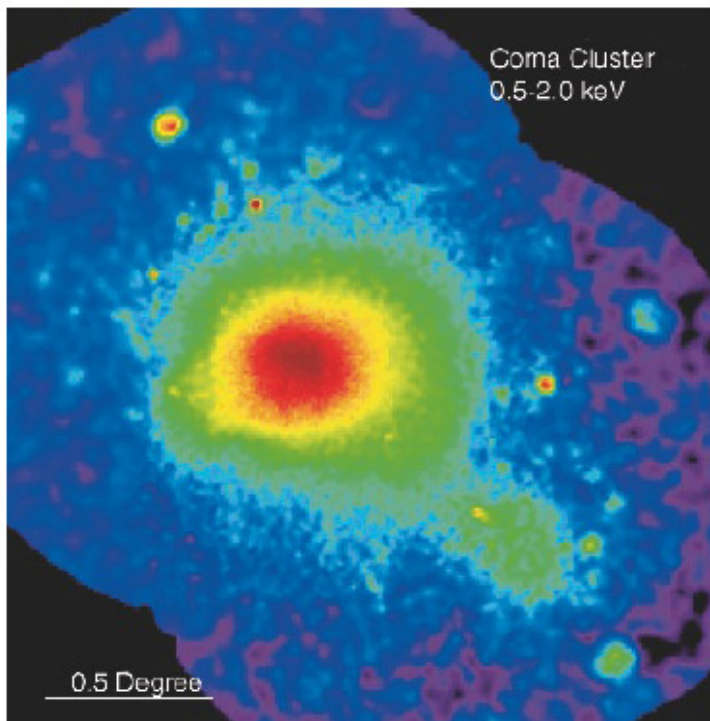


Figure 1.4: X-ray image of Coma cluster observed by ROSAT. The size of image is $2.7^\circ \times 2.5^\circ$ (Schneider, 2006).

Knobel et al. 2012). In following sections, each method is described briefly.

X-ray emission of galaxy clusters

The detection of X-ray emission from massive galaxy clusters was one of the most important discoveries of UHURU X-ray satellite (Schneider, 2006). In recent decades, thousands of galaxy clusters have been observed in X-ray by ROSAT, XMM-Newton and Chandra X-ray satellites. Figure 1.5 is the X-ray image of Coma cluster taken by ROSAT telescope in 0.5 – 2.0 keV band. Beside AGNs (active galactic nuclei), galaxy clusters are the most luminous X-ray sources. The X-ray luminosity of clusters is between 10^{43} to 10^{45} erg/s for the least massive and the most massive ones, respectively.

The spatial size of the region from which X-ray photons are detected is about 1 Mpc so it can not originate from individual galaxies. The spectral energy distribution of the X-rays leads to the conclusion that the emission process is optically thin thermal bremsstrahlung (free-free radiation) from a hot gas. The bremsstrahlung is a electromagnetic radiation produced by acceleration of a charged particle. The X-ray photons are emitted by acceleration of free electrons in Coulomb field. The Coulomb field is produced by protons and atomic nuclei of ionized gas. The temperature of the ionized gas in galaxy clusters can be estimated by the spectral energy distribution of X-ray emission. This temperature is in the range of $10^7 - 10^8$ K ($1 - 10$ keV) for clusters in the mass range of $10^{14} - 10^{15} M_\odot$.

For an ionized gas with number density of electrons n_e and number density of ions n_i , the emissivity of bremsstrahlung is given by:

$$\epsilon_\nu^{ff} = \frac{32\pi Z^2 e^6 n_e n_i}{3m_e c^3} \sqrt{\frac{2\pi}{3k_B T m_e}} e^{-h\nu/k_B T} g_{ff}(T, \nu) \quad (1.23)$$

where e is the charge of proton, Z is the charge of ions, and m_e is the electron mass. The Gaunt factor $g_{ff}(T, \nu)$ is given by:

$$g_{ff}(T, \nu) \approx \frac{3}{\sqrt{\pi}} \ln \left(\frac{9k_B T}{4h_p \nu} \right). \quad (1.24)$$

This spectrum is flat for $h_p \nu \ll k_B T$. For $k_B T < h_p \nu$, it exponentially decreases.

In order to derive the properties of ICM using X-ray observation, the distribution of the gas should be modeled. The speed of sound for a gas with pressure P and density of ρ_g is $c_s = \sqrt{\frac{P}{\rho_g}}$. For ICM gas,

$$c_s \approx \sqrt{\frac{nk_B T}{\rho_g}} = \sqrt{\frac{k_B T}{\mu m_p}} \approx 1000 \text{ km s}^{-1} \quad (1.25)$$

where n is the number density of particles and $T \sim 10^8$ K. The average molecular mass μ is defined as average mass of a gas particle in units of the proton mass. Since the mass of electron is negligible in comparison to the mass of proton, $\mu \sim 0.5$ for fully ionized hydrogen and $\mu \sim 0.63$ for cluster gas including hydrogen, helium and heavier elements.

Because the sound-crossing time for a cluster is much smaller than the lifetime of the cluster, it can be assumed that the gas is in hydrostatic equilibrium. In the case of a gas in hydrostatic equilibrium, the gas pressure force is balanced by gravitational force, so

$$\nabla P = -\rho_g \nabla \Phi \quad (1.26)$$

where Φ is the gravitational potential. Note that the Φ is related to the total mass (not just the mass of gas). Assuming a spherically symmetric distribution for gas density and total mass, equation 1.26 can be written in the form of

$$\frac{1}{\rho_g} \frac{dP}{dr} = -\frac{d\Phi}{dr} - \frac{GM(r)}{r^2}. \quad (1.27)$$

where Φ is produced by total mass M_r . By replacing the pressure term using $P = nk_B T = \rho_g k_B T / (\rho m_p)$, we obtain:

$$M(r) = -\frac{k_B R r^2}{G \rho m_p} \left(\frac{d \ln(T)}{dr} + \frac{d \ln(\rho_g)}{dr} \right). \quad (1.28)$$

this relation indicates that the total mass profile $M(r)$ can be derived by measuring the profiles of ρ_g and T .

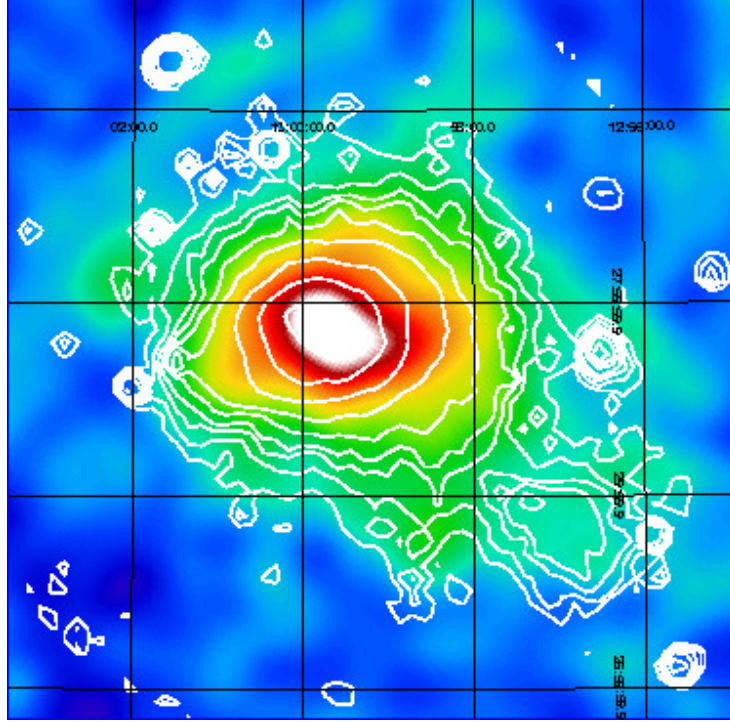


Figure 1.5: Planck y -map of Coma on a $\sim 3 \text{ deg} \times 3 \text{ deg}$ patch with the *ROSAT-PSPC* iso-luminosity contours overlaid (Planck Collaboration et al., 2011).

The most common model for fitting the X-ray data is β -model which is based on the assumptions that the total mass profile has a isothermal distribution and the gas temperature is independent of radius. These two assumption in combination of equation 1.28 lead to following form of gas density profile:

$$\rho_g(r) \propto \rho_g^\beta \quad (1.29)$$

where,

$$\beta := \frac{\mu m_p \sigma_v^2}{k_B T_g}, \quad (1.30)$$

σ_v is velocity dispersion of dark matter sub-halos or galaxies. The index β is proportional to the ratio of dynamical temperature and gas temperature.

The Sunyaev–Zeldovich effect

The CMB photons are scattered by electrons in hot intracluster gas. Although the optical depth and so the probability of Compton scattering is low for such an effect, its observation is feasible. During the Compton scattering of photons by hot electrons, on average the energy transferred from the electrons to the photons, so the frequency of the photons increases. This effect is called *Sunyaev–Zeldovich effect* (Sunyaev & Zeldovich, 1970).

The change in the intensity of CMB radiation is determined by the *Compton-y*:

$$y = \int dl \frac{k_B T_g}{m_e c^2} \sigma_T n_e \quad (1.31)$$

where $\sigma_T = 4\pi e^4 / (3m_e^2 c^4)$ is the Thomson cross section for electrons. y is proportional to the integrated gas pressure $P = nk_B T$ through the cluster along the line of sight. Analyzing the spatially resolved SZ effect of clusters provides the information about the projected profile of density and temperature of ICM. The integrated Compton parameter is the SZ signal of cluster:

$$Y = \int y dA \quad (1.32)$$

where dA is the projected area of cluster.

Since the X-ray emissivity is proportional to n_e^2 , the X-ray emission is more sensitive to the gas density distribution and small-scale clumps strongly increase the X-ray emission. In contrast, SZ effect is proportional to n_e so it is less sensitive to inhomogeneities in ICM density. Another important point about the SZ effect is that although the surface brightness of an object fades by a factor $(1+z)^{-4}$, the intensity of CMB photons varies by $a^{-4} = (1+z)^4$. Thus, the signal of SZ effect from clusters is almost independent of redshift. Figure 1.6 compares the mass versus the redshift distribution of two important SZ selected cluster surveys, South Pole Telescope (SPT) and Planck, with ROSAT cluster catalog. The mass measurements with the SZ effect is complicated by some challenges such as the identification and removal of radio point sources (Vale & White, 2006), and possibly a larger scatter in the Y -mass relation caused by feedback processes (Shaw, Holder & Bode, 2008).

Gravitational lensing

A gravitational lensing effect refers to a bending (lensing) of light from a source when it travels towards an observer through a curved space-time around a mass distribution. The papers by Chwolson (1924), Frantisek Klin (1936), and Einstein (1936) are credited as being the firsts to discuss the gravitational lensing effect. In 1986, two unusually arc-shaped sources were discovered in two clusters. Figure 1.7 illustrates similar features in cluster Abell 2218. At that time, the nature of the arcs was unknown and different hypotheses for explaining them were formulated. The spectroscopy of one of the arcs revealed that it is located at much higher redshift in comparison to the cluster and it is a background source which is affected by *gravitational lens* of the cluster. Figure 1.8 schematically shows the light paths from a source behind a gravitational lens.

Spacetime around a massive object such as a cluster is curved, and as a result light rays from a background source propagating through spacetime are bent. By differential light deflection, the light beam of the source can be distorted in such a way that highly elongated arc-shaped images are produced. The lensing effect can also magnify and distort the image of the background source.

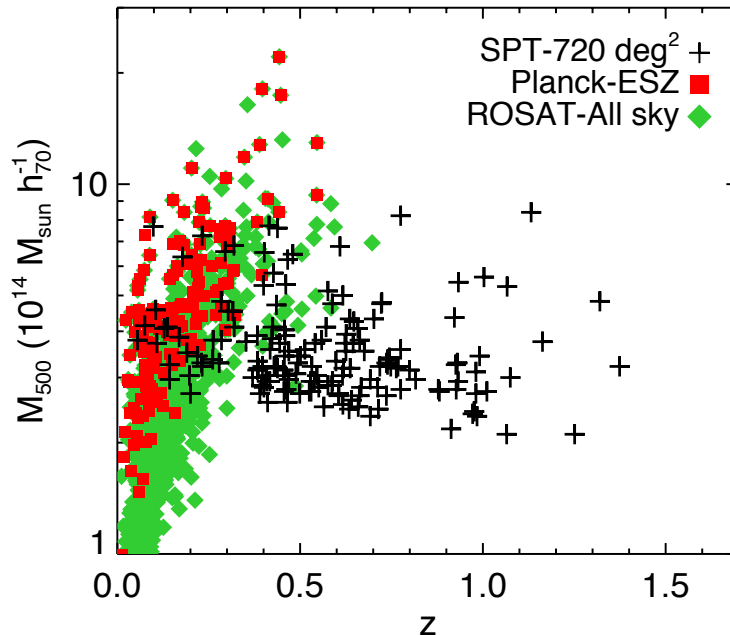


Figure 1.6: Mass as a function of redshift for three major cluster samples (Reichardt et al., 2013): SZ-selected galaxy clusters from the South Pole Telescope (SPT) survey, SZ-selected galaxy clusters from the Planck survey (Planck Collaboration et al., 2011), and X-ray-selected galaxy clusters from the ROSAT all-sky survey (RASS) (Piffaretti et al., 2011). Since the SPT uniquely have high-resolution SZ detection, its cluster sample is a nearly redshift independent selection function. In contrast, the redshift dependent selection of Planck survey is caused beam dilution. The redshift dependence of X-ray surveys such as ROSAT catalog is due to cosmological dimming.

The gravitational lensing is the simplest technique in terms of the underlying physics and is the only method for which the total halo mass can be directly probed, independently of both the baryons and the dynamical state of the cluster. Thus, measuring the scaling relations between X-ray and SZ properties versus the lensing mass of clusters is critical for improving cosmological constraints derived with the halo mass function and also for understanding the physical processes that control the heating and cooling of the ICM. Leauthaud et al. (2010) used a sample of 206 X-ray-selected galaxy groups to investigate the scaling relation between X-ray luminosity (L_X) and halo mass (M_{200c}) where M_{200c} is derived via stacked weak gravitational lensing.

$$\frac{M_{200}E(z)}{M_0} = A \left(\frac{L_X E(z)^{-1}}{L_{X,0}} \right)^\alpha, \quad (1.33)$$

where $L_{X,0} = 10^{42.7} \text{ erg s}^{-1}$ and $M_0 = 10^{13.7} M_\odot$ are characteristic X-ray luminosity and mass of the relation, $\log(A) = 0.03 \pm 0.06$, $\alpha = 0.64 \pm 0.03$.

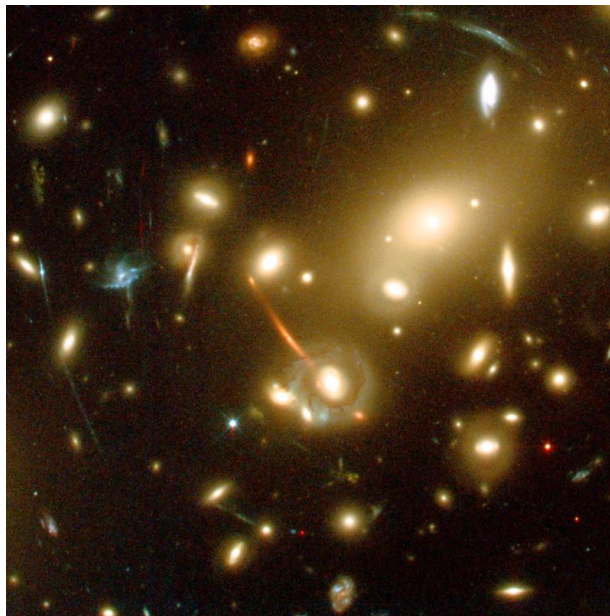


Figure 1.7: Example of gravitational lensing features in Abell 2218.

Red sequence method

The galaxies in a cluster form a well-defined nearly horizontal sequence if one plots the color versus the magnitude of the cluster galaxies. Since this sequence is populated by red (early-type) galaxies, it is called red sequence. This tight sequence indicates that at least the red galaxies in a cluster have almost the same ages. The location of the sequence in color–magnitude space depends on the redshift of cluster and roughly speaking, higher redshift clusters have redder sequence. Using the red sequence method, one can measure the redshift of clusters with accuracy between $\delta z \sim 0.01$ to 0.05 depending on the quality of the optical data and the cluster redshift. Since the most prominent spectral feature of early-type galaxies is the 4000 \AA break, the best filters for deriving the color of red sequence are those encompassing this break. In Chapter 2, we will describe this method in detail and apply it on our optical data.

Spectroscopic cluster detection

As mentioned in the section of FoF mass definition, Huchra & Geller (1982); Press & Davis (1982); Einasto et al. (1984) introduced and applied a method for identifying clusters using redshift surveys by searching for nearby neighbor galaxies around each galaxy. In FoF algorithm, the friendship between two objects means that they belong to the same group or cluster. Two objects are friends if the distance between them is less than a given linking length. The linking length is the free parameter of the method and can be defined according to the mean galaxy distance in the field. This method is implemented for finding the overdensity of galaxies and dark matter particles in observations and N-body

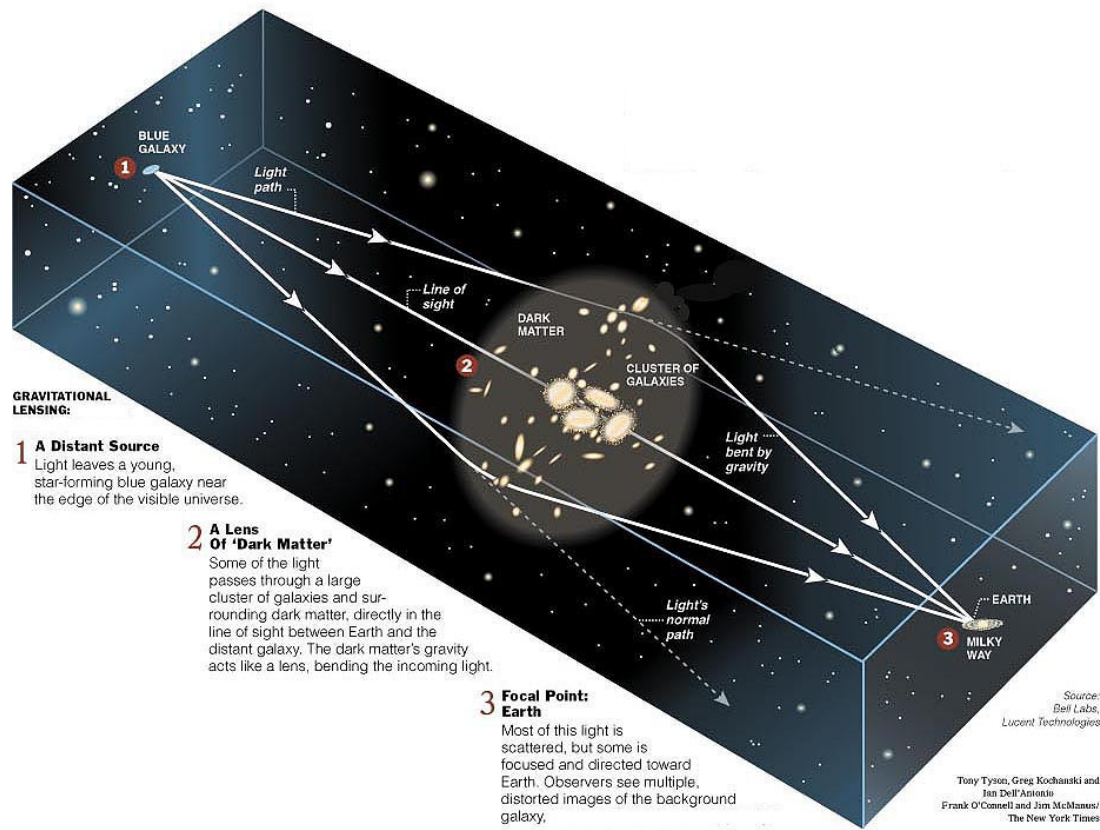


Figure 1.8: Geometry of a gravitational lens system.

simulations, respectively.

1.3 Galaxies

In this section, we explain the most important properties of galaxies and the processes playing roles in formation and evolution of galaxies. A dynamically bound system consisting many stars is a galaxy. The number of stars can vary from $\sim 10^7$ stars in dwarf to $\sim 10^{14}$ stars in giant galaxies. Besides stars, a galaxy also contains dark matter, star clusters, interstellar medium, stellar remnants and planets.

1.3.1 Classification

The classification of galaxies depends on the type of observation according to which the classification is made. The first classification is a morphological one which was invented by Edwin Hubble using the optical photometry and it is still be most common today. Figure 1.9 shows this classification known as Hubble sequence. In Hubble sequence, the galaxies divided into three main types. The first type (left side of figure 1.9) are *Elliptical* galaxies

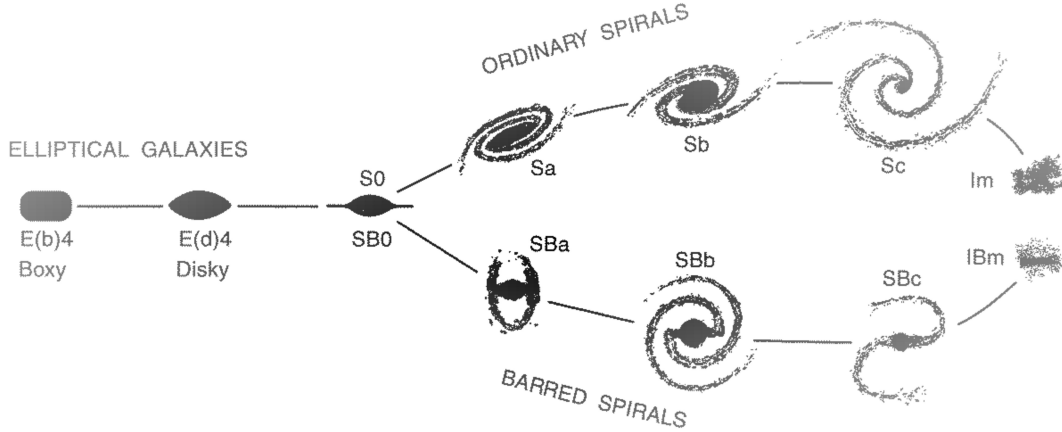


Figure 1.9: Hubble sequence.

(E). These galaxies have isophotes similar to ellipse shape without any clear substructures. The galaxies in elliptical class are also subdivided according to their ellipticity, $\epsilon = 1 - a/b$, where a and b are the semi-major and semi-minor axes, respectively. The subclasses E_n is defined as $n = 10\epsilon$ for example galaxies with $\epsilon = 0.4$ belongs to subclass of E_4 .

The second type is *spiral galaxies* which consists of a central bulge and disk structure with spiral arms. Normal spirals (S) and barred spirals (SB) are subclass of spiral galaxies. For each subclasses, the ratio between the brightnesses of bulge and disk defines the sequence. The third type is *irregular* (Irr) galaxies with weak (Irr I) or no (Irr II) regular structure. The final category is *S0* or lenticular which is a transition between spiral and elliptical.

Historically the mentioned classification was done by eyeball inspection. Using the images of galaxies, one can define some quantities for automatic morphological classification of galaxies. The earliest works on studying the surface brightness profiles are done by Reynolds (1913) and Hubble (1930). They fitted the brightness profile of galaxies with a number parameters including characteristic radius, characteristic surface brightness and few other ones for the shape of the profile. de Vaucouleurs (1948) profile has been widely used in the literature. In this profile, the surface brightness of a galaxy declines proportional to $r^{1/4}$ where r is the distance from the centre. A generalized version of de Vaucouleurs profile, Sérsic profile (Sérsic 1963; Sérsic & Pastoriza 1967), is the most common for describing the light profile of galaxies:

$$I(r) = A \exp\left[-\left(\frac{r}{r_e}\right)^{1/n}\right], \quad (1.34)$$

where $I(r)$ is the surface luminosity at distance r from the centre, r_e is the radius that encloses half of the light of galaxy (half-light radius or effective radius), and n is Sérsic index. The dwarf ellipticals have n between 1 and 2 while ellipticals with intermediate luminosity have n value between 2 and 4. For giant ellipticals the n can reach to the values

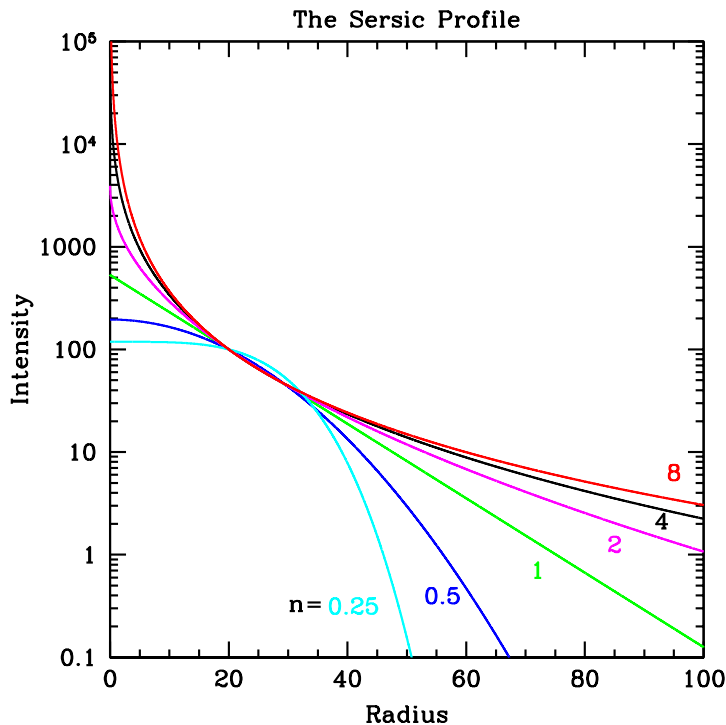


Figure 1.10: Sérsic profile, where r_e is held fixed. The profiles with higher Sérsic values have steeper central core and extended wings. Therefore, extended wings of large Sérsic values are sensitive to sky background subtraction. In contrast, the profiles with low Sérsic index have flatter core and more sharply truncated wings (Peng et al., 2010).

above 4 (Caon, Capaccioli & D’Onofrio 1993; Graham et al. 1996; Graham & Guzmán 2003; Hoyos et al. 2011).

Most of the elliptical galaxies appear in optical bands suggesting that they have old stellar population. Some elliptical galaxy have detectable X-ray, H_α , and HI (21-cm) emissions from hot gas ($\sim 10^7$ K), warm gas ($\sim 10^4$ K), and cold gas ($\sim 10^2$ K). But the mass-fractions of gas and dust in elliptical galaxies are much lower in comparison with spiral galaxies.

A large fraction of elliptical galaxies have visible amount of dust in disk shape. By exploring the color gradients of elliptical and S0 galaxies, one can show that the metallicity increases toward the centre in these types of galaxies. The disk of S0 galaxies is also bluer than their bulge. The observations with Spitzer Space Telescope also indicate that S0 galaxies contains spatially extended distribution of warm dust.

The later type galaxies are bluer in optical bands, for example $B - V$ colors of Sa, Sc, and Irr are ~ 0.75 , 0.52 and 0.4 . This suggests that fraction of young stars increases toward later types. Generally, later type galaxies have larger fraction of gas which are required for star formations. The amount of gas can be measured via observation of 21-cm emission of HI and also HII and CO emissions. For example, the ratio M_{gas}/M_{tot} for Sa, Sb, Sc and Irr

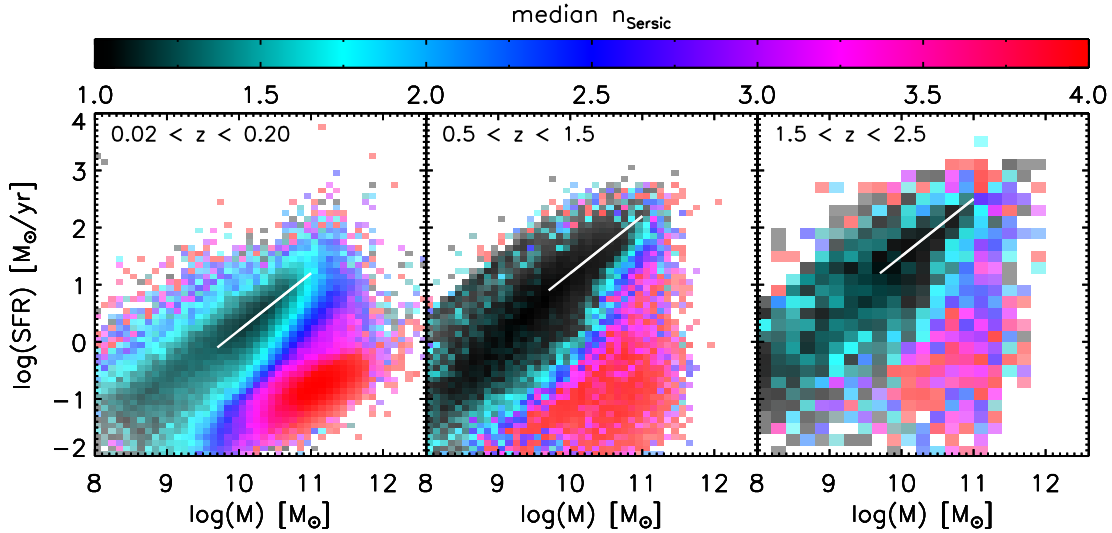


Figure 1.11: Star formation rate versus stellar mass for different redshift ranges. The color code shows the Sérsic index (Wuyts et al., 2011).

galaxies are $\sim 0.04, 0.08, 0.16$ and 0.25 respectively. In comparison with elliptical galaxies, the color gradient has the same trend towards the centre, the red central regions and bluer at outer regions. The first reason is that the metallicity increases toward the centre and stars with higher metallicity are redder. The second reason is related to distribution of gas in the spiral galaxies. Since the gas fraction in the arms are higher, more star formation occurs in the arms in comparison with the bulge. Therefore, the fraction of young and blue stars is higher in the outer regions. It is worth mentioning that for spiral galaxies, the metallicity increases with luminosity.

Figure 1.11 illustrates the distribution of galaxies in star formation rate versus stellar mass space at different redshift ranges. The color code for each galaxy represents the Sérsic value. The star forming galaxies formed a sequence called *main sequence* in star formation rate – mass plane. The slope of the sequence is ~ 1 but it has a zero point that increases with look-back time. While the surface brightness profile of star-forming galaxies are well described by Sérsic index of 1 (exponential disk), galaxies with low star formation rate (passive galaxies) are characterized by Sérsic value of ~ 4 (de Vaucouleurs profile).

1.3.2 Luminosity and stellar mass functions

In this section, we introduce the luminosity and stellar mass functions of galaxies in the local Universe (Blanton & Moustakas, 2009). We also mention the general information which can be derived from these functions. The luminosity function (LF) which is defined as the number density as a function of luminosity is a fundamental measurement of galaxy population. The upper left panel in Figure 1.13 is the r -band LF for galaxies in SDSS (Blanton et al., 2005b). The late-type population includes all blue or star-forming galaxies.

The other galaxies are considered as early-type and split into concentrated ($n > 2$) and diffuse ($n < 2$) early-types. The density of the late-type galaxies is higher at the faint end but at the bright end the early-types are dominant.

The upper right panel of Figure 1.13 illustrates the stellar mass function. Since the ratio of stellar mass to light is higher for early-type galaxies in comparison to late-types, the stellar mass function accentuates the distinction between the blue and red populations. Thus, the dominance of early-type galaxies at high mass end of mass function are even more severe in comparison with bright end of the luminosity function. A solid curve shows the double Schechter fit of Baldry, Glazebrook & Driver (2008).

The near-UV luminosity function, which traces recent star formation, is illustrated in the lower left panel of Figure 1.13. The near-UV luminosity is obtained by matching the SDSS sample to GALEX data (Martin et al., 2005). The smooth black line is their full luminosity function. The blue, star-forming galaxies completely dominate the UV luminosity of the Universe.

Finally, the Schechter function fitted to HI mass functions of Springob, Haynes & Giovanelli (2005) are shown in lower right panel. Since most of elliptical galaxies have very low content of atomic gas, this sample is limited to spiral galaxies. It is worth mentioning that some of the elliptical galaxies have significant content of ionized gas (Mathews & Brighenti, 2003). Using visual inspection, this sample is divided to late-type subclasses. The most noticeable effect mass cut-off in HI mass function is significantly lower than stellar mass function which means that massive galaxies are mostly dominated by star and not atomic gas (e.g. neutral hydrogen) but the mass fraction of atomic gas is much higher at low stellar masses.

1.3.3 Environmental dependence of galaxy properties

All properties of galaxies are strongly correlated with the local environment – whether a galaxy is located in a void, poor group or a cluster. One of the most fundamental correlations between the properties of galaxies and their host environment in the local Universe is the so-called morphology-density relation Dressler (1980). The morphology-density relation expresses the relation between the occurrence of specific Hubble types (Fig. 1.9) and the local density. The relation shows that disc-dominated (late-type) galaxies tend to reside in lower density region of the Universe, opposite to elliptical and lenticular galaxies (Fig. 1.12). Postman & Geller (1984) extend this relation to group regime and strengthen the hypothesis of group environment effect on its galaxy population. Another pieces of empirical evidence supporting this claim is the observation by Butcher & Oemler that galaxy clusters consist of a higher fraction of blue galaxies at progressively higher redshift, the so-called Butcher-Oemler effect (Butcher & Oemler, 1978, 1984). Since these early papers, Butcher-Oemler effect has been confirmed photometrically and spectroscopically (e.g. Rakos & Schombert 1995; Margoniner et al. 2001; Goto et al. 2003; Lavery & Henry 1986, 1988; Poggianti et al. 2006), and has been extended to galaxy groups (e.g. Allington-Smith et al. 1993; Wilman et al. 2005; Gerke et al. 2007; Cucciati et al. 2010). The blue colors of galaxies is mostly created when galaxies are involved in merging or tidal

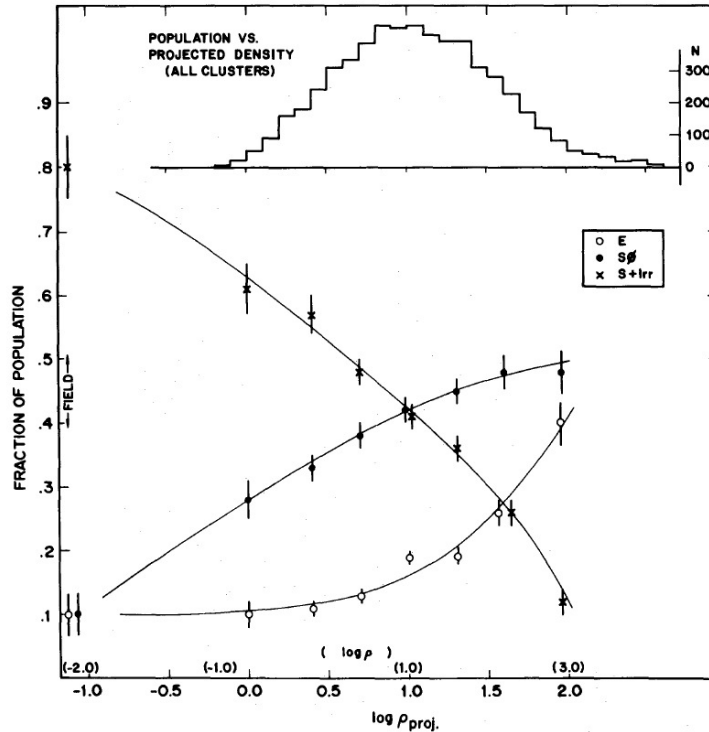


Figure 1.12: Morphology-density relation (Dressler, 1980). The fraction of elliptical and lenticular galaxies (Es and S0s) increases as a function of projected density while the fraction of Spiral and Irregular galaxies (S+Irr) decreases with increasing density.

interactions which indicate that Butcher-Oemler effect is a proxy of the transformation of spiral galaxies to Elliptical/S0.

Now large data sets shed light on details of these dependences. One method for quantifying the environment parameter is to count the neighbor galaxy above a luminosity threshold. Blanton & Moustakas (2009) estimates the environment using the number of neighboring galaxy, N_n , with $M_r - 5 \log 10 h < 18.5$, a velocity of 600 km s^{-1} , and within a projected distance of $500 h^{-1} \text{ kpc}$. The adopted luminosity threshold is roughly that of the Large Magellanic Cloud. Most of galaxies with the luminosity of $0.01 L_* < L < L_*$ are located in the lowest density environments. In contrast, the most massive galaxies are in dense regions. These points indicate the variation in the shape of luminosity function from voids (Hoyle et al., 2005) to average density regions (Blanton et al., 2005a), and to galaxy clusters (Popesso et al., 2005). Figure 1.14 represents the galaxy stellar mass function of optically selected groups with different N_n ranges. Even at low dense regions the density of early-type galaxies are substantial and in the high dense region the population of massive galaxies is completely dominated by this type. The characteristic mass of early-type population also increases with the density. Regardless of density of a region, the fraction of the blue disk galaxies is significant the at low mass part of mass functions.

Besides color, more detailed properties of galaxies, such as $D_n(4000)$, show the varia-

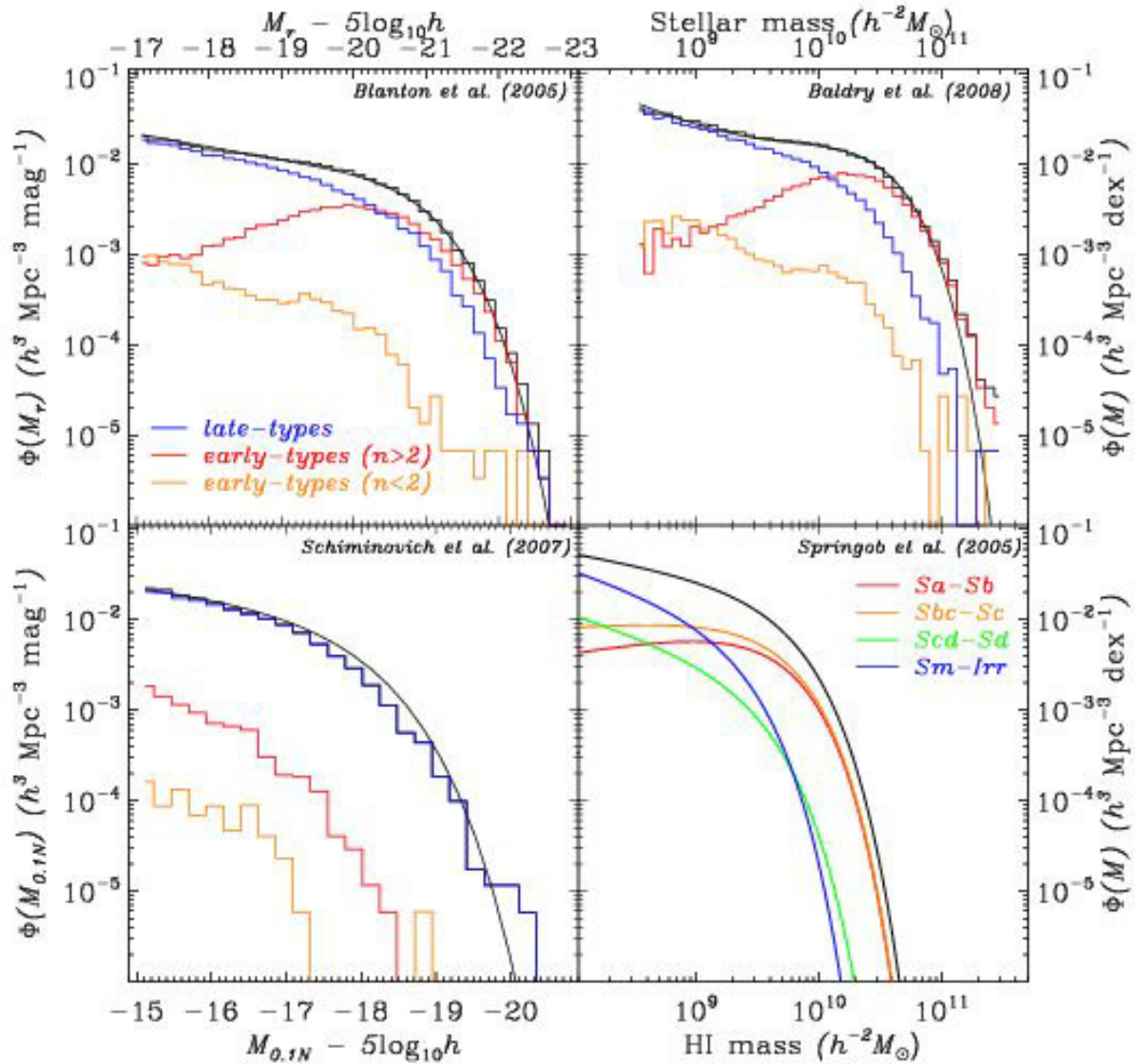


Figure 1.13: Luminosity and mass functions of galaxies in the local Universe. The upper left panel illustrates the r-band luminosity function of all populations of galaxies, late-types, concentrated early-types and diffuse early-types with black, blue, red, and orange histograms (Blanton & Moustakas, 2009). A smooth curve shows the double Schechter function fit. The upper left panel belongs to stellar mass function of the same galaxies with similar color code. The GALEX near-UV luminosity functions for several types of galaxies and the fit to the full luminosity function from Schiminovich et al. (2007) are shown in the bottom left panel. The HI mass function fits from Springob, Haynes & Giovanelli (2005) for all galaxies and as a function of morphological type are illustrated in the lower right panel.

tion with the environment. The index $D_n(4000)$, a measure of the 4000-Å break, traces the stellar population age. Kauffmann et al. (2004) found that galaxies with old stellar populations preferentially located in dense regions. Measurement of the Sersic index (e.g., Blanton et al. 2005c; Yang et al. 2007), star-formation rate, and H_α emission (e.g., Lewis et al. 2002; Norberg et al. 2002; Gómez et al. 2003; Boselli & Gavazzi 2006) change with environment and also track the segregation of galaxy types.

Some studies show that controlling variables of all these properties are those related to mass and star-formation history – not those having to do with structure (Kauffmann et al., 2004; Blanton et al., 2005c; Christlein & Zabludoff, 2005; Quintero et al., 2006). Once galaxies are appropriately classified (e.g. according to star-formation history) one finds that the scaling laws of galaxies are weak functions of environment. For instance, Park et al. (2007) classifies the galaxy using the color and color gradients selection. Then they figure out that the scaling relations of each types weakly depend on environment. The study of (Ball, Loveday & Brunner, 2008) show that for a fixed galaxy color, there is no relation between the artificial neural network determination of morphology and the environment. Similar results are concluded by Bamford et al. (2008) and van den Bergh (2002) using eyeball classifications of galaxies.

Although most of the studies show no strong difference between the galaxies with a given type but at different environment, there are some exceptions. For example, central galaxies of the clusters appear to be special galaxies. Most of them are very similar to other early-type galaxies but their position in the centre of clusters seems to be substantial in their properties. The most luminous galaxies in the dense regions tend to be larger and more diffuse suggesting the role of multiple dry mergers with red galaxies in the formation of central galaxies (Blanton et al., 2005c).

In past few years, studies on environmental dependence of galaxies properties extended to high redshift. A recent study on a sample of optically selected clusters at redshift ~ 1 shows higher fraction of quiescent galaxies in clusters with respect to the field but no clear difference between the shape of stellar mass function in field and clusters (van der Burg et al. 2013). In contrast, there is a feature in the shape of GSMF for passive field galaxies with $\log M_*/M_\odot < 10.5$. This feature shrink gradually by increasing of halo mass.

Giodini et al. (2012) illustrate that the fraction of star-forming galaxies increases with redshift in all environments but the shape of their GSMF are the same in all host halos. Giodini et al. (2012) also fitted Schechter function on the mass function of star-forming galaxies and showed that characteristic mass of star-forming galaxies in lower mass groups is 50% higher than the same parameter in higher mass group (clusters). In other words, at redshift 0.2-0.4 the bulk of star-forming galaxies in low mass groups ($M_{200} \leq 6 \times 10^{14} M_\odot$) is more massive than the bulk of star-forming galaxies in more massive clusters. Therefore, it seems that quenching mechanisms in low mass groups is less efficient than in higher mass clusters.

The outline of this thesis is described in following. We present the catalog of X-ray selected clusters in CFHTLS wide fields in Chapter 2. The clusters are observed by XMM-Newton or ROSAT X-ray satellites. In this chapter, the red sequence method for measuring the redshift of clusters is explained. We also present the scaling relations between X-ray

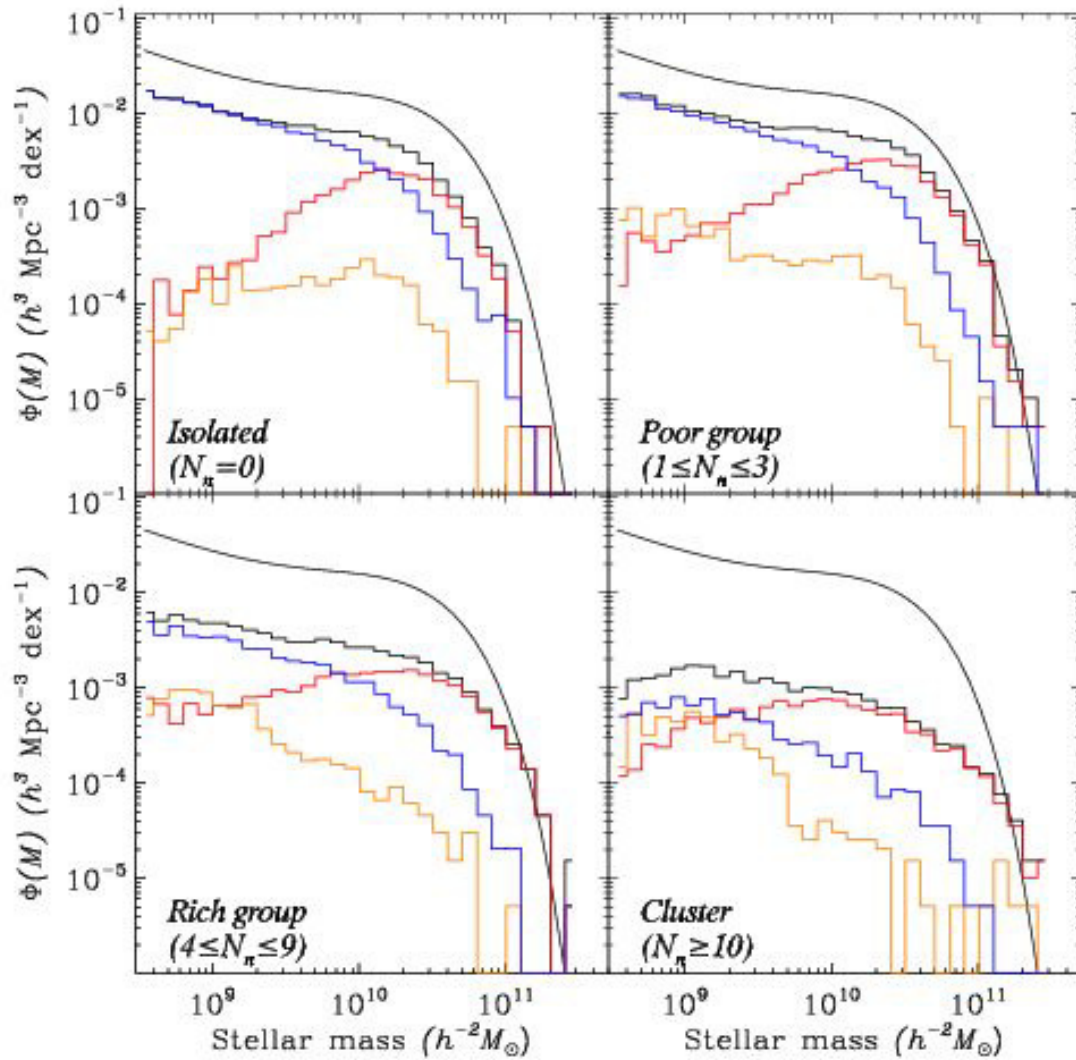


Figure 1.14: Stellar mass function of galaxies in different environments. The classification of galaxies are the same as Figure 1.13. The top left, top right, bottom left, and bottom right panels correspond to isolated, poor groups, rich groups and clusters respectively (Blanton & Moustakas, 2009). The black smooth curve is the double Schechter function fitted to whole galaxy population in the local Universe (Baldry, Glazebrook & Driver, 2008).

luminosity of clusters versus stellar luminosity and the galaxy velocity dispersion. In Chapter 3, we provide the analysis of dependence of galaxy stellar mass function on halo mass of clusters. In this work, we use the X-ray selected clusters in CFHTLS and COSMOS surveys up to redshift 1. The characteristics of central and satellite galaxies are compared at different redshift and halo masses. We also explore the uncertainties in stellar mass measurement. Finally, in Chapter 4, we study the morphological properties of member galaxies in a redshift 1.6 X-ray selected group. The group is observed in Chandra Deep Field South survey with extensive available data including Chandra and Hubble space telescope. Using high spatial resolution images of HST, we measure the Sersic index and radius of the member galaxies and compare them with the early-type galaxies in the local Universe. The uncertainties in measurement of structural parameters are computed using Monte-Carlo simulations.

Chapter 2

Brightest X-ray clusters of galaxies in the CFHTLS wide fields: Catalog and optical mass estimator

Submitted to ApJ

2.1 Abstract

The CFHTLS presents a unique data set for weak lensing studies, having high quality imaging and deep multi-band photometry. We have initiated an XMM-CFHTLS project to provide X-ray observations of the brightest X-ray clusters within the wide CFHTLS area. We solve for the problem of identification of the unresolved X-ray sources in the RASS through a novel red sequence finder, which uses the multi-color space. We provide the calibration of the red sequence observed in the CFHT filters and compare the results with the traditional single color red sequence. We test the identification algorithm on the subset of highly significant XMM clusters and identify a 100% of the sample. We find that the integrated z-band luminosity of the red sequence galaxies correlates well with the X-ray luminosity with a surprisingly small scatter of 0.24 dex. We further use the multi-color red sequence to reduce spurious detections in the full XMM and RASS data sets, resulting in catalogs of 196 and 27 clusters, respectively. We made follow-up observations of some of these systems with HECTOSPEC and in combination with BOSS DR9 data spectroscopically confirmed 71 clusters. We also describe the modifications needed to the source detection algorithm in order to keep high purity of extended sources in the shallow X-ray data. For clusters with more than ten spectroscopic members, we present the scaling relation between X-ray luminosity and velocity dispersion. This is the first paper from our project and the catalogs presented here will form the basis of our forthcoming papers.

2.2 Introduction

In the past two decades the accelerating expansion of the universe has been confirmed by several experiments, such as observations of supernovae (e.g. Riess et al. 1998; Perlmutter et al. 1999) and measurements of the cosmic microwave background (e.g. Spergel et al. 2003). This acceleration is thought to be a consequence of dark energy density which, in the simplest way, can be modelled by a non-zero Einstein’s cosmological constant. Understanding the origin of the associated phenomenon of dark energy has been set among the most important tasks for understanding the formation and evolution of the Universe. Galaxy clusters play an important role in this, through their sensitivity to the growth of structure. One of the first efforts in constraining cosmology with galaxy clusters was made by Borgani et al. (2001). They measured Ω_M using 103 galaxy clusters in the ROSAT Deep Cluster Survey (RDCS; Rosati et al. 1998) out to $z \simeq 0.85$. In the subsequent study, Vikhlinin et al. (2009) obtained updated measurements of $\Omega_M h$, as well as the dark energy equation-of-state, ω_0 and the amplitude of power spectrum, σ_8 . For a review of cosmological constraints obtained using galaxy clusters in the past decade, see Weinberg et al. (2012) and Allen, Evrard & Mantz (2011). The 2013 Planck results have revealed a tension between a combination of CMB TT fluctuation spectrum and baryonic acoustic oscillation (BAO) measurements versus galaxy cluster abundance (Planck Collaboration et al. 2013). The physical interpretation of the results in view of the non-zero neutrino mass, requires a robust understanding of the cluster scaling relations.

From an astrophysical point of view, X-ray cluster survey data provides an important definition of high-density environment, critical for studies of galaxy formation e.g. Tanaka et al. 2008; Giodini et al., 2009; Balogh et al., 2011; Giodini et al., 2012) and active galactic nuclei (AGN) (e.g. Silverman et al. 2009, Tanaka 2012, Allevato et al. 2012).

The main aim of this *Paper* is address the cluster identification using CFHTLS data, provide the cluster sample and scaling relations between optical and X-ray luminosity. The calibration between weak lensing mass and X-ray observables (luminosity and temperature) will be presented in Kettula et al. (in prep.).

Optical galaxy cluster searches are often hindered by galaxy projection effects. Several algorithms have been applied to solve this problem. In addition to employing photometric methods such as red sequence identification (Gladders & Yee 2000) and MaxBCG (Annis et al. 1999; Koester et al. 2007), the detection of extended X-ray sources is often a reliable indication of galaxy clusters (Rosati, Borgani & Norman 2002). With the increased number of X-ray surveys in the past decade such as Chandra Deep Field North (CDFN; Bauer et al. 2002), Chandra Deep Field South (CDFS; Giacconi et al. 2002), Lockman Hole (Finoguenov et al. 2005), Cosmic Evolution Survey (COSMOS; Finoguenov et al. 2007), XMM-Large Scale Structure (XMM-LSS; Pcaud et al. 2007), Canadian Network for Observational Cosmology (CNOC2; Finoguenov et al. 2009) and Subaru-XMM Deep Field (SXDF; Finoguenov et al. 2010), X-ray astronomy introduced itself as an efficient cluster and group detection tool. In addition, X-ray properties of clusters can be used to best characterise the cluster mass, a requirement for precision cosmology work (Kravtsov, Vikhlinin & Nagai 2006; Nagai, Vikhlinin & Kravtsov 2007).

In this paper, we explore the use of multi-wavelength data to identify the X-ray cluster within the RASS data. RASS data are both faint and unresolved, so cluster confirmation is challenging. In order to establish a reliable method, we used the highly significant extended sources, obtained through our XMM-Newton follow-up program. Thus, we start with a description of the XMM data reduction and detection of extended sources in §2. In §3 we present the cluster identification and validation, including spectroscopic follow-up program and velocity dispersion measurements for a subsample of clusters. §4 provides the X-ray cluster catalogs both for XMM and RASS and compares the optical luminosity and X-ray luminosity of clusters. In §5 we summarise and discuss the results.

Throughout this paper, we use the AB magnitude system and consider a cosmological model with $H_0 = 72 \text{ km s}^{-1} \text{ Mpc}^{-1}$, $\Omega_\Lambda = 0.75$ and $\Omega_M = 0.25$.

2.3 Data

2.3.1 X-ray data

The main aim of the XMM-CFHTLS program is to efficiently find massive galaxy clusters, through series of short XMM-Newton follow-up observations of faint RASS sources (Voges et al. 1999) identified as galaxy clusters using CFHTLS imaging data. In total, 73 observations of cluster candidates have been performed, using 220ks of allocated time. At the time of scheduling XMM observations, only T0005 CFHTLS data have been publicly released, which covered 100 square degrees in partial W1 and W4 fields and the full W2 field. In order to use the mosaicing mode of XMM-Newton, we had to fulfil the re-pointing constraint of 1 degree. Given the low density of RASS sources, the number of robust clusters were rather low and for XMM snap-shot observations we also pointed at the RASS sources identified with a photo-z galaxy overdensity. Performance of this program has allowed us to both select the adequate method for cluster identification and to perform extensive XMM studies of optically selected clusters. We would like to advise against using our data for studying the cluster abundance, as our fields exhibit an unusually large number of clusters even at flux levels below the formal RASS sensitivity.

In our final catalog, we also include existing serendipitous observations, since some candidate clusters have already been previously observed with XMM. We exclude from our survey the XMM-LSS fields, where clusters are identified by the corresponding teams (e.g. Pacaud et al. 2007). We point out interested reader to Gozaliasl et al. (2014) where we present our catalog using the 2 square degree overlap between XMM-LSS survey and CFHTLS.

Our survey methodology is to cover a large area of the sky with short X-ray exposures. The detection of sources in such a shallow survey explores the Poisson regime, so there is a need for tailored data reduction methods. Confirming RASS sources does not require any sophisticated modelling, given that they are typically $> 20\sigma$ sources, but detection of fainter serendipitous sources requires a new approach.

The procedure of Finoguenov et al. (2007, 2009) with updates described in Bielby et al.

(2010) has been further revised to store the locally estimated background and exposure maps separately in order to treat the Poisson noise within the source detection program (wvdetect - Vikhlinin et al. 1998). The detection statistics have been set to Poisson. Furthermore, we modified the ratio of thresholds for point and extended sources, setting the detection of point sources to 3.3σ and that of extended sources to 4.6σ . This choice of thresholds prevents detection of point sources only on large spatial scales. The consideration of the detection effect is very general, but the ratio of thresholds is tailored for the XMM PSF and the scales of source detection we employ. In detecting the extended source, we avoid detecting the point sources, by detecting them on small scales and subtracting their flux according to PSF model, so no detection occurs on any scale anymore. If the source is not detected on small scales, but only detected on large scales, it would be mistaken for an extended source. For XMM-Newton 40% of the flux is on scales we use for the extended source detection. The odds of not detecting the central 60% of the source flux, while detecting the 100% of the source flux by including the outskirts are large, especially if only a few counts suffice a detection. To beat this contamination down, we need to increase the threshold for detecting the large scales, so that odds of detecting the outer 40% of the flux with a new large threshold and not detecting the central flux of the source with the original threshold are small, where small is set to be 1%, since this makes a 10% contamination to extended sources, given that point sources are 10 times more abundant. We also decrease the threshold for detecting the flux on small scales. Given the PSF shape of XMM, we find the suitable detection limits to be 3.3σ for the central flux and 4.6σ for the outskirts. We also required the significance of the flux determination associated with the detection to be above 4.6σ . The problem described above is typical to shallow surveys, and e.g. will be important for eROSITA (Predehl et al., 2010). In deep surveys extended source detection is background limited, which requires more counts for large scales to be detected at similar thresholds and so the flux on small scales is always detected from a point source.

The chosen set of thresholds still retains a 10% contamination of point sources to the extended source catalogs, which we consider acceptable, given that the highest identification rate for extended sources in deep fields is 90% (e.g. Finoguenov et al. 2010). The corresponding chance identification rate is 2%. As in our previous work, while removing flux from point sources, we are not going through the step of cataloguing the sources, as we model the point-source contamination by convolving the wavelet images on small scales with PSF shape on large scales.

We catalog sources found at lower X-ray σ (< 4.6) separately but they are not included in the analysis of scaling relation between X-ray luminosity and integrated optical luminosity. At these levels, the contamination from point sources increases to 50%. The final rate for spurious identification in this dirty list is reduced due to sparse density of matching sources (optical clusters) and amounts to 10%.

2.3.2 Optical, photometric redshift and spectroscopic data

During 2003–2009, the 3.6-m Canada-France-Hawaii Telescope (CFHT) completed a very large imaging programme known as the Canada-France-Hawaii Telescope Legacy Survey (CFHTLS) using the 2048×4612 pixel wide field optical imaging camera MegaCam. With a 0.185 arcsec pixel size, CFHT MegaCam gives a $0.96 \text{ degree} \times 0.96 \text{ degree}$ field of view. All the observations were done in dark and grey telescope time ($\sim 2\,300$ hours). Four wide fields of this survey, with a total area amounting to 170 square degrees, were observed in u^* , g' , r' , i' and z' band down to $i'=24.5$. We use the i' band selected photometric catalog provided by Brimiouille et al. (2008). Their achieved photometric redshift accuracy and outlier rates are $\sigma_{\Delta z \setminus 1+z} \cong 0.035$ and $\eta \cong 2\%$ for galaxies with $17.5 \leq i' \leq 22.5$. We use optical data from three wide fields of CFHTLS: W1, W2 and W4.

Follow-up observations of clusters in W1, W2 and W4 fields were performed using Hectospec on MMT. Hectospec is a 300-fiber multi-object spectrograph with a circular field of view of 1° in diameter (Fabricant et al. 2005). We used the 270 line grating, which provides a wide wavelength range ($3\,650 - 9\,200 \text{ \AA}$) at 6.2 \AA resolution. We reduced the spectra and measured redshifts using the HSRED pipeline (Cool et al. 2005). Redshifts were determined by comparing the reduced spectra with stellar, galaxy and quasar template spectra and choosing the template and redshift which minimises the χ^2 between model and data. We then visually inspected the template fits and assigned quality flags based on the certainty of the redshift estimate.

Targets for spectroscopic follow-up were culled from the list of candidates in the XMM-CFHTLS fields and prioritised based on a combination of their X-ray flux and photometric redshift. High priority clusters (with X-ray flux $> 7 \times 10^{-14} \text{ erg cm}^{-2} \text{ s}^{-1}$ and $0.15 < z < 0.6$) dictated the locations of the Hectospec pointings; fainter clusters or clusters beyond these redshift limits were used as fillers, and therefore only observed if they lay within $30'$ of a high priority target. AGN candidates based on the XMM-CFHTLS point source catalogs were also used as low priority fillers. The cluster follow-up strategy used varied according to the certainty in the red sequence redshift estimate. For clusters with reliable redshifts, i.e. red sequence significance ($\alpha > 9$), we use photometric redshift catalogs to select only galaxies which lie in the photo- z slice ($dz < n \times (1+z) \times \sigma_{\text{photo}z}$, where $\sigma_{\text{photo}z}$ is the photometric redshift error and n is an integer number between 2 and 4). The red sequence significance, α , is a parameter that shows the overdensity of galaxies in comparison to the number of background galaxies at the cluster redshift. This parameter will be defined more accurately in section 2.4.1. This narrower target selection means we were able to explore the infall regions of the clusters out to larger radii. For clusters with few number of photo- z counterparts, we performed a magnitude limited survey at smaller radial distances, with the goal of identifying the optical counterparts and securing a redshift for the X-ray emission. Over the 3 fields, 32 fiber configurations were observed, mainly in W1 and W2, and secure redshifts for 6 170 objects were measured.

In performing the analysis, we have also added spectroscopic data in W1, W2 and W3 from SDSS-III survey (Aihara et al. 2011). In total, we have 13k, 3.5k and 9k spectroscopic redshifts in W1, W2 and W4.

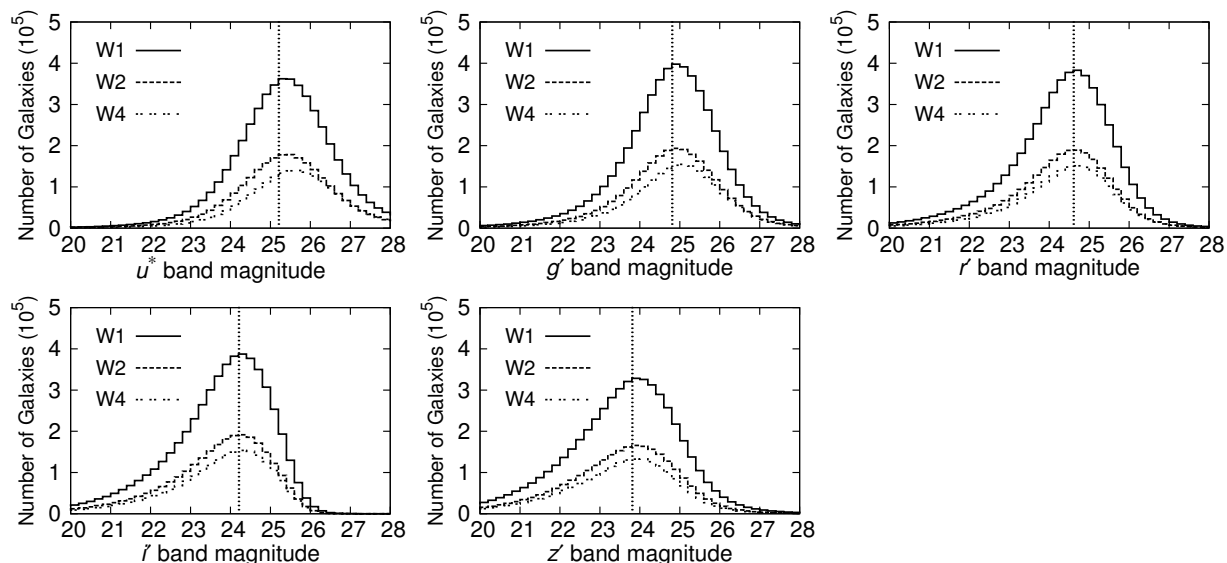


Figure 2.1: Distribution of the u^* , g' , r' , i' and z' magnitudes in W1 (solid line), W2 (dashed line) and W4 (dotted line) fields. A vertical dotted line in each plot shows the selected limiting magnitudes in each filters.

2.4 Optical counterparts for X-ray sources

2.4.1 Red sequence method

The red sequence (Baum 1959; Bower, Lucey & Ellis 1992; Gladders & Yee 2000) is the name given to the linear overdensity of early-type cluster galaxies in color-magnitude space. Usually a single color is used to find overdensities of early-type galaxies in a limited range of redshift. This color is selected so that the 4000 \AA break is located in the bluer filter. For example Rykoff et al. (2012) used $g'-r'$ for a redshift range between 0.1 and 0.3. However, if we select another color, such as $r'-i'$ for redshifts below 0.3, early-type galaxies (ETGs) in a cluster still produce a sequence since they have similar formation redshifts and a mostly passive evolution. While background and foreground galaxies (e.g. a late-type galaxy at higher redshift) can have similar color to the color of member ETGs, one can exclude them using other filters. This approach leads to finding member ETGs with less contamination and higher purity in selection of member galaxies, and higher sensitivity for cluster detection. On the other hand, multi color selection of red sequence galaxies may miss some of the red sequence galaxies (lower completeness). In this work, we will apply the multi color selection of red sequence galaxies to find the clusters. We will compare the relation between X-ray luminosity and integrated optical luminosity of clusters using both methods (regardless of purity and completeness for each method) to know which method gives a better optical proxy for X-ray luminosity (or mass) of clusters.

In the red sequence method, a model for describing the color of galaxies and its corresponding dispersion as a function of redshift is assumed. Then, at each redshift step, the

Table 2.1: The completeness magnitude limits for each field.

filter	W1	W2	W4
u^*	25.2	25.4	25.6
g'	24.8	24.8	25.0
r'	24.6	24.6	24.6
i'	24.2	24.2	24.2
z'	23.8	23.8	24.0

number of red galaxies with absolute magnitude lower than a threshold (M_{cut}) is counted (using expectation color value from model and its dispersion) and corrected for the number of background red galaxies at the same redshift. This corrected number is the cluster richness.

As we move to higher redshifts, galaxies more luminous than M_{cut} can still be below the completeness limit of the sample in one or more filters. Figure 2.1 shows the magnitude distributions in the 5 bands of CFHTLS survey of galaxies in the W1, W2 and W4 fields. We employ 0.2 magnitude bin width in calculating the distributions. To be conservative, a limit of 0.1 magnitude brighter than the maximum of each distribution is considered as the completeness of the galaxy sample in each filter. Table 2.1 shows the magnitude completeness limits for each fields, derived this way. Among the 3 fields, the W1 has the worst completeness in all bands (or equals to other fields), which we adopt for evaluating the performance of the optical identification. We display these limits with the dotted vertical lines in Figure 2.1.

Estimating the cluster richness requires a luminosity cut (as a function of redshift), as otherwise one may go deeper at low redshift and find fainter red galaxies in comparison with a higher redshift which leads to estimating higher richness for nearby clusters. Selection of the luminosity cut affects the scatter in the relation between richness and X-ray luminosity (L_X) of galaxy clusters. Rykoff et al. (2012) tested series of richness estimations with different L_{cut} from $0.1L_*$ to $0.4L_*$, showing that the richness- L_X relation of a cluster sample has the least scatter with $L_{\text{cut}} = 0.2L_*$. In addition to minimising the scatter in the richness- L_X relation, we need to check the feasibility of selecting a given value of L_{cut} , given the depths of the survey. Using Maraston et al. (2009) stellar population model and combining its spectral energy distribution (SED) with CFHT/MegaCam filters, we derived apparent magnitude $m_*(z)$ for all filters and subsequently k -correction model. The computations is done by ‘‘Le Phare’’ package (Ilbert et al., 2006). Maraston et al. (2009) showed that their model is in agreement with color evolution of luminous red galaxies in SDSS. This model is based on a single-burst model with a solar metallicity. Similar to Rykoff et al. (2012), we adopt $L_* = 2.25 \times 10^{10} L_\odot$.

Figure 2.2 illustrates $m_*(z)$ for all five filters derived from our model for redshifts below 1.2. Based on the magnitude completeness of the survey, we estimate the maximum redshift at which a galaxy with luminosity of 0.2, 0.4 and 1 times of L_{cut} can be observed in each

Table 2.2: The maximum redshift at which galaxies with luminosity of $0.2L_*$, $0.4L_*$ and $1.0L_*$ are detectable in each filter.

filter	$0.2L_*$	$0.4L_*$	$1L_*$
u^*	0.37	0.43	0.52
g'	0.56	0.66	0.80
r'	0.79	0.97	1.09
i'	0.99	1.18	>1.2
z'	1.12	>1.2	>1.2

filter. Table 2.2 shows the redshift limits for each M_{cut} .

Given that u^* band is not deep enough to cover at least half of the redshift range of 0.05 to 1.1, this filter is not used in this work. We chose the following set of redshift ranges, filters and L_{cut} for red sequence algorithm:

$$0.05 \leq z \leq 0.66 : L_{\text{cut}}=0.4L_* \text{ and } g', r', i'$$

$$0.66 < z \leq 1.1 : L_{\text{cut}}=0.4L_* \text{ and } r', i', z'$$

The r' band detections become incomplete at redshifts beyond 0.97, so the identification there has to rely on a single color. As shown in Figure 2.2 and Table 2.2, z' band has the deepest imaging. We have therefore adopted z' band for the magnitude parameter in color-magnitude space. Hereinafter we use m to denote the z' magnitude.

A galaxy is assumed to be on the red sequence at a redshift z if:

$$|GC_{a-b} - MC_{a-b}(z)| < 2 \times \sigma_{a-b}(z), \quad (2.1)$$

where $a-b$ represents a color ($g'-r'$, etc). GC_{a-b} and $MC_{a-b}(z)$ are galaxy color and model color for red sequence galaxies at redshift z , respectively. $\sigma_{a-b}(z)$ is the dispersion of the observed galaxy $a-b$ color around the model color. $\sigma_{a-b}(z)$ is a total dispersion, given by the sum in quadrature of two other parameters, the magnitudes error and the intrinsic width of the color. In the following, we look in detail on these two parameters.

We use our spectroscopic sample of galaxies to model the color evolution. First, we select galaxies brighter than $m_*(z)+1$ (or $\leq 0.4L_*$) and exclude those with AGN or star-forming classification in spectroscopic data or non-ET spectral energy distribution (SED), yielding a sample of 7969 early-type galaxies out of the full spectroscopic redshift catalog. Second, we calculate the average color values and their standard deviation for these galaxies in 16 spectroscopic redshift bins from 0.05 to 0.80 with the bin size of 0.05. For each bin, we discard the galaxies with color offset from the average value exceeding two standard deviations and repeat the calculation of average. Figure 2.3 shows the $g'-r'$, $r'-i'$ and $i'-z'$ colors of ETGs and derived color model as a function of redshift (solid lines). Given

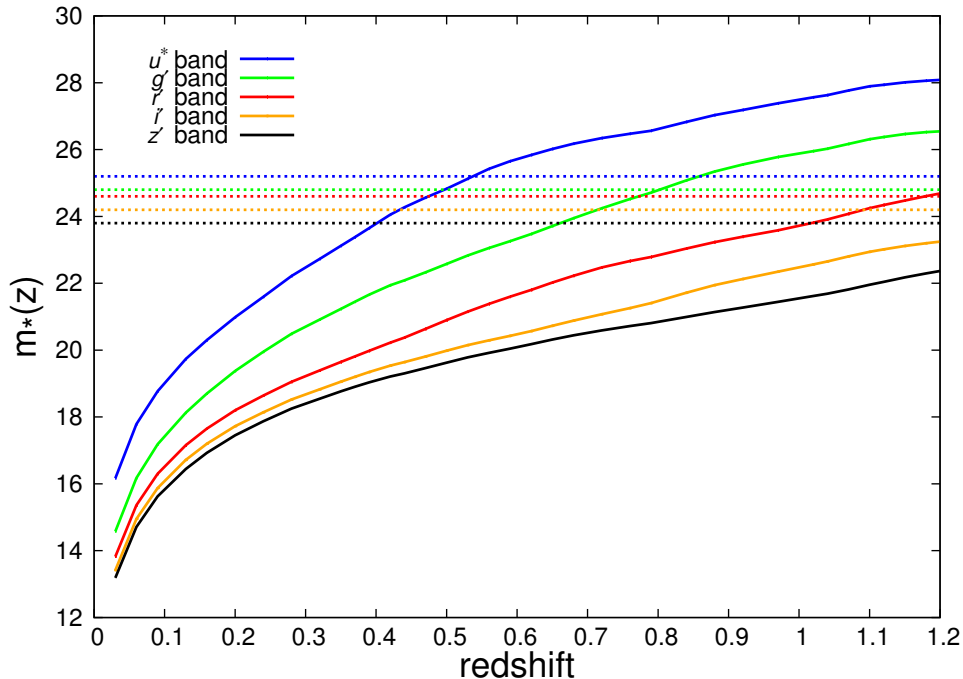


Figure 2.2: Characteristic magnitude $m_*(z)$ for different filters as a function of redshift. Blue, green, red, yellow and black solid lines correspond to the magnitudes in u^* , g' , r' , i' and z' bands, respectively. The dotted lines show the completeness limits of survey for each filter with the same colors.

that the sample of galaxies brighter than $0.4L_*$ is incomplete in g band for redshifts above 0.66, the modelling of $g'-r'$ color is limited to z of 0.66. Above the redshift of 0.75, the spectroscopic sample of ETGs becomes poor, so we derive $MC_{a-b}(z)$ from the $m_*(z)$ model in Figure 2.2.

In order to determine the dispersion of the red-sequence color, $\sigma_{a-b}(z)$, We assume that it has two components, an intrinsic dispersion, $\sigma_{a-b,int}(z)$, and a color error $\sigma_{a-b,color}(z)$. In estimating $\sigma_{a-b,color}(z)$, we selected the galaxies with photometric redshift below 1.2 and brighter than $m_*(z)+1$ (similar to the original work of Gladders & Yee (2000)). Using the redshift bin width of 0.1, we determine the mean magnitude error for each band, and approximate it with the fourth order polynomials. Figure 2.4 illustrates the magnitude errors and the polynomial curves as functions of a redshift. The total color dispersion is calculated as a sum of the color errors (derived from the magnitudes errors) and the intrinsic color dispersion in quadrature.

Red sequence is known to exhibit a tilt in the color-magnitude space, due to the age-metallicity relation (Nelán et al. 2005). Since we work with both low-mass and high- z clusters, where the age-metallicity relation can be different, we prefer to consider the tilt as part of color scatter. We note that a similar approach is adopted in RedMapper (Rykoff et al., 2013). In estimating the intrinsic color dispersion, we assume that the variation of color in cluster ETGs can be modelled by a variation in metallicity. We use PEGASE.2

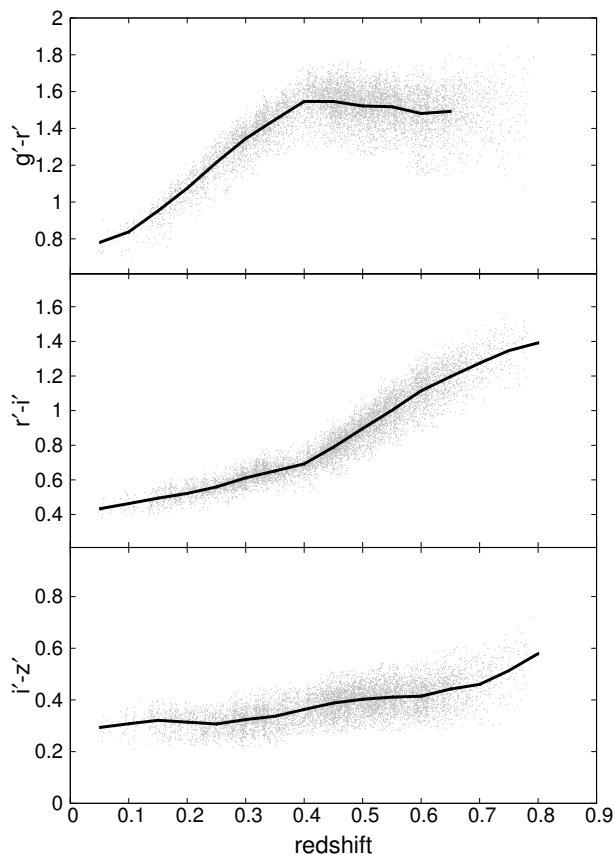


Figure 2.3: Model colors for ETGs as a function of redshift. Grey dots show the ETGs and solid lines are the average at each redshift.

stellar population/galaxy formation models to estimate the intrinsic color dispersion. For the reference model, a unit solar metallicity is considered (similar to Eisenstein et al., 2001; Rykoff et al., 2012) and we model the evolution of the dispersion, by selecting the metallicity that reproduces the observed color scatter for a subsample of well observed clusters and high number (> 10) of spectroscopic redshifts. We model $r'-i'$ and $i'-z'$ colors between redshifts 0.05 and 1.2 and $g'-r'$ between 0.05 and 0.66. In Appendix 2.8, it is shown that a linear evolution for intrinsic color dispersion of ETGs is a reasonable assumption especially for $g'-r'$ and $i'-z'$ colors. Thus the intrinsic color dispersions at redshifts between two models were derived by interpolating the model points. We check the color-magnitude diagram for the training sample with different σ_{a-b} associated with different $\sigma_{a-b,int}$ and realize that the metallicity of 0.75 solar is appropriate for the second model to enclose the bulk of red sequence galaxies within two times σ_{a-b} . Figure 2.5 illustrates color – magnitude diagrams for three clusters at different redshifts with metallicity of 0.75 and 1 for modeling the intrinsic color dispersion. We do not optimize the width of red sequence for minimizing the contamination or maximizing the number of member galaxies.

The derived intrinsic dispersion of colors as functions of redshift are:

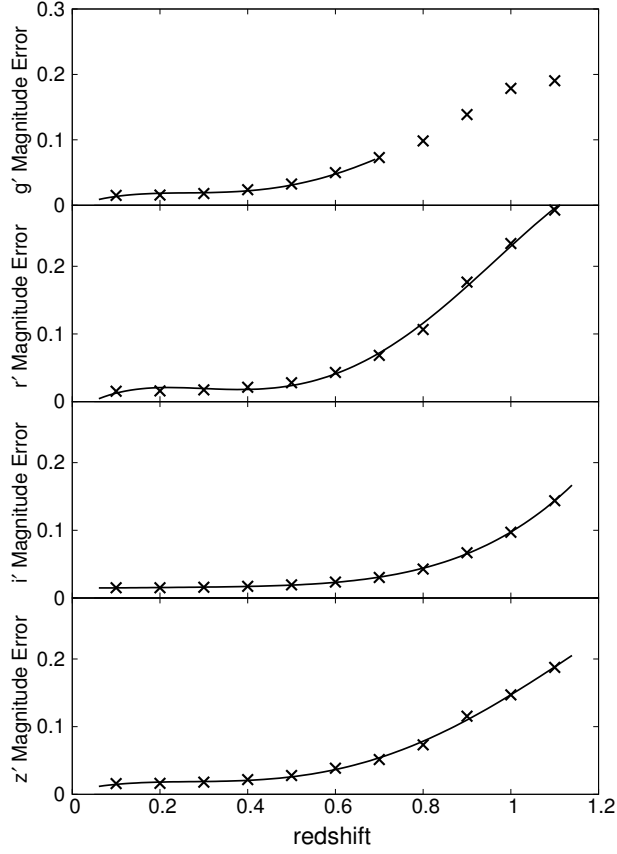


Figure 2.4: Magnitude errors in g' , r' , i' and z' band versus redshift for galaxies brighter than $m_{*(z)}+1$. Crosses show the mean magnitude error for each redshift bin and solid lines are polynomial fits to the mean values.

$$\sigma_{g'-r',\text{int}}(z) = 0.029 + 0.044 \times z \quad (2.2)$$

$$\sigma_{r'-i',\text{int}}(z) = 0.011 + 0.046 \times z \quad (2.3)$$

$$\sigma_{i'-z',\text{int}}(z) = 0.021 + 0.035 \times z \quad (2.4)$$

When running the red-sequence finder, we consider a fixed physical radius for galaxy selection and vary the redshift of red sequence from 0.05 and 1.1 with a step of 0.01. At each redshift, we calculate the number of red sequence galaxies brighter than $0.4L_*$, $N_{0.4,R}(z)$. Using 294 random areas in three optical fields we estimate the background, $NB_{0.4,R}(z)$, and its standard deviation, $\sigma_{NB}(z)$. At each redshift we compute the red sequence significance, α , as

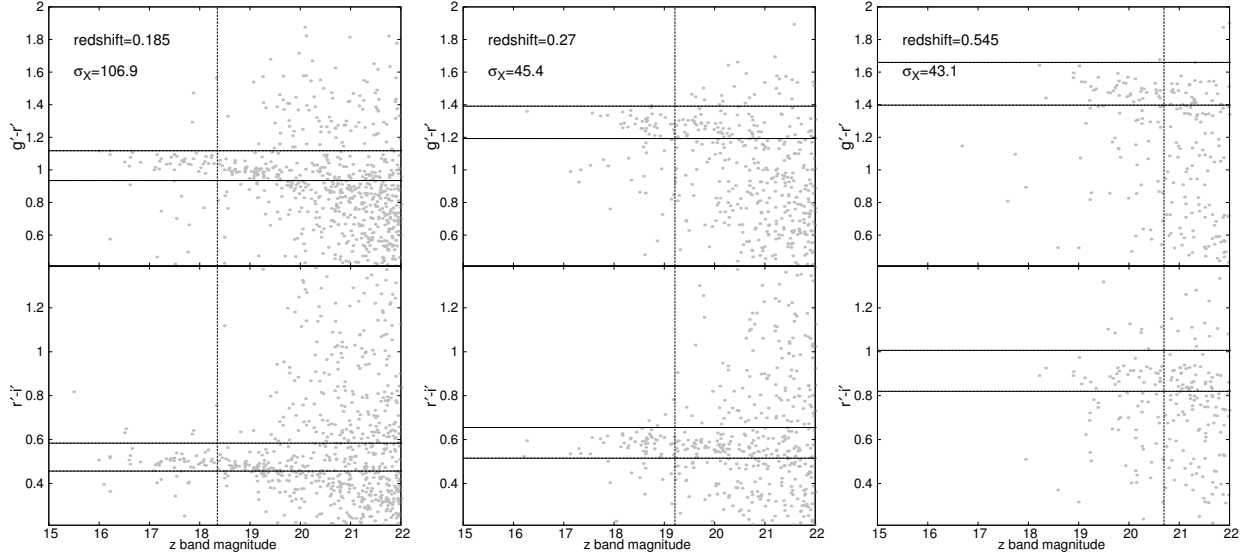


Figure 2.5: Color – magnitude diagrams for three clusters with high detection level in X-ray. The solid lines are upper and lower limits on the colors to envelop the bulk of red sequence galaxies. The dashed line is the m_*+1 at the redshift of clusters.

$$\alpha = \frac{N_{0.4,R}(z) - NB_{0.4,R}(z)}{\sigma_{NR}(z)} \quad (2.5)$$

. The overdensity with the highest red sequence significance is adopted as the X-ray counterpart. The uncertainty in α is estimated by randomly changing the magnitudes of catalog galaxies according to the corresponding photometric errors.

2.4.2 Applying the red sequence finder to identify XMM-Newton extended sources

We utilize our red sequence finder to identify the counterparts for 133 XMM-Newton extended sources in our *primary* sample with a 4.6σ detection limit. We use a galaxy selection radius of 0.5 Mpc, as centers of XMM sources are accurately known (15 arcseconds, George et al. 2012). Figure 2.6 illustrates the results of applying the red sequence on a cluster at a redshift of 0.28. After applying the red sequence finder on all the X-ray sources, we visually inspect them to compare the correspondence of a two-dimensional distribution of X-ray photons and location of galaxies, presence of secondary peaks in X-rays and optical quality of the images. The photometric and spectroscopic galaxy catalogs are fully utilized during visual inspection for optical counterparts of the X-ray sources. Obvious cluster candidates are marked with a visual flag= 1 in the catalog. Visual flag= 2 is assigned to X-ray sources which have low significance of the optical counterpart or concentration of galaxies almost on the edge or out of X-ray source, indicative of a confused X-ray source. Figure 2.7 illustrates clusters with different visual flags. We provide an identification

to all XMM sources with flux significance above 4.6 sigma. During this inspection, we also visually checked faint sources with detection levels below 4.6, discarding the sources revealing no visual concentration of galaxies. We added 63 clusters from the lower X-ray detection threshold sample, we arrive at a sample of 196 clusters with assigned RS redshift.

81 clusters among 196 clusters have spectroscopic redshift. First, we visually select the redshift of the brightest galaxy with spectroscopic redshift close to the red sequence redshift of a cluster and assume it as an initial redshift of a cluster. Then we select all galaxies within 0.5Mpc from X-ray centre and the sigma clipping is done within $\pm 0.005(1+z)$ around the initial redshift. Finally, the mean of spectroscopic redshifts is computed. The number of spectroscopic counterparts per cluster varies from 1 to 10 member galaxies. In Figure 2.8 we compare the red sequence redshift with mean of spectroscopic redshift of member galaxies. The average difference between the red sequence and spectroscopic redshift is 0.009 with a standard deviation of 0.034.

2.4.3 Velocity dispersion

We can also use velocity dispersion measurements as an independent confirmation for the existence of a galaxy cluster and a characteristic for the system. Such a calculation is only reliable for a high number of member galaxies (typically more than 10), though we provisionally calculate dispersions down to systems with 5 member galaxies and present them in the catalog. We limit the sample for relation between X-ray luminosity and velocity dispersion to the cluster with more than 10 member galaxies ($N_\sigma \leq 10$) because of lower error in velocity dispersion measurement.

We follow the analysis of Connelly et al. (2012). In detail, we select galaxies iteratively, starting with an initial guess for the observed velocity dispersion of $\sigma(z)_{\text{obs}} = 500(1+z)$ km s⁻¹ as

$$\delta(z)_{\text{max}} = 2 \frac{\sigma(z)_{\text{obs}}}{c} \quad (2.6)$$

We then calculate the spatial distribution associated with $\delta(z)_{\text{max}}$:

$$\delta(r)_{\text{max}} = \frac{c\delta(z)_{\text{max}}}{bh_{71}(z)} \quad (2.7)$$

where $b=9.5$ is the aspect ratio. We use the peak of the X-ray emission as the cluster center. The observed velocity dispersion, $\sigma(z)_{\text{obs}}$ is then calculated for galaxies within $\delta(r)_{\text{max}}$ using the *gapper* estimator method (Wilman et al. (2005); Beers, Flynn & Gebhardt (1990)), and the new value is then used to re-estimate $\delta(z)_{\text{max}}$ and $\delta(r)_{\text{max}}$. The procedure is repeated until convergence is achieved. The rest-frame velocity dispersion $\sigma(z)_{\text{rest}}$ and intrinsic velocity dispersion $\sigma(z)_{\text{int}}$ are finally given by

$$\sigma(v)_{\text{rest}} = \frac{\sigma(v)_{\text{obs}}}{1+z} \quad (2.8)$$

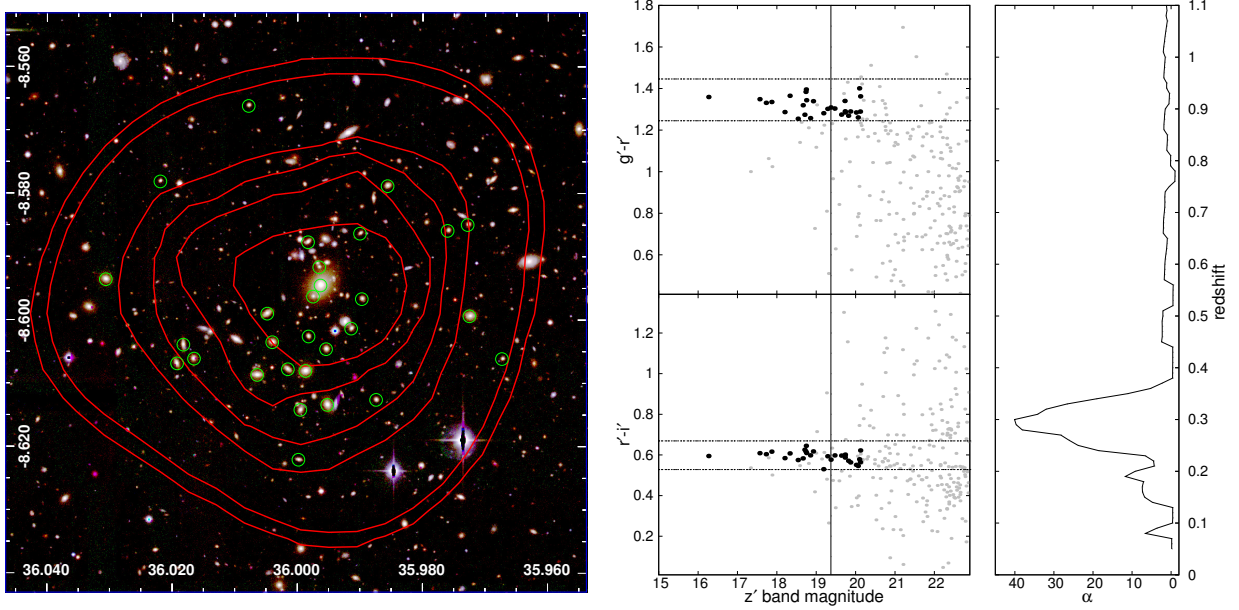


Figure 2.6: Illustration of the red sequence finder using XMM cluster XCC J0224.0-0835 at a red sequence redshift of 0.28. Left panel shows the RGB image of the cluster, where i' , r' , and g' images are used as red, green and blue components, respectively. The X-ray flux levels are presented by the red contours and the green circles are red sequence galaxies brighter than $0.2L_*$ within 0.5 Mpc from X-ray centre. The middle panels are color magnitude diagrams, $g'-r'$ (top) and $r'-i'$ (bottom) versus z' band magnitude. Grey points are all galaxies within the radius of 0.5 Mpc at the redshift of the cluster from the X-ray source centre. Black dots are red galaxies brighter than $0.2L_*$ within 0.5 Mpc. In each color magnitude diagram two horizontal dotted lines are upper and lower limits of color for selecting red galaxies according to an estimate of the color scatter, described in the text. The solid vertical line shows $0.4L_*$ at the redshift of 0.3. The middle panels show the corresponding color-magnitude diagrams. The horizontal dashed lines are the lower and upper limits on the color of red sequence galaxies at a redshift of 0.3 and the solid vertical line is $L_{\text{cut}}=0.4L_*$ at the same redshift. The grey dots are all the galaxies with projected distance of 0.5 Mpc from the X-ray source centre. The black dots are the galaxies with green circle in left panel. The right panel is the variation of α as a function of redshift with a maximum at redshift of 0.3. The red sequence significance, α as a function of redshift is shown in the right panel and exhibit a maximum at a redshift of 0.3.

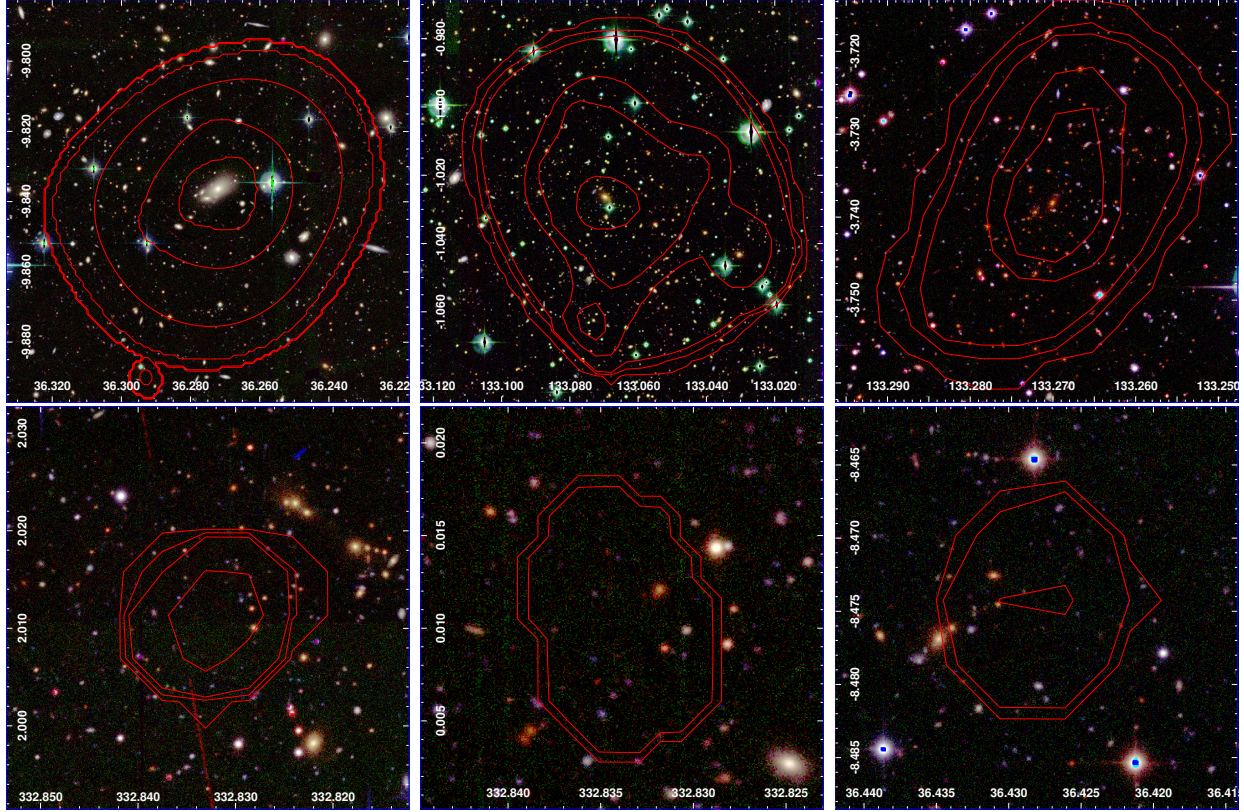


Figure 2.7: Examples of clusters with different visual flags. Top panels are examples of CFHTLS clusters with visual flag=1 at $z=0.16$, 0.46 and 0.92 (from left to right) and bottom panels are clusters with visual flag=2 at $z=0.46$, 0.83 and 0.55 (from left to right). We use g' band image as blue, r' – as green and i' – as red component of RGB image. The red contours show the X-ray emission.

$$\langle \Delta(v) \rangle^2 = \frac{1}{N} \sum_{i=1}^N \Delta(v)_i^2 \quad (2.9)$$

$$\sigma(v)_{\text{intr}}^2 = \sigma(v)_{\text{rest}}^2 - \langle \Delta(v) \rangle^2 \quad (2.10)$$

where $\Delta(v)$ is the uncertainty in the spectroscopic velocity measurement. For computing velocity dispersion, we use the galaxies with spectroscopic redshift error less than 3×10^{-4} .

The intrinsic velocity dispersion is calculated by subtracting the contribution of redshift errors from the rest frame velocity dispersion. To assess the velocity dispersion error associated with galaxy sampling, a Jackknife method is applied (Efron (1982)) and the associated error is computed as $[\frac{N}{N-1} \sum (\delta_i^2)]^{\frac{1}{2}}$, where $\delta_i = \sigma(v)_{\text{obs}} - \sigma(v)_{\text{obs, excluding } i_{\text{th}} \text{ member}}$, for a cluster with N member galaxies. Connelly et al. (2012) showed that for calculation of velocity dispersion, applying luminosity weighted recentering can change the center up to 0.18 arcminutes but it does not change the velocity dispersion value. For more detailed description of velocity dispersion calculation, see Connelly et al. (2012) and Erfanianfar

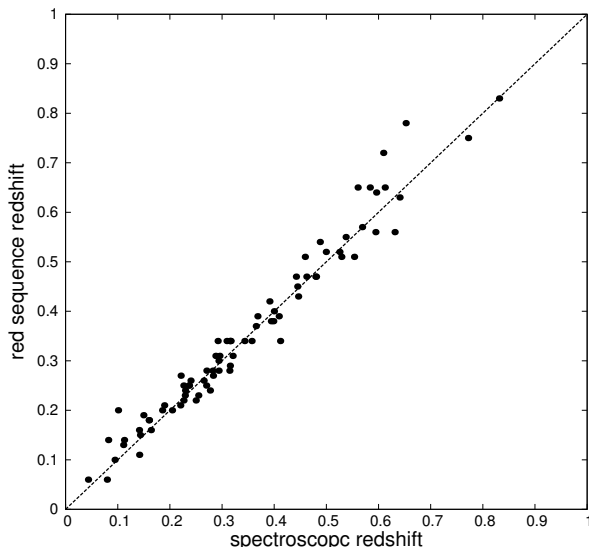


Figure 2.8: Red sequence redshifts versus spectroscopic redshifts for 81 clusters with spectroscopic counterparts. The dashed line shows a 1:1 correspondence.

et al. (2013).

To investigate the results of our red sequence finder and velocity dispersion calculation, let us compare σ_v to L_X . Figure 2.9 shows the X-ray luminosity as a function of velocity dispersion for 16 XMM clusters with more than ten spectroscopic counterparts. The black line shows the expected relation between velocity dispersion and X-ray luminosity from Leauthaud et al. (2010). The grey area also show a 20% error on mass from L_X - M_{200c} relation (Allevato et al., 2012). We do not account for the intrinsic scatter between velocity dispersion and M_{200c} . The blue and red lines are fitted lines using bisector and orthogonal fitting methods (Akritas & Bershady (1996)). The bisector method minimizes the square distance independently in X and Y directions. The orthogonal method minimizes the squared orthogonal distances. The result of bisector fitting method is very close to the relation, expected from the weak lensing calibration. While most of the clusters are close to the predicted relation, three of them have significantly larger L_X than the values of L_X predicted by the scaling relation. Since this offset is about one order of magnitude in L_X , a significant contribution of unresolved X-ray point sources can be ruled out. Among these three clusters, two less luminous ones have N_σ of 12 and 13 and the more luminous one has 20. As discussed in Ruel et al. (2013) the low number of spectroscopic members can be a reason for these deviations.

2.4.4 Stellar luminosity as a L_X estimator

We calculate the integrated z' -band stellar luminosity, L_S , of red sequence galaxies (brighter than $0.4L_*$) within r_{200c} , for clusters in the redshift range of $0.1 < z < 0.6$ and the X-ray detection threshold above 4.6. The r_{200c} is also calculated from M_{200c} (see section 2.5). The

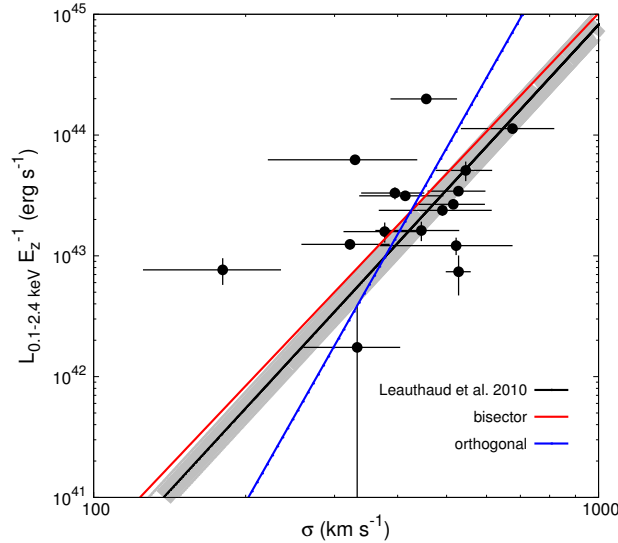


Figure 2.9: X-ray luminosity versus the velocity dispersion for XMM clusters with more than ten spectroscopic members from gapper estimator method. The black line shows expected $L_X - \sigma$ from scaling relation. The grey area marks the 20% uncertainty in the mass estimate using the $L_X - M_{200c}$ relation. The red and blue lines are fitted lines with bisector and orthogonal methods. Their equations are $\log(L_X) = (31.77 \pm 4.41) + (5.49 \pm 2.07)\log(\sigma)$ and $\log(L_X) = (24.01 \pm 7.37) + (10.17 \pm 3.84)\log(\sigma)$ respectively.

luminosity of red sequence galaxies are added to each other and subtracted by background luminosity of the same redshift. The background is the mean of integrated luminosity of red sequence galaxies at random points in the sky and within the similar radius. In §2.4.1, we mentioned that we define the width of red sequence to enclose the bulk of bright red sequence galaxies. Here we show that the adopted width does not affect the measured stellar luminosity of the clusters. For this purpose, we increase the widths of all colors in the red sequence selection to three times the $\sigma_{a-b}(z)$ (1.5 times the previous width) and re-computed the stellar luminosity. The background computation was also repeated for changing the width of red sequence. Figure 2.10 illustrates the variation of L_S after increasing the width of red sequence by 50%. The change in L_S is 0.03 dex with a standard deviation of 0.07 dex. We conclude that the obtained L_S values have converged.

In some cases, g' band coverage is lacking. In some other cases, bright stars affect the photometry. We discard the affected clusters from determination of L_X . Figure 2.11 illustrates the relation between L_S and L_X for the sample of clusters in the redshift range of $0.1 < z < 0.6$ and the X-ray detection threshold above 4.6. There is a strong correlation between $\log(L_S)$ and $\log(L_X)$ for the bulk of sample. The Spearman test coefficient for this relation is 0.649 with the zero value for the probability of null hypothesis of null correlation between two quantities.

The good relation between L_S and L_X , is a motivation for using L_S as an estimator for L_X and, consequently, the cluster mass. For this purpose, besides of L_S within r_{200c} , we also

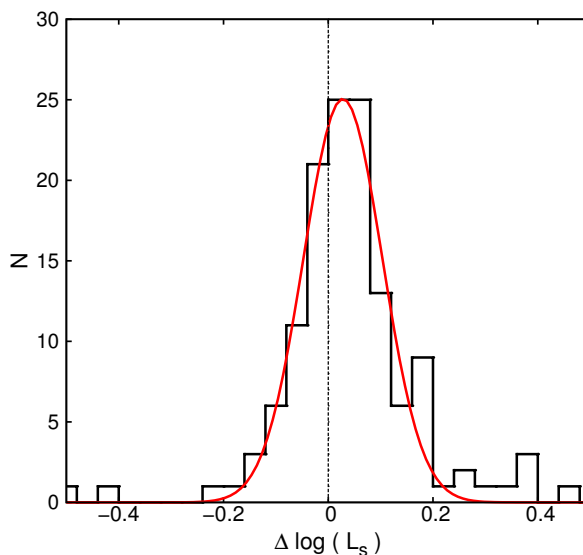


Figure 2.10: Convergence test for calculating L_S . The plot shows the distribution of L_S calculated within three times of $\sigma_{a-b}(z)$ subtracted by the L_S calculated within two times of $\sigma_{a-b}(z)$. The distribution is fitted by a Gaussian with a standard deviation of 0.07 dex. The peak offset is 0.03 dex.

measure the L_S within 1 Mpc from the X-ray centre. Figure 2.12 illustrates the relation between L_S and L_X for the sample of clusters. The upper left and lower left panels show the L_S computed within r_{200c} and 1 Mpc, respectively. The later is useful in the situations when the measurement of the virial radius is not possible or noisy. In Figure 2.12, the lines show the power-law fits to the relation. The procedures of Akritas & Bershady (1996) ordinary least square (OLS) and bi-variate correlated errors and intrinsic scatter (BCES) estimators are used to produce the fits. The ordinary least square estimators in L_X direction ($OLS(L_X|L_S)$) and L_S direction ($OLS(L_S|L_X)$) are shown as black and green solid curves, respectively. The red dashed lines are the results of BCES orthogonal fitting method, which minimizes the squared orthogonal distances. The parameters of the plotted relations are listed in Table 2.3.

For comparison to the multi-color red sequence, we also computed the L_S with a single-color selection of red sequence galaxies ($g' - r'$ for $0.05 \leq z \leq 0.4$ and $r' - i'$ for $0.4 < z \leq 0.6$). The best method is sought to provide the lowest scatter versus L_X . The results are compared in Figure 2.12, using r_{200c} and 1 Mpc as an extraction radius. The upper right and lower right panels of Figure 2.12 show the relation between the cluster X-ray luminosity and the single color L_S computed within r_{200c} and 1 Mpc, respectively. These relations are fitted with power-law models, with the results shown in Table 2.3.

For all $L_X - L_S$ scaling relations, the scatter for the multi-color red sequence finder is smaller than or equal to the single-color values, independent of the selection radius and the fitting method. For example, for L_S computed with r_{200c} , the $OLS(L_S|L_X)$ relation has a scatter of 0.28 and 0.31 dex in L_X for multi-color and single color, respectively.

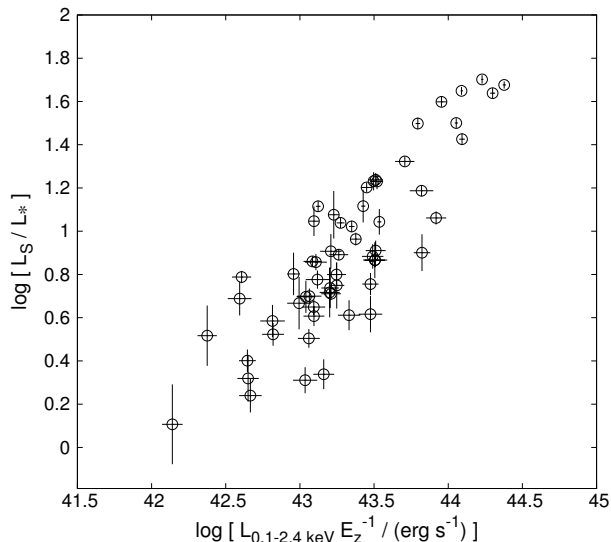


Figure 2.11: Integrated stellar luminosity in z' band versus L_X for clusters with X-ray detection level above 4.6 and $0.1 < z < 0.6$.

The reduction of scatter is even more significant in the case of a fixed 1 Mpc radius. For instance, the $\text{OLS}(L_S|L_X)$ scatter is 0.33 dex for the multi-color and 0.49 dex for the single-color red galaxy finder. Our results on the tight relation between the L_S and other mass proxies, such as L_X are in line with the low redshift studies of Rykoff et al. (2012) at $0.1 < z < 0.3$, and Andreon (2012) for $z < 0.14$.

In Figure 2.13, we considered the redshift evolution of the L_S – L_X relation. Using two subsamples with $0.1 < z < 0.3$ and $0.3 < z < 0.6$, we find a difference in the relation to X-ray luminosity ($L_X > 42.5 \text{ ergs s}^{-1}$). The low redshift relation is within the errors of high redshift relation. The results of fitting procedure for two subsamples are summarized in Table 2.4.

To compare our red sequence finder to other work, Figure 2.14 shows L_X versus richness parameter λ used in redMaPPer (next generation of MaxBCG method, Rykoff et al. 2013), designed to find clusters in SDSS data. Briefly, redMaPPer applies a red sequence model and assumes radial and luminosity filters to calculate the probability that a given galaxy belongs to a cluster. The parameter λ is the sum of mentioned probabilities. There are 10 RASS clusters in overlap between SDSS and the CFHTLS fields. The large errors in λ for a few clusters are caused by the shallow depths of SDSS data. Rozo et al. (2014) reported a scatter of 0.23 dex in X-ray temperature at fixed λ . Figure 2.14 shows that L_S and λ correlate.

2.4.5 Applying the red sequence finder to identify RASS sources

We apply the red sequence finder to identify clusters associated with 181 RASS sources within the three CFHTLS fields in our study and visually inspect the results. According

2. Brightest X-ray clusters of galaxies in the CFHTLS wide fields:
Catalog and optical mass estimator

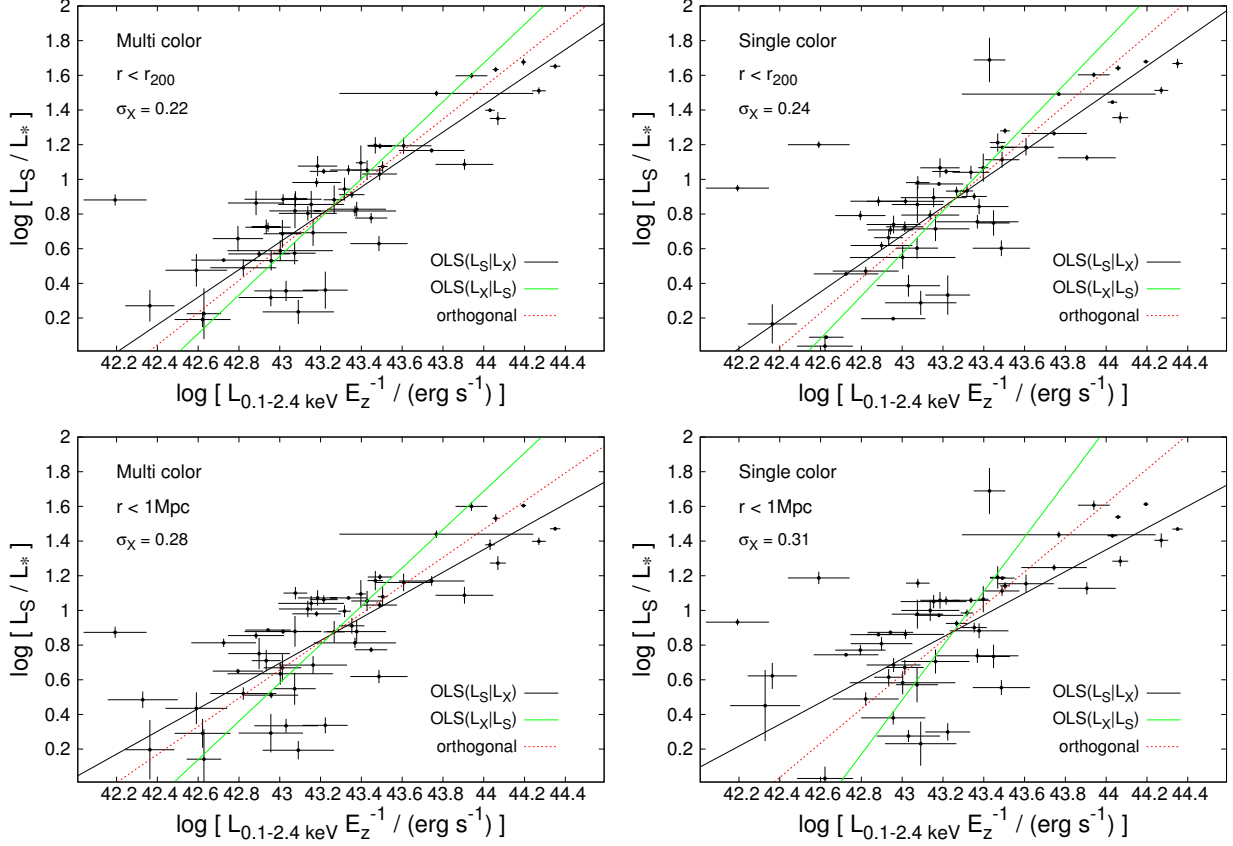


Figure 2.12: Integrated stellar luminosity in z' band versus L_X for clusters with visual flag=1 and at $0.1 < z < 0.6$. The upper and bottom panels show the results within r_{200c} and 1 Mpc, respectively. Left panels use galaxy selection from multi-color red sequence and right panels are the single-color red sequence. The filled circles show XMM clusters in overlap with RASS clusters. The solid black, solid green and dashed red lines show OLS($L_S|L_X$), OLS($L_X|L_S$) and orthogonal fits, respectively. In each panel, σ_X is the scatter in L_X direction for the orthogonal fits.

Table 2.3: Fitting parameters of $\log(L_X)-\log(L_S)$ relation. The Eddington bias correction is considered in fitting procedure (see §2.9). Col.(1) indicates the type of selection of red galaxies; col.(2) is the radius within which L_X is calculated. The fitting procedure is listed in col.(3). The cols. (4–5) present the intercept and slope of fittings respectively. The scatter in $\log L_X$ and $\log L_S$ direction are in cols. (6–7).

red sequence	radius	Fitting	intercept	slope	L_X scatter dex	L_S scatter dex
multi color	r_{200c}	OLS($L_S L_X$)	-33.50 ± 4.39	0.79 ± 0.10	0.25	0.20
		OLS($L_X L_S$)	-47.38 ± 6.09	1.11 ± 0.14	0.22	0.24
		orthogonal	-39.40 ± 4.67	0.93 ± 0.11	0.22	0.21
single color	r_{200c}	OLS($L_S L_X$)	-34.36 ± 5.69	0.81 ± 0.13	0.25	0.20
		OLS($L_X L_S$)	-52.14 ± 5.71	1.22 ± 0.13	0.24	0.29
		orthogonal	-42.33 ± 5.71	1.00 ± 0.13	0.28	0.22
multi color	1 Mpc	OLS($L_S L_X$)	-27.50 ± 3.61	0.65 ± 0.08	0.30	0.20
		OLS($L_X L_S$)	-46.95 ± 8.50	1.10 ± 0.19	0.27	0.30
		orthogonal	-34.26 ± 5.06	0.81 ± 0.12	0.28	0.22
single color	1 Mpc	OLS($L_S L_X$)	-26.35 ± 4.57	0.63 ± 0.11	0.44	0.28
		OLS($L_X L_S$)	-66.81 ± 18.4	1.56 ± 0.43	0.31	0.49
		orthogonal	-41.87 ± 10.9	0.99 ± 0.25	0.31	0.30

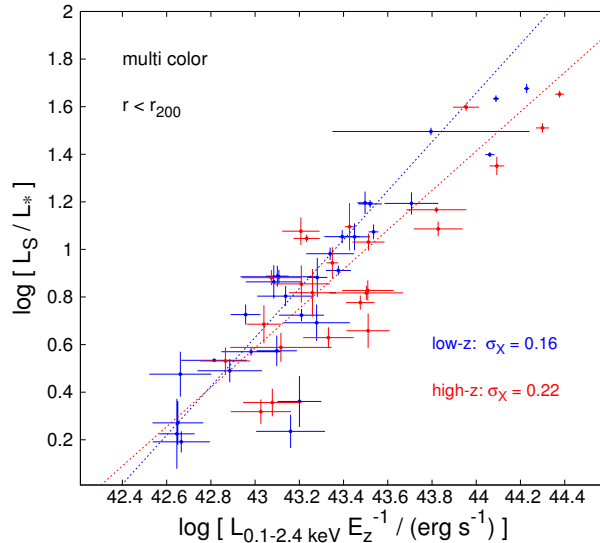


Figure 2.13: Stellar luminosity versus X-ray luminosity of clusters for low redshift (blue circles) and high redshift (red circles) subsamples. The blue and red lines show the orthogonal fitting results for each subsample, with the parameters presented in Tab.2.3.

Table 2.4: Fitting parameters of $\log(L_X - \log(L_S))$ relation for high redshift and low redshift samples.

redshift	radius	Fitting	intercept	slope	L_X scatter dex	L_S scatter dex
$0.1 < z < 0.3$	r_{200c}	OLS($L_S L_X$)	-41.81 ± 4.23	0.99 ± 0.10	0.17	0.18
		OLS($L_X L_S$)	-45.24 ± 4.38	1.07 ± 0.10	0.17	0.19
		orthogonal	-43.54 ± 4.17	1.03 ± 0.10	0.17	0.18
$0.3 < z < 0.6$	r_{200c}	OLS($L_S L_X$)	-25.72 ± 7.54	0.61 ± 0.17	0.23	0.19
		OLS($L_X L_S$)	-53.22 ± 15.3	1.25 ± 0.35	0.21	0.21
		orthogonal	-34.98 ± 10.6	0.83 ± 0.24	0.22	0.19
$0.1 < z < 0.3$	1 Mpc	OLS($L_S L_X$)	-33.59 ± 3.31	0.80 ± 0.08	0.24	0.21
		OLS($L_X L_S$)	-41.60 ± 5.71	0.98 ± 0.13	0.23	0.23
		orthogonal	-36.88 ± 3.98	0.87 ± 0.09	0.23	0.21
$0.3 < z < 0.6$	1 Mpc	OLS($L_S L_X$)	-22.74 ± 6.80	0.54 ± 0.16	0.29	0.20
		OLS($L_X L_S$)	-56.89 ± 19.2	1.33 ± 0.44	0.24	0.25
		orthogonal	-32.92 ± 11.9	0.78 ± 0.27	0.26	0.21

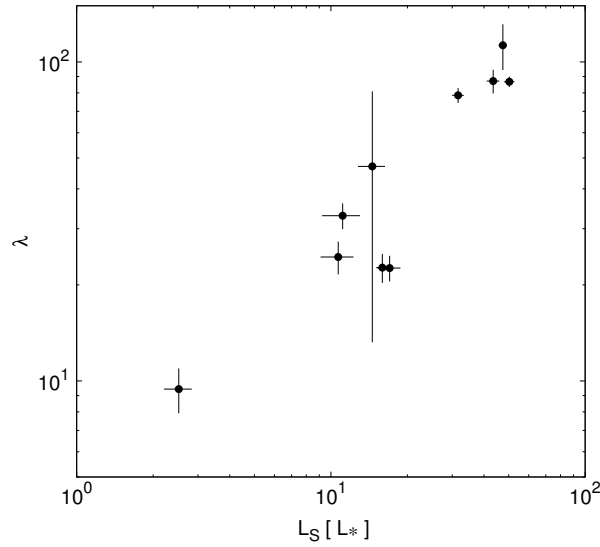


Figure 2.14: redMaPPer richness parameter λ (calculated using SDSS data) versus stellar luminosity within r_{200c} , L_S . A good correspondence between two measurements is observed.

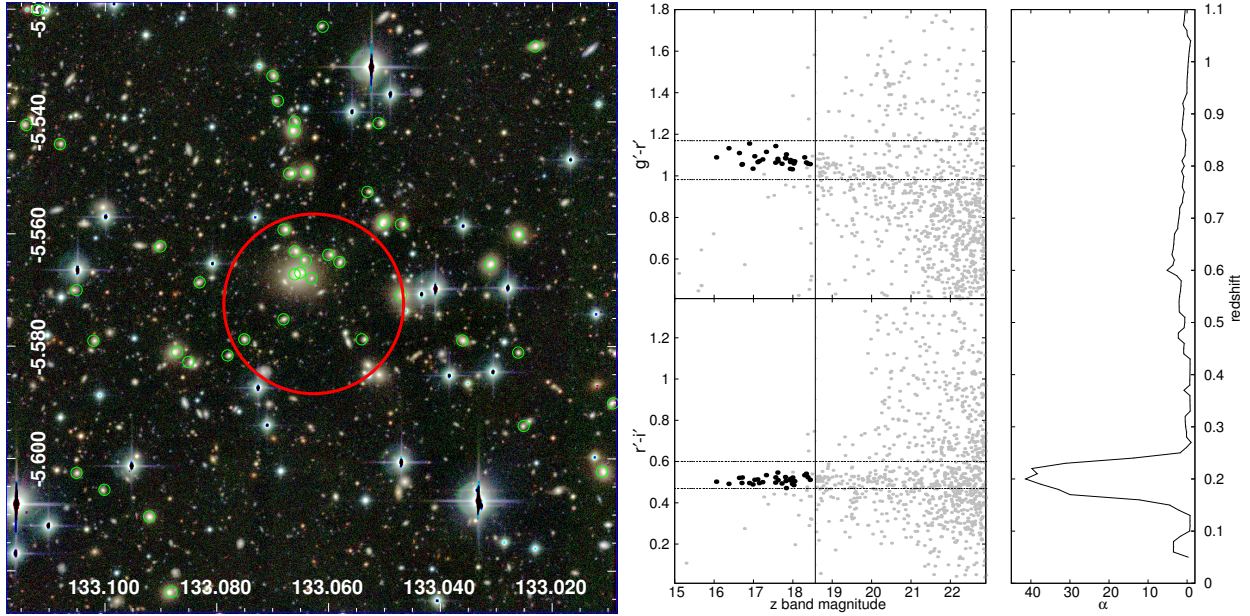


Figure 2.15: As in Figure 2.6 but for a RASS cluster at the redshift of 0.2. The position of the RASS source is shown by a large red circle with a radius of one arcminute.

to the $\log(N) - \log(S)$ relation, clusters make up only 10% of X-ray sources (Finoguenov et al. 2007; Cappelluti et al. 2007), making cluster identification difficult using unresolved X-ray sources in RASS data. The radius for galaxy selection has been set to 0.5 Mpc at each redshift plus two arcminutes to account for the survey PSF of RASS. After finding the red member galaxies, we derive the z' -band luminosity weighted center for each cluster candidate, which then defines the distance between the optical counterpart and the X-ray source position (hereafter Opt–X-ray distance). Figure 2.15 shows the red sequence finder results for a cluster at a redshift of 0.2. Through visual inspection, we realize that in many cases where the Opt–X-ray distance is small and α is low, there is a small overdensity of red galaxies at some redshift (according to the red sequence finder), but the galaxy positions are not concentrated on the sky. Figure 2.16 illustrates two cluster candidates with comparable redshifts and α values. Red sequence galaxies are marked with small circles and the X-ray sources are shown by big circles. The cluster candidate displayed on the left panel of Figure 2.16 is visually confirmed, since the concentration of red sequence galaxies is clear. On the right panel, on the other hand, red galaxies are distributed on the sky without any obvious concentration. In both images the centre of images is the optical centre of red galaxies. We only select the clusters that have a concentration of red galaxies close to the center of the X-ray source.

Figure 2.17 shows α versus redshift and Opt–X-ray distance for 182 RASS X-ray sources. The black dots represent the 27 galaxy clusters confirmed by visual inspection and grey dots are unconfirmed clusters. As shown on the left panel, confirmed clusters are mostly distributed from redshift 0 to 0.5 with one exception at redshift 0.83. In this case, a low

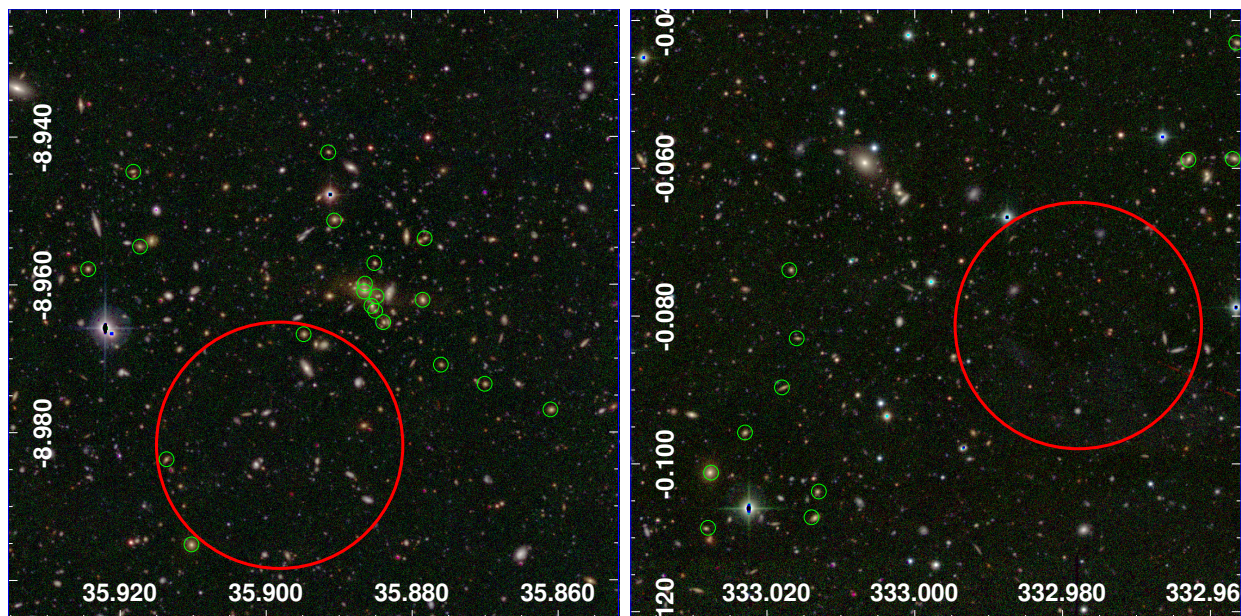


Figure 2.16: RGB images of two RASS X-ray sources produced using CFHTLS broadband images in g' as blue, r' as green and i' as red. The small green circles and large red circles show the positions of red sequence galaxies and RASS X-ray sources, respectively. The radius of the circles related to X-ray sources is one arcminute (for reference, the PSF of RASS images is about two arcminutes). The images are centered on the optical centre of the galaxies marked with green circles. The clusters shown on the left (right) panels have redshift=0.43 (0.40) and α =16.9 (14.3). Cluster candidates with a clear concentration of red galaxies, such as the one on the left panel, are considered as real clusters.

redshift spiral galaxy with $r'=18.6$ is located 25 arcseconds from the center of the X-ray source, making it questionable whether the X-ray emission from RASS is associated to an X-ray luminous cluster at high redshift or a spiral galaxy. X-ray observations with higher spatial resolution are required to answer this question.

2.5 RASS-CFHTLS and XMM-CFHTLS catalogs of X-ray selected clusters

In this section, we present the RASS and XMM (X-ray) selected cluster catalogs, with 27 and 196 systems, respectively. The first 133 clusters in this catalog belong to the sample with X-ray detection threshold above 4.6 sigma. Column 1 in table 2.5 shows the cluster ID for the XMM-CFHTLS sample with the first digit referring to the CFHTLS wide field (1,2 or 4). Columns 2 and 3 are respectively R.A. and Dec. of the X-ray source centers. Columns 4 and 5 are the red sequence redshift and red sequence significance, α , of the clusters. Column 6 lists cluster flux and one sigma error in flux corresponding to the

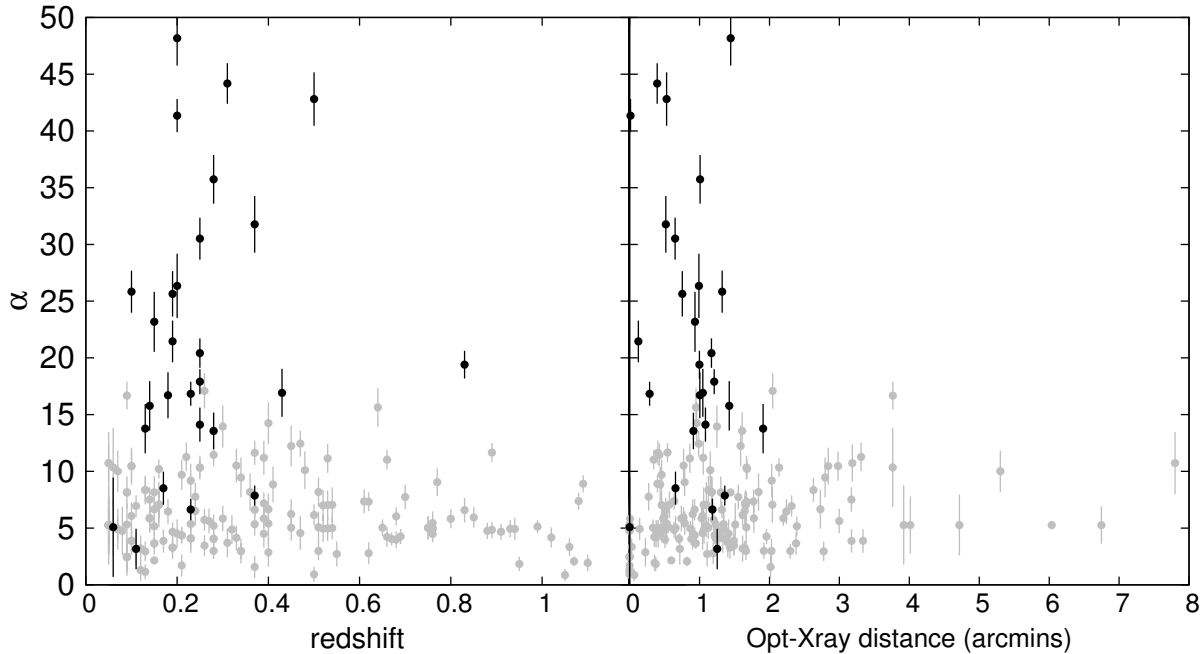


Figure 2.17: *Left*: Red sequence significance, α , versus redshift for RASS X-ray sources. *Right*: Red sequence significance, α , vs offset between optical and X-ray cluster centers. Black dots mark the visually confirmed clusters and grey ones are other RASS X-ray sources.

0.5–2 keV band in units of 10^{-14} ergs cm^{-2} s^{-1} . Column 7 reports the rest-frame X-ray luminosity, L_X , in the 0.1–2.4 keV band. The total mass M_{200c} , estimated from the X-ray luminosity using the L_X – M scaling relation and its evolution from Leauthaud et al. (2010), is given in column 8. Column 9 lists corresponding radius, r_{200c} , in arcminutes. Spectroscopic redshifts of the clusters are provided in column 10. For clusters with a spectroscopic redshift in this column, M_{200c} , and, r_{200c} are computed using spectroscopic redshift. Column 11 reports the visual flag described in Sect. 2.4.2. Velocity dispersion and number of spectroscopic members (both described in Sect. 2.4.3) for clusters having more than five spectroscopic members are given in columns 12 and 13, respectively.

The RASS-CFHTLS cluster catalog is listed in Tab. 2.5. Column 1 is the cluster ID. The coordinates (RA and DEC, Equinox J2000) of the clusters are given in columns 2 and 3. The red sequence redshift and significance (α) are listed in column 4 and 5. The position of the optical center is reported in column 6 and 7. Column 8 reports ROSAT X-ray flux in units of 10^{-13} erg s^{-1} cm^{-2} . The spectroscopic redshifts which were also verified visually are given in column 9. The columns 10 and 11 present the velocity dispersion and the number of spectroscopic member galaxies from Sect. 2.4.3. Based on the derived relation between L_X and L_S , we estimate the $L_X(L_S)$ for 27 RASS clusters. We measured L_S within 1 Mpc from the optical center of clusters (column 6 and 7 in table 2.5). The estimated cluster L_X using orthogonal fitting result (with 0.26 dex scatter in X-ray luminosity) are

listed in column 12 of table 2.5.

The inferred mass and X-ray luminosity of the XMM clusters as a function of redshift are illustrated in Figure 2.18. We mark 16 XMM clusters in common to RASS clusters as squares. This sub-sample of RASS clusters stems from our targeted follow-up observations of RASS clusters found inside the part of CFHTLS survey publicly released in T0005 and presents an effective search for massive clusters in the area of 90 square degrees. The two curves in Figure 2.18 show the detection boundary related to $2 \times 10^{-13} \text{erg cm}^{-2} \text{s}^{-1}$ in X-ray flux. This flux is associated with a detection limit over 85% of the survey area. The mass (and luminosity) detection limit, shown with a curve in Figure 2.18, implies that only extreme clusters ($\sim 10^{15} M_{\odot}$) at redshift ~ 1 are detectable in RASS data.

We added COSMOS X-ray selected galaxy clusters (Finoguenov et al. 2007, George et al. 2011) to the plots, to show the difference in the cluster sample. At a fixed redshift, the typical mass (and luminosity) of XMM-CFHTLS clusters are an order of magnitude more massive (and more luminous) in comparison with a typical group in deep surveys such as COSMOS. For example at the redshift range of $0.2 \leq z \leq 0.3$, the median of the M_{200c} of XMM-CFHTLS and COSMOS clusters are respectively $1.1 \times 10^{14} M_{\odot}$ and $2.6 \times 10^{13} M_{\odot}$. This difference between the mean total mass (and luminosity) is even larger between COSMOS and RASS-CFHTLS clusters.

A comparison of the X-ray fluxes from RASS and XMM is presented in Figure 2.19. At low flux levels, the RASS flux estimates are subject to the Malmquist bias, as shown by a model curve. We also report that the mean of distances between the centre of RASS and XMM X-ray emissions is 0.6 arcminutes for 16 clusters in overlap between RASS and XMM samples.

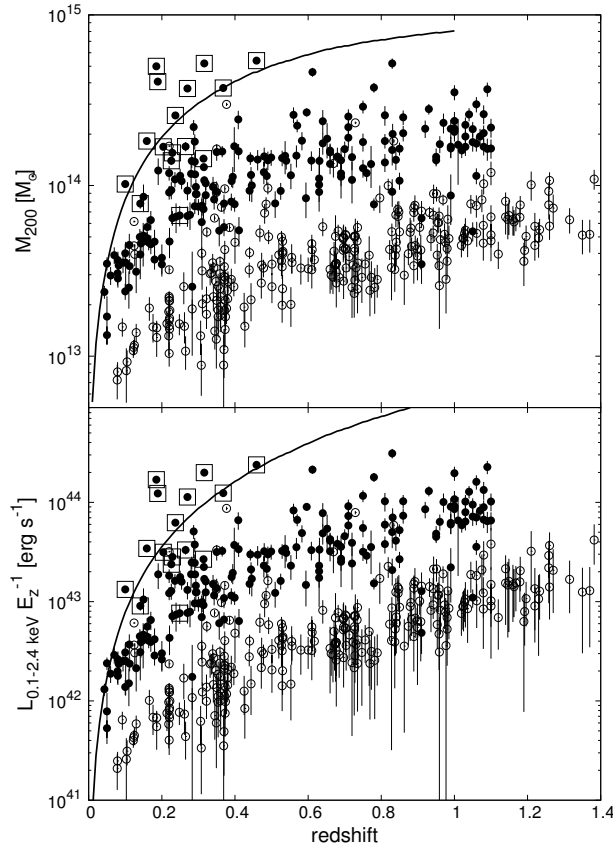


Figure 2.18: X-ray mass (top) and X-ray luminosity (bottom) as functions of redshift. Black dots and open circles show XMM-CFHTLS and COSMOS X-ray selected galaxy clusters. The errors are calculated with statistical errors in the X-ray flux measurements. 16 XMM clusters in common to RASS clusters are marked as squares. In both panels, the solid curves show the detection limits in luminosity- and mass-redshift spaces corresponding to X-ray flux limit of $2 \times 10^{-13} \text{ erg cm}^{-2} \text{ s}^{-1}$.

2.6 Summary

We have presented the results of an X-ray search for bright clusters in the CFHTLS fields. In this work we presented the cluster identification in RASS and XMM data. We developed a method for identifying clusters at the limits of RASS data, reaching flux levels of $2 \times 10^{-13} \text{ erg cm}^{-2} \text{ s}^{-1}$, with the help of deep photometric data, such as that of CFHTLS.

We have described a multi-color red sequence finder and calibrated it for CFHTLS $u^*g'r'i'z'$ filters and the redshift below 1.1. The spectroscopic follow-up was done using the Hectospec spectrograph on MMT, with higher priority for clusters with high X-ray flux. To increase the efficiency of spectroscopic follow-up, target galaxies were selected within a range of photometric redshift around the red sequence redshift of clusters. In this work we also used SDSS spectroscopic data in the CFHTLS wide fields. We applied our red sequence

2. Brightest X-ray clusters of galaxies in the CFHTLS wide fields: Catalog and optical mass estimator

56

Table 2.5: Catalog of XMM-CFHTLS X-ray Selected Galaxy Clusters

ID XMM-CFHTLS (1)	RA (degrees) (2)	DEC (degrees) (3)	R.S. (4)	z (5)	α (6)	X-ray Flux $10^{-14} \text{ erg cm}^{-2} \text{ s}^{-1}$ (7)	L_X $10^{42} \text{ erg s}^{-1}$ (8)	M_{200c} $10^{13} M_\odot$ (9)	r_{200c} arcmin (10)	specz (11)	visual flag (12)	$\sigma(v)$ (km s^{-1}) (13)	N_σ (14)
XCC J0210.4-0343	32.6184	-3.7202	0.47	2.27±0.59	3.4±0.46	29.89±4.02	14.43±1.21	2.73	0.4417	1	-	1	
XCC J0211.0-0905	32.7665	-9.0977	0.41	2.41±1.4	4.54±0.75	33.75±5.59	15.87±1.64	2.98	-0	2	-	-	
XCC J0211.2-0343	32.8079	-3.7226	0.78	19.25±2.17	7.44±0.77	179.16±18.61	37.51±2.45	2.52	-0	1	-	-	
XCC J0211.3-0927	32.8338	-9.4567	1.03	0.75±0.43	2.35±0.39	101.68±17.06	22.67±2.37	1.79	-0	2	-	-	
XCC J0211.4-0920	32.8551	-9.3366	0.81	3.43±1.17	3.75±0.8	102.61±21.86	25.82±3.4	2.17	-0	2	-	-	
XCC J0211.5-0939	32.8894	-9.6606	0.47	13.12±1.77	3.07±0.63	32.16±6.6	14.81±1.88	2.59	0.4801	2	-	1	
XCC J0212.2-0852	33.0716	-8.8752	0.1	5.95±1.51	7.94±1.71	2.52±0.54	3.53±0.47	6.32	0.094	2	-	3	
XCC J0213.4-0813	33.37	-8.2204	0.25	6.78±1.12	6.96±1.15	16.21±2.68	10.86±1.11	4.08	0.2358	1	446±84	12	
XCC J0213.6-0552	33.4141	-5.8707	1.0	0.81±0.5	2.2±0.37	91.47±15.17	21.54±2.22	1.79	-0	2	-	-	
XCC J0214.1-0630	33.545	-6.516	0.81	1.22±0.9	1.24±0.24	37.93±7.41	13.65±1.66	1.76	-0	2	-	-	
XCC J0214.4-0627	33.6064	-6.4605	0.25	38.42±2.91	27.67±0.97	62.39±2.2	25.74±0.58	5.42	0.2366	1	329±108	12	
XCC J0215.6-0702	33.9113	-7.0478	1.02	0.03±0.51	1.28±0.2	58.84±9.32	16.06±1.58	1.6	-0	2	-	-	
XCC J0215.7-0654	33.9274	-6.9051	0.27	5.18±1.14	5.79±0.97	15.87±2.68	10.62±1.11	3.8	0.2544	1	377±65	10	
XCC J0216.1-0935	34.0291	-9.5885	0.64	36.89±3.26	5.95±0.51	89.99±7.75	26.81±1.45	2.71	0.5955	1	-	4	
XCC J0216.5-0658	34.1416	-6.9691	1.1	0.62±0.56	1.26±0.26	65.69±13.67	16.48±2.12	1.54	-0	2	-	-	
XCC J0216.7-0934	34.1938	-9.5702	0.99	4.43±0.94	2.21±0.47	90.39±19.03	21.5±2.8	1.8	-0	2	-	-	
XCC J0217.5-0655	34.3779	-6.9236	1.03	1.09±0.52	1.39±0.26	64.03±11.94	16.86±1.95	1.62	-0	2	-	-	
XCC J0217.5-0936	34.3788	-9.6136	0.37	10.75±1.89	1.73±0.36	10.85±2.25	7.84±1.0	2.55	-0	2	-	-	
XCC J0217.5-0927	34.3874	-9.462	0.65	12.68±1.54	6.17±1.04	82.87±14.03	25.95±2.72	2.8	0.56	1	-	2	
XCC J0217.8-0641	34.4574	-6.689	1.05	0.8±0.39	2.09±0.34	94.68±15.15	21.41±2.14	1.73	-0	2	-	-	
XCC J0217.9-0648	34.4871	-6.8068	0.84	-0.05±0.49	1.26±0.26	41.19±8.67	14.15±1.84	1.73	-0	2	-	-	
XCC J0218.0-0937	34.5029	-9.6256	0.18	4.54±1.01	4.46±0.62	4.43±0.62	4.92±0.43	4.37	0.1598	1	232±73	9	
XCC J0218.3-0942	34.5814	-9.7028	0.41	10.88±2.91	2.55±0.32	17.72±2.19	10.61±0.82	2.71	0.3908	1	-	1	
XCC J0219.6-0759	34.9039	-7.9882	0.85	3.03±1.06	1.62±0.23	52.48±7.34	16.43±1.43	1.81	-0	1	-	-	
XCC J0220.1-0836	35.031	-8.6072	0.07	6.57±2.4	16.88±3.07	2.9±0.53	3.91±0.44	8.6	-0	2	-	-	
XCC J0220.3-0730	35.0849	-7.5027	1.06	0.65±0.46	3.75±0.62	161.0±26.57	29.91±3.08	1.93	-0	2	-	-	
XCC J0220.6-0839	35.167	-8.6639	0.14	4.77±1.46	5.17±0.84	2.37±0.38	3.37±0.34	5.29	0.1121	1	410±174	5	
XCC J0220.9-0838	35.2279	-8.6402	0.52	19.96±1.96	1.21±0.22	16.18±2.95	9.3±1.05	2.08	0.5251	1	-	1	
XCC J0221.2-0846	35.3163	-8.7702	0.08	6.57±0.0	7.94±1.5	1.79±0.34	2.85±0.33	6.83	-0	2	-	-	
XCC J0221.5-0630	35.3822	-6.515	1.0	2.86±0.81	2.15±0.4	89.46±16.69	21.24±2.46	1.78	-0	2	-	-	
XCC J0221.5-0830	35.3904	-8.5108	1.08	1.3±0.61	1.86±0.32	89.32±15.48	20.29±2.19	1.67	-0	2	-	-	
XCC J0221.6-0618	35.4101	-6.316	0.66	10.42±1.07	2.13±0.29	42.6±5.77	16.02±1.36	2.12	-0	2	-	-	
XCC J0221.6-0825	35.4113	-8.4271	1.05	0.24±0.65	1.53±0.3	71.87±13.93	17.95±2.16	1.63	-0	2	-	-	
XCC J0221.9-0857	35.4915	-8.9622	0.28	5.85±1.27	3.32±0.59	12.44±2.19	8.91±0.98	3.19	0.2933	1	-	4	
XCC J0222.8-0623	35.7098	-6.3935	0.49	5.04±1.86	2.72±0.54	29.91±5.96	14.06±1.73	2.51	-0	2	-	-	
XCC J0223.2-0830	35.8101	-8.514	0.14	4.77±1.28	5.98±1.08	4.47±0.81	4.99±0.56	4.94	-0	2	-	-	
XCC J0223.8-0826	35.9663	-8.4449	0.69	4.61±1.29	1.09±0.21	25.2±4.83	11.25±1.34	1.83	-0	1	-	-	
XCC J0223.8-0821	35.967	-8.3552	0.23	23.35±0.52	13.08±1.22	28.17±2.62	15.53±0.91	4.72	0.2287	1	435±109	7	
XCC J0223.9-0830	35.9826	-8.5069	0.16	9.92±1.53	3.89±0.62	4.05±0.65	4.63±0.46	4.2	0.1635	1	407±214	9	
XCC J0224.0-0835	35.998	-8.5956	0.28	38.1±2.57	38.9±0.86	113.18±2.5	37.05±0.52	5.49	0.2701	1	675±142	10	
XCC J0224.1-0816	36.0234	-8.2682	0.25	16.51±2.58	6.71±1.06	17.65±2.8	11.4±1.12	3.95	-0	2	-	-	
XCC J0224.3-0917	36.0903	-9.289	0.7	0.43±0.65	2.04±0.35	45.56±7.94	16.35±1.76	2.05	-0	2	-	-	
XCC J0224.4-0924	36.0983	-9.4054	0.54	9.92±1.76	1.92±0.36	21.45±4.06	11.38±1.33	2.35	0.4874	2	-	1	
XCC J0224.4-0827	36.1046	-8.4578	0.06	6.57±2.4	15.16±2.95	1.88±0.36	2.97±0.36	9.08	-0	2	-	-	
XCC J0224.6-0931	36.1586	-9.5279	0.75	0.48±0.69	2.2±0.43	55.23±10.7	17.97±2.16	2.02	-0	2	-	-	
XCC J0224.6-0919	36.1606	-9.3302	1.0	0.81±0.55	2.04±0.4	85.51±16.92	20.63±2.53	1.76	-0	2	-	-	
XCC J0224.7-0924	36.1888	-9.4073	0.96	1.17±0.17	1.58±0.29	63.69±11.69	17.47±1.99	1.71	-0	2	-	-	
XCC J0224.8-0620	36.2207	-6.3371	1.08	5.99±0.79	1.34±0.24	67.01±12.04	16.88±1.89	1.57	-0	2	-	-	
XCC J0225.0-0950	36.2713	-9.8381	0.18	19.65±2.01	34.41±1.11	34.32±1.11	18.23±0.37	6.79	0.1594	1	528±69	18	
XCC J0225.2-0623	36.3021	-6.3837	0.2	21.38±1.21	18.66±0.93	31.41±1.56	16.86±0.53	5.33	0.2041	1	414±78	10	
XCC J0225.5-0619	36.3929	-6.3228	0.99	1.61±0.77	1.38±0.28	59.81±12.03	16.5±2.05	1.64	-0	2	-	-	
XCC J0225.5-0612	36.3953	-6.2134	0.3	9.02±1.33	3.87±0.68	14.47±2.55	9.82±1.08	3.3	0.2932	2	-	1	
XCC J0225.6-0946	36.4034	-9.7797	0.34	13.55±1.87	2.19±0.45	11.58±2.39	8.29±1.06	2.75	0.3429	1	452±152	5	
XCC J0225.9-0830	36.479	-8.5086	1.06	0.13±0.62	1.46±0.24	70.36±11.55	17.61±1.8	1.61	-0	2	-	-	
XCC J0226.4-0845	36.6144	-8.766	0.32	9.5±1.98	2.74±0.53	12.41±2.4	8.77±1.05	2.96	-0	2	-	-	
XCC J0229.0-0549	37.2606	-5.8297	0.18	2.02±1.15	2.25±0.47	2.87±0.6	3.68±0.47	3.58	-0	2	-	-	
XCC J0229.2-0553	37.3203	-5.8983	0.34	13.55±2.09	5.13±0.32	18.79±1.17	11.61±0.46	3.5	0.2915	1	505±94	7	
XCC J0229.5-0553	37.3826	-5.8998	0.31	14.39±1.92	3.27±0.27	12.44±1.01	8.9±0.46	3.18	0.295	1	322±64	13	
XCC J0230.1-0540	37.5371	-5.6803	0.52	14.85±2.5	2.81±0.48	31.97±5.49	14.6±1.56	2.51	0.4991	1	-	3	
XCC J0230.8-0421	37.7203	-4.3507	0.16	7.32±2.03	11.75±1.23	9.06±0.95	7.84±0.52	5.71	0.1408	1	427±132	9	
XCC J0230.9-0431	37.7413	-4.5285	0.86	0.87±0.58	2.3±0.39	73.39±12.3	20.25±2.11	1.93	-0	2	-	-	
XCC J0231.7-0452	37.927	-4.8814	0.2	67.62±3.55	128.74±1.2	168.99±1.57	49.94±0.3	8.33	0.1852	1	426±194	9	
XCC J0232.6-0449	38.1654	-4.8331	0.17	7.39±1.78	5.71±1.2	6.53±1.37	6.27±0.82	4.49	-0	2	-	-	
XCC J0233.4-0540	38.3625	-5.6749	0.51	14.98±2.29	2.52±0.42	32.43±5.45	14.49±1.51	2.4	0.5287	1	-	4	
XCC J0233.6-0542	38.4048	-5.701	0.3	1.85±0.96	2.43±0.42	9.59±1.66	7.52±0.81	2.96	-0	2	-	-	
XCC J0233.6-0941	38.4183	-9.6995	0.26	15.02±1.42	11.34±1.13	33.11±3.3	16.92±1.06	4.3	0.2646	1	395±56	20	

Continued on next page.

Table 2.4: Continued from previous page.

ID	RA	DEC	R.S. z	α	X-ray Flux	L_X	M_{200c}	r_{200c}	specz	visual flag	$\sigma(v)$	N_σ
XMM-CFHTLS	(degrees)	(degrees)			$10^{-14} \text{ erg cm}^{-2} \text{ s}^{-1}$	$10^{42} \text{ erg s}^{-1}$	$10^{13} M_\odot$	arcmin			(km s^{-1})	
(1)	(2)	(3)	(4)	(5)	(6)	(7)	(8)	(9)	(10)	(11)	(12)	(13)
XCC J0233.8-0939	38.4607	-9.6656	0.25	4.34±0.87	4.22±0.83	13.12±2.59	9.33±1.14	3.47	0.2695	1	475±117	7
XCC J0234.3-0940	38.5794	-9.6711	0.83	31.07±2.88	12.05±1.32	311.28±34.32	51.93±3.59	2.7	-0	1	-	-
XCC J0234.3-0936	38.5851	-9.6158	1.08	4.12±0.75	2.93±0.6	133.16±27.21	26.2±3.32	1.82	-0	2	-	-
XCC J0234.3-0951	38.586	-9.8583	0.65	24.39±2.01	14.29±1.35	213.56±20.29	46.19±2.75	3.18	0.6119	1	-	4
XCC J0234.7-0548	38.6768	-5.8095	0.97	3.31±0.87	2.6±0.56	100.72±21.84	23.3±3.12	1.87	-0	2	-	-
XCC J0234.9-0400	38.7257	-4.013	0.63	4.76±1.14	0.88±0.18	17.36±3.54	9.17±1.16	1.82	-0	2	-	-
XCC J0849.2-0252	132.307	-2.8775	0.25	21.38±1.8	11.31±0.98	23.8±2.07	13.96±0.77	4.6	0.2259	1	491±124	11
XCC J0849.9-0312	132.473	-3.2009	0.54	15.11±4.03	2.29±0.41	30.94±5.6	13.97±1.57	2.33	-0	1	-	-
XCC J0849.9-0159	132.491	-1.9925	0.05	6.57±1.47	28.05±3.97	2.39±0.34	3.48±0.31	11.39	-0	2	-	-
XCC J0850.0-0149	132.5	-1.8261	0.37	10.75±2.48	1.05±0.19	6.59±1.22	5.7±0.65	2.29	-0	1	-	-
XCC J0850.0-0235	132.504	-2.5955	0.22	14.50±1.24	6.02±1.12	12.81±2.38	9.39±1.08	4.03	0.226	1	-	3
XCC J0850.1-0149	132.53	-1.8279	1.06	4.31±0.77	0.67±0.11	35.63±6.1	11.39±1.21	1.39	-0	2	-	-
XCC J0850.7-0140	132.674	-1.682	0.31	6.94±1.73	2.33±0.47	9.87±2.01	7.62±0.96	2.9	-0	1	-	-
XCC J0852.0-0134	133.022	-1.5738	0.71	2.87±0.84	2.61±0.55	58.42±12.28	19.06±2.47	2.14	-0	1	-	-
XCC J0852.2-0533	133.066	-5.5651	0.21	47.84±2.89	88.92±1.27	122.83±1.74	40.64±0.37	7.64	0.1891	1	385±85	7
XCC J0852.2-0101	133.067	-1.0261	0.51	35.59±4.5	28.47±0.66	238.33±5.54	53.98±0.8	4.12	0.4587	1	-	4
XCC J0852.4-0345	133.118	-3.752	1.04	2.73±0.68	2.99±0.43	127.85±18.19	26.1±2.32	1.86	-0	2	-	-
XCC J0852.5-0112	133.123	-1.2128	0.56	13.8±3.72	4.7±0.64	66.56±9.08	22.43±1.91	2.63	-0	1	-	-
XCC J0852.6-0152	133.154	-1.8826	1.1	4.01±1.47	2.09±0.43	102.01±20.77	21.85±2.75	1.69	-0	2	-	-
XCC J0852.9-0503	133.236	-5.0593	0.06	6.57±3.21	21.01±2.94	1.31±0.18	2.38±0.21	11.59	0.043	1	300±100	9
XCC J0853.0-0344	133.269	-3.7363	0.93	31.34±1.44	3.74±0.43	129.88±14.85	28.04±2.01	2.04	-0	1	-	-
XCC J0853.1-0459	133.282	-4.9996	0.44	5.3±1.66	1.66±0.36	15.09±3.23	9.32±1.23	2.37	-0	2	-	-
XCC J0853.3-0144	133.333	-1.7485	0.66	18.8±1.55	1.57±0.33	32.19±6.76	13.39±1.74	2.0	-0	1	-	-
XCC J0853.4-0341	133.361	-3.6866	0.75	10.18±1.83	5.0±0.69	116.4±16.1	28.96±2.51	2.37	-0	1	-	-
XCC J0853.6-0348	133.403	-3.8094	0.95	8.01±1.07	1.18±0.23	48.29±9.39	14.72±1.77	1.63	-0	1	-	-
XCC J0853.6-0532	133.416	-5.543	0.85	1.99±0.75	0.75±0.14	26.73±4.93	10.67±1.22	1.57	-0	2	-	-
XCC J0853.9-0503	133.484	-5.0618	0.39	11.74±1.51	1.63±0.3	11.49±2.13	8.05±0.93	2.47	-0	2	-	-
XCC J0854.1-0342	133.524	-3.7154	0.71	11.63±1.99	4.27±0.7	91.4±14.99	25.38±2.59	2.36	-0	1	-	-
XCC J0854.2-0221	133.555	-2.3499	0.39	42.02±2.97	22.49±1.0	123.93±5.5	37.31±1.05	4.31	0.3679	1	451±133	9
XCC J0854.8-0530	133.702	-5.4999	0.05	6.57±2.91	6.08±1.21	0.53±0.11	1.33±0.16	8.26	-0	2	-	-
XCC J0854.9-0147	133.743	-1.7927	0.76	4.31±1.09	1.04±0.18	28.99±4.91	11.83±1.24	1.75	-0	2	-	-
XCC J0856.4-0146	134.105	-1.7725	0.15	6.78±1.12	5.35±1.03	4.64±0.89	5.09±0.6	4.67	-0	2	-	-
XCC J0857.1-0106	134.293	-1.1138	0.72	11.53±1.82	1.91±0.41	33.02±7.03	14.01±1.84	2.15	0.609	1	-	1
XCC J0857.4-0532	134.367	-5.5371	0.08	6.57±1.47	11.58±2.3	2.62±0.52	3.65±0.45	7.42	-0	2	-	-
XCC J0858.3-0438	134.595	-4.6448	0.71	20.38±2.28	3.33±0.43	72.93±9.4	21.96±1.77	2.24	-0	1	-	-
XCC J0858.6-0525	134.661	-5.4212	0.1	34.36±3.17	35.22±1.3	13.28±0.49	10.2±0.24	8.5	-0	1	-	-
XCC J0859.7-0419	134.923	-4.3263	0.75	4.64±1.2	1.19±0.23	31.81±6.12	12.62±1.51	1.8	-0	2	-	-
XCC J0900.3-0318	135.083	-3.3071	0.1	2.8±1.57	3.84±0.66	1.38±0.24	2.4±0.26	5.24	-0	2	-	-
XCC J0901.5-0139	135.377	-1.6532	0.34	35.89±3.54	50.39±2.05	199.21±8.09	51.95±1.34	5.41	0.3163	1	456±69	20
XCC J0901.6-0154	135.406	-1.9074	0.28	23.05±1.98	5.19±0.23	22.35±0.97	12.82±0.35	3.41	0.3151	1	454±46	7
XCC J0901.6-0158	135.415	-1.9799	0.34	27.51±3.52	6.29±0.21	26.71±0.87	14.38±0.3	3.55	0.3141	1	516±80	11
XCC J0901.7-0228	135.437	-2.4809	0.86	3.84±0.89	3.34±0.52	102.58±16.03	25.09±2.44	2.07	-0	2	-	-
XCC J0901.7-0208	135.439	-2.1378	0.4	16.91±2.66	1.48±0.23	10.96±1.7	7.77±0.75	2.39	0.3994	1	334±64	5
XCC J0901.8-0143	135.45	-1.7226	0.22	14.5±1.5	9.14±1.43	18.28±2.87	11.83±1.15	4.45	-0	2	-	-
XCC J0901.9-0200	135.494	-2.0115	0.95	1.18±1.0	1.08±0.11	44.94±4.64	14.06±0.91	1.6	-0	2	-	-
XCC J0902.0-0228	135.5	-2.4734	1.0	2.86±0.75	2.65±0.55	107.55±22.47	23.89±3.09	1.85	-0	2	-	-
XCC J0902.3-0230	135.582	-2.5034	0.35	2.48±1.03	5.94±1.06	31.61±5.63	15.71±1.74	3.35	-0	2	-	-
XCC J0902.4-0219	135.604	-2.3188	0.28	3.7±1.2	2.62±0.42	9.6±1.56	7.56±0.76	3.05	-0	2	-	-
XCC J0903.5-0518	135.873	-5.3151	0.17	10.01±1.78	3.47±0.7	3.92±0.79	4.53±0.57	4.03	-0	2	-	-
XCC J0904.0-0151	136.01	-1.8636	1.09	2.37±0.96	5.23±0.8	226.81±34.65	36.63±3.49	2.02	-0	2	-	-
XCC J0904.0-0142	136.02	-1.7036	0.28	3.7±1.23	10.6±1.73	37.5±6.13	18.08±1.83	4.08	-0	2	-	-
XCC J0904.1-0329	136.026	-3.492	0.68	1.96±0.66	1.78±0.37	38.19±7.97	14.77±1.91	2.02	-0	2	-	-
XCC J0904.1-0202	136.043	-2.0333	0.31	19.35±1.24	14.89±2.4	50.93±8.22	22.03±2.21	4.39	0.2874	1	546±70	17
XCC J0904.6-0202	136.154	-2.0496	0.39	29.91±4.16	9.31±1.87	66.05±13.24	24.4±3.03	3.45	0.4087	1	553±243	5
XCC J0904.6-0200	136.161	-2.0138	1.0	6.29±1.2	5.19±0.85	196.66±32.11	35.16±3.57	2.11	-0	2	-	-
XCC J2202.1+0142	330.539	1.716	0.21	11.56±1.38	6.05±0.9	12.14±1.81	9.11±0.84	4.08	0.2199	2	522±153	10
XCC J2206.3+0146	331.576	1.7725	1.07	4.87±0.53	1.72±0.3	82.4±14.29	19.38±2.09	1.66	-0	2	-	-
XCC J2206.4+0139	331.603	1.6554	0.28	1.55±1.32	7.33±1.08	24.76±3.63	13.92±1.28	3.83	0.2818	1	-	1
XCC J2212.1-0010	333.029	-0.168	0.81	5.65±1.01	2.05±0.32	59.61±9.32	18.24±1.78	1.93	-0	2	-	-
XCC J2212.1-0008	333.045	-0.1348	0.37	13.55±2.91	5.58±0.68	32.4±3.93	15.84±1.2	3.26	0.3647	1	-	3
XCC J2212.2+0005	333.072	0.0957	1.03	2.32±0.79	1.78±0.38	79.55±16.81	19.37±2.53	1.69	-0	1	-	-
XCC J2214.3+0047	333.59	0.7857	0.31	19.35±3.09	3.54±0.52	15.98±2.33	10.31±0.94	3.13	0.3202	1	-	2
XCC J2214.8+0047	333.706	0.7837	0.34	16.34±4.58	3.88±0.34	16.92±1.47	10.72±0.59	3.2	0.3155	1	-	3
XCC J2214.9-0039	333.736	-0.6541	0.92	4.64±0.87	2.38±0.45	85.11±16.06	21.52±2.52	1.88	-0	2	-	-
XCC J2217.7+0017	334.436	0.2914	0.78	4.95±1.1	0.48±0.06	15.27±2.02	7.76±0.64	1.49	-0	2	-	-
XCC J2217.8+0023	334.458	0.3835	0.91	9.16±1.25	0.28±0.06	12.76±2.54	6.43±0.79	1.27	-0	1	-	-

Continued on next page.

2. Brightest X-ray clusters of galaxies in the CFHTLS wide fields: Catalog and optical mass estimator

58

Table 2.4: Continued from previous page.

ID	RA	DEC	R.S. z	α	X-ray Flux	L_X	M_{200c}	r_{200c}	specz	visual flag	$\sigma(v)$	N_σ
XMM-CFHTLS	(degrees)	(degrees)			$10^{-14} \text{ erg cm}^{-2} \text{ s}^{-1}$	$10^{42} \text{ erg s}^{-1}$	$10^{13} M_\odot$	arcmin			(km s^{-1})	
(1)	(2)	(3)	(4)	(5)	(6)	(7)	(8)	(9)	(10)	(11)	(12)	(13)
XCC J2217.8+0016	334.471	0.279	1.05	1.35±0.61	0.16±0.03	10.96±2.29	5.39±0.7	1.09	-0	2	-	-
XCC J0210.4-0345	32.6203	-3.7545	0.51	9.83±1.68	0.96±0.28	12.25±3.56	7.85±1.39	2.0	-0	2	-	-
XCC J0211.0-0853	32.7522	-8.8984	0.43	19.13±2.83	1.82±0.6	16.94±5.65	10.01±2.02	2.4	0.4459	2	-	1
XCC J0214.1-0808	33.5342	-8.1451	0.22	4.5±1.0	2.9±0.65	7.65±1.7	6.67±0.92	3.31	0.2495	1	180±55	13
XCC J0214.7-0618	33.676	-6.309	0.26	12.79±1.78	3.06±1.0	7.39±2.4	6.56±1.3	3.41	0.2395	1	528±30	25
XCC J0214.7-0804	33.6919	-8.069	0.72	2.84±1.07	0.96±0.44	24.24±11.08	10.79±2.94	1.75	-0	1	-	-
XCC J0215.0-0626	33.764	-6.4469	0.14	2.15±1.25	9.98±2.28	2.36±0.53	3.4±0.48	7.11	0.0817	1	-	-
XCC J0216.1-0702	34.0324	-7.0483	0.34	13.55±1.63	0.8±0.26	6.38±2.07	5.46±1.07	2.08	0.4114	1	232±74	9
XCC J0216.7-0648	34.1805	-6.8093	0.18	2.91±1.11	3.26±0.93	4.18±1.19	4.69±0.82	3.88	-0	2	-	-
XCC J0216.7-0935	34.1859	-9.585	0.56	13.8±2.38	0.84±0.33	14.73±5.79	8.43±1.99	1.84	0.5941	1	-	3
XCC J0216.8-0918	34.2012	-9.3103	0.78	20.44±1.78	2.86±1.11	54.28±21.01	18.79±4.39	2.26	0.652	2	-	3
XCC J0219.3-0735	34.8297	-7.5998	0.56	16.18±2.98	2.37±0.57	35.33±8.5	14.97±2.21	2.3	0.5684	1	-	2
XCC J0221.5-0626	35.394	-6.4377	0.28	14.45±2.14	2.11±0.55	9.21±2.42	7.27±1.17	2.83	0.314	1	-	2
XCC J0222.2-0617	35.5689	-6.2946	0.75	6.02±1.23	1.27±0.59	35.44±16.5	13.36±3.7	1.8	0.7716	2	-	1
XCC J0223.5-0828	35.8887	-8.4739	0.27	12.86±1.37	0.51±0.56	1.75±1.92	2.55±1.55	2.17	0.2826	1	333±72	13
XCC J0224.4-0915	36.1137	-9.2658	0.34	5.17±1.87	2.91±0.69	14.99±3.58	9.8±1.43	2.93	-0	2	-	-
XCC J0225.7-0828	36.4279	-8.4744	0.51	9.83±1.8	1.58±0.44	23.02±6.42	11.48±1.96	2.15	0.5531	2	-	2
XCC J0230.9-0418	37.7467	-4.3051	0.15	4.34±0.0	5.02±1.51	3.91±1.18	4.57±0.84	4.72	0.1428	1	396±119	5
XCC J0233.3-0550	38.3245	-5.8364	0.34	5.17±1.28	1.66±1.06	6.98±4.42	6.1±2.26	2.71	0.3086	2	-	3
XCC J0233.8-0543	38.4688	-5.7187	0.34	0.42±0.0	1.04±0.33	6.05±1.91	5.44±1.04	2.32	0.3566	2	-	4
XCC J0234.7-0542	38.6846	-5.7055	0.11	2.37±1.33	4.11±1.97	3.1±1.49	3.94±1.12	4.54	0.1412	1	-	1
XCC J0849.2-0157	132.309	-1.9545	0.2	1.91±1.05	1.64±0.41	2.62±0.65	3.45±0.52	3.2	-0	2	-	-
XCC J0850.3-0324	132.593	-3.4152	0.55	19.65±2.23	2.58±0.94	34.22±12.48	14.92±3.29	2.39	0.537	1	-	3
XCC J0850.4-0312	132.61	-3.2091	0.47	13.12±1.35	2.16±0.53	23.05±5.6	11.97±1.79	2.42	0.4789	1	-	2
XCC J0851.2-0528	132.806	-5.4789	0.83	6.21±1.0	2.35±0.56	70.39±16.71	20.04±2.94	1.96	0.8311	1	-	1
XCC J0851.4-0532	132.861	-5.5427	0.24	4.24±1.19	2.39±0.72	7.91±2.39	6.72±1.24	3.05	0.2768	2	-	3
XCC J0851.4-0537	132.869	-5.6233	0.66	3.43±1.66	2.05±0.42	41.06±8.32	15.65±1.96	2.11	-0	2	-	-
XCC J0851.5-0104	132.884	-1.0747	0.69	3.24±1.08	1.18±0.57	27.04±13.04	11.77±3.38	1.86	-0	2	-	-
XCC J0851.5-0451	132.893	-4.8642	0.06	6.57±3.08	9.01±2.22	1.99±0.49	3.05±0.46	7.06	0.0792	1	-	2
XCC J0851.6-0451	132.913	-4.8567	0.56	9.02±2.17	1.79±0.56	33.4±10.49	13.94±2.66	2.09	0.6309	1	-	2
XCC J0851.9-0507	132.981	-5.1185	0.38	14.57±2.5	5.34±2.64	37.17±18.4	16.98±4.98	3.12	0.3981	1	-	4
XCC J0852.8-0152	133.203	-1.8718	1.09	3.68±0.85	1.26±0.3	64.62±15.54	16.4±2.43	1.55	-0	1	-	-
XCC J0852.8-0137	133.219	-1.6214	0.35	25.56±3.47	2.49±0.61	13.68±3.34	9.19±1.38	2.81	-0	1	-	-
XCC J0852.9-0529	133.244	-5.493	0.64	18.11±3.03	4.39±1.16	77.8±20.45	23.82±3.85	2.47	-0	1	-	-
XCC J0853.1-0348	133.296	-3.8084	0.27	3.26±1.12	2.45±0.54	7.69±1.69	6.63±0.9	3.1	-0	2	-	-
XCC J0853.8-0223	133.448	-2.392	0.38	11.58±2.59	2.76±0.63	19.44±4.45	11.25±1.59	2.74	0.3938	2	-	3
XCC J0854.5-0140	133.646	-1.6745	0.65	14.35±1.79	3.21±0.63	49.05±9.64	18.31±2.22	2.42	0.5833	1	-	1
XCC J0855.7-0146	133.933	-1.7745	0.63	4.76±1.66	1.04±0.22	20.22±4.32	10.11±1.34	1.88	-0	2	-	-
XCC J0856.4-0136	134.098	-1.6031	0.45	16.71±3.01	2.32±0.42	21.12±3.8	11.54±1.29	2.53	0.4443	1	-	3
XCC J0856.4-0107	134.122	-1.1329	0.63	17.41±2.33	1.2±0.74	23.02±14.2	10.99±3.96	1.93	-0	1	-	-
XCC J0858.1-0342	134.532	-3.7164	0.72	7.8±1.27	1.63±0.43	39.12±10.3	14.66±2.36	1.94	-0	2	-	-
XCC J0858.9-0433	134.737	-4.5637	0.11	7.96±1.21	3.42±1.41	1.5±0.62	2.52±0.62	4.89	-0	1	-	-
XCC J0859.4-0432	134.872	-4.5438	0.1	5.95±1.87	8.5±1.9	3.08±0.69	4.01±0.55	6.23	-0	1	-	-
XCC J0859.6-0416	134.906	-4.2764	0.2	1.91±0.87	1.89±0.61	3.01±0.99	3.77±0.75	3.29	-0	2	-	-
XCC J0859.9-0422	134.993	-4.3686	0.15	11.65±2.02	11.9±3.5	10.51±3.09	8.59±1.54	5.57	-0	1	-	-
XCC J0900.7-0306	135.173	-3.1143	0.24	13.8±1.84	3.25±0.51	7.13±1.12	6.44±0.63	3.51	0.2292	1	-	4
XCC J0901.7-0138	135.435	-1.6384	0.28	18.75±1.34	6.82±1.5	24.51±5.42	13.78±1.87	3.73	-0	1	-	-
XCC J0902.3-0226	135.583	-2.4422	0.16	4.72±1.16	5.59±1.23	5.6±1.24	5.71±0.78	4.59	-0	1	-	-
XCC J0902.8-0213	135.708	-2.2305	1.01	5.28±0.71	1.48±1.07	65.68±47.55	17.33±7.23	1.65	-0	1	-	-
XCC J0903.1-0537	135.793	-5.6259	0.28	5.85±1.65	5.62±1.53	18.86±5.14	11.71±1.96	3.64	-0	1	-	-
XCC J0904.0-0343	136.0	-3.7195	0.99	8.67±0.98	1.44±0.33	62.1±14.15	16.91±2.37	1.66	-0	1	-	-
XCC J0904.2-0158	136.065	-1.9808	0.19	6.83±1.31	12.89±3.74	18.84±5.46	12.24±2.17	5.1	-0	1	-	-
XCC J2200.4+0058	330.103	0.9804	0.2	4.34±1.06	6.94±3.82	2.53±1.4	3.53±1.14	5.94	0.1005	2	-	3
XCC J2200.9+0125	330.241	1.4297	0.13	2.37±1.12	8.22±2.18	3.7±0.98	4.48±0.73	5.9	0.1105	1	356±177	6
XCC J2201.4+0152	330.37	1.8668	0.19	9.28±2.25	4.79±2.3	4.09±1.97	4.7±1.34	4.58	0.1492	2	-	1
XCC J2202.3+0148	330.573	1.8152	0.13	5.17±1.39	3.4±1.42	2.14±0.89	3.13±0.78	4.52	-0	1	-	-
XCC J2204.5+0239	331.131	2.6648	0.63	15.6±2.22	2.63±0.61	48.79±11.24	17.67±2.51	2.24	0.6404	1	-	1
XCC J2210.4+0203	332.605	2.0554	0.69	11.43±1.61	1.6±0.46	35.69±10.32	14.06±2.49	1.97	-0	2	-	-
XCC J2211.3+0200	332.832	2.0111	0.47	15.83±3.02	3.06±0.68	29.66±6.6	14.2±1.94	2.63	0.4617	2	-	2
XCC J2211.3+0000	332.834	0.0103	0.83	4.14±0.9	0.6±0.18	20.81±6.3	9.19±1.69	1.51	-0	2	-	-
XCC J2211.9-0001	332.981	-0.0311	0.05	13.29±3.36	9.15±4.86	0.78±0.42	1.71±0.53	8.98	-0	2	-	-
XCC J2214.0+0057	333.512	0.9574	0.83	12.43±1.29	1.61±0.5	50.27±15.7	16.17±3.06	1.83	-0	1	-	-
XCC J2214.0-0055	333.52	-0.9273	0.27	9.02±1.65	2.16±0.72	4.32±1.42	4.7±0.94	3.26	0.2207	1	-	4
XCC J2217.0+0016	334.258	0.2693	0.91	3.99±0.96	0.09±0.03	4.85±1.88	3.46±0.81	1.03	-0	2	-	-

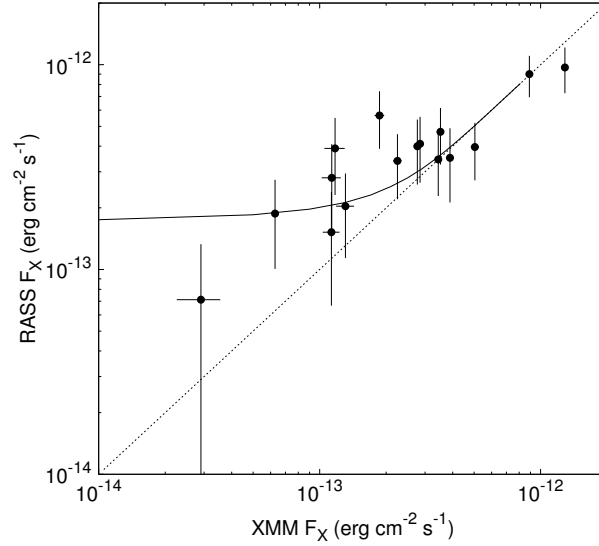


Figure 2.19: RASS X-ray flux versus XMM-Newton X-ray flux for 16 clusters in overlap between the RASS and XMM cluster samples. A solid curve shows the the prediction for Malmquist bias in RASS flux measurement.

Table 2.5: Catalog of RASS-CFHTLS X-ray Selected Galaxy Clusters

ID	RA	DEC	R.S. z	α	Opt. R.A.	Opt. Dec.	X-ray Flux	spec z	$\sigma(v)$	N_{σ}	$\log[L_X(L_{\odot})]$
RASS-CFHTLS	(degrees)	(degrees)			(degrees)	(degrees)	$10^{-13} \text{ erg cm}^{-2} \text{ s}^{-1}$		(km s^{-1})		erg s^{-1}
(1)	(2)	(3)	(4)	(5)	(6)	(7)	(8)	(9)	(10)	(11)	(12)
RCC J0211.1-0454	32.7836	-4.9044	0.14	15.8±2.2	32.7649	-4.88968	1.52±0.78	0.1379	-	3	43.18
RCC J0214.1-0808	33.5396	-8.13589	0.23	6.6±0.9	33.5593	-8.13878	0.71±0.62	0.2495	184±73	11	42.84
RCC J0214.6-0433	33.661	-4.56333	0.15	23.2±2.6	33.6717	-4.55197	8.18±1.76	0.1456	-	4	43.78
RCC J0222.0-0545	35.5108	-5.76391	0.25	17.9±1.1	35.4913	-5.75843	2.03±0.94	0.2591	-	2	43.29
RCC J0223.4-0852	35.8678	-8.86884	0.19	25.6±2.0	35.8734	-8.85757	2.13±0.93	0.1632	381±154	5	43.60
RCC J0223.5-0858	35.8981	-8.98174	0.43	16.9±2.1	35.8948	-8.96458	1.76±0.87	0.4145	-	3	43.31
RCC J0223.8-0821	35.9671	-8.36164	0.23	16.8±1.1	35.9649	-8.35741	2.04±0.90	0.2287	435±109	7	43.45
RCC J0225.1-0950	36.285	-9.83422	0.18	16.7±2.0	36.2707	-9.8252	3.45±1.16	0.1594	516±74	18	43.18
RCC J0230.8-0421	37.723	-4.35303	0.17	8.5±1.5	37.7218	-4.36389	3.90±1.59	0.1408	397±126	10	42.78
RCC J0231.7-0451	37.9465	-4.86471	0.2	48.2±2.4	37.9257	-4.87701	9.69±2.44	0.1852	425±194	9	44.01
RCC J0233.7-0942	38.4439	-9.70813	0.25	20.4±1.3	38.4244	-9.70487	2.80±1.29	0.2646	382±57	19	43.36
RCC J0210.7-0635	32.6952	-6.58427	0.06	5.1±4.4	32.6952	-6.58427	7.82±1.82	0.0416	-	1	41.79
RCC J0223.9-0836	35.977	-8.60424	0.29	35.7±2.1	35.9922	-8.59644	3.51±1.38	0.2701	675±142	10	43.84
RCC J0225.2-0623	36.3029	-6.39542	0.19	21.5±1.8	36.3016	-6.39377	5.65±1.77	0.2041	452±82	12	43.45
RCC J0214.4-0628	33.6162	-6.47615	0.25	30.5±1.8	33.6124	-6.46598	4.00±1.40	0.2366	344±93	13	43.79
RCC J0214.8-0350	33.7193	-3.83385	0.83	19.4±1.2	33.7039	-3.82746	2.68±1.19	-	-	-	44.22
RCC J0219.1-0554	34.7769	-5.90739	0.13	13.8±2.2	34.8089	-5.90748	1.65±1.01	0.149	-	1	43.09
RCC J0852.2-0534	133.063	-5.57346	0.2	41.4±1.5	133.063	-5.57368	8.99±2.06	0.1893	620±156	9	43.92
RCC J0858.5-0525	134.668	-5.41993	0.1	25.8±1.9	134.687	-5.40854	4.70±1.45	-	-	-	43.37
RCC J0901.5-0138	135.387	-1.64256	0.31	44.2±1.8	135.39	-1.64841	3.96±1.23	0.3163	358±45	17	43.92
RCC J0901.6-0157	135.424	-1.96503	0.29	13.6±1.6	135.412	-1.96332	1.87±0.87	0.3131	387±104	8	43.44
RCC J0854.2-0220	133.569	-2.34827	0.37	31.8±2.5	133.561	-2.35155	3.39±1.19	0.3679	451±133	9	43.57
RCC J0849.1-0253	132.292	-2.89579	0.25	14.1±1.5	132.304	-2.88226	1.52±0.85	0.2259	516±125	12	43.14
RCC J0852.1-0101	133.048	-1.02552	0.5	42.8±2.4	133.055	-1.03088	4.11±1.46	0.4587	415±143	5	43.95
RCC J0857.2-0343	134.315	-3.7199	0.2	26.3±2.8	134.329	-3.71106	3.03±1.22	-	-	-	43.68
RCC J2211.1-0003	332.788	-0.05481	0.37	7.9±0.9	332.809	-0.04621	7.07±1.79	0.3628	-	3	43.13
RCC J2216.7-0051	334.177	-0.86128	0.11	3.2±1.8	334.164	-0.87762	1.43±0.94	0.0609	236±70	7	42.41

finder on RASS and XMM-Newton X-ray sources in the W1, W2, and W4 CFHTLS fields. In total, we identified 27 clusters associated with RASS sources and 196 clusters among XMM X-ray sources, with a 100% identification rate achieved for the high-significance XMM sample. We computed the X-ray luminosity and mass from the X-ray flux and the scaling relations from the literature. In comparison to other XMM samples, the XMM clusters are typically of $\sim 10^{14} M_{\odot}$ mass, while e.g. COSMOS X-ray selected groups are of an order of magnitude lower mass. This is a result of shallower observations but covering larger area, characteristic of our program. We calculated the velocity dispersions with an iterative gapper method and derive the scaling relation between velocity dispersion and X-ray luminosity of clusters.

We also explored a correlation of integrated optical luminosity and X-ray luminosity. We showed that multi-color red sequence reduces the scatter in relation between the relation down to 0.26 dex in X-ray luminosity direction. This set of optical methods for cluster finding are particularly useful for providing large samples of X-ray luminous (or massive) clusters (especially for cosmological studies) using shallow X-ray data and wide optical surveys. First, by applying the red sequence finder and maximising α , we can extract a pure sample of clusters out of a list of X-ray sources. Second, by measuring the optical luminosity of clusters within an appropriate fixed radius we can estimate the cluster total mass, allowing an efficient separation of high X-ray luminous (high-mass) clusters for further studies.

2.7 acknowledgments

We thank Mara Salvato, Daniele Pierini, Claudia Maraston, and Natascha Greisel for help in providing stellar population models.

This work is based on observations obtained with MegaPrime/MegaCam, a joint project of CFHT and CEA/DAPNIA, at the Canada-France-Hawaii Telescope (CFHT) which is operated by the National Research Council (NRC) of Canada, the Institut National des Sciences de l'Univers of the Centre National de la Recherche Scientifique (CNRS) of France, and the University of Hawaii. This research used the facilities of the Canadian Astronomy Data Centre operated by the National Research Council of Canada with the support of the Canadian Space Agency. CFHTLenS data processing was made possible thanks to significant computing support from the NSERC Research Tools and Instruments grant program.

This work has been supported by a DLR project 50 OR 1013 to MPE.

Funding for SDSS-III has been provided by the Alfred P. Sloan Foundation, the Participating Institutions, the National Science Foundation, and the U.S. Department of Energy Office of Science. The SDSS-III web site is <http://www.sdss3.org/>. SDSS-III is managed by the Astrophysical Research Consortium for the Participating Institutions of the SDSS-III Collaboration including the University of Arizona, the Brazilian Participation Group, Brookhaven National Laboratory, University of Cambridge, Carnegie Mellon University, University of Florida, the French Participation Group, the German Participation Group,

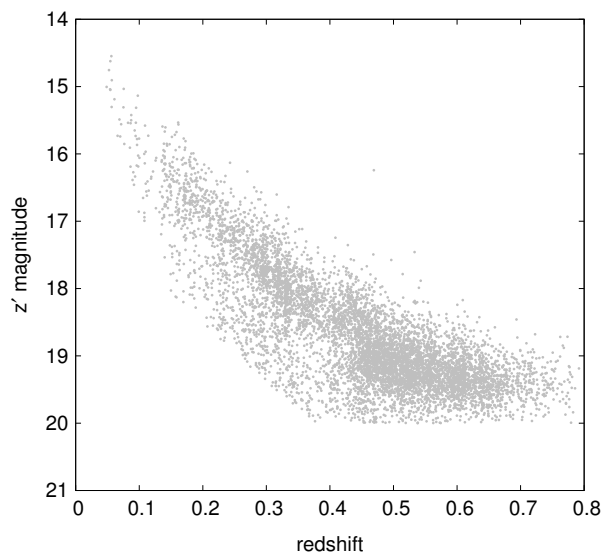


Figure 2.20: Magnitude–redshift distribution of the ETGs brighter than $z'=20$ and $m_*(z)$.

Harvard University, the Instituto de Astrofísica de Canarias, the Michigan State/Notre Dame/JINA Participation Group, Johns Hopkins University, Lawrence Berkeley National Laboratory, Max Planck Institute for Astrophysics, Max Planck Institute for Extraterrestrial Physics, New Mexico State University, New York University, Ohio State University, Pennsylvania State University, University of Portsmouth, Princeton University, the Spanish Participation Group, University of Tokyo, University of Utah, Vanderbilt University, University of Virginia, University of Washington, and Yale University.

2.8 Appendix: Color variation of early-type galaxies as a function of redshift

In this section, we show that intrinsic colors of ETGs have a linear like evolution through the redshift. In section 2.4.1 we derived the color evolution of ETGs using a sample of galaxies with spectroscopic redshift. Here, we used the a sub-sample of those galaxies to show that the linear assumption about evolution of intrinsic color dispersion for red sequence galaxies is acceptable. To reduce the effect of error in galaxies observed magnitude, the sample of section 2.4.1 was cut by $20 < z'$ and brighter than $m_*(z)$. Figure 2.20 show magnitude and the redshift distribution of this sample.

For the faintest galaxies in the sample ($z'=20$), the typical error in g' , r' , and z' are ~ 0.01 , 0.008, 0.005, and 0.01. Thus magnitude errors can not have induce significant effect on dispersion of colors. Dots in Figure 2.21 illustrates the color evolution of ETGs as a function of different redshift bins. Dashed lines are linear fitted lines on the color evolution. The mean of difference between linear fits and measured color dispersions at a

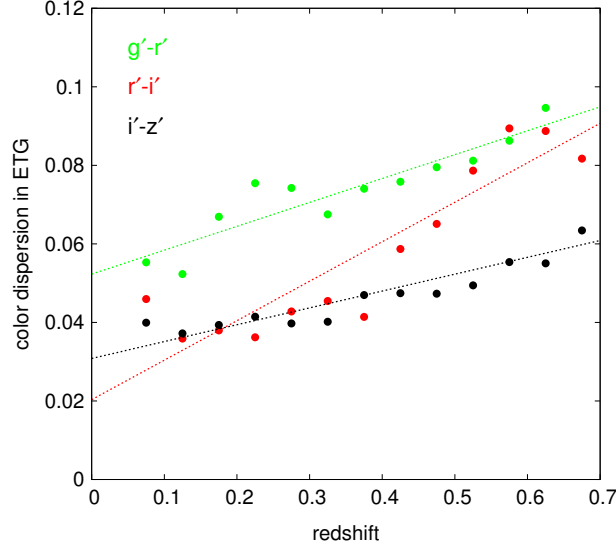


Figure 2.21: Colors evolution of ETGs as functions of redshifts. The green, red and black dots respectively shows the evolution of $g'-r'$, $r'-i'$ and $i'-z'$ in ETGs with spectroscopic redshift. The dashed lines with the same color codes are linear fit to each galaxy color.

given redshift are 10%, 18% and, 7% respectively for $g'-r'$, $r'-i'$ and $i'-z'$. Thus considering linear evolution for intrinsic color dispersion of ETGs is acceptable and we generalized this assumption to red sequence galaxies. Optimizing the characterization of red sequence method is out of aim of this work, However, assuming linear evolution for intrinsic color dispersion doesn't have significant influence on the results.

2.9 Appendix: Correction for Eddington Bias

In the presence of scatter in the scaling relations, selection of clusters for the scaling relation studies introduces a bias. The straightforward application is in using exactly the same quantity that has been used in the selection. The Eddington bias is associated to the detection of sources in XMM data. A 4.6 sigma detection threshold results in detection of the some systems with X-ray counts below 4.6 sigma. Following the formulation of Vikhlinin et al. (2009), we can write the bias correction as

$$b(x_o) = \frac{\int_{-\infty}^{+\infty} (x - x_o) P(T|C(x, z)) e^{-\frac{(x-x_o)^2}{2\sigma^2}}}{\int_{-\infty}^{+\infty} P(T|C(x, z)) e^{-\frac{(x-x_o)^2}{2\sigma^2}}}, \quad (2.11)$$

where T is the XMM count threshold, C(x,z) is the predicted XMM counts from the cluster at a redshift z and luminosity x, P(T|C(x,z)) is the probability of detection, σ is the scatter of the scaling relation. Using the $\sigma = 0.2$ dex correction, we have computed the bias corrections for each of the CFHTLS cluster.

Chapter 3

Dependence of galaxy stellar mass function on halo mass of clusters

3.1 Introduction

The hierarchical growth of dark matter halos is now rather well understood and modeled by N-body simulations (e.g. Springel et al. 2005), since their evolution is affected only by the effect of gravity. In contrast, modeling the evolution of baryonic matter and the effects of the related processes consistently with observations is still rather uncertain and poorly understood because of the complexity of the involved processes such as star formation and feedback. The analysis of the evolution of galaxy properties can help us in better constrain the details of the above processes and, gain an understanding of the dominant mechanisms that rule the formation and evolution of galaxies. In particular, the analysis of the galaxy stellar mass function (GSMF) is one of the most robust tools to understand the evolution of the stellar mass assembly of galaxy.

The galaxy GSMF has been measured and studied in several deep fields with optical and near-infrared (NIR) surveys (Marchesini et al., 2009; Ilbert et al., 2010; Bielby et al., 2012)). Earlier study by Pozzetti et al. (2007) on K20 galaxy sample show that more than half of massive galaxies ($\log M_*/M_\odot > 10.8$) have already assembled their mass by redshift ~ 1 . This is consistent with the results of Arnouts et al. (2007), which observe the build-up of the quiescent population from $z \sim 2$ to $z \sim 1.2$ with an increase in stellar mass by an order of magnitude. This is in agreement with the downsizing picture in evolution of galaxies which leads to the massive galaxies to form earlier and evolve faster than lower mass systems.

Ilbert et al. (2010) measure the mass and the GSMF of 196000 galaxies in the COSMOS 2 deg² field. They show that 80% to 90% of the quiescent galaxies (with very low star-formation activities) with mass of $\log M_*/M_\odot \sim 11$ have elliptical morphology at redshift ≤ 0.8 (Fig. 3.2). Thus, they conclude that the quenching of the star formation activity and the acquisition of an elliptical morphology in massive galaxies are strictly related processes. On the other hand, at lower masses ($\log M_*/M_\odot \sim 9.5$) about 50% of quiescent galaxies are

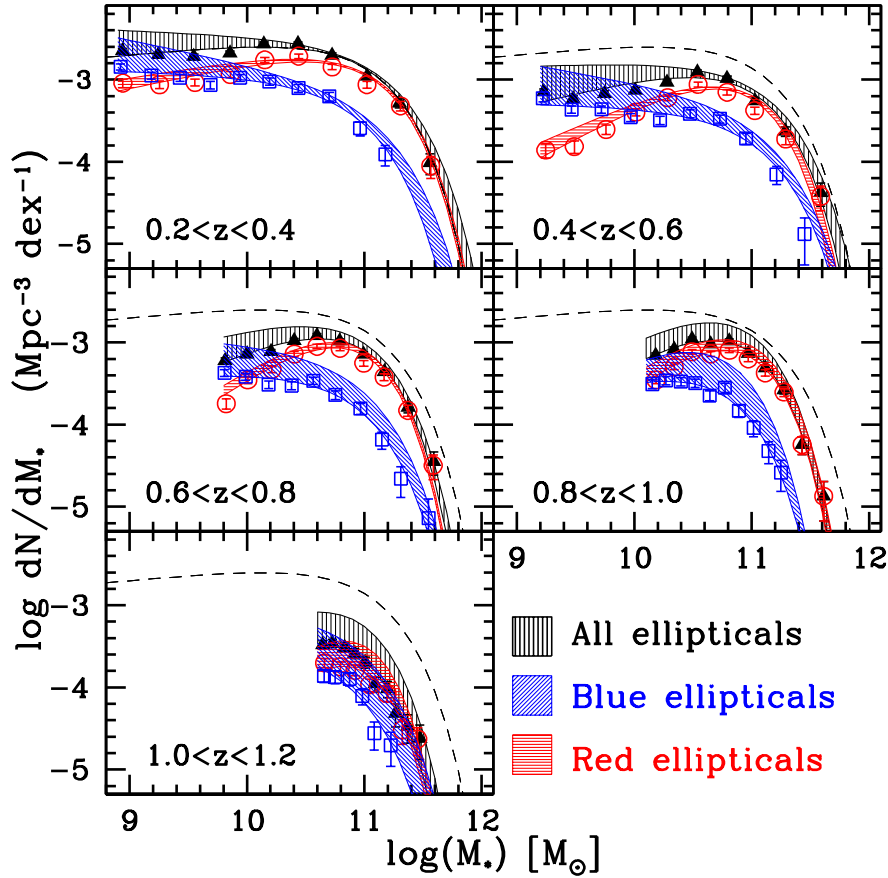


Figure 3.1: Stellar mass function of elliptical galaxies from Ilbert et al. (2010). The blue and red regions belong to star-forming and passive elliptical galaxies at different redshifts. The dashed region is mass function of all elliptical galaxies. For redshifts below 1 and high stellar masses, the volume density of quiescent elliptical galaxies is significantly higher than that of the star-forming ellipticals.

spiral or irregular. The comparison of the GSMF for active and quiescent galaxy, show also that the space density of massive quiescent galaxies becomes higher than the space density of massive star forming systems at $z < 1$. Therefore, the rate of wet mergers (merging between gas rich galaxies), which are associated with the formation of the most massive ellipticals must decline very rapidly at $z < 1$, leading to a slowdown in the assembly of the quiescent and massive sources (Fig 3.2).

Bielby et al. (2012) estimate the GSMF in the CFHTLS up to a redshift of 2.5, applying a double Schechter function. Their results indicate that the number density of relatively low mass galaxies ($\log M_*/M_\odot \leq 10.75$) is evolving significantly with time, while the number density of higher mass galaxies does not vary since redshift 0.8–1, consistently with the results of Ilbert et al. (2010).

From the theoretical point of view, the observation of quiescent and very massive galax-

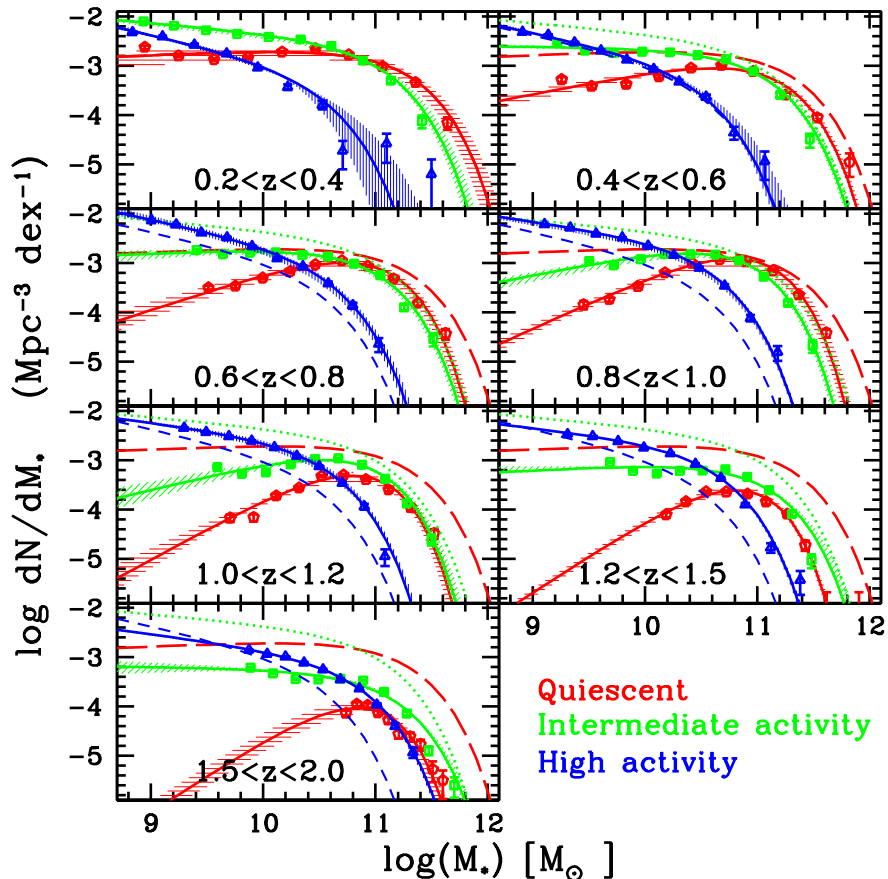


Figure 3.2: Stellar mass function of quiescent, high star-forming and intermediate star-formation activities galaxies from Ilbert et al. (2010). From redshift 2, the density of quiescent galaxies (red shaded area) at high mass become higher than density of star-forming galaxies (blue dashed area) gradually. For comparison, dashed lines at each panel indicate the mass function at $0.2 \leq z \leq 0.4$.

ies at high redshift rules out the probability of dry mergers (mergers between gas poor galaxies) as a dominant mechanism in evolution of massive galaxies. Instead, this leads to the increasing importance of feedback processes such as AGN activities in stopping the galaxy star formation activity and thus, the mass growth. The semi-analytic simulations based on these models, in particular AGN feedback as a main quenching mechanism, reproduce not only the substantial population of high mass galaxies at redshifts above 1 but also the luminosity function of galaxies at low redshift (e.g. Guo et al. 2011; De Lucia & Blaizot 2007).

In addition to studying the evolution of galactic stellar mass growth, one of the fundamental goals in observational cosmology is to understand the link between the baryonic content of galaxies and the dark matter halos in which they reside. The existence of the strong mass segregation observed at least up to $z \sim 1$, would suggest that the GSMF de-

depends on the environment. From the theoretical point of view, semi-analytical models also suggest that galaxies born with the same stellar mass can end up with quite different stellar masses in different environment since the galaxy evolution and its environment are strongly coupled (De Lucia et al. 2012). The processes related to the dark matter halos mass scale can determine the history of stellar mass assembly of the hosted galaxies either by quenching the star formation activity or by affecting the mass accretion through minor and major merger. For instance, van den Bosch et al. (2008) show that, in simulated low redshift massive clusters, 70 percent of satellite galaxies with $\log M_*/M_\odot \sim 10^9$ on the so called “red sequence” at redshift 0, undergo a substantial satellite quenching in the final host halo, while 65% of the more massive satellites ($M_* = 10^{10} h^{-2} M_\odot$), are already red at accretion. Yang et al. (2012) show also that the stellar mass accretion history of the central galaxy, in particular, strongly depends on the host halo mass, whereas the central galaxies in low mass halos continue to accrete via minor mergers or star formation below $z \sim 1$, while in higher mass halos the accretion is already stopped at $z > 1$.

On the observational side, the differences in the shape of the GSMF in halos of different mass are still a debated issue. At low redshift, Yang et al. (2007) study the GSMF of galaxies in groups and clusters ranging from $10^{12} M_\odot$ to $10^{14.5} M_\odot$. They describe with two different fitting functions the GSMF of central and satellite galaxies, respectively, and they find, in particular, a clear dependence of the former on the host halo mass, which indicates a clear mass segregation in more massive halos. In contrast, a recent study on a sample of optically selected clusters at a redshift ~ 1 shows a higher fraction of quiescent galaxies in clusters with respect to the field, but no clear difference between the shape of stellar mass function in the two different environments (van der Burg et al. 2013).

Giodini et al. (2012) illustrate that the fraction of star-forming galaxies increases with redshift in all environments but the shape of their GSMF is the same in all host halos (Figure 3.3). Giodini et al. (2012) also show that characteristic mass of the GSMF for star-forming galaxies in low mass groups is 50% higher than in high mass group (clusters). In other words, in the redshift range of 0.2–0.4 the bulk of star-forming galaxies in low mass groups ($M_{200} \leq 6 \times 10^{14} M_\odot$) is more massive than bulk of star-forming galaxies in more massive clusters. Therefore, it seems that quenching mechanisms in low mass groups are less efficient than in higher mass clusters.

In order to shed light on the evolution of the GSMF in different environments, in this work we use the data available in the CFHTLS and the COSMOS fields to study the evolution of the GSMF in groups and clusters up to redshift $\sim 0.8 - 1.0$. We use the deep X-ray XMM data available in the two fields, and, in particular, the available catalogs of the X-ray selected groups and clusters to properly define a sample of halos of different masses. This is done by using the X-ray emission of the Intragroup and Intracluster Medium as a tracer of the underlying dark matter distribution. We use, then, the multi-wavelength optical and near-infrared data available in the two fields to estimate the galaxy stellar mass of group and cluster members to study the evolution of their GSMF as a function of the halo mass. This chapter is organized as follows. In § 3.2, we describe the X-ray and optical data and the characteristics of the X-ray selected galaxy clusters and groups. In this section, we also explain the method adopted for the computation of the galaxy stellar

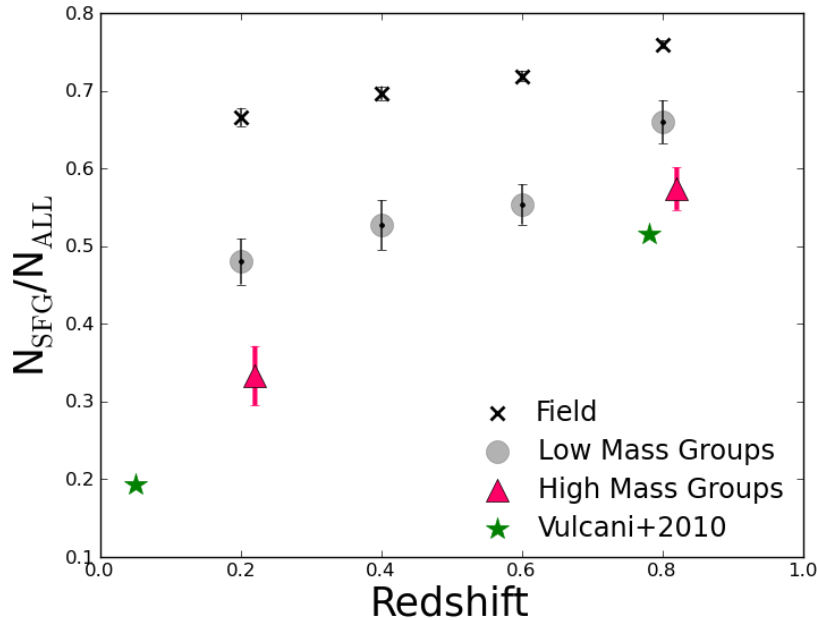


Figure 3.3: Fraction of star-forming galaxies to the total galaxies in all environments and its evolution through the redshift (Giodini et al., 2012). The black crosses, grey large circles, and magenta triangles belong to field, low mass and high mass groups respectively. The green stars mark the fraction measured in massive clusters (Vulcani et al. 2011).

mass. In § 3.3, we derive the error in the galaxy stellar mass due to the photometric error and the photometric redshift error. In § 3.4.2, we use mock catalog to check the robustness of method used to derive the GSMF. We present the results of the GSMF as a function of the host halo mass in § 3.6.

Throughout this work, we use the AB magnitude system and consider a cosmological model with $H_0 = 72 \text{ km s}^{-1} \text{ Mpc}^{-1}$, $\Omega_\Lambda = 0.75$ and $\Omega_M = 0.25$.

3.2 Data

In this section, we summarize the different type of data in overlap with COSMOS and CFHTLS which are utilized in this work.

3.2.1 COSMOS

The Cosmos Evolution survey (COSMOS) is the largest survey ever made using the Hubble Space Telescope (HST). With 2 square degrees of coverage, COSMOS enables the sampling of the large scale structure of the universe, and reduces the cosmic variance. In particular COSMOS guarantees a full spectral coverage, with X-ray (Chandra & XMM-Newton),

UV (GALEX), optical (SUBARU), near-infrared (CFHT), mid-infrared (Spitzer), sub-millimetre (MAMBO) and radio (VLA) imaging. Furthermore, the X-ray observations provided by an 1.5 Msec observational time with XMM-Newton (53 pointings on the whole field, 50 ksec each, Hasinger et al. 2007) and an additional 1.8 Msec observations with Chandra in the central square degree (Elvis et al., 2009), enable a robust detection of galaxy groups down to $z \sim 1.2$ (Finoguenov et al., 2007). The imaging survey is complemented by a spectroscopic program, *zCOSMOS* (Lilly et al., 2007), which provides 20000 spectroscopic redshifts down to $i_{AB} = 22.5$ in addition to parallel programs such as MMT/Hectospec (Prescott et al. 2006), Magellan/IMACS (Trump et al. 2007), FLWO/FAST (Wright, Drake & Civano 2010), and Keck/DEIMOS (several observations by Scoville, Capak, Salvato, Sanders, and Kartaltepe).

Extensive photometric and spectroscopic coverage, combined with the large area of the survey, enables the study of the coupled evolution of stellar populations, AGN and dark matter throughout the cosmic time.

The COSMOS photometric catalog (Capak et al., 2007, 2008) includes multi-wavelength photometric information for $\sim 2 \times 10^6$ galaxies in the entire field. The position of the galaxies has been extracted by deep i-band imaging obtained with Supreme-Cam mounted on the SUBARU telescope (Taniguchi et al., 2007). A completeness limit of 80% is achieved at $i_{AB} = 26.5$.

Ilbert et al. (2010) cross-match S-COSMOS (Sanders et al., 2007) $3.6\mu\text{m}$ selected catalog with COSMOS photometric (Capak et al., 2008) and photo-z catalogs (Ilbert et al., 2009). The photo-z are derived for all the sources in the COSMOS photometric catalog. The photometric fluxes are measured in 31 bands (2 bands from the Galaxy Evolution Explorer (GALEX), 6 broad bands from the Supreme/Subaru camera, 2 broad bands from MEGACAM at CFHT, 14 medium and narrow bands from SupremeCam/Subaru, J band from the WFCAM/UKIRT camera, H and K band from the WIRCAM/CFHT camera, and 4 IRAC/Spitzer channels). The imaging data are extremely deep, reaching $u^* \sim 27$, $i = 26.2$, and $K_s \sim 23.5$ for a 5σ detection in a $3''$ aperture (the sensitivities are listed in Capak et al. (2007) and Salvato et al. (2009)). The photometric redshift are derived using the *Le Phare* code (Arnouts et al. 2002; Ilbert et al. 2006) with an accuracy of $\Delta z/(1+z) \sim 0.008$ at $i < 22.5$, $\Delta z/(1+z) \sim 0.011$ at $22.5 < i < 24$. and $\Delta z/(1+z) \sim 0.053$ at $24 < i < 25$. The photometric redshifts are computed by employing 21 spectral energy distribution (SED) templates. Twelve of them are generated using Bruzual & Charlot (2003) code and the remaining are taken from Polletta et al. (2007), generated by using the code GRASIL (Silva et al., 1998). Fig. 3.4 illustrates the templates. The extinction laws of Prevot et al. (1984) and Calzetti et al. (2000) are applied to the SED templates.

Stellar masses, SFR and additional galaxy properties are derived at $0 < z < 2$ by applying the same SED fitting technique adopted for the photometric redshift (Ilbert et al. 2010) but with slightly different SED templates. Bruzual & Charlot (2003) SED templates were generated assuming two different metallicities of 0.02 and 0.008 Z_{\odot} and exponentially declining star formation history $\sim e^{-t/\tau}$. t is the age of modeled galaxy and the τ is the time scale of star-formation history. Nine different τ values are opted in the range of 0.1 Gyr to 30 Gyr. Calzetti et al. (2000) dust extinction law was also applied to the templates. Ilbert

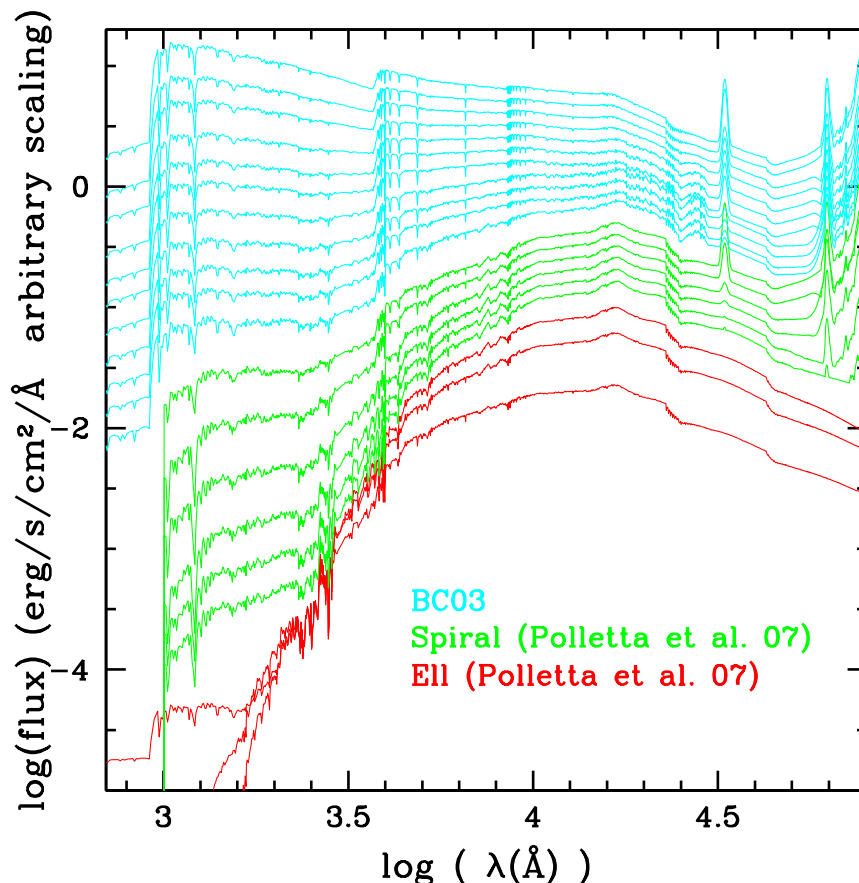


Figure 3.4: SED templates used for photometric redshift of galaxies in COSMOS survey Ilbert et al. (2009). The top 12 SEDs (cyan) are generated using Bruzual & Charlot (2003) code. The green (related to spiral galaxies) and red (related to elliptical galaxies) SEDs are from Polletta et al. (2007). The flux scale is arbitrary.

et al. (2010) showed that error in photometric redshift induces a 0.03 dex uncertainties in stellar mass estimation in their sample. The difference between stellar mass computation using different stellar population synthesis models is ~ 0.14 dex (Polletta et al., 2007; Ilbert et al., 2010).

Groups and clusters in the COSMOS field are X-ray selected, using the mosaic image combining XMM and Chandra data after removal of point source emission. The detection significance is 4σ with respect to the background (see Finoguenov et al. 2009 for further details on the precise definition of background and, thus, detection significance level). Finoguenov et al. (2009) and George et al. (2011) assigned redshift to the systems on the basis of spectroscopic redshift, when available, or photometric redshift. The X-ray luminosity L_X is estimated within R_{200} after taking into account the possible missed flux through the use of the beta-model. The X-ray masses M_{200} , within R_{200} , are estimated on the basis of the scaling relation of Leauthaud et al. (2010) between weak lensing mass and

L_X . The X-ray group catalogs derived with this approach comprise 277 detections in the COSMOS field.

3.2.2 CFHTLS

The Canada-France-Hawaii Telescope Legacy Survey (CFHTLS) includes four wide and four deep fields. The wide fields, W1, W2, W3, and W4 have areas of 72, 25, 49 and 25 degree², respectively, and the area of each deep field is 1 degree². In this work, we use T0007 released data of CFHTLS. The observations for the wide fields are done using MegaCam filters, u^* , g' , r' , i' , and z' with the completeness threshold of $i'=24.5$. The deep fields (D1, D2, D3, and D4) have data in three CFHT/WIRCAM or UKIRT/WFCAM filters, J , H , and Ks , in addition to five mentioned bands of MegaCam. The completeness threshold in deep fields is $i'=27$ (Ilbert et al. 2006; Coupon et al. 2009). In addition to SDSS DR10 spectroscopic redshifts, we did a spectroscopic follow-up of the photometric redshift selected cluster galaxy member candidates using MMT/Hectospec in W1, W2 and W4. The details of the procedure are described in Mirkazemi et al. (2014, chapter 2 of this thesis). The D1 and D3 are respectively located in W1 and W3 while D2 and D4 are out of coverage of wide fields. D2 and D3 (therefor W3) have overlap with COSMOS and AEGIS (All-wavelength Extended Growth strip International Survey) coverages, thus they benefit from the availability of the deep spectroscopic redshift catalogs of these fields.

The photometric redshifts are computed using SED fitting method and LePhare code at TERAPIX¹ and LAM². The photometric redshifts in wide fields are computed for galaxies brighter than $i'=24$ with similar procedure of Ilbert et al. (2006); Coupon et al. (2009) and its catalog is publicly available³.

The X-ray selected cluster catalog in CFHTLS is presented in Mirkazemi et al. (2014). Briefly, RASS (ROSAT All-Sky Survey; Voges et al. 1999) X-ray sources are follow-up in W1, W2, and W4 fields by 70 XMM-Newton telescope pointings with short exposures time (3ks). In total 196 clusters were discovered up to redshift 1.1. The cluster redshift is determined by applying the red sequence method or by using spectroscopic redshift, where available. The X-ray luminosity (L_X) is then used to estimate the cluster mass (M_{200c}) by using the Leauthaud et al. (2010) scaling relation between weak-lensing mass and L_X .

Fig 3.5 shows the M_{200c} -redshift distribution for two samples of X-ray selected galaxy clusters in COSMOS and CFHTLS. The sample of CFHTLS clusters include more massive systems, since the area of XMM-Newton coverage in CFHTLS is ~ 7 times larger than COSMOS survey but with much lower exposure times. In § 3.5, we explain how we select a clean subsample of clusters and groups for our analysis.

¹TERAPIX (Traitement Élémentaire, Réduction et Analyse des PIXels) is an astronomical data reduction centre dedicated to the processing of very large data flows from digital sky surveys.

²Laboratoire d'Astrophysique de Marseille

³<ftp://ftpix.iap.fr/pub/CFHTLS-zphot-T0007>

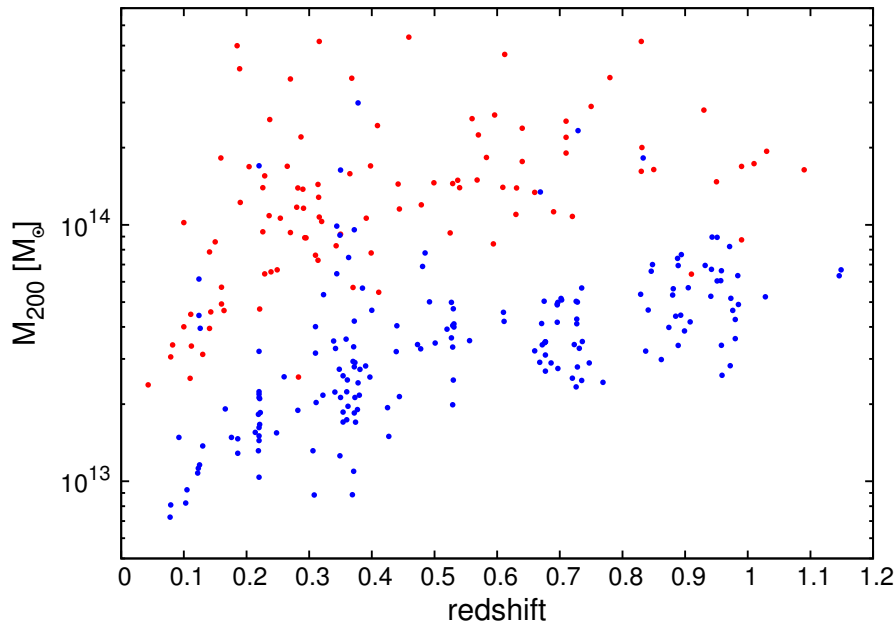


Figure 3.5: M_{200c} as a function of redshift for COSMOS clusters (blue dots) and CFHTLS clusters (red dots).

3.2.3 Stellar mass computation

While the stellar masses of galaxies are available in the COSMOS field from the catalog based on the work of Ilbert et al. (2010), they must be computed for the galaxy sample in CFHTLS. In this section, we explain our method for computing the stellar mass of galaxies in this field. We used the *LePhare* package for applying the SED fitting method (Arnouts et al. 2002; Ilbert et al. 2006) and for consistency with the COSMOS galaxy stellar masses. *LePhare* is a set of FORTRAN codes developed for finding the best-fit templates of observed SED. The fitting procedure is performed with a simple χ^2 minimization method. This package generates a set of templates from a library of SED for a given set of filters and related transmission functions. In this work, the libraries of models are generated by using the ten MegaCam and WIRCAM filters. However, in the four CFHTLS fields only the CFHT/MegaCam u , g , r , i , and z bands are available and the SED fitting is limited to this dataset. In the deeper D1 field J , H , and K CFHT-WIRCAM bands are available. The surveys in the other bands are still ongoing and the data are not available for the fields considered in this work. Fig. 3.6 illustrates the response functions of MegaCam and WIRCAM filters. For comparison, a passive and a star-forming SED models are also shown with arbitrary flux scaling.

Similar to Ilbert et al. (2010), the SED templates were generated by Bruzual & Charlot (2003) package for two different metallicities, 0.02 and 0.008 Z_{\odot} and Chabrier (2003) IMF. The star-formation rates are assumed to be exponentially declining as $\text{SFR} \propto e^{-t/\tau}$ where τ defines the time scale of star formation rate declination. For each metallicity, nine models

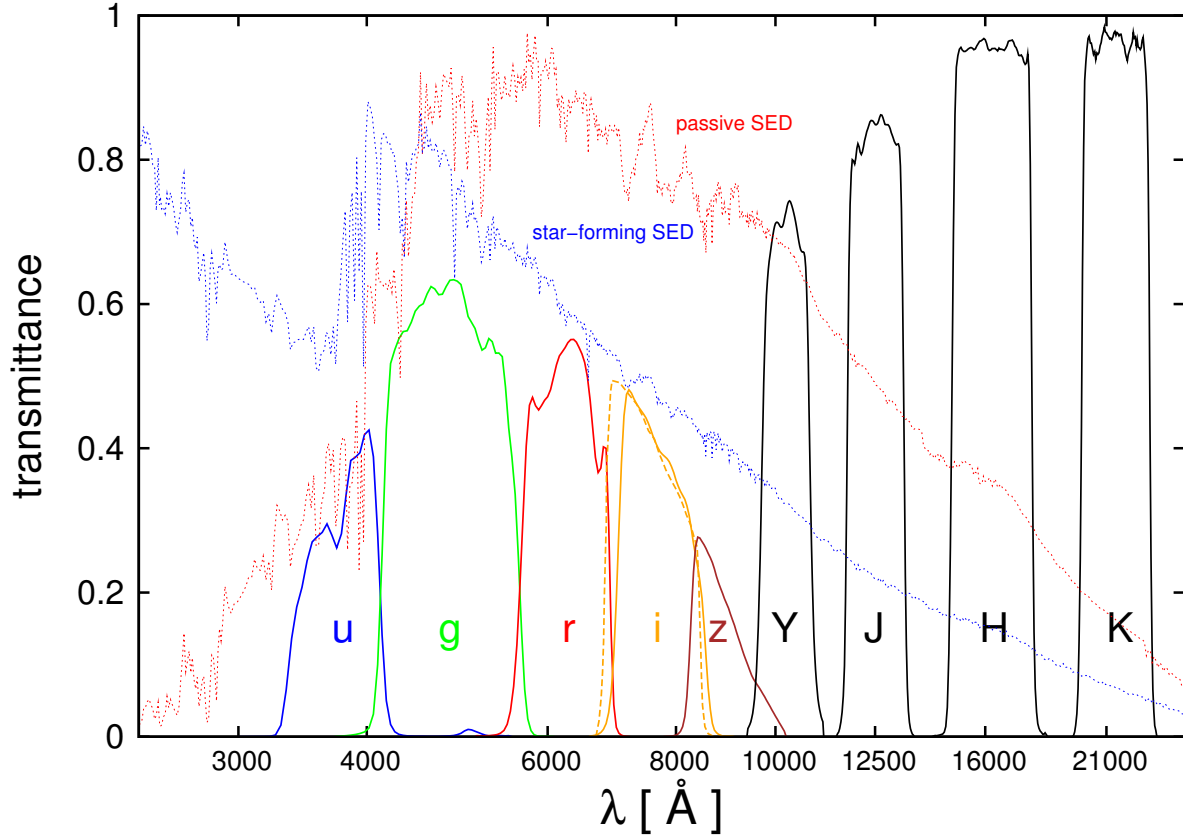


Figure 3.6: Response function of MegaCam and WIRCAM filters. Blue, green, red, orange, and brown solid curves respectively belong to u , g , r , old i and z bands. A dashed orange curve shows the transmission function of new i band. WIRCAM filters are shown by black solid curves. Two dotted curves with blue and red colors respectively illustrate the SEDs of a star-forming and a passive models generated by Bruzual & Charlot (2003) model. The flux of the SEDs were arbitrarily rescaled.

are produced with different τ from 0.1 Gyr to 30 Gyr. Thus, we have 2×9 models at the age of zero. The models were evolved for 51 different ages from 0.01 to 13.5 Gyr. Then for each of $2 \times 9 \times 51$ SED models, we assumed six different values of extinction. In this work, we applied Calzetti et al. (2000) extinction law. The extinction magnitude is given by:

$$A_\lambda = m_\lambda - m_{\lambda,0} \quad (3.1)$$

where m_λ and $m_{\lambda,0}$ are the magnitudes with and without absorptions. This difference in magnitude is represented in terms of color excess of $E(B - V)$ and the ratio of total selective extinction R_V :

$$A_\lambda = R_V \times E(B - V) \quad (3.2)$$

According to Calzetti et al. (2000), for interstellar medium of star-forming galaxies R_V

Table 3.1: Parameters used to generate the SED templates.

τ [Gyr]	$E(B - V)$	z [Z_{\odot}]
0.1	0	0.008
0.3	0.1	0.02
1	0.2	
2	0.3	
3	0.4	
5	0.5	
10		
15		
30		

is 4.05. Similar to Ilbert et al. (2010), we also adopted six $E(B - V)$ values of 0.0, 0.1, 0.2, 0.3, 0.4, and 0.5. Finally, we arrive at $2 \times 9 \times 51 \times 6$ SED models to cover all type of galaxies and evolutionary paths. The high extinction values ($0.2 \leq E(B - V)$) are only applied to the galaxies with high star formation rates. Thus models with $\text{age}/\tau < 4$ are discarded during the fitting procedure. Table 3.1 summarizes the age, extinction, and metallicity parameters used in building the SED templates. The method explained here is applied to ~ 7 million CFHTLS galaxies brighter than $i = 24$ mag and with redshift below 1.5. Figure 3.7 illustrates three example of galaxies with different best-fitted SEDs and redshifts.

3.3 Error analysis

In this section, we characterize the error in the photometric redshift as a function of the i band magnitude in the CFHTLS fields. This is done because the cluster member selection for the X-ray selected groups and clusters is performed using the photometric redshifts to overcome the problem of high spectroscopic incompleteness in CFHTLS fields. Thus, a characterization of the photometric redshift error is mandatory to understand the bias introduced by the z_{phot} error in the member selection. In addition, Ilbert et al. (2010) provide already an extensive analysis of the uncertainty of their galaxy stellar mass estimate. We perform here a similar analysis for the CFHTLS dataset which is shallower with respect to the COSMOS survey and having poorer multi-wavelength coverage. This is done to investigate, in particular, how this error is affecting the accuracy in stellar mass estimation.

3.3.1 Completeness in stellar mass measurement

In order to study the galaxy stellar mass function, we need first to set a complete sample of galaxies in terms of stellar mass. Since our original galaxy sample, both in COSMOS

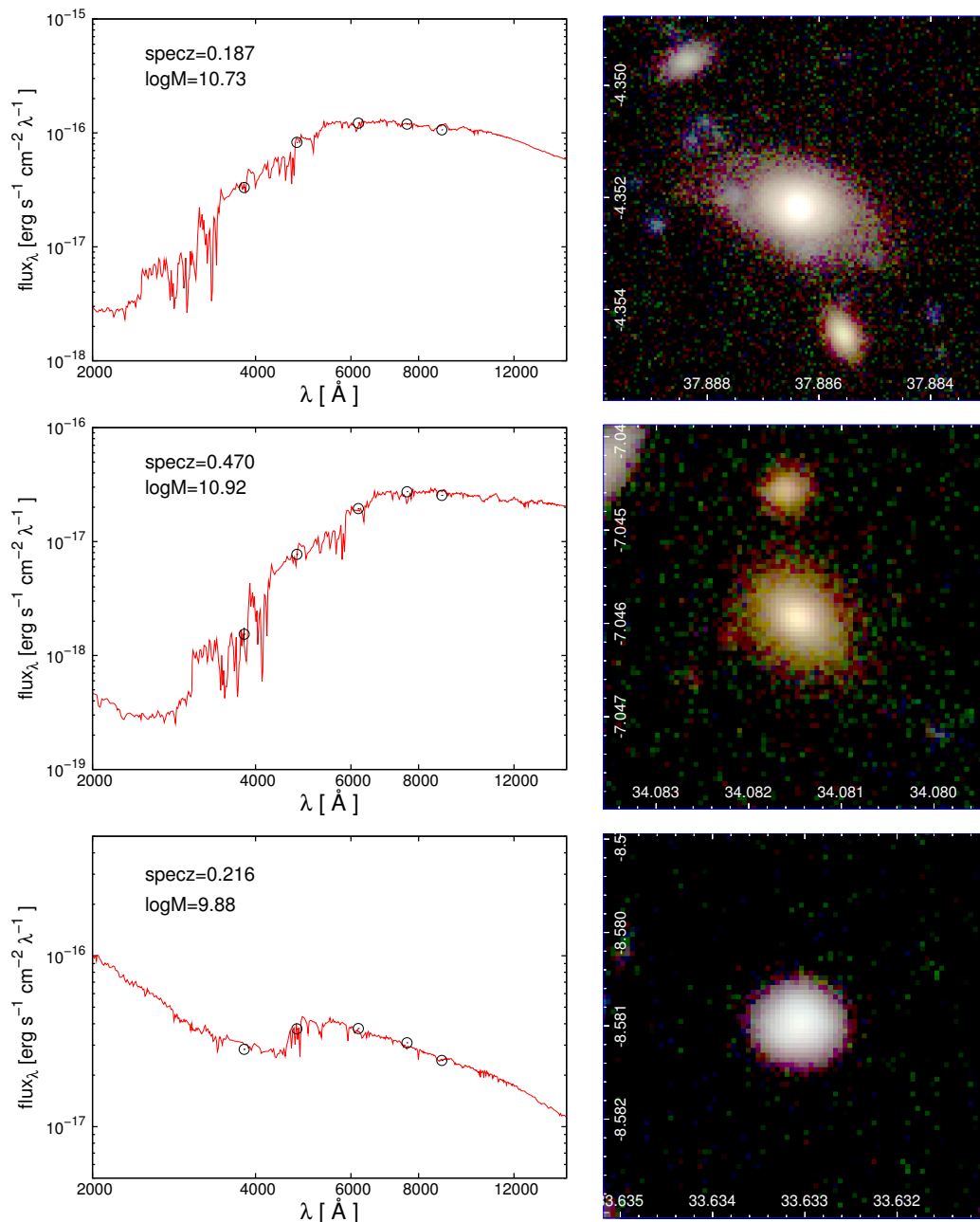


Figure 3.7: Results of SED fitting method for galaxies in CFHTLS. The left panel are best-fit SED models and observed photometry for three examples of galaxies at different redshifts. The red curves are the energy flux versus wavelength of SED template. The open circles show the observed magnitude in the unit of energy flux. The right panels are color images of the same galaxies. The g , r , and i bands are respectively used as blue, green and red images.

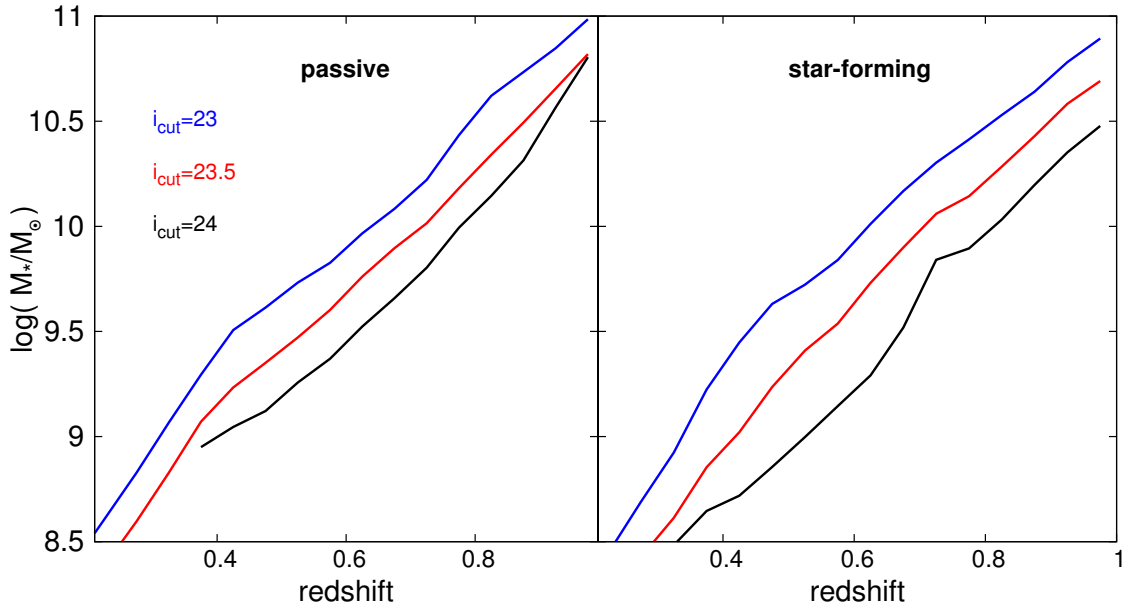


Figure 3.8: Completeness mass threshold for star-forming and passive galaxies as a function of redshift. The blue, red, and black curves respectively belong to $i=23$, 23.5 , and 24 cuts on the luminosity. Since there is no galaxy in the catalog with $23.9 < i < 24$ with passive SEDs below redshift 0.35 one can consider the more conservative mass of completeness threshold of $i=23.5$ instead of $i=24$ for passive galaxies below redshift 0.35 .

and CFHTLS, is magnitude limited in the i band, we need to translate the completeness threshold into a stellar mass threshold. For this purpose, we apply the same method of Giodini et al. (2012) and Ilbert et al. (2010). Since the stellar mass threshold is redshift dependent (an apparent magnitude limit translates into a redshift dependent absolute magnitude limit), we first separate galaxies in redshift bins of 0.1 width. In each bin of redshift we select galaxies in the magnitude bin $23.9 < i < 24$, that is at the apparent magnitude limit of the sample. We, then, identify the stellar mass value higher than 95% of the remaining galaxies at $23.9 < i < 24$. We use this value as the stellar mass completeness limit as a function of redshift. This procedure is separately done for early-type and late-type galaxies according to the classification made according to the best SED templates. The classification is described in details in Ilbert et al. (2010). Fig 3.8 shows the stellar mass completeness threshold as a function of redshift for star-forming and passive galaxies with different limits of luminosity.

3.3.2 Photometric redshift error

Using the galaxy photometric and spectroscopic redshift catalogs available in CFHTLS and COSMOS, we derive the photometric redshift error and we investigate how it varies as a function of the observed i band magnitude. We define the photometric redshift error as a combination of two terms: dispersion and systematic offset. The dispersion, σ_{photoz} ,

is defined as the standard deviation of a Gaussian function fitted to the distribution of $(photoz - specz)/(specz + 1)$. The offset of the Gaussian function peak from zero is the offset in the photometric redshift, Δ_{photoz} . Since the sample of spectroscopic redshift in CFHTLS (from SDSS and Hectospec in W1, W2, and W4) are almost limited to $i < 22$, we use spectroscopic redshift from AEGIS survey located in W3 to reach fainter magnitudes. Fig 3.9 shows the distribution of photometric redshift error as a function of the i band magnitude in four magnitude ranges ($17 < i < 17.5$, $21 < i < 21.5$, $22 < i < 22.5$, and $23 < i < 23.5$). The photometric redshift error increases from 0.03 for $21 < i < 21.5$ to 0.78 for $23 < i < 23.5$. This larger uncertainties at fainter magnitudes can lead to a poor definition of the cluster galaxy membership what photometric redshift are used to define the redshift intervals where to look for member candidates. Fig 3.10 shows how the two components of the the photometric redshift error, dispersion (upper panel) and systematic offset (lower panel), vary as a function of the galaxy magnitude in the CFHTLS catalog. The σ_{photoz} is rather constant for galaxies brighter than $i = 20$. It slightly increases at $20 < i < 22$. For $i > 22$ the photometric redshift significantly loses the accuracy. In terms of systematic offset, the value of Δ_{photoz} is less than 0.01 in all magnitude ranges except at $i > 23.5$ where it reaches a value of 0.04.

The spectroscopic redshift data in COSMOS is also limited to $i < 22.5$. Since the offset in photometric redshift of COSMOS is insignificant (less than 0.005), we assume the offset at $i = 22.5$ for fainter galaxies. The dispersion of photometric redshift at $i > 22.5$ is also extrapolated by a polynomial. Figure 3.11 illustrates the dispersion and the offset of photometric redshift for COSMOS survey. The extrapolation for $i > 22.5$ is plotted as a red curve.

3.3.3 Uncertainty in stellar mass induced by error in redshift

To investigate the effect of redshift uncertainty on the estimate of the stellar mass, we quantify the difference between the stellar masses estimated with photometric ($M_{*,photoz}$) and spectroscopic redshift $M_{*,specz}$, respectively. This error in stellar mass, $\sigma_{M_{photoz}}$, is not only caused by the change in the distance of galaxy from us but also by degeneracy between the age, dust attenuation, typical of SED and fitting technique. As in the previous analysis, we use the SDSS and Hectospec redshift catalog available in W1, W2 and W4 down to $i \sim 22$, and the AEGIS spectroscopic redshift catalog available in W3 for considering also galaxies at $22 < i < 24$. As in the previous analysis, we define the stellar mass error as a combination of two terms: dispersion and systematic offset. The dispersion, σ_{photoz} , is defined as the standard deviation of a Gaussian function fitted to the distribution of $M_{photoz} - M_{specz}$. The offset of the Gaussian function peak from zero is the offset in the stellar mass estimate, Δ_{photoz} . Fig 3.12 shows the error in $\log(M_*)$ as a function of i band magnitude due to uncertainties in the photometric redshift derivation. To understand if this uncertainty varies with redshift, the sample is divided in three redshift ranges: $0.1 < z < 0.4$, $0.4 < z < 0.7$, and $0.7 < z < 1.0$. We find out that the uncertainty σ_{photoz} in stellar mass is almost independent of redshift and it is constant with a value of 0.05 dex up to $i \sim 23$, where it increases up to 0.15-0.2 dex. The offset is always negligible but at

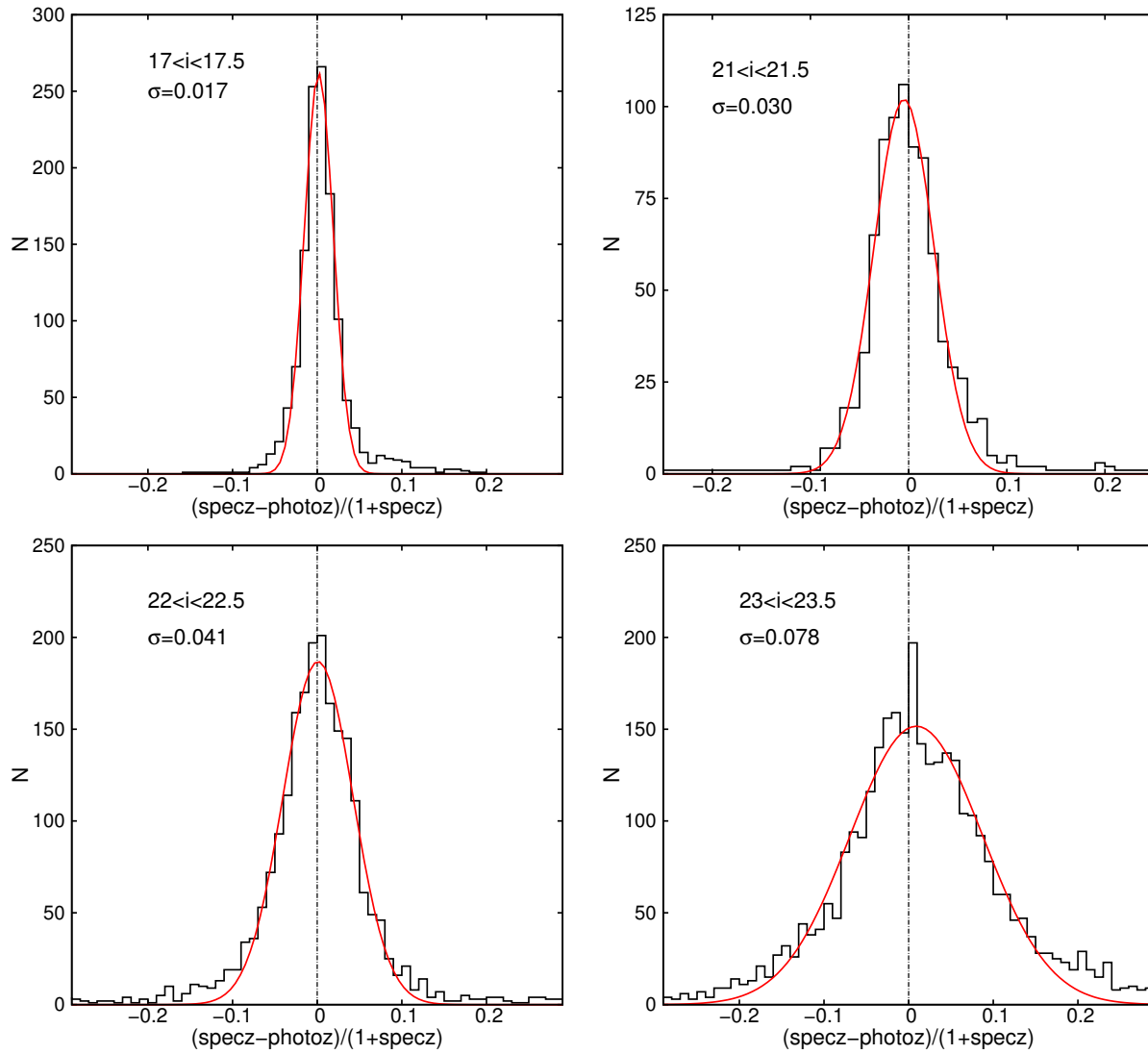


Figure 3.9: Distribution of photometric redshift deviation from spectroscopic redshift for different magnitude brightness ranges. The red curves show the Gaussian fit to the distributions.

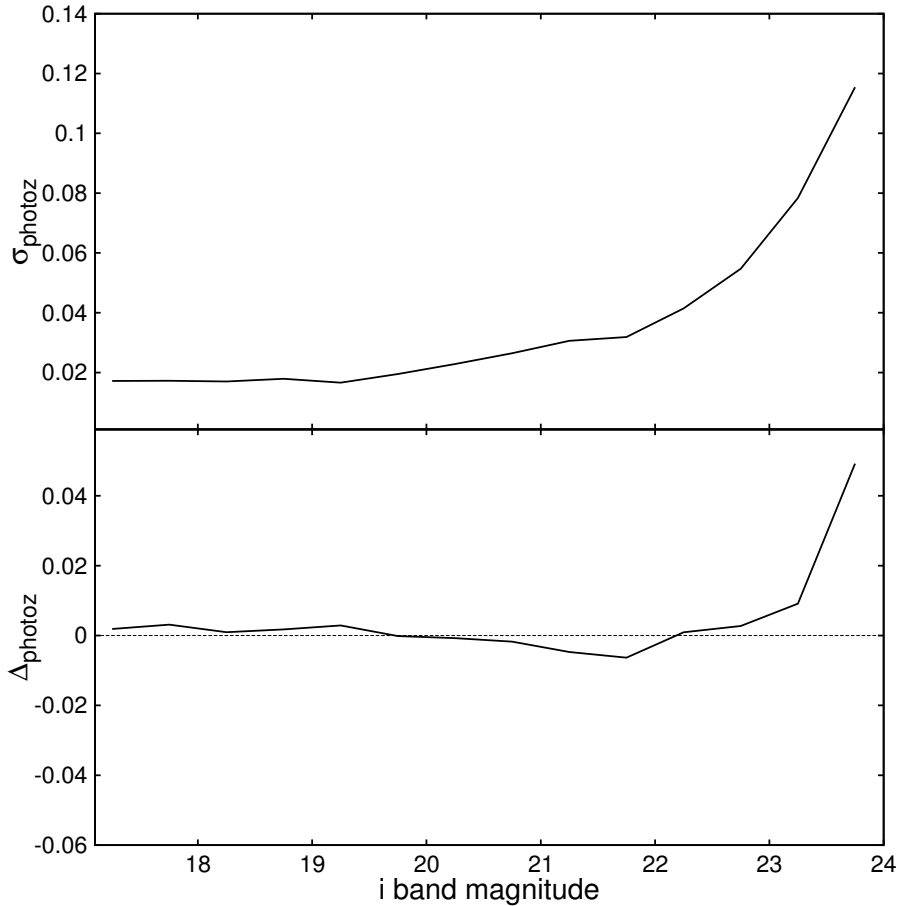


Figure 3.10: Error in photometric redshift as a function of i band magnitude for CFHTLS. The top panel is the dispersion of $(\text{photoz}-\text{specz})/(\text{specz}+1)$ and the bottom panel is the offset in $(\text{photoz}-\text{specz})/(\text{specz}+1)$.

$i > 23$.

3.3.4 Uncertainty in stellar mass induced by error in photometry and absence of NIR data

The photometric completeness threshold of the CFHTLS photometry catalog is $i \sim 24.5$ ($i=24$ for photometric redshift catalog). Since we go deep close to the boundary of photometry completeness the magnitude measurement has a significant error. Besides the depths of data, lack of NIR data (J , H , and K bands) increases the uncertainty in measurement of stellar mass of galaxies in particular at $z > 0.5$. To understand how much these two effects can increase the uncertainty, we calculate the stellar mass in the deep D1 field of CFHTLS which has a depth of $i \sim 27$, a rather deep J, HK coverage and it is overlapping with W1, where the photometry is limited to u, g, r, i, z . We define the total error induced by these two sources of uncertainty as δM_{photom} . We applied the same method as described in § 3.2.3

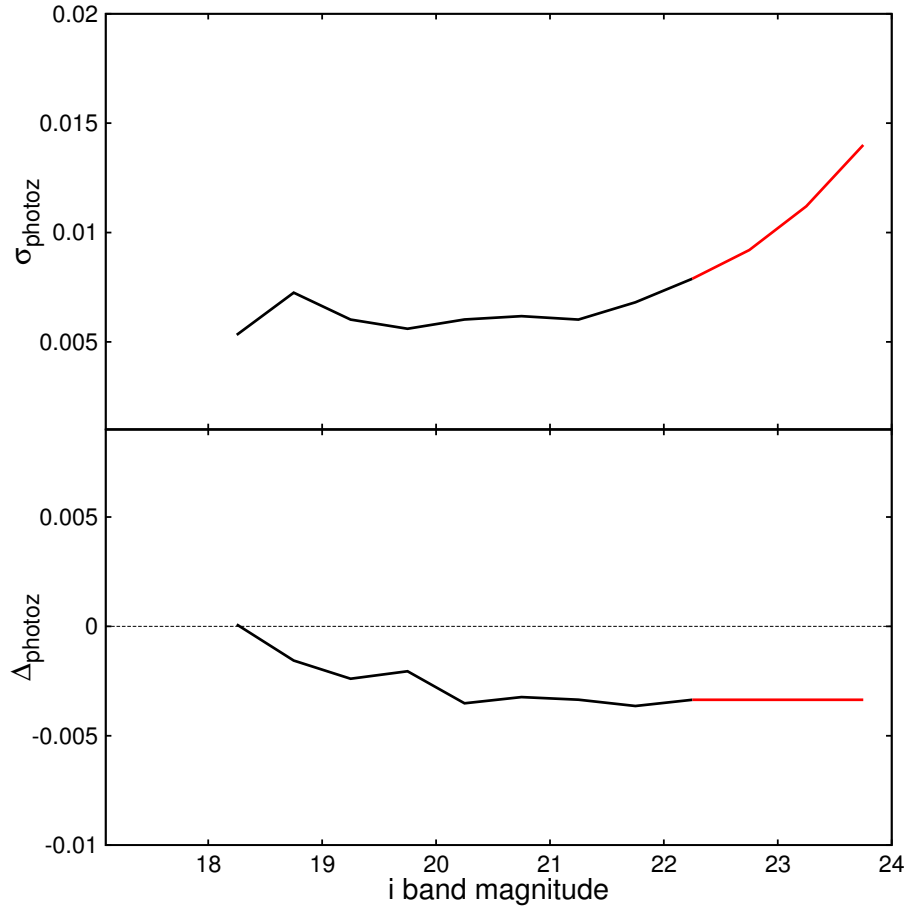


Figure 3.11: Error in photometric redshift as a function of i band magnitude for COSMOS. The top panel is the dispersion of $(\text{photoz}-\text{specz})/(\text{specz}+1)$ and the bottom panels is the offset in $(\text{photoz}-\text{specz})/(\text{specz}+1)$. The black curves are derived by the Gaussian fitting procedure similar to Figure 3.10. The red curves are the extrapolations of the black curves.

for computing the mass using all eight u, g, r, i, z, J, H, K bands and the same redshifts as used for W1. Fig 3.13 is the stellar mass derived from W1 data, $M_{*,W1}$, versus the stellar mass from D1 data $M_{*,D1}$. In this plot, we do not discriminate between galaxies according to their luminosity or redshifts. This plot shows a tight correlation between $M_{*,W1}$ and $M_{*,D1}$. To better investigate the deviation of $M_{*,W1}$ from $M_{*,D1}$, the sample is divided into three redshift ranges, $(0.1,0.4)$, $(0.4,0.7)$, and $(0.7,1.0)$ and the standard deviation of $M_{*,W1}-M_{*,D1}$ is calculated for different magnitude bins. Fig. 3.14 shows the δM_{photom} for different redshift ranges as a function of magnitude. For all ranges of galaxy brightness, $M_{*,W1}$ has very similar scatter (varying between 0.12 and 0.18 dex) from $M_{*,D1}$ for low redshift range of galaxies. For intermediate and high redshifts the scatter is comparable to the low redshift only at $i < 22$.

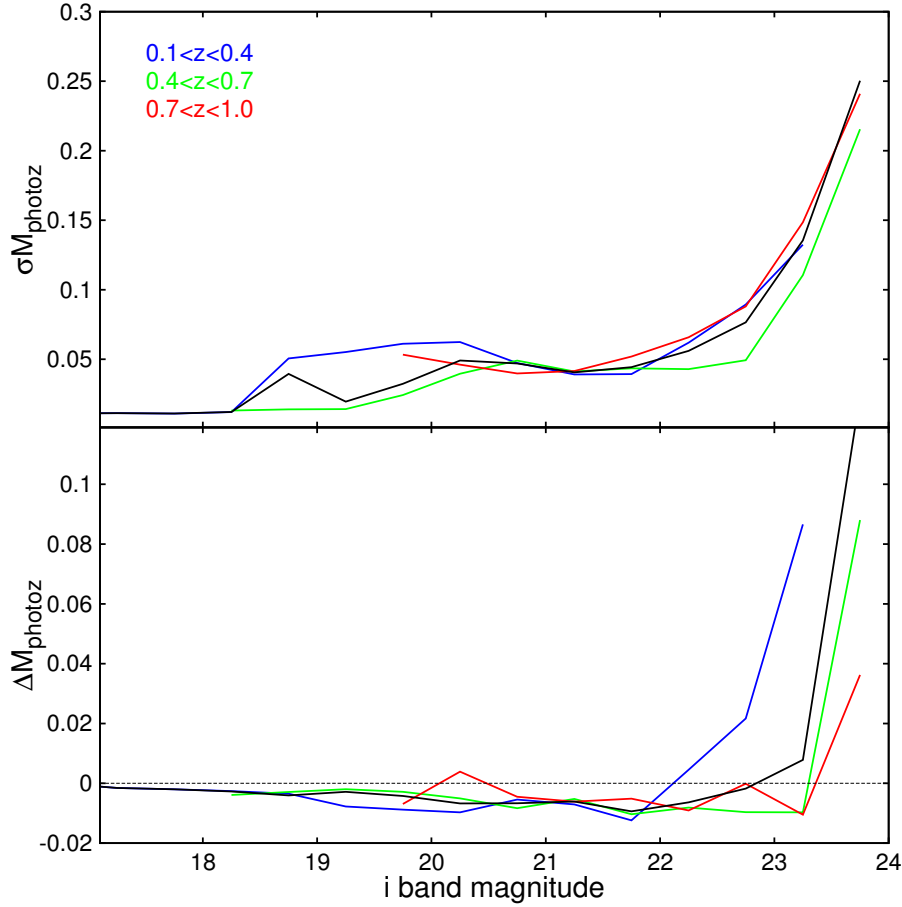


Figure 3.12: Variation of stellar mass induced by uncertainty in the photometric redshift as a function of i band magnitude for different redshift ranges. This error in stellar mass (Y axis) is the standard deviation of Gaussian function fitting to $M_{*,\text{photoz}} - M_{*,\text{specz}}$. The overall shape of this plot is expected from Fig. 3.10.

3.3.5 Total uncertainty in stellar mass

In this section, we characterize the sum of all type of errors in the stellar mass estimate as a function of galaxy redshift and magnitude. Besides the stellar mass measurement errors induced by lack of NIR data and uncertainty in the photometry (δM_{photom}) and the photometric redshift error (δM_{photoz}), we also consider an intrinsic error in stellar mass computation using SED fitting method, δM_{SED} . Ilbert et al. (2010) use different stellar population synthesis models and extinction laws to provide several sets of SED templates. They compute the stellar mass of galaxies in COSMOS field with different SED template sets. Their comparison show that there is a dispersion of 0.14 dex between the results derived from the use of different SED templates. Thus, we assume a typical value of $\delta M_{\text{SED}} = 0.14$ dex. This value is close to the adopted value of 0.12 dex by Giodini et al. (2012).

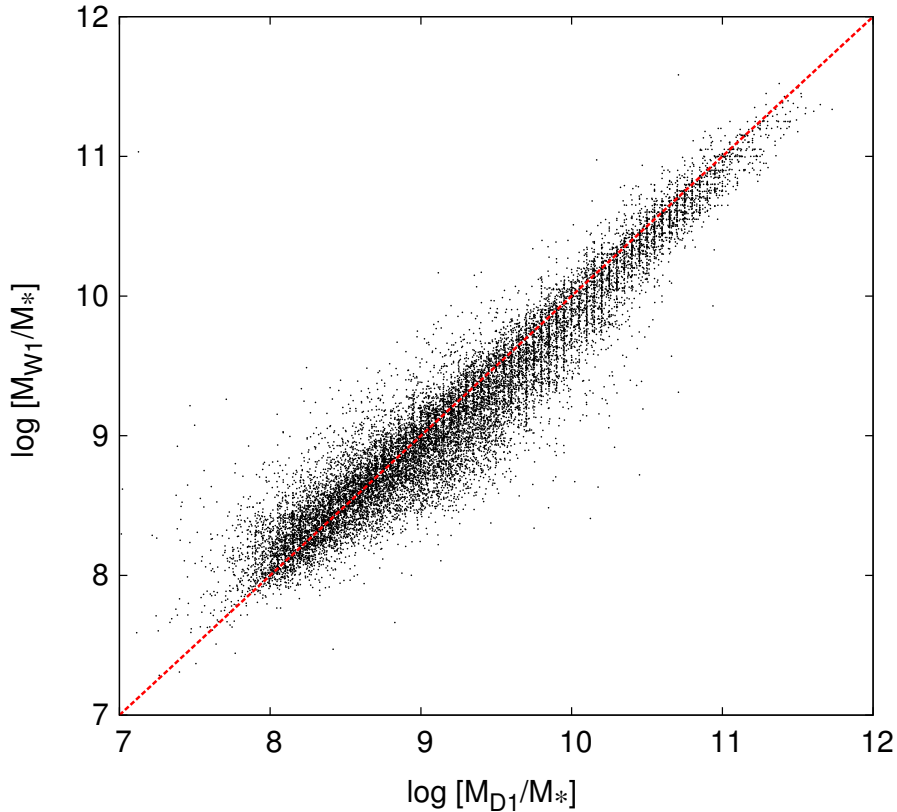


Figure 3.13: Mass derived using u, g, r, i, z filters in W1 versus the mass calculated using D1 u, g, r, i, z, J, H, K bands. The red dashed line shows the 1:1 relation.

In order to derive the total errors in the stellar mass estimation for CFHTLS, we assume no correlation between mentioned errors and sum up them in quadrature. Figure 3.15 shows the total errors, δM_{total} , in redshift-magnitude space. For bright galaxies ($i < 21$), the total error is less than 0.25 dex at all redshifts. Figure 3.15 also show that at redshifts below 0.3, only faint galaxies ($23 < i$) have stellar mass error more than 0.25 dex. This means that for low redshifts the computed stellar mass is highly reliable. For faint galaxies the accuracy gradually decreases with increasing redshift. Here we characterize the error in the stellar mass of individual galaxies. In § 3.4.2, using the characterized error in Figure 3.15, we will test the reliability of stellar mass function derived from CFHTLS data.

3.4 The group and cluster membership

Due to the high level of spectroscopic incompleteness in the CFHTLS and COSMOS fields, we select the group and cluster member galaxies using the photometric redshifts. In this section, we discuss how the error in the redshift measurement can affect the cluster membership.

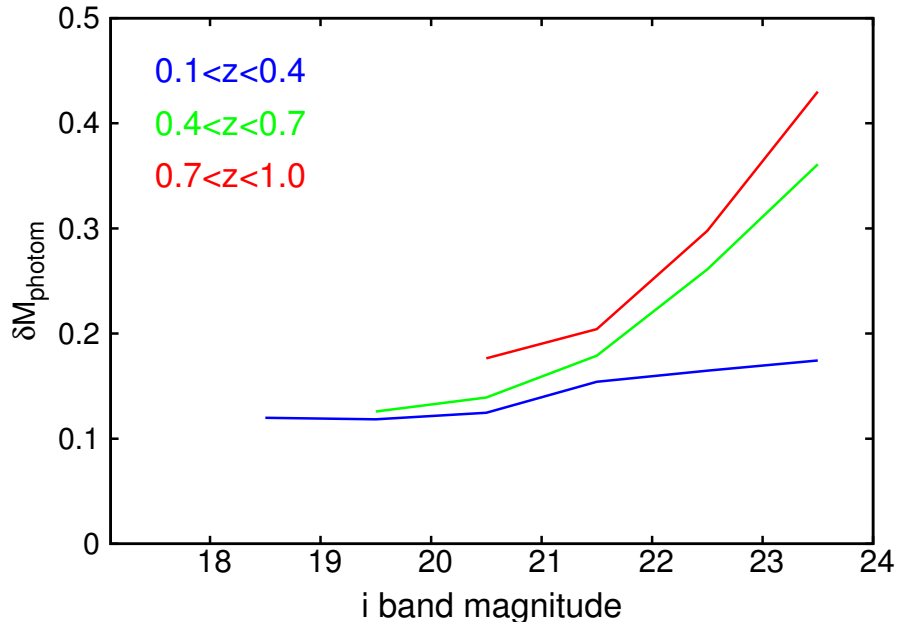


Figure 3.14: Deviation of the stellar mass computed with W1 data from the mass computed using D1 data as a function of galaxy brightness. The blue green and red curves show different redshift ranges.

Due to uncertainties in photometric redshifts, a percentage of background and foreground galaxies can be included in the cluster galaxy selection, while a fraction of members can be lost. If the photometric $\delta_{\text{photo}z}$, chosen for selecting all galaxies around the cluster mean redshift is too large (e.g. 5 times of photometric redshift error), it can lead to the selection of all cluster members (high completeness) but also to a quite large percentage of interlopers (poor purity). In contrast, if the $\delta_{\text{photo}z}$ value is too small, it will lead to a very low completeness and to a very high purity. In other words, to properly select cluster galaxy members on the basis of photometric redshift, the $\delta_{\text{photo}z}$ window must be set according to the z_{phot} error.

For this purpose, we use a mock catalog and the photometric redshift error characterization of the previous section, to explore how to properly set $\delta_{\text{photo}z}$. In particular, we use the mock catalogs of the Millennium simulation (Springel et al. 2005) catalog. The Millennium simulation traces the growth of dark matter halos from redshift 127 to zero with 2160^3 particles within a cubic region ~ 500 Mpc on a side by assuming the concordance Λ CDM cosmology. We use the Kitzbichler & White (2007) mock galaxy catalog in which De Lucia et al. (2006) semi-analytic model is used for modeling the evolution of baryonic matter. The mock catalog is produced by assuming an observer at redshift zero. The light-like world-lines that pass through the position of the observer define a backward light-cone. Then the galaxies within this backward light-cone are selected as the observed galaxies.

From the Kitzbichler & White (2007) mock catalog, we extract observed redshift, co-

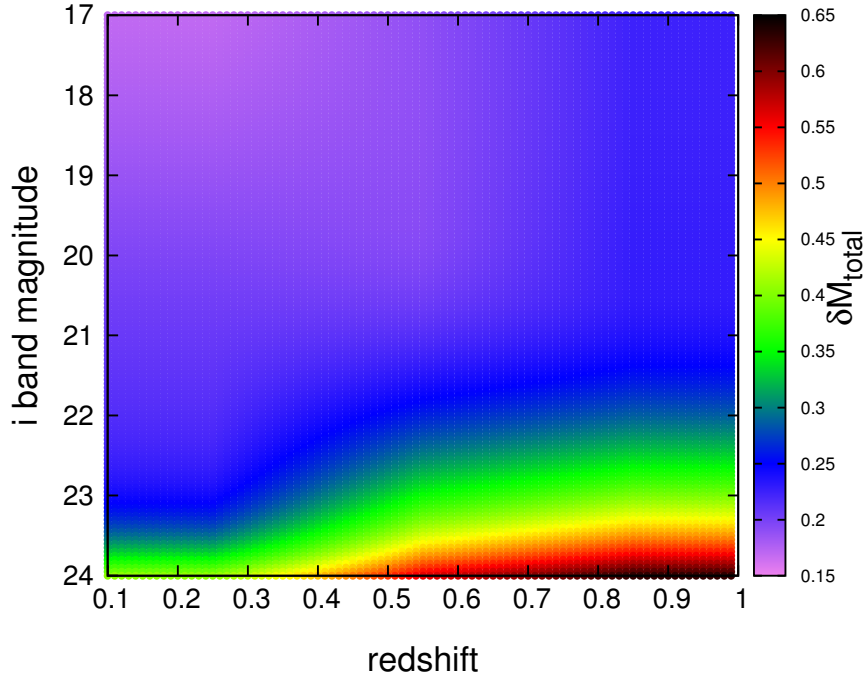


Figure 3.15: Total error in estimating stellar mass in redshift-magnitude space. This figure shows the sum in quadrature of δM_{photoz} , δM_{photom} , and δM_{SED} for individual galaxies up to redshift 1.

ordinates, stellar mass and Johnson photometric I band. The selection of clusters in mock catalog is based on the dark matter halo virial mass which, according to De Lucia et al. (2006), is consistent with the mass calculated within r_{200} , as in the observed cluster sample. The members of the groups are identified by the observed redshift of the galaxies in the mock catalog. The members are identified as the galaxies with recession velocity within 3 times the cluster velocity dispersion and within r_{200} provided by the mock catalog.

In order to produce a set of simulated photometric redshifts as in our observed catalog, the redshift systematic and random errors are added to the mock catalog redshifts as a function of I band magnitude similarly to Fig. 3.10. The systematic and random errors in stellar mass are also added to the mock stellar mass according to the noise terms shown in Figures 3.12 and 3.14. An additional 0.14 dex noise for δM_{SED} is also added to the stellar masses to simulate the error induced by the SED fitting technique. In this way the mock catalog exhibit the same photometric redshift and stellar mass error characterisation as the observed dataset.

The left panel of Figure 3.16 shows the magnitude–spectroscopic redshift distribution of mock catalog galaxies within r_{200c} from the center of a cluster at redshift 0.25. The

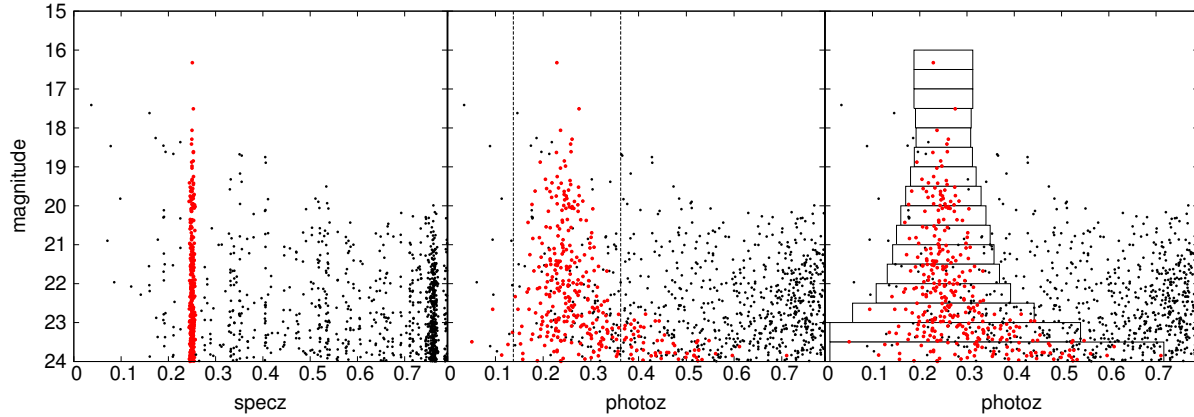


Figure 3.16: Left: Magnitude–redshift distribution of all galaxies within r_{200c} of a mock cluster at redshift 0.25. The red dots are spectroscopic member galaxies having a redshift difference to the BCG less than three times the velocity dispersion of galaxies. Grey dots are background and foreground galaxies. Middle: magnitude – redshift of the same galaxies as in right panel after adding the photometric redshift errors of CFHTLS galaxy catalog to the spectroscopic redshift of the mock galaxies. Two vertical dashed lines show $\pm 3 \times (1+z)\delta_z$ from the redshift of BCG ($\delta_z=0.03$) as a range for selecting the member galaxies. Although this range (or even smaller range) can be large enough for selecting bright galaxies with small redshift error, a large number of faint member galaxies with large photometric redshift error are located outside of this range. In contrast, larger redshift range for selection of member galaxies would guarantee high fraction of member galaxies (even at faint end with high redshift error) but it can induce more background and foreground galaxies which increase more uncertainties in derivation of GSMF. Right: The same distribution as middle panel but with variable redshift ranges. After characterizing the photometric redshift error as a function of magnitude, the redshift range for selection of member galaxies can be adopted as a function of the galaxy magnitude.

red dots are spectroscopic members, e.g. simulated catalog with the original mock catalog redshift. The spectroscopic members are defined as those with recessional velocity within ± 3 times the cluster velocity dispersion and within r_{200c} from the brightest cluster galaxy (BCG). The black dots are background and foreground galaxies. The middle panel shows the magnitude – photometric redshift distribution for the same galaxy sample as in the left panel. The impact of the large uncertainty of the photometric redshift, in particular at faint magnitudes, is quite remarkable.

To take into account the effect of the error on the photometric redshift in identifying the cluster membership, we choose to use a redshift selection δ_{photoz} that is magnitude dependent. As shown on the right panel of Fig. 3.16 by the black rectangles, we define a δ_{photoz} which is as large as $\pm 3 \times (1+z) \sigma_{photoz}(i)$, where $\sigma_{photoz}(i)$ is characterized on the top panel of Figure 3.10. In this way, δ_{photoz} is larger at fainter magnitudes and it is able to capture all cluster members (red points). However, this method can not lead to a

pure cluster member selection as many background and foreground galaxies are captured in the same δ_{photoz} window (black points in the right panel of Fig. 3.16). To overcome this problem when estimating the GSMF, we developed a method capable of removing the remaining interlopers with a statistical background subtraction. We also test the width of the $\delta_{photoz} = n \times (1+z) \sigma_{photoz}(i)$ with the mock catalog in order to ensure the best accuracy in the estimate of the GSMF.

3.4.1 The individual and composite GSMF

Given the membership assignment described above, we estimate the GSMF of each object in the following way. We divide the galaxy sample within r_{200} in bins of i band magnitude. We estimate several “raw” GSMFs of a cluster in each magnitude bin and in a δ_{photoz} window that is $\pm n \times (1+z) \sigma_{photoz}(i)$. As explained above, these GSMF should be complete with respect to the galaxy members but highly contaminated by interlopers. In order to remove this contamination we estimate also the background GSMFs in the same i magnitude bins and δ_{photoz} windows. Each i magnitude bin raw GSMF is, then, subtracted by the corresponding background GSMF to derive the clean cluster GSMF. As next, all the clean GSMF in different i magnitude bins are summed up to create the total cluster GSMF.

Figure 3.17 shows an example of background GSMF at different magnitudes: the red, green, and blue circles are background GSMFs respectively related to the magnitude ranges of $19.5 < i < 20$, $21.5 < i < 22$, and $23.5 < i < 24$ at the redshift range $0.3 < z < 0.4$.

However, the individual GSMF are too noisy to provide a useful constraint on the relation between GSMF and the environment. Thus, to improve the statistics, we derive a composite GSMF by following the method of Colless (1989). This method was originally established for deriving the mean of member galaxies luminosity function for samples of galaxy cluster (e.g. Popesso et al. 2004; Colless 1989) but its concept is also applicable to mass function of member galaxies. We use the notation of Popesso et al. (2004). The number of galaxies in j th stellar mass bin of composite mass function is:

$$N_{cj} = \frac{N_{c0}}{m_j} \sum_i \frac{N_{ij}}{N_{i0}} \quad (3.3)$$

where N_{ij} is the number of galaxies in the j th mass bin of i th cluster and m_j is the number of cluster that have contribution in the j th mass bin. For each cluster, m_j is determined by the cluster completeness mass threshold. N_{i0} is the the normalisation factor for i th cluster:

$$N_{i0} = \sum_k N_{ik} \quad (3.4)$$

for k th mass bin more massive than m_i . N_{c0} is the normalization factor for composite mass function:

$$N_{c0} = \sum_k N_{ck}. \quad (3.5)$$

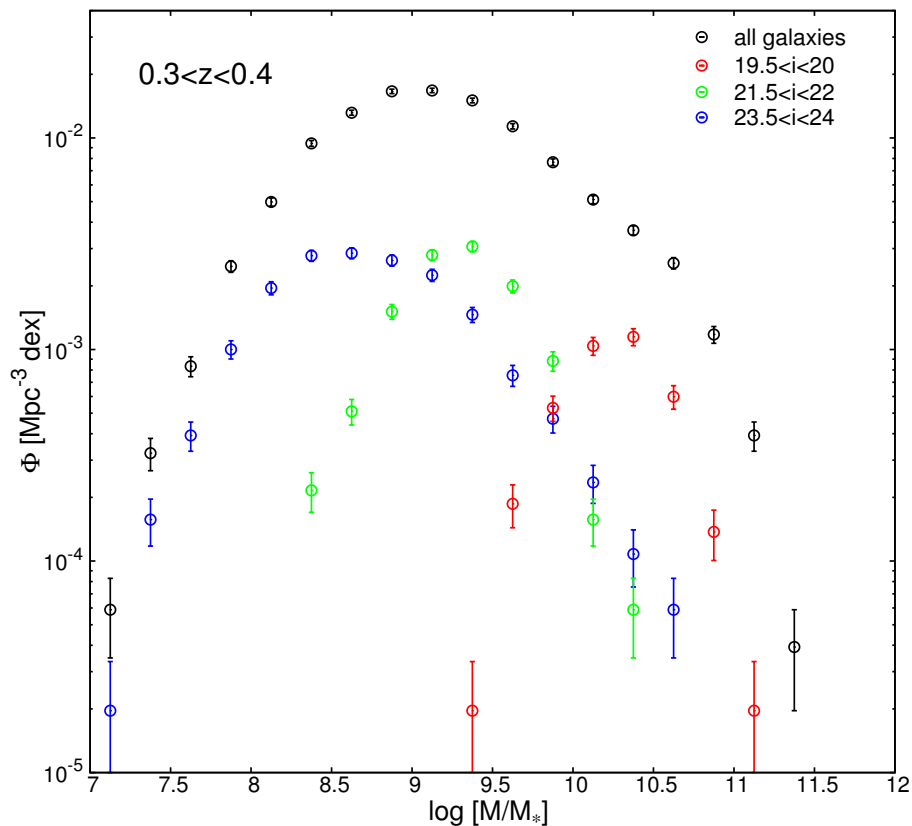


Figure 3.17: The black circles are GSMF of the whole galaxy population at $0.3 < z < 0.4$. In the method with constant redshift range for selection of member galaxies at all magnitudes, this GSMF and similar ones using different redshift ranges are considered as background GSMF for clusters (see also middle panel of Figure 3.16). The red, green, and blue circles show GSMF for galaxies at the same redshift range but with different cuts on magnitude. These GSMF and similar ones at other ranges of redshift and magnitude are subtracted as background from clusters GSMF (see also to right panel of Fig. 3.16).

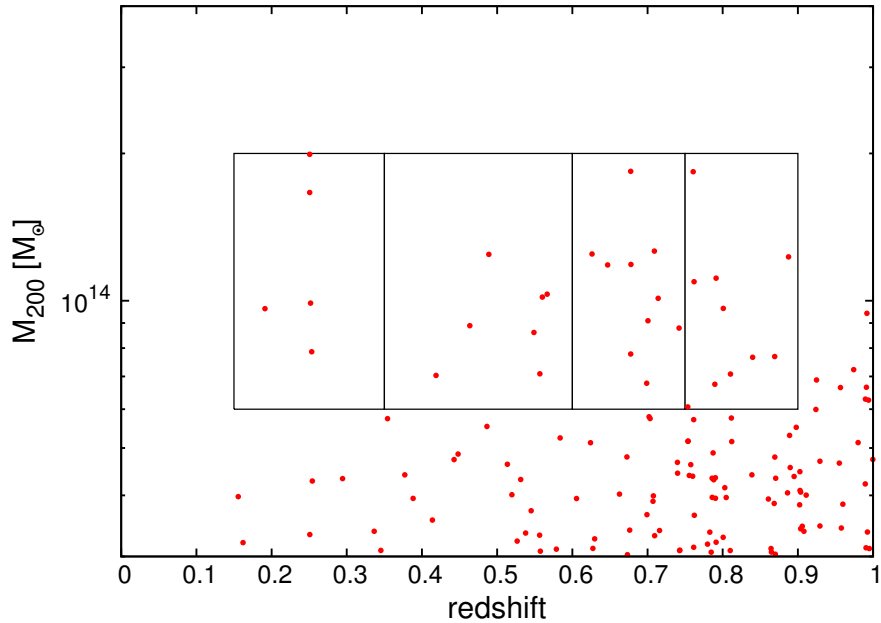


Figure 3.18: Mass versus redshift of clusters in mock catalog. The rectangles show our mass-redshift gridding.

The formal error in N_{cj} is calculated according to:

$$\delta N_{cj} = \frac{N_{c0}}{m_j} \left[\sum_k \left(\frac{\delta N_{ij}}{N_{i0}} \right)^2 \right]^{\frac{1}{2}} \quad (3.6)$$

where δN_{ij} is the error in the j th mass bin of the i th cluster.

One can compute the composite GSMF as an average of clusters by dividing the right hand side of equation 3.3 by the number of clusters, $N_{cluster}$, in following form:

$$N_{cj} = \frac{N_{c0}}{m_j N_{cluster}} \sum_i \frac{N_{ij}}{N_{i0}} \quad (3.7)$$

Before showing the results of the composite GSMF in clusters and groups, we first test the reliability of our method in the next section on the basis of the mock catalog described above.

3.4.2 Robustness of the method

In this section, we use the mock catalog to verify the robustness of our method for selecting member galaxies and computing GSMF based on photometric redshifts. For this purpose, we simulate the photometric redshift inaccuracy by adding the photometric error as a function of the i band magnitude as explained above. The same is done for the error of the stellar mass. We produce 500 different realizations of the mock catalog by adding random

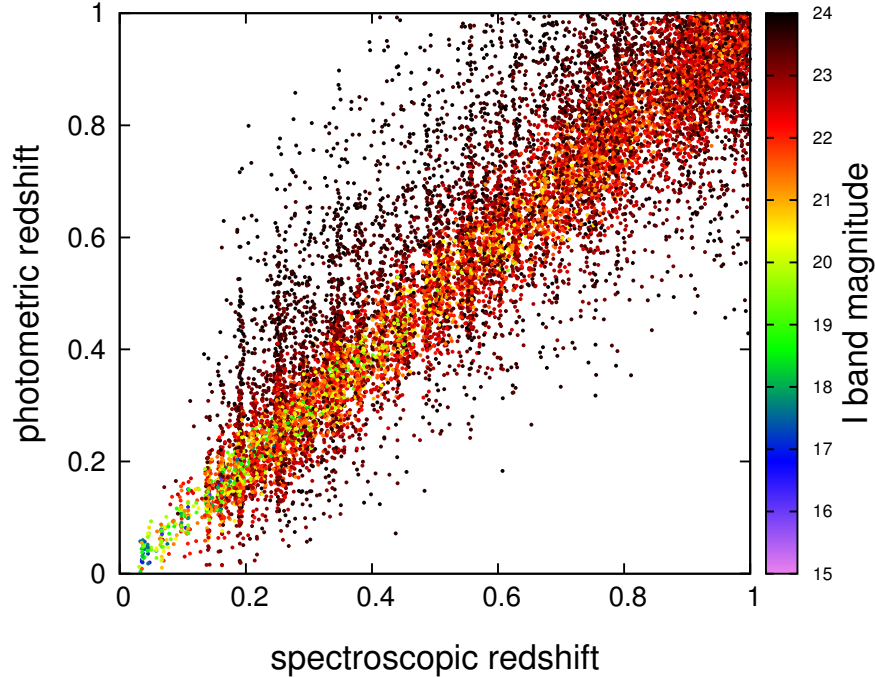


Figure 3.19: Simulated photometric redshift versus the spectroscopic redshift in the mock catalog. Since the photometric redshift uncertainty of a galaxy depends on its brightness, the galaxies are color coded by their magnitude.

error with the same properties as in the observed dataset. The Figures 3.19 and 3.20 show the simulated photometric redshifts and stellar mass in mock catalog, respectively. As in the observed dataset we apply a magnitude cut at $i = 24$ mag.

Figure 3.18 shows the clusters identified in the mock catalog in the same redshift and halo mass range used in the observed dataset. A small number of massive clusters is observed in the mock catalog. The reason is that the mock catalog has the area of 2 degree² and more massive systems would be rare in such small area. Since the GSMF accuracy is expected to be redshift dependent, different redshift ranges are chosen for deriving the composite GSMF of clusters: $0.15 < z < 0.35$, $0.35 < z < 0.6$, $0.6 < z < 0.75$ and $0.75 < z < 0.9$. We also select the clusters with mass between 6×10^{13} and $2 \times 10^{14} M_{\odot}$ which is similar to mass range of clusters in CFHTLS.

We estimate the “true” composite GSMF of the cluster members, identified by the friend of friend algorithm of De Lucia et al. (2006) in the mock catalog within r_{200} from the cluster center (the BCG position) and with velocity within 3 times the cluster velocity dispersion. We, then, used our method, based on the photometric redshift and observed stellar mass, to estimate the “observed” composite GSMF of clusters exactly as in the

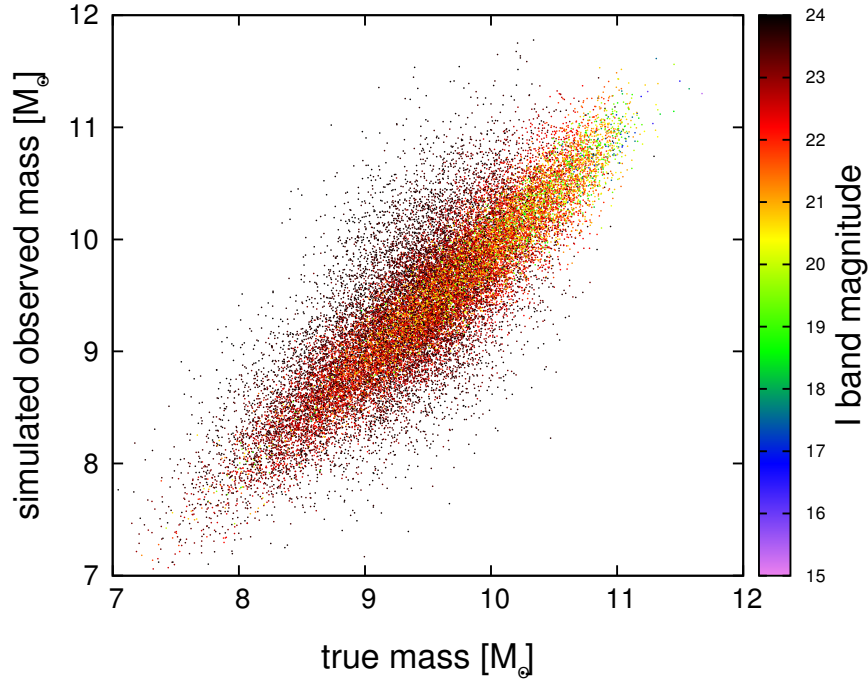


Figure 3.20: Simulated measured stellar mass versus the true stellar mass in the mock catalog. Since the stellar mass uncertainty of a galaxy depends on its brightness the galaxies are color coded by their magnitude.

observed datasets. This is done for each photometric redshift and observed stellar mass catalog realizations. In addition, we perform the analysis for different values of δ_z (fixed and variable as a function of the i band) to identify the best value in order to obtain the most accurate composite GSMF. The comparison between the “true” and the observed GSMF obtained with this different parameter setting is shown in Fig. 3.21, 3.22, 3.23, 3.24. For each parameter setting the “observed” GSMF is obtained as the mean of the 500 GSMF obtained in the different redshift and observed stellar mass catalog realisations. The errors are estimated using the dispersion around the mean. Fig. 3.21 shows the result obtained by choosing a variable $\delta_z(i)$ as a function of i band magnitude. Fig. 3.22, 3.23, and 3.24, respectively, show the results for a constant value of δ_z of 0.02, 0.04 and 0.06.

In all cases, we are able to reproduce within the errors the input GSMF. However, we note that the error induced by the choice of a $\delta_z=0.06$ (and larger δ_z) leads to a large uncertainty in the GSMF at low redshift ($z < 0.6$, Figure 3.24). In all other cases, the errors of the GSMF are not changing as a function of redshift. However, at redshift ranges below 0.6, the $\delta_z=0.02$ and 0.04 cases underestimate the galaxy density for masses below $10^{9.5} M_{\odot}$ (see the upper panels of Figures 3.21, Fig. 3.22, and 3.23). At higher redshifts,

instead, the choice of a variable $\delta_z(i)$, and a fixed δ_z of 0.02 and 0.04 leads to the same residuals with respect to the input GSMF. Since the variable $\delta_z(i)$ (Figure 3.21) reproduces the shape of input GSMF at any redshift, we adopted this method for our analysis.

3.5 Group and cluster sample

As we mentioned before in § 3.2.1 and 3.2.2, the COSMOS and CFHTLS contains 277 and 196 X-ray selected clusters, respectively (see Figure 3.5 in § 3.2). To have a clean sample of clusters with secure redshift, we select those clusters which have visual flag 1 and at least two spectroscopic member galaxies. The visual flag assignment is described in Chapter 2 for CFHTLS sample and by Finoguenov et al. (2007) for COSMOS sample. Briefly, visual flag 1 means that the clustering of the galaxies around the X-ray extended source is visually clear and there is no significant offset between the optical galaxy concentration and X-ray emission centres.

The procedure of finding the spectroscopic counterparts for CFHTLS is also explained in detail in Chapter 2. Similar method is also applied by Erfanianfar et al. (submitted) for assigning the spectroscopic counterparts for COSMOS sample. With the above conditions, we provide a sample of 136 X-ray selected clusters and groups in two fields. The selected sample is shown in Figure 3.25. We divide the sample in 10 subsamples with different mass and redshift ranges. Finally we select systems above $z \sim 0.2$ for a final sample of 108 systems with mass between 6×10^{12} and $6 \times 10^{14} M_\odot$.

3.6 GSMF of X-ray selected clusters

For each cluster, the most massive galaxy within r_{200} is considered as the central galaxies and the other ones are assumed to be satellite ones. Then the GSMF of satellite galaxies is computed according to equation 3.7 for each mass–redshift bin. According to Yang, Mo & van den Bosch (2009), the population of central galaxies forms a Gaussian distribution in mass space and whole population of galaxies in clusters can be described by a combination of a Schechter and a Gaussian functions. In this work, we fit the distribution of central galaxies with a Gaussian and then separately fit the satellite galaxies mass function using a Schechter function.

3.6.1 Central galaxies

The two most massive halo mass bins count 5 and 4 clusters at redshift ranges of $0.2 < z < 0.4$ and $0.4 < z < 0.6$, respectively. Since it turns out that the distribution of central galaxies mass in these two bins is very similar, we combine them to increase the statistics. Figure 3.26 shows the central galaxies mass distribution for these two subsamples. Table 3.2 lists the results of Gaussian fitting on stellar mass distribution of central galaxies. Besides the Gaussian fitting, we also calculate the mean and standard deviation of the central galaxies mass distribution and summarize them in Table 3.3. For two highest redshift subsamples

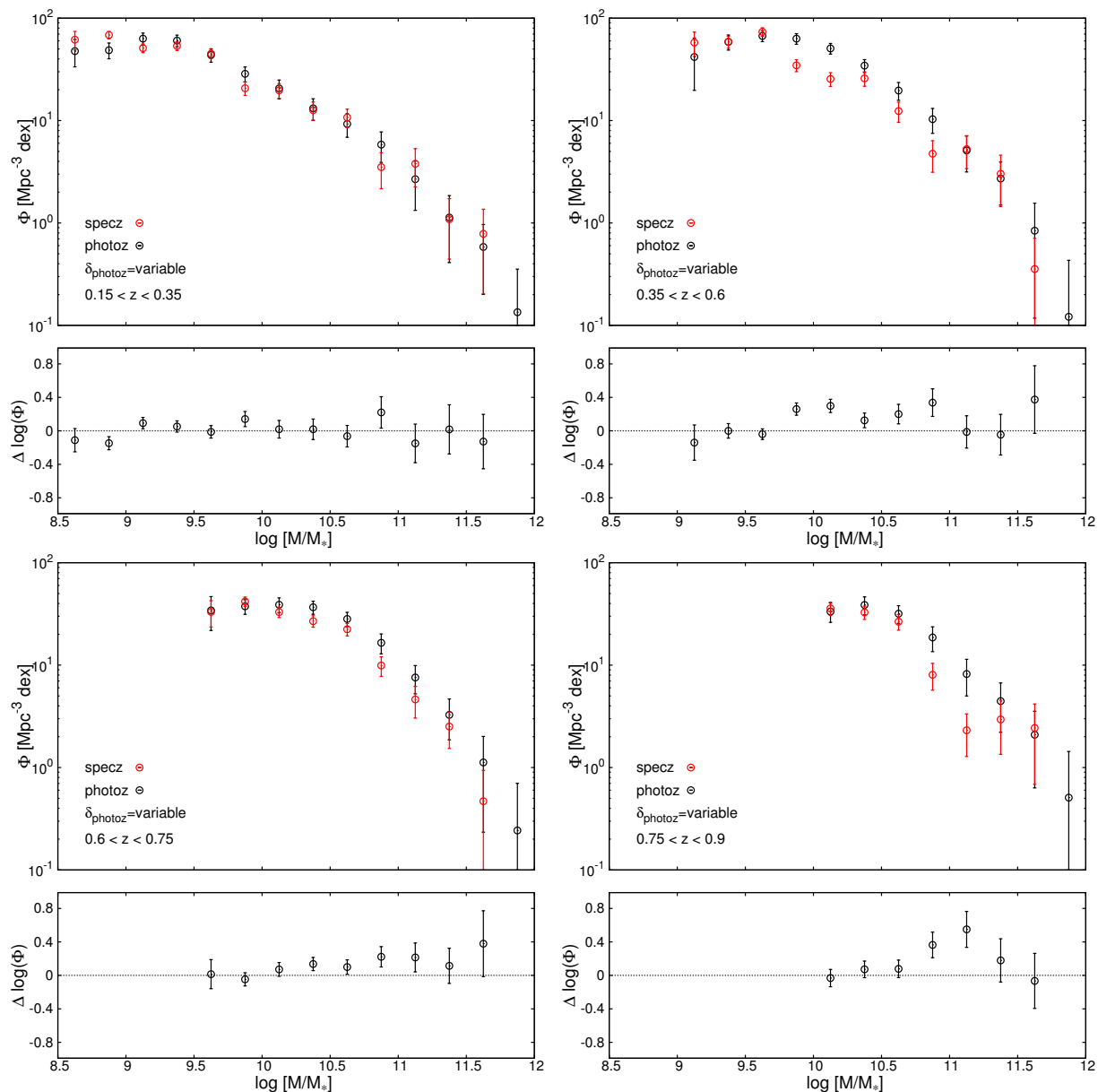


Figure 3.21: Composite GSMF for mock clusters with the mass of $6 \times 10^{13} \leq M_{200c} \leq 2 \times 10^{14} M_{\odot}$ at different redshift ranges. The red circles are the GSMF derived from the original mock catalog and the black ones are computed GSMF after adding noise to spectroscopic redshift and stellar mass. The member galaxies are selected by variable redshift ranges as a function of galaxy magnitude.

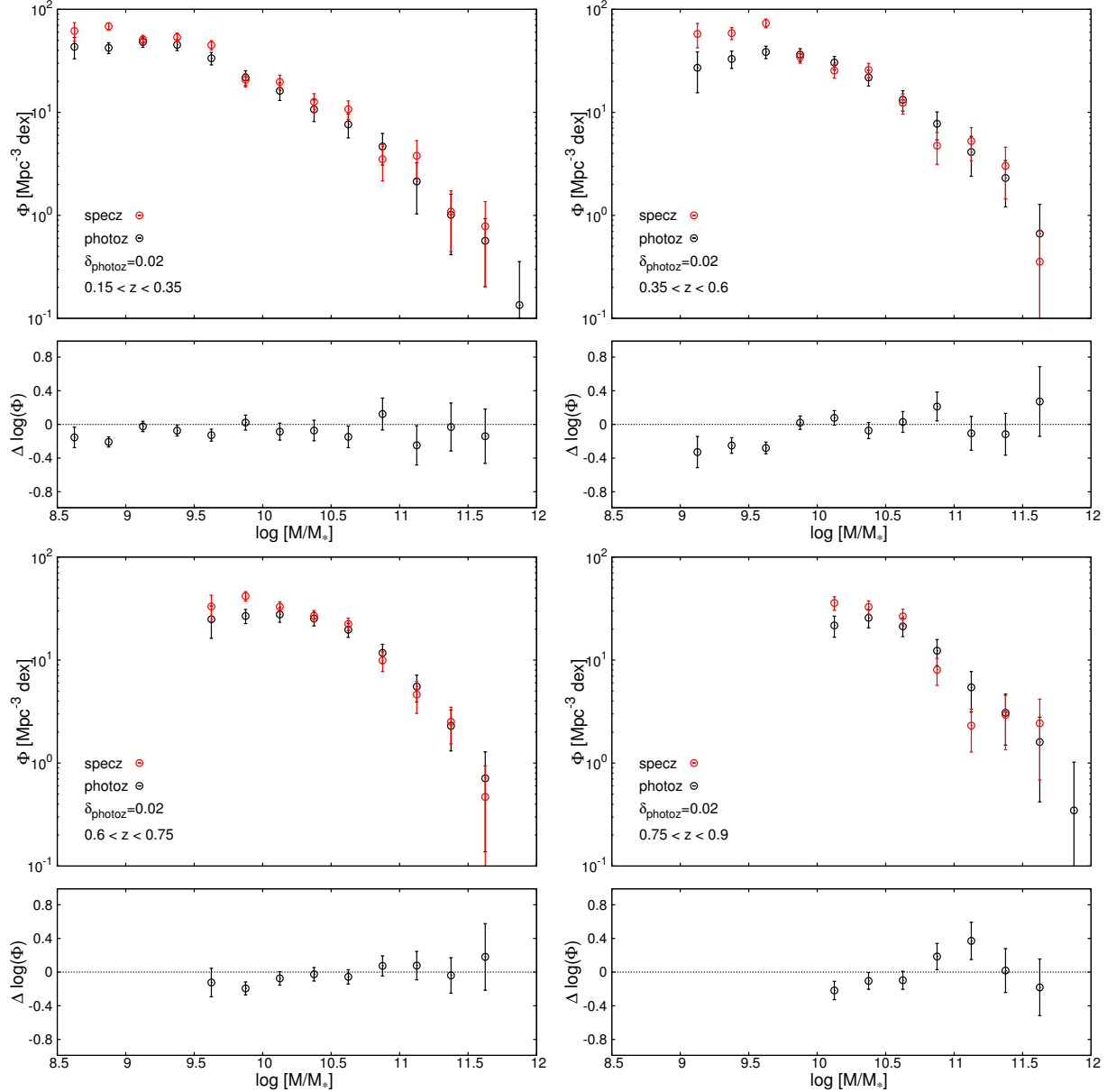


Figure 3.22: Composite GSMF for mock clusters with the mass $6 \times 10^{13} \leq M_{200c} \leq 2 \times 10^{14} M_\odot$ at different redshifts. The red circles are the GSMF derived from the original mock catalog and the black ones are computed GSMF after adding noise to spectroscopic redshift and stellar mass. The member galaxies are selected by a fixed redshift range of $dz = 3 \times \delta_z(1+z)$ where $\delta_z = 0.02$.

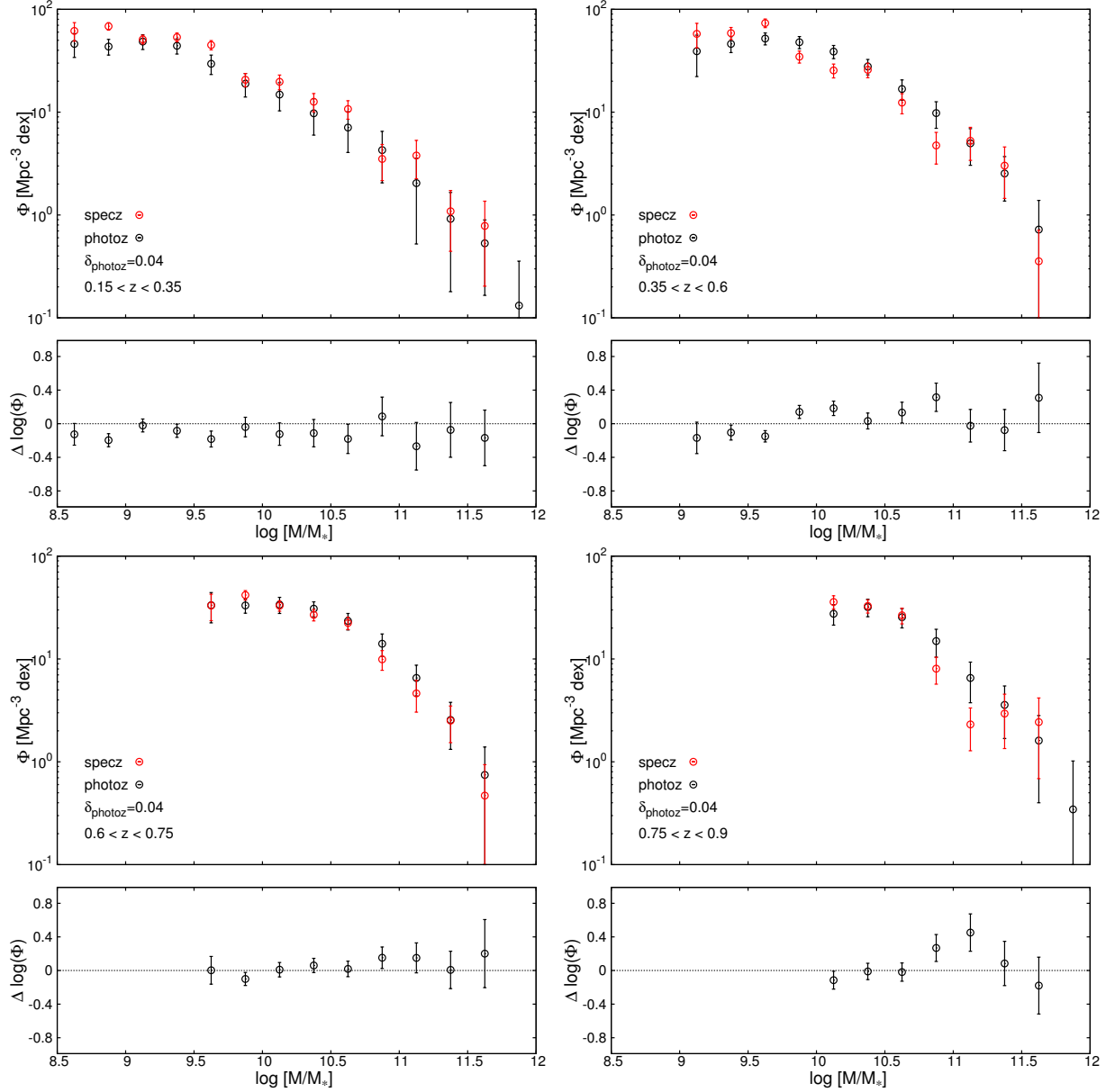


Figure 3.23: Composite GSMF for mock clusters with total mass of $6 \times 10^{13} \leq M_{200c} \leq 2 \times 10^{14} M_{\odot}$ at different redshift ranges. The red circles are the GSMF derived from the original mock catalog and the black ones are computed GSMF after adding noise to spectroscopic redshift and stellar mass. The member galaxies are selected by a fixed redshift range of $dz = 3 \times \delta_z(1+z)$ where $\delta_z = 0.04$.

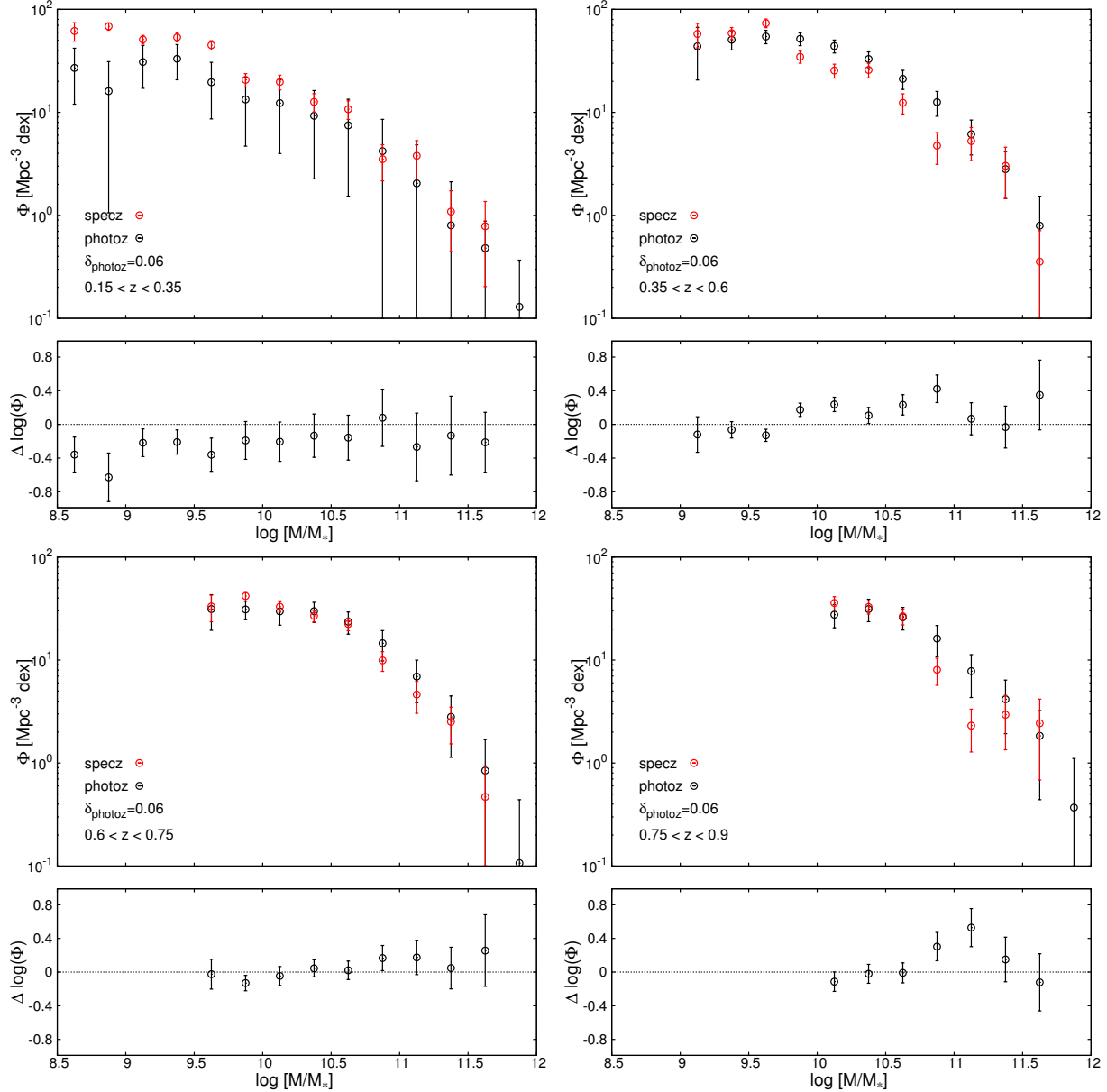


Figure 3.24: Composite GSMF for mock clusters with total mass of $6 \times 10^{13} \leq M_{200c} \leq 2 \times 10^{14} M_\odot$ at different redshift ranges. The red circles are the GSMF derived from the original mock catalog and the black ones are computed GSMF after adding noise to spectroscopic redshift and stellar mass. The member galaxies are selected by a fixed redshift range of $dz = 3 \times \delta_z(1+z)$ where $\delta_z = 0.06$.

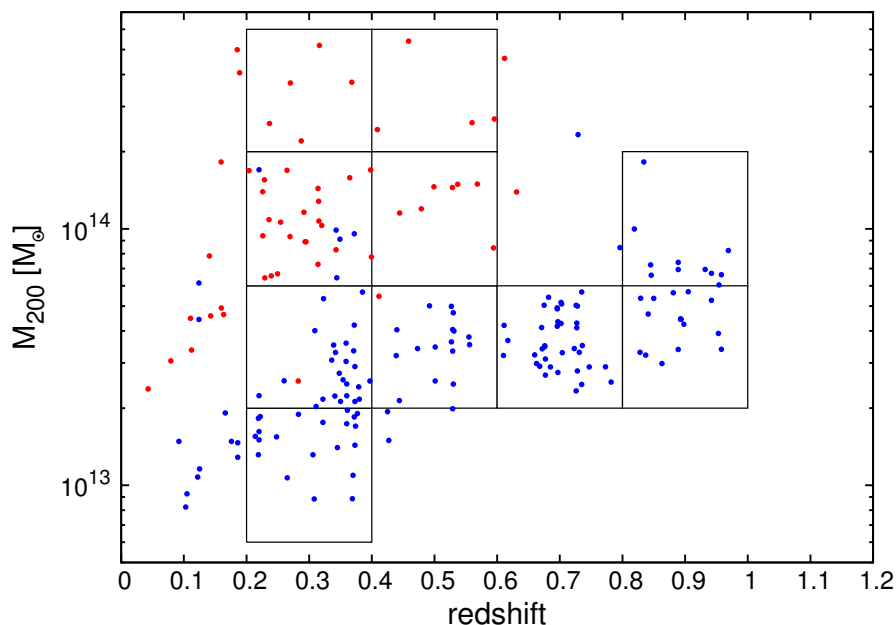


Figure 3.25: Mass versus the redshift for the final cluster sample. It includes the clusters with at least two spectroscopic counterparts and reliable visual flag. The boxes determined the boundaries of each subsamples. Blue and red dots shows the CFHTLS and COSMOS clusters respectively.

the Gaussian fit is not constrained. For few of the mass–redshift bins (with a few clusters) the Gaussian fit is not possible, so we only report the mean and the standard deviation around the mean value for them. Figure 3.27 is the mean of central galaxies in each bin as a function of mean redshift of the bin. The errors are the dispersion around each quantity. It seems that the mass of central galaxies has no evolution since a redshift of 1 for two middle mass ranges. A comparison between the dispersions reported in Tables 3.2 and 3.3 indicates that existence of some outliers in stellar mass distribution of central galaxies (e.g. left panel of Figure 3.26) leads to an overestimation of mass dispersion of central galaxies. This point partially explain the large error bars in mass direction of Figure 3.28. Furthermore, the error in stellar mass measurement and perhaps low number of clusters in some subsamples increase the dispersion.

There is an obvious halo mass dependence of stellar mass of central galaxies. Figure 3.28 illustrates this dependence. For reference, the relation between the characteristic mass of central galaxies and the cluster total mass derived by Yang, Mo & van den Bosch (2009) is also overplotted.

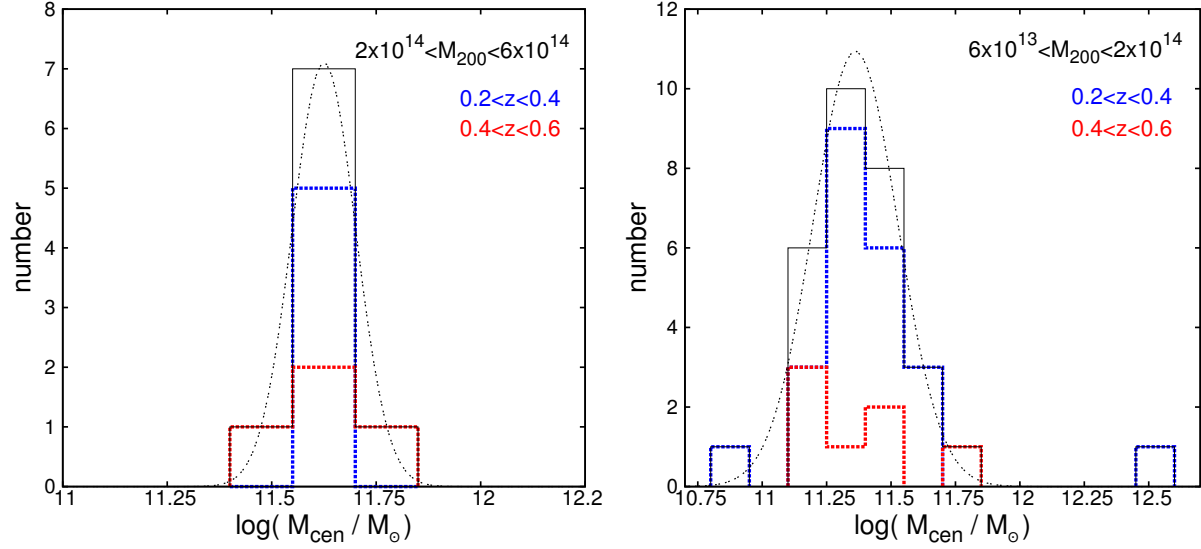


Figure 3.26: Stellar mass distributions for central galaxies of the cluster with the masses of $2 \times 10^{14} < M_{200} < 6 \times 10^{14} M_{\odot}$ (left panel) and $6 \times 10^{13} < M_{200} < 2 \times 10^{14} M_{\odot}$ (right panel) at redshift $0.2 < z < 0.4$ (blue) and $0.4 < z < 0.6$ (red). Black curves show the stacked distribution of higher and lower redshift samples and a dashed lines are Gaussian fits to the stacked distributions.

Table 3.2: Mean and the dispersion of the central galaxies within each bin of mass and redshift derived from Gaussian fitting.

M_{200} range [M_{\odot}]	$0.2 < z < 0.4$	$0.4 < z < 0.6$	$0.6 < z < 0.8$	$0.8 < z < 1.0$
$2 \times 10^{14} - 6 \times 10^{14}$	11.63 ± 0.08	11.63 ± 0.08	-	-
$6 \times 10^{13} - 2 \times 10^{14}$	11.36 ± 0.16	11.36 ± 0.16	-	-
$2 \times 10^{13} - 6 \times 10^{13}$	11.24 ± 0.22	11.20 ± 0.27	11.19 ± 0.27	-
$6 \times 10^{12} - 2 \times 10^{13}$	11.02 ± 0.26	-	-	-

Table 3.3: Mean and the dispersion of the central galaxies within each bin of mass and redshift.

M_{200} range [M_{\odot}]	$0.2 < z < 0.4$	$0.4 < z < 0.6$	$0.6 < z < 0.8$	$0.8 < z < 1.0$
$2 \times 10^{14} - 6 \times 10^{14}$	11.63 ± 0.05	11.60 ± 0.14	-	-
$6 \times 10^{13} - 2 \times 10^{14}$	11.42 ± 0.30	11.36 ± 0.19	-	-
$2 \times 10^{13} - 6 \times 10^{13}$	11.30 ± 0.27	11.28 ± 0.21	11.29 ± 0.19	11.21 ± 0.21
$6 \times 10^{12} - 2 \times 10^{13}$	11.04 ± 0.23	-	-	11.48 ± 0.17

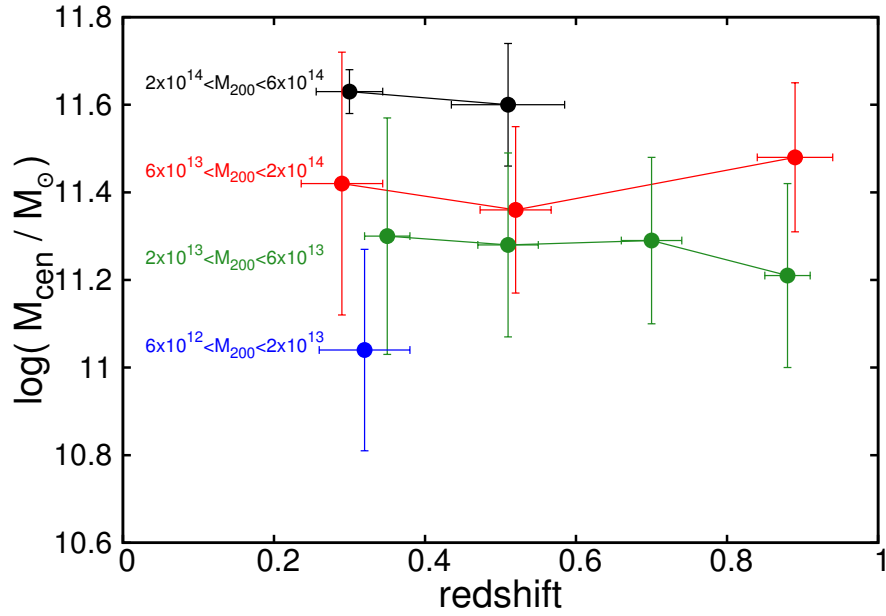


Figure 3.27: Mean central galaxy stellar mass as a function of redshift for different halo masses.

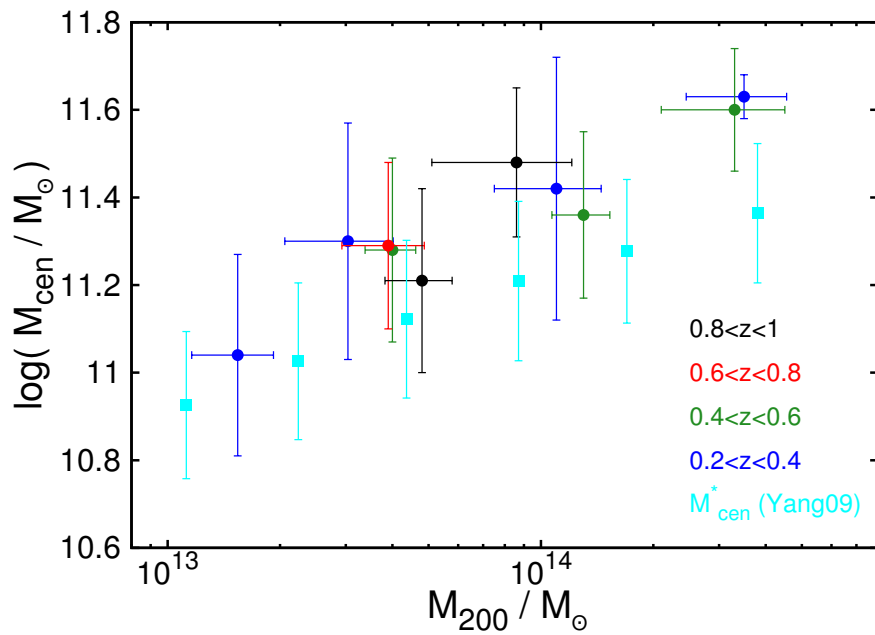


Figure 3.28: Mean central galaxy stellar mass as a function of cluster total mass, M_{200} , for different redshift ranges.

Table 3.4: Parameters of Schechter fitting on mass function of satellite galaxies.

M ₂₀₀ range	redshift range	N _{cluster}	Φ [dex ⁻¹ N _{cluster} ⁻¹]	log(M*) [M _⊙]	α
2×10 ¹⁴ –6×10 ¹⁴	0.2<z<0.4	5	36.36±1.92	10.87±0.03	-1.357±0.008
	0.4<z<0.6	4	69.29±3.53	10.78±0.03	-1.070±0.016
6×10 ¹³ –2×10 ¹⁴	0.2<z<0.4	23	12.88±1.04	10.83±0.04	-1.384±0.011
	0.4<z<0.6	7	49.02±3.38	10.56±0.04	-0.702±0.045
	0.8<z<1.0	9	17.16±1.71	10.56±0.08	0.477±0.311
2×10 ¹³ –6×10 ¹³	0.2<z<0.4	20	3.53±0.88	10.82±0.13	-1.016±0.076
	0.4<z<0.6	11	6.21±1.47	10.81±0.11	-0.793±0.121
	0.6<z<0.8	21	8.98±1.43	10.76±0.08	-0.533±0.141
	0.8<z<1.0	8	10.88±2.07	10.52±0.11	0.663±0.458

3.6.2 Satellite galaxies

The mass functions of satellite galaxies are fitted using Schechter function. The Schechter function is:

$$\phi(M) = \ln(10)\phi^* \left(\frac{10^M}{10^{M^*}}\right)^{\alpha+1} \exp\left(-\frac{10^M}{10^{M^*}}\right) \quad (3.8)$$

where M is the stellar mass of galaxies in the units of M_{\odot} , ϕ^* is the number of galaxies per cluster, M^* is the characteristic mass and α is the slope of low mass end (Schechter, 1976). The best fit results are summarized in Table 3.4. The mass function for each subsample of clusters is derived according to equation 3.7. The mass function and fitted Schechter functions are shown in Figures 3.29 and 3.30. We also plot the mass function related to combination of central and satellite galaxies and a curve presenting the sum of Schechter (for satellite galaxies) and Gaussian (for central galaxies) functions. One should consider that these two functions are fitted separately. For eight groups in the lowest mass bin at $0.2 < z < 0.4$, the numbers of member galaxies at each bin of galaxy mass are very low so we can not fit a Schechter function on it (bottom-left panel in Figure 3.29).

The Figure 3.31 is the characteristics mass of satellite galaxies GSMF as a function of redshift for different ranges of halo mass. Two mass bins show significant evolution in their M_{sat}^* from redshift 0.9 to 0.3 (red and green dots). Although the clusters belong to these two halo mass ranges have similar M_{sat}^* at 0.9 and 0.3 the path of evolution for their M_{sat}^* are different. While the M_{sat}^* in the halos with mass between 2×10^{13} and $6 \times 10^{13} M_{\odot}$ increases between redshift 0.9 to 0.5, at the same redshift M_{sat}^* is almost constant for halos with mass between 6×10^{13} and $2 \times 10^{14} M_{\odot}$. The M_{sat}^* in latter halo mass range increases from redshift 0.5 to 0.3.

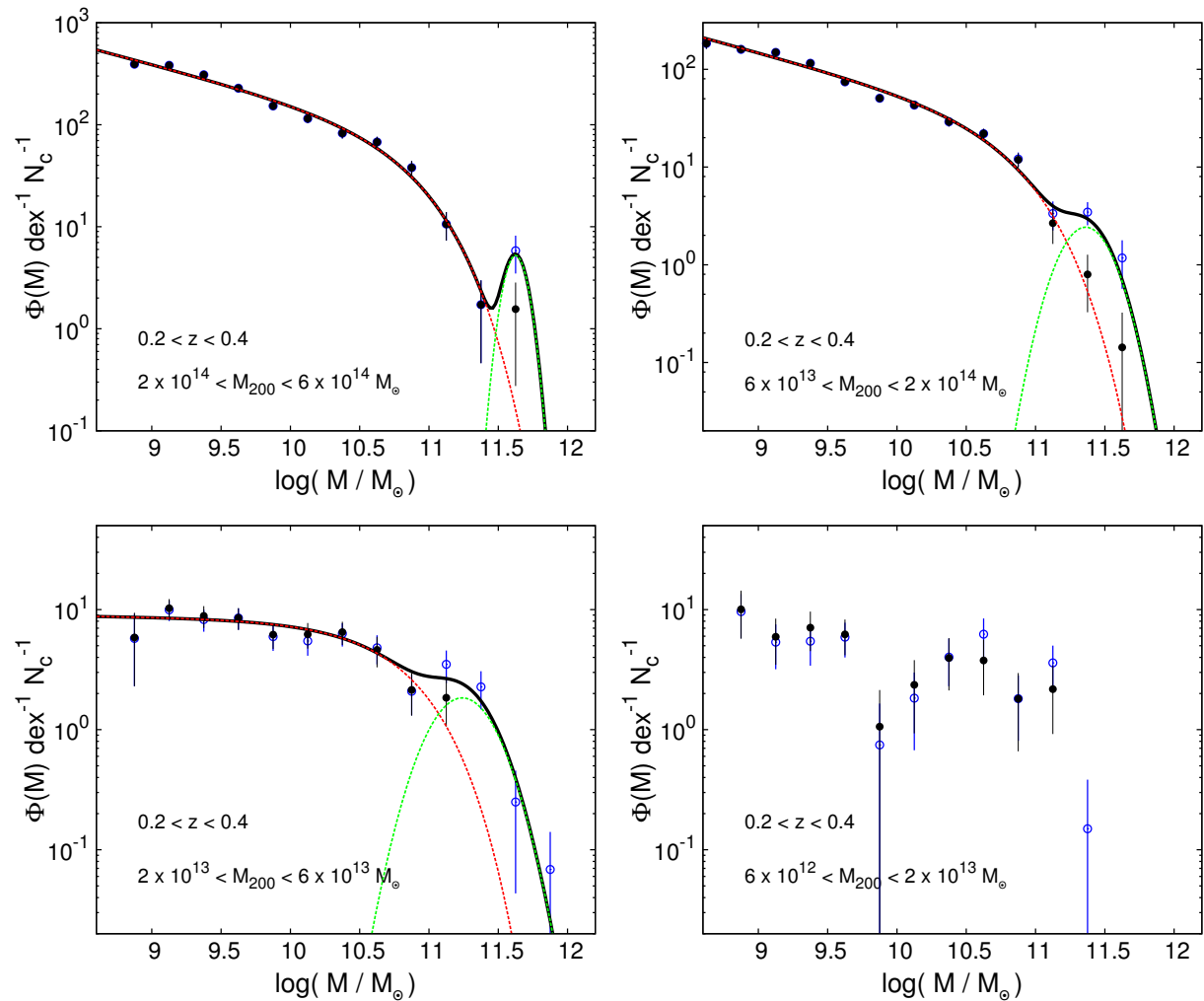


Figure 3.29: Composite GSMF for clusters of different mass and redshift. The black dots are the number of satellite galaxies per each cluster and the blue circles are the combination of satellite and central galaxies. The red dashed line is the fitted Schechter function on mass function of satellites. The green dashed curve represents the Gaussian distribution of central galaxies. The black curve is the sum of Gaussian and Schechter functions. For one of the mass functions (with $0.2 < z < 0.4$ and $6 \times 10^{12} < M_{200} < 2 \times 10^{13} M_{\odot}$) we can not fit a Schechter function because of very low statistics in number of galaxies.

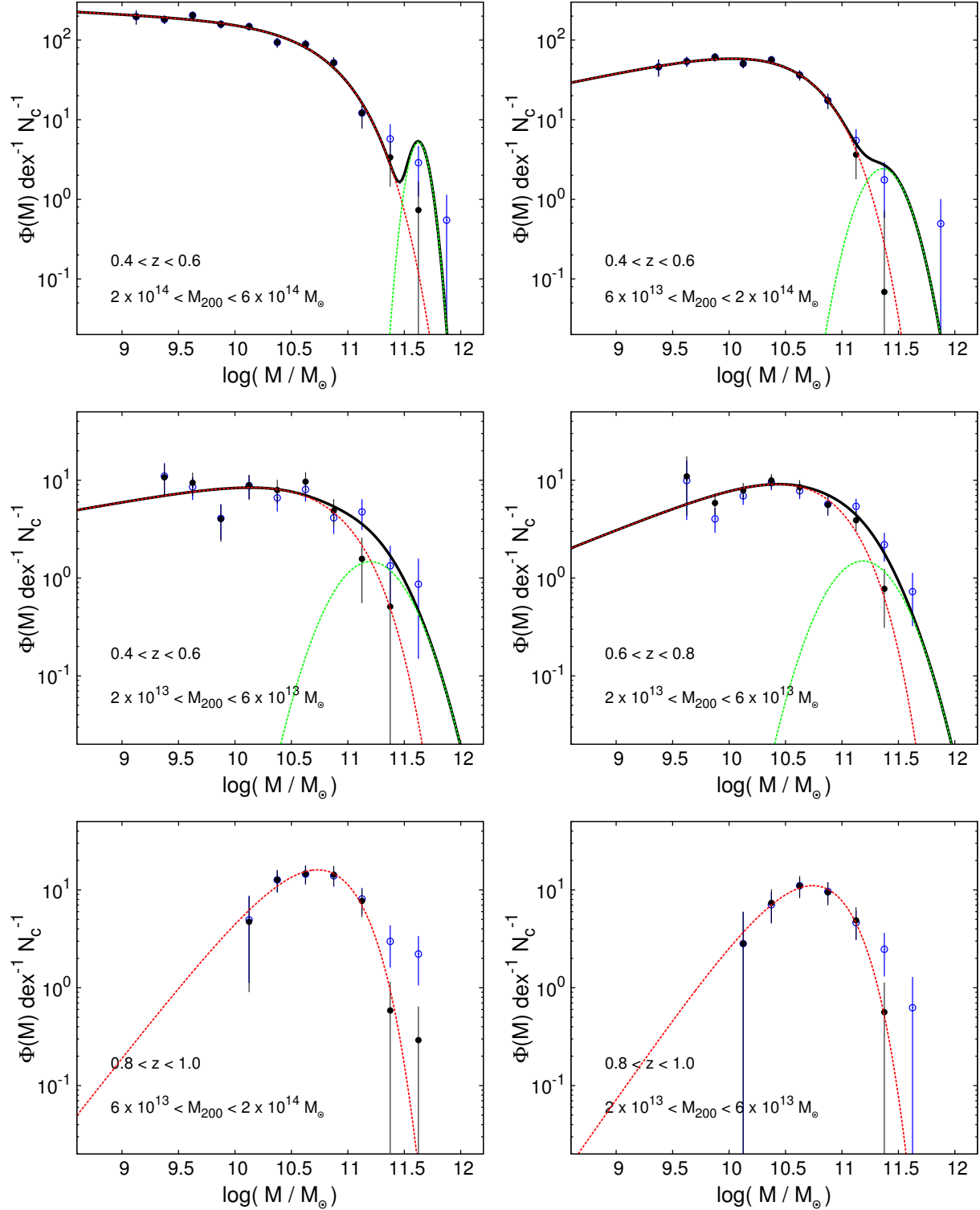


Figure 3.30: Similar to Figure 3.29 for different subsamples.

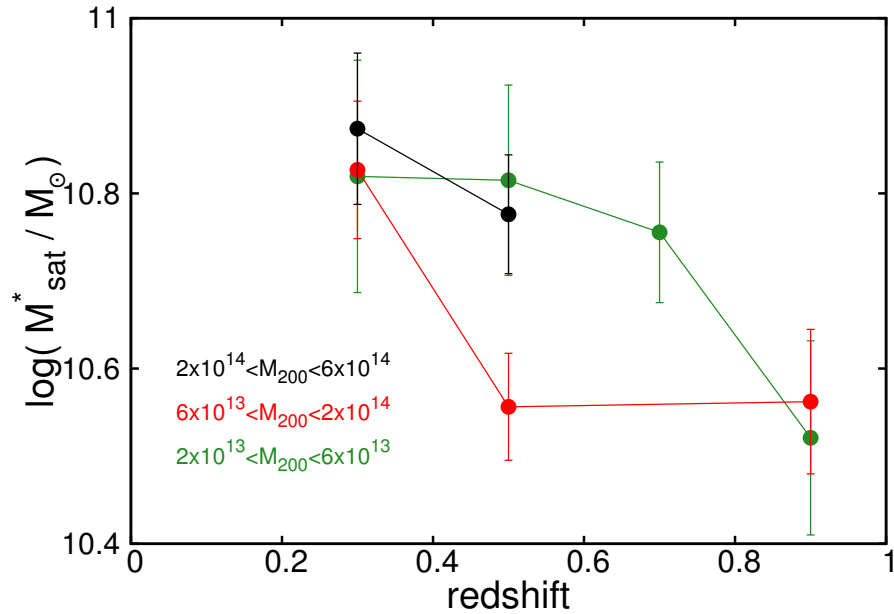


Figure 3.31: Characteristics mass of satellite galaxies as a function of redshift for different halo masses.

3.6.3 GSMF of member galaxies vs field

In this section, we compare the mass function of galaxy clusters with all population of galaxies in the field. The aim is to investigate the contribution of member galaxies of different halo masses to the mass function of all galaxies. First, we should compute the mass function of member galaxies in a way that both mass functions are comparable. In this work, we use field galaxy mass function presented by Ilbert et al. (2010) for different redshifts. Since the mass function of field galaxies is computed as the co-moving volume density of galaxies at each mass bins, in this section, we also define the GSMF as the total number of member galaxies belonging to any halo bin divided by the co-moving volume appropriate for the field.

For this purpose we use our estimate of the the mean GSMF in a given halo mass bin and a redshift bin. We multiply this GSMF by the number of halos in the considered halo mass bin observed in CFHTLS. In this way we can consider also the clusters not included in the sample due to bad photometry. Table 3.5 summarizes the number of halos within a given range of mass and redshift in one square degree area in CFHTLS. This GSMF is, then, divided by the co-moving volume related to one square degree within a given redshift range. Figure 3.32 shows the comparison between the GSMFs of member galaxies and all the population. This figure can be used to understand what is the contribution of galaxies in massive halos to the global GSMF of Ilbert et al. (2010) and to see the evolution, if any, of the mass segregation in massive halos. On average, the larger the mass of the host halo, the lower the contribution of the galaxy members to the global GSMF both at low

Table 3.5: Number of halos within a given mass range at the volume between various redshift ranges. The first column is redshift range. The second column is the co-moving volume of one degree² of sky within the redshift range. The third to sixth column are the number of halos within given mass ranges.

redshift range	volume	$6 \times 10^{12} - 2 \times 10^{13}$	$2 \times 10^{13} - 6 \times 10^{13}$	$6 \times 10^{13} - 2 \times 10^{14}$	$2 \times 10^{14} - 6 \times 10^{14}$
	$10^6 Mpc^3$				
$0.2 < z < 0.4$	0.329	163.79	42.34	10.75	1.40
$0.4 < z < 0.6$	0.734	340.25	81.84	18.46	1.93
$0.6 < z < 0.8$	1.159	487.93	107.75	21.15	1.72
$0.8 < z < 1.0$	1.631	604.17	120.57	20.12	1.22

($0.2 < z < 0.4$) and high redshift ($0.4 < z < 0.6$). At masses below $\sim 10^{11} M_{\text{dot}}$ the density of galaxies in massive halos, both groups and clusters, is more than one order of magnitude lower than the density of the whole galaxy population at low and high redshift. Thus, in this mass range, very low mass halos host the bulk of the galaxy population. However, at masses above the same mass threshold, massive halos provide a substantial contribution to the global GSMF. Groups having total masses in the range $2 - 6 \times 10^{13} M_{\odot}$ provide 40-50% of the massive galaxies. The sum of the group and cluster contribution indicate that massive halos host the bulk of the most massive galaxies of the Universe at low and high redshift. This indicates a substantial mass segregation in the most massive halos. Figure 3.32 also shows that the Gaussian component of the central group and cluster galaxies at masses above $\sim 10^{11.5} M_{\text{dot}}$ is dominating the very high mass end of the global GSMF.

3.7 Conclusion

We compute the stellar mass for galaxies in CFHTLS wide field and COSMOS field by applying the SED fitting method. We also accurately characterized the errors in photometric redshifts and stellar mass of galaxies. We use the photometric redshift information to define the galaxy membership of a clean sample of clusters and groups in COSMOS and CFHTLS. We use stellar masses and membership to estimate the GSMF in massive halos. Using a mock catalog and considering also the error in photometric redshift and stellar mass as in the observed galaxy sample, we successfully tested our method for computing the stellar mass function of galaxies. We study separately the GSMF of satellite and central galaxies by fitting the former with a Schechter function and the latter with a Gaussian. We analyze the redshift evolution of the characteristic and mean mass, respectively, of satellite and central galaxies in several host halo mass ranges.

Our results show that the characteristic mass of satellite galaxies in groups and clusters is independent on the host halo mass. In addition, it increases by 0.25-0.3 dex from redshift 0.9 to 0.3. This mass growth can be caused either by star-formation or by merger

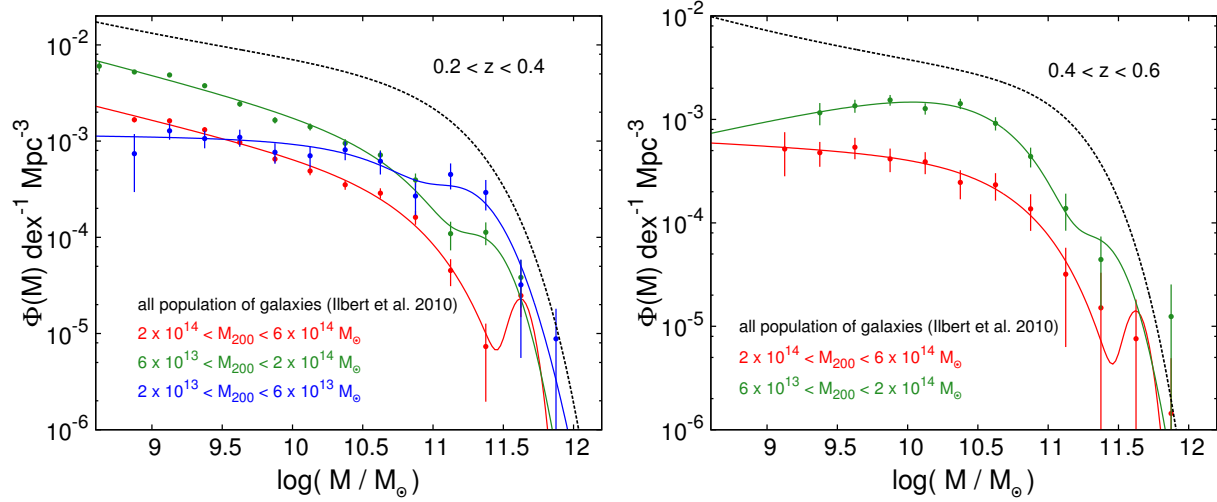


Figure 3.32: Comparison between the GSMF of field galaxies and member galaxies. The left and right panels respectively belong to redshift ranges of $0.2 < z < 0.4$ and $0.4 < z < 0.6$. The dashed lines shows the GSMF of all galaxy populations from Ilbert et al. (2010). The blue, green and red dots show the mass function of member galaxies in galaxy clusters with different halo mass ranges. The solid lines are the combination of Schechter and Gaussian functions fitted to mass distribution of satellite and central galaxies.

and accretion. Interestingly enough, Erfanianfar et al. (in prep) derive the average star-formation rate of galaxies with stellar mass above $10^{10} M_{\odot}$ in a sample of X-ray selected groups. They show that means of star-formation are 2.94, 6.16, 12.16, and $12.55 M_{\odot} yr^{-1}$ respectively for redshifts of 0.3, 0.5, 0.7, and 0.9. Figure 3.33 is similar to Figure 3.31 but overplotted by assumed characteristics mass of satellite galaxies with star-formation history of Erfanianfar et al. We suppose a $\log M_{sat}^* = 10.55$ and evolve it according to mentioned star formation history. The orange curve shows the evolution of stellar mass for such a galaxy. The consistency between the mass evolution of satellite galaxies and their mass growth caused by star-formation is impressive. This would suggest that star formation is the main mechanism for satellite galaxies to accrete their mass.

Differently from satellite galaxies, the mass of central galaxies is correlated with host halo mass. We do not find any redshift evolution in relation between the mean central galaxy stellar mass and the host halo mass. This indicates that that the mass growth of central galaxy is controlled by hierarchical mass growth of the host halo. Thus, in contrast to satellite galaxies, likely merger events play a more important role in mass accretion history of central galaxies with respect to the star formation activity.

We finally compare the GSMF in the massive halos with the global population GSMF. We show that although a low fraction of low mass galaxies reside in group and clusters, almost all massive galaxies with masses above $10^{11} M_{\odot}$ are in group and clusters. The density of cluster galaxies with stellar masses above $10^{11.5} M_{\odot}$, which is described by Gaussian component, is comparable to the density of galaxies with similar mass in the field. This

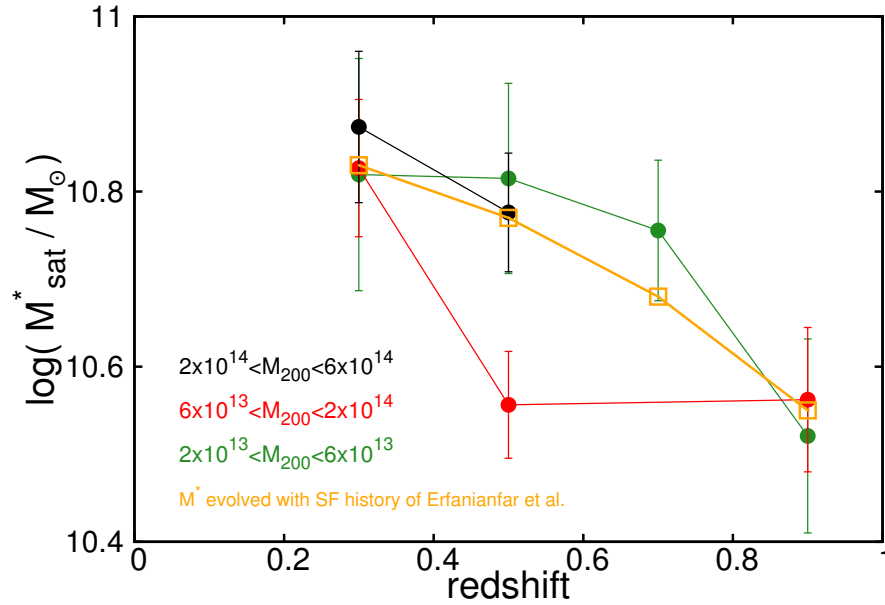


Figure 3.33: Characteristics mass of satellite galaxies as a function of redshift for different halo masses. The orange curve shows an assumed galaxy with $\log M = 10.55$ at redshift 0.9 that evolve according to satellite galaxies star-formation history from Erfanianfar et al (in prep.).

means that strong mass segregation in massive halos is mostly caused by central galaxies.

Chapter 4

Morphological properties of galaxies in an X-ray detected group at redshift $z = 1.6$

This chapter is a part of a published paper (Tanaka et al. 2013: “An X-ray Detected Group of Quiescent Early-type Galaxies at $z = 1.6$ in the Chandra Deep Field South“, PASJ, 65, 17). In this paper, we studied the member galaxies in an X-ray selected group at redshift $z = 1.6$ and showed that a high fraction of member galaxies are similar to local Universe early-type galaxies in terms of their color, star formation rate and morphology. My contribution to this paper is the morphological study of member galaxies. First, the detection of the group and stellar mass estimation of the group are shortly reported. Then the procedure of morphological classification is explained in details.

4.1 Introduction

In recent years, a significant amount of studies indicated the influence of environment on the evolution of galaxies. For instance, the existence of higher fraction of early-type galaxies in groups and clusters in comparison to field population in local universe is widely accepted (the so-called morphology-density relation Dressler 1980; Davis & Geller 1976). Moreover, the local dichotomy between early-type and late-type galaxy populations, in terms of color, star formation rate and morphology, occurred at earlier epochs for member galaxies in groups and clusters. This rapidity in evolution is more severe for galaxies with higher stellar mass (Cooper et al. 2007; Wilman et al. 2009; Iovino et al. 2010; Wilman & Erwin 2012). Besides of time of evolution, the path of evolution for field and group galaxies is also different. For instance, galaxy morphology transformation, which happens at redshifts below 1, leads to a transient “red spirals” population but this population is not observed in the field (Balogh et al. 2009; Wolf et al. 2009; Mei et al. 2012). However, the details of processes that are playing a role in interaction between surrounding structure and hosted galaxy is not clear yet. Studying the galaxy population properties of groups

and clusters at wide range of redshift can answer the questions of how and when a host large structure can change the evolution of a galaxy.

Finding groups and clusters at high redshifts became feasible with modern instruments in recent years. In the following, we mention some of high redshift X-ray cluster discoveries in recent years and galaxy population studies on their member galaxies. Mullis et al. (2005) identified an X-ray luminous cluster at redshift 1.39. Lidman et al. (2008) reported a tight red sequence for this cluster. Other studies also reported low star formation rate in the core of this cluster (Bauer et al. 2011). Stanford et al. (2006) discovered another X-ray luminous cluster at redshift 1.45 using XMM observation. While this cluster also has a significant red sequence, in contrast to the cluster discovered by Mullis et al. (2005), a high number of emission-line objects reside in its core (Hayashi et al. 2010). In last years, discoveries of clusters at redshift above 1.5 are also reported. Two groups of researchers independently identified a $z=1.62$ cluster in Subaru/XMM-Newton Deep Field (SXDF) (Papovich et al. 2010; Tanaka, Finoguenov & Ueda 2010). After 2010, several X-ray groups were discovered at redshift ~ 1.5 as results of XMM-Newton Deep Cluster Project (Fassbender et al. 2011; Nastasi et al. 2011; Santos et al. 2011). At higher redshift, Stanford et al. (2012) found a massive $z=1.75$ X-ray selected cluster.

In order to provide a clear picture of galaxy evolution in groups and clusters, we provided a sample of X-ray selected in COSMOS, CFHT Deep Fields, AEGIS (All-Wavelength Extended Groth Strip International Survey), CDFS (Chandra Deep Field South), CDFN (Chandra Deep Field North) and SXDF (Subaru-XMM deep field) fields (Finoguenov et al. 2007, 2010; Bielby et al. 2010; Erfanianfar et al. 2013). During group identification in CDFS, a group at redshift 1.6 was discovered. Previously, Kurk et al. (2009) found a large structure at $z=1.6$ in this field and this group is the first X-ray detected gravitationally bound system in this structure. Fortunately, this group is located in the CANDELS (Cosmic Assembly Near-infrared Deep Extragalactic Legacy Survey) where high quality deep imaging data of HST (Hubble Space Telescope) are available. In this work, we study the galaxy population of the member galaxies in this group.

4.2 Data

All the data used in this work are from public data sets. In this section we describe X-ray, optical and IR data.

4.2.1 Chandra and XMM-Newton X-ray data

The Chandra observation time in CDFS were extended from 1 Ms to 4 Ms during several observations between 2002 to 2011 (Giacconi et al. 2002; Luo et al. 2008; Rafferty et al. 2011; Xue et al. 2011). This field was also observed by XMM-Newton X-ray telescope with 1Ms exposure time. In the Chandra analysis, the light curve events were filtered by *LC_CLEAN* tool for removing flares counts. According to prescription of Hickox and Markevitch (2006) the background model maps were provided. We estimate the particle

background by using the ACIS stowed position1 observations, and rescale them by the ratio $(\text{counts}_{9.5-12\text{keV};\text{data}})/(\text{counts}_{9.5-12\text{keV};\text{stowed}})$. The cosmic background flux is evaluated by subtracting the particle background maps from the real data, and masking the area occupied by the detected sources.

For the XMM-Newton analysis, we follow the prescription outlined in Finoguenov et al. (2007) on data screening and background evaluation, with updates described in Bielby et al. (2010). After cleaning those observations, the resulting net total observing time with XMM-Newton are 1.946 Ms for pn, 2.552 Ms for MOS1, 2.530 Ms for MOS2. We carefully remove point sources following Finoguenov et al. (2009) and Finoguenov et al. (2010). This is done independently from the Chandra data to allow for AGN variability and difference in the astrometry. Furthermore, we do not detect individual sources and catalog them, but instead we directly work with images. This is important for XMM-Newton because it is confusion limited at the depths of CDFS (in the soft band) and the source deblending is not trivial.

4.2.2 Optical and IR Data

Optical and IR data are from public data sets of MUSIC (Grazian et al. 2006; Santini et al. 2009) and CANDELS (Grogin et al. 2011; Koekemoer et al. 2011). The MUSIC catalog includes 15 bands data from u to $24\ \mu\text{m}$. In this catalog, the objects were detected in HST-ACS z -band and then the photometry was done in other bands. After masking out the z -band detected, the detection was repeated in Ks and IRAC $4.6\ \mu\text{m}$ bands. We also used three bands of CANDELS public data set observed by $F814W$, $F125W$, and $F160W$ of ACS and WFC3. For simplicity, $F814W$, $F125W$, and $F160W$ are respectively denoted as I , J , and H , in what follows. The stacked images of I , J , and H respectively have the limiting magnitudes of 28.3, 27.3, and 27.0 within an aperture of size $4 \times \text{FWHM}$. The detection in $F160W$ and photometry in other bands are done by Source Extractor (Bertin & Arnouts 1996).

In this work, we use the photometric redshift catalogs of Rafferty et al. (2011) and Cardamone et al. (2010). Rafferty et al. (2011) computed the photometric redshift using photo- z code ZEBRA Feldmann et al. (2006). To provide the input photometry catalog, Rafferty et al. (2011) merged the photometric catalogs in the literature (Wolf et al. 2004; Gawiser et al. 2006; Grazian et al. 2006; Wolf et al. 2008; Nonino et al. 2009; Taylor et al. 2009; Damen et al. 2011). Comparison with spectroscopic redshift shows that Rafferty et al. (2011) reach to the $\sigma_{dz/(1+z)} = 0.03$ for objects with $R < 24$ and $\sigma_{dz/(1+z)} = 0.2$ for fainter objects. Cardamone et al. (2010) used a BVR -selected catalog so their catalog is not suitable for faint and high redshift sources. Therefore we do not use the later catalog for primary selection of member galaxies. Besides of two mentioned photo- z catalogs, we also apply SED fitting method for estimation of physical properties of galaxies so we derive a redshift catalog for the galaxies.

4.3 X-ray selected group catalog in CDFS and a group at $z=1.6$

Point sources are removed from coadded XMM and Chandra images mosaic (Finoguenov et al. (2009)). Then extended sources are detected by a wavelet transform technique. Similar to Bielby et al. (2010) and Finoguenov et al. (2010), the optical counterparts are identified by red sequence technique. Using Rafferty et al. (2011) photo- z catalog, part of background and foreground galaxies are removed during applying the red sequence method. All of the public spectroscopic redshifts in CDFS (Cristiani et al. 2000; Croom et al. 2001; Strolger et al. 2004; Szokoly et al. 2004; van der Wel et al. 2004; Doherty et al. 2005; Le Fèvre et al. 2005; Mignoli et al. 2005; Ravikumar et al. 2007; Vanzella et al. 2008; Popesso et al. 2009; Balestra et al. 2010; Cooper et al. 2012) are also used for assigning the spectroscopic redshift to the systems. Finally, 47 systems are identified and among them 39 group have spectroscopic confirmation. The details of the group identification is presented in Finoguenov et al. (in prep.).

During identification of galaxy groups, a group candidate at redshift 1.6 was discovered. Figure 4.1 illustrates the colorful image of the this group with X-ray flux contours. The red sequence indicates a remarkable signal at this redshift. Figure 4.2 shows the color-magnitude diagrams for this group. For member, foreground, and background galaxies according to photometric and spectroscopic redshifts are labeled with different signs. Three dotted lines are the color-magnitude models based on three different formation redshift of 2, 3, and 5. Three member galaxies are also X-ray point sources. The galaxies A and C have secure spectroscopic redshifts of 1.610 and 1.625 respectively. The galaxy B has a tentative spectroscopic redshift of 1.605.

Given the redshift of 1.61 for this group, we derive the X-ray properties of the this group. We estimated the mass using Leauthaud et al. (2010) calibration between the X-ray luminosity and weak lensing mass,

$$\frac{M_{200}E(z)}{M_0} = A \left(\frac{L_X E(z)^{-1}}{L_{X,0}} \right)^\alpha, \quad (4.1)$$

where $L_{X,0} = 10^{42.7}$ erg s⁻¹ and $M_0 = 10^{13.7} M_\odot$ are characteristic X-ray luminosity and mass of the relation, $E(z) = \sqrt{(1+z)^3 \Omega_M + \Omega_\Lambda}$, $\log(A) = 0.03 \pm 0.06$, $\alpha = 0.64 \pm 0.03$. The computed mass of group using this scaling relation is $M_{200} = (3.2 \pm 0.8) \times 10^{13} M_\odot$. The uncertainty on mass include the error in X-ray flux measurement, and the scatter in $M_{200} - L_X$ relation. The Leauthaud et al. (2010) scaling relation is calibrated for $z < 1$ but there is no available calibration for higher redshift. Assuming this mass for the group, this group is the lowest confirmed system at $z > 1.5$.

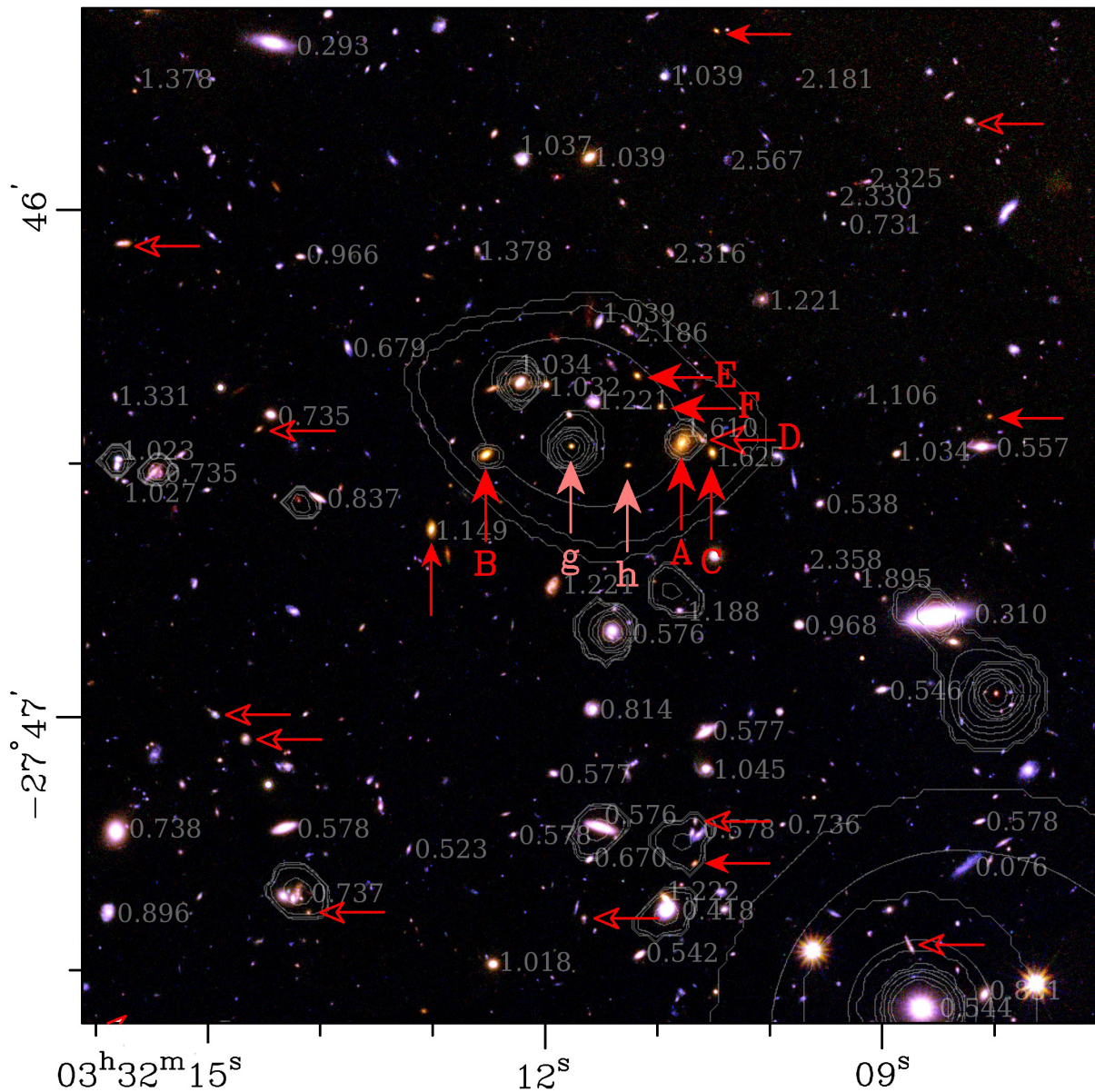


Figure 4.1: RGB image of $z=1.6$ galaxy group. The I , J , and H band images are respectively used as blue, green and red colors. The white contours shows different levels of X-ray flux. The spectroscopic redshifts are also mentioned. The arrows point to member galaxies candidates according to photometric redshift. The filled arrows belong to galaxies on the red sequence. Member galaxy candidates in the core of group (within r_{200c}) are labeled from A to F according to their luminosities.

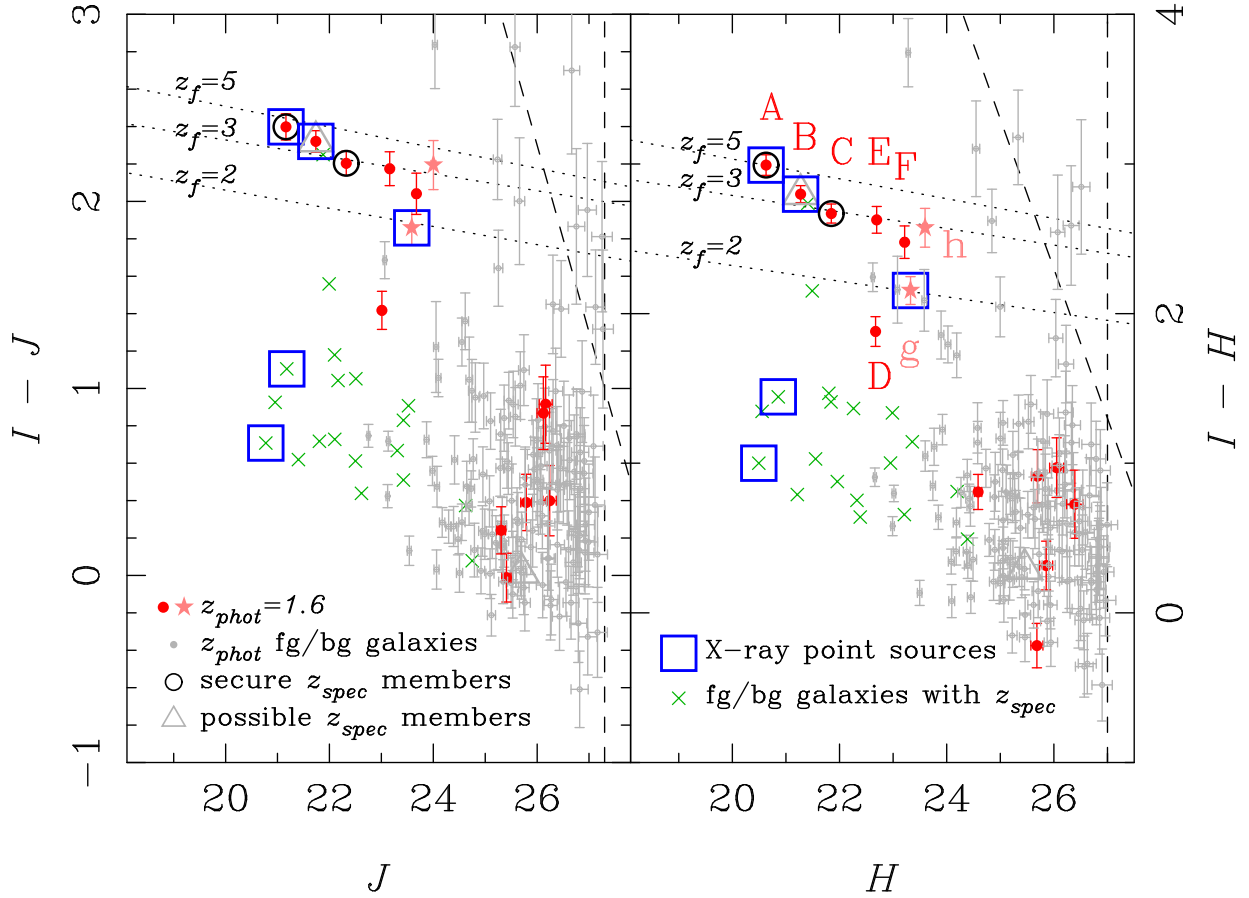


Figure 4.2: Color-magnitude diagrams using CANDELS I , J , and H bands. This plot is limited to all galaxies within projected distance of r_{200c} from the X-ray centre. The red and pink symbols are members and likely members according to photometric redshifts respectively. Grey and greens are background and foreground galaxies according to photometric and spectroscopic redshifts. The black circles and grey triangles show secure and possible spectroscopic members, respectively. The blue squares are the object that are X-ray point sources. The dotted lines indicate red sequence models with different redshift of formation.

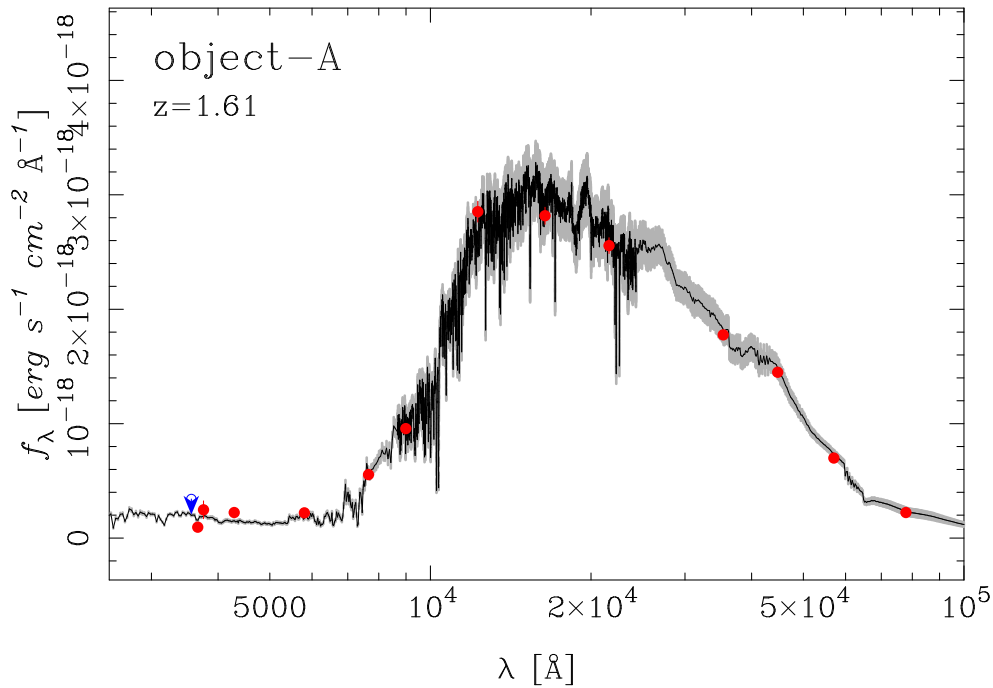


Figure 4.3: Best-fitted model and the photometry of object-A (BGG). The black curve is the best model SED and the shaded area is the uncertainty in the SED. The red dots are the flux in each band and a blue point with arrow indicates the upper limit on a flux.

4.4 Properties of member galaxies

In this section, first, we shortly describe the methods of deriving the stellar mass of member galaxies. Then we explain the morphological study on the member galaxies in details. Finally, we will compare the group member galaxies at $z = 1.6$ with member galaxies at local universe.

4.4.1 Stellar mass of member galaxies

The stellar mass of member galaxies are estimated using SED fitting method. The observed broad band photometry of MUSIC catalog (Santini et al. 2009) is fitted by SED templates generated by Bruzual & Charlot (2003) code. The Chabrier initial mass function (Chabrier 2003) and solar metallicity are assumed. Calzetti et al. (2000) extinction law applied to the templates. The observed broad bands of u_{VIMOS} , u_{38} , u_{50} , B , V , R , I , z , J , H , K_s , $3.5\mu m$, $4.6\mu m$, $5.7\mu m$, $8.0\mu m$ are used during standard χ^2 minimizing technique. The redshift of galaxies with spectroscopic redshift fixed to their spectroscopic redshifts (objects A and C). Figure 4.3 illustrates the flux of observed bands and the fitting model on them. Object g is significantly contaminated by AGN point source light and the fitting method fail to derive a reliable result. The estimated stellar masses are listed in Table 4.1.

Table 4.1: Results of SED fitting on the member galaxies photometry. The column *photoz* is the photometric redshift derived from SED fitting method. The redshift of object A and C are fixed their spectroscopic redshift. $M_{stellar}$ column is the stellar mass of member galaxies in the unit of $10^{10}M_{\odot}$. Because of huge AGN contamination in photometry of object g the fitting method can not derive a reliable result.

ID	χ_{ν}	<i>photoz</i>	$M_{stellar}$ [$10^{10}M_{\odot}$]
object-A	1.6	$z_{spec} = 1.61$	$31.6^{+0.1}_{-13.9}$
object-B	0.3	$1.64^{+0.06}_{-0.09}$	$7.9^{+1.1}_{-0.1}$
object-C	0.6	$z_{spec} = 1.62$	$4.5^{+0.1}_{-0.1}$
object-D	0.7	$1.59^{+0.26}_{-0.10}$	$1.4^{+1.2}_{-0.4}$
object-E	0.2	$1.56^{+0.07}_{-0.09}$	$1.8^{+1.1}_{-0.6}$
object-F	0.4	$1.64^{+0.12}_{-0.13}$	$1.3^{+0.6}_{-0.4}$
object-g	2.5	$1.57^{+0.23}_{-0.25}$	—
object-h	0.3	$1.61^{+0.11}_{-0.10}$	$0.6^{+0.4}_{-0.2}$

4.4.2 Morphology of member galaxies

Surface brightness distribution of galaxies is a robust tool for understanding the properties and classification of galaxies. The earliest works on studying the surface brightness profiles were done by Reynolds (1913) and Hubble (1930). They fitted the brightness profile of galaxies with a number parameters including characteristic radius, characteristic surface brightness and few other ones for the shape of profile. de Vaucouleurs (1948) profile has been widely used in the literature. In this profile, the surface brightness of a galaxy declines proportional to $r^{1/4}$ where r is the distance from the centre. A generalized version of de Vaucouleurs profile, Sérsic profile (Sérsic 1963; Sérsic & Pastoriza 1967), is the most common for describing the light profile of galaxies:

$$I(r) = A \exp\left[-\left(\frac{r}{r_e}\right)^{1/n}\right], \quad (4.2)$$

where $I(r)$ is the surface luminosity at distance r from the centre, r_e is the radius that encloses half of the light of galaxy (half-light radius or effective radius), and n is Sérsic index. The dwarf elliptical have n between 1 and 2 while ellipticals with intermediate luminosity have n value between 2 and 4. For giant elliptical the n can reach to the values above 4 (Caon, Capaccioli & D’Onofrio 1993; Graham et al. 1996; Graham & Guzmán 2003; Hoyos et al. 2011).

For morphological analysis, we use GALFIT (Peng et al. 2002, 2010) to measure the structural parameters of the group galaxies. GALFIT performs two-dimensional surface brightness fitting of a galaxy using an input image, a bad pixel map, a PSF image, and a noise image. The WFC3 F160W image from CANDELS, which probes the rest frame r-band at $z = 1.6$, is used as an input image of the group. Figure 4.4 displays part of CANDELS F160W (H band) image which includes the group. The mosaic pixel scale of this is 0.06 arcseconds. We use a nearby unsaturated star for the PSF image (Figure 4.5).

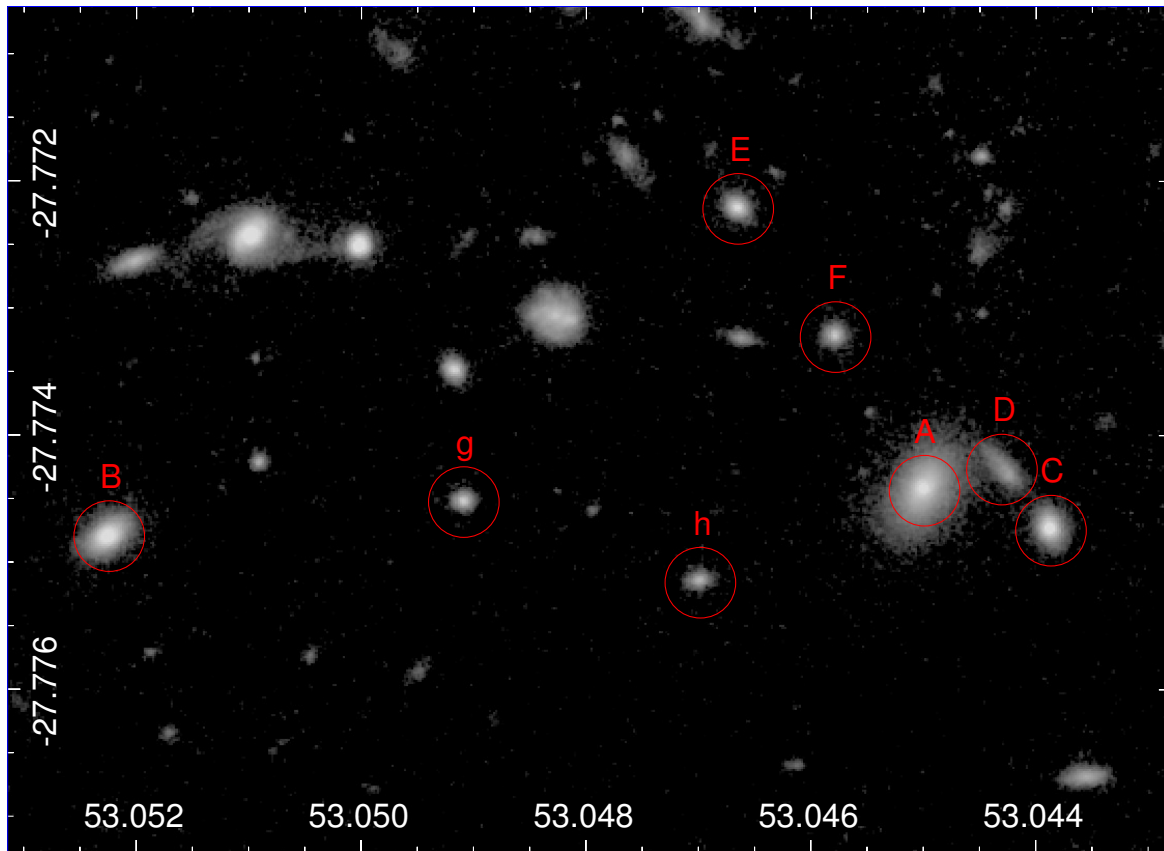


Figure 4.4: Group image in WFC3 F160W band. The member galaxies are marked by red circles. The radius of red circles are 1 arcsecond which corresponds to 8.5 Kpc at $z = 1.6$.

The FWHM (full width at half maximum) of the image is ~ 0.18 arcseconds which is equal to 3 pixels.

The noise image is generated from the weight map (Koekemoer et al. 2011). We fit the galaxies with a single Sérsic profile. Due to the fact that a galaxy group is crowded with galaxies by definition, one must decide how to determine the boundary of the galaxy of interest, and how to exclude the neighboring objects light from a fit. We attempt to solve these problems by defining elliptical regions around the galaxy of interest and neighboring objects to specify their boundaries. The elliptical regions are determined using the Source Extractor (Bertin & Arnouts 1996). After some experiments, we find that 6 and 2.5 times of the half-light radius are respectively optimum for the galaxy and neighboring objects. A larger radius for the object of interest is necessary, since it must contain not only light from the outskirts of the galaxy, but also the sky background. All of the initial values for the fitting parameters (position of galaxy center, integrated magnitude, half-light radius, axis ratio, position angle, Sérsic parameter) are set to those derived by Source Extractor,

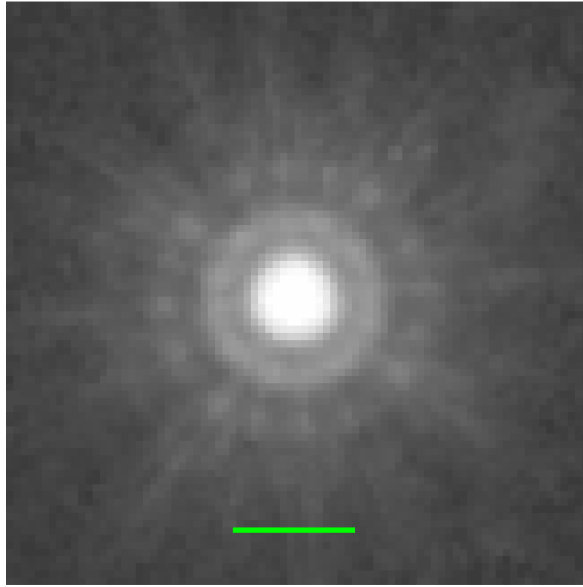


Figure 4.5: Image of an unsaturated star used as a PSF image. A green bar shows 1 arcsec.

except for the last parameter.

The initial Sérsic index is set to 2, which is a boundary of early and late-type galaxies, so that we do not bias our fits. Figures 4.6 and 4.7 show the input image, best-fit model image, residuals, and mask image for the good and likely candidates, respectively. The fits are generally good, and the residuals are relatively small for most objects. This verifies that the assumption of a single Sérsic profile is reasonable. We fail to fit object-D due to its irregular morphology and to its close proximity to the BGG.

Here we focus on two of the most important structural parameters; Sérsic index (n) and half-light radius. We quote half-light radius as $r_{50} \equiv \sqrt{ab}$, where a and b are half-light radius measured along the semi-major and semi-minor axes, respectively. We estimate an error on each of the Sérsic index and half-light radius by Monte-Carlo simulations. First, we generate the same background level as in the real H -band data assuming Gaussian noise and place a model galaxy with a given brightness, effective radius and Sérsic index. We then run GALFIT and measure the structural parameters. We allow the brightness, effective radius, and Sérsic index to vary and repeat the analysis above. A difference between the input and output parameters is fairly small (a few percent) for bright objects with $H < 22$ mag. For fainter objects, the systematic offset and dispersion increases to 5% and 10% respectively for objects with $H = 23$ mag. This is roughly the average brightness of the objects that we study in this section. For objects with $H = 24$, we measure a 10% systematics and a 20% scatter. We note that all of the objects studied here are brighter than $H = 24$.

We then perform another set of simulation. We generate background noise of the same

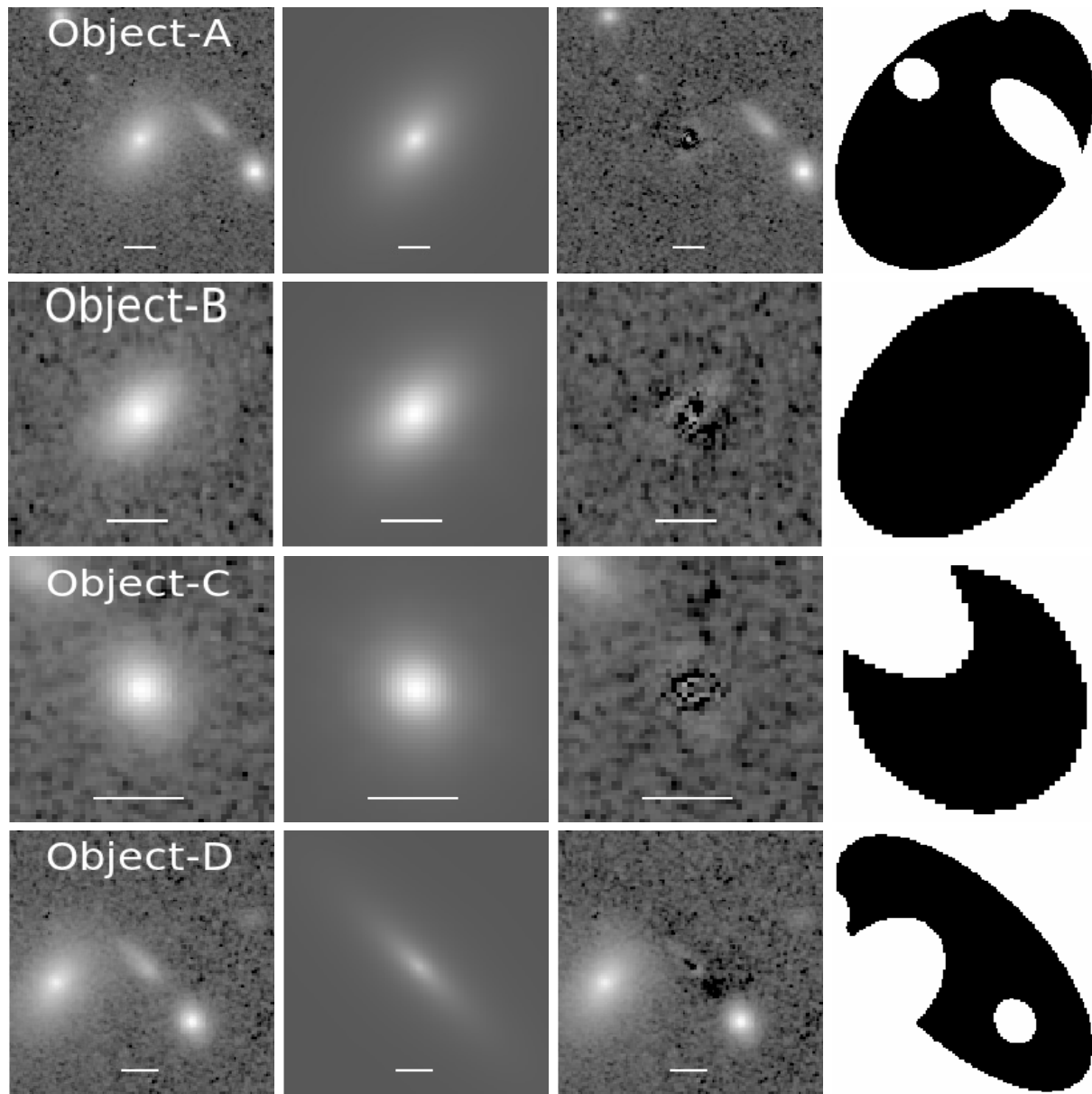


Figure 4.6: In each plot, the panels show the input image, model galaxy, residual, and mask images from left to right. The plots are for object-A to D from top to bottom, respectively. The horizontal bar in each panel is 1 arcsec, which corresponds to 8.5 kpc (physical) at $z = 1.6$.

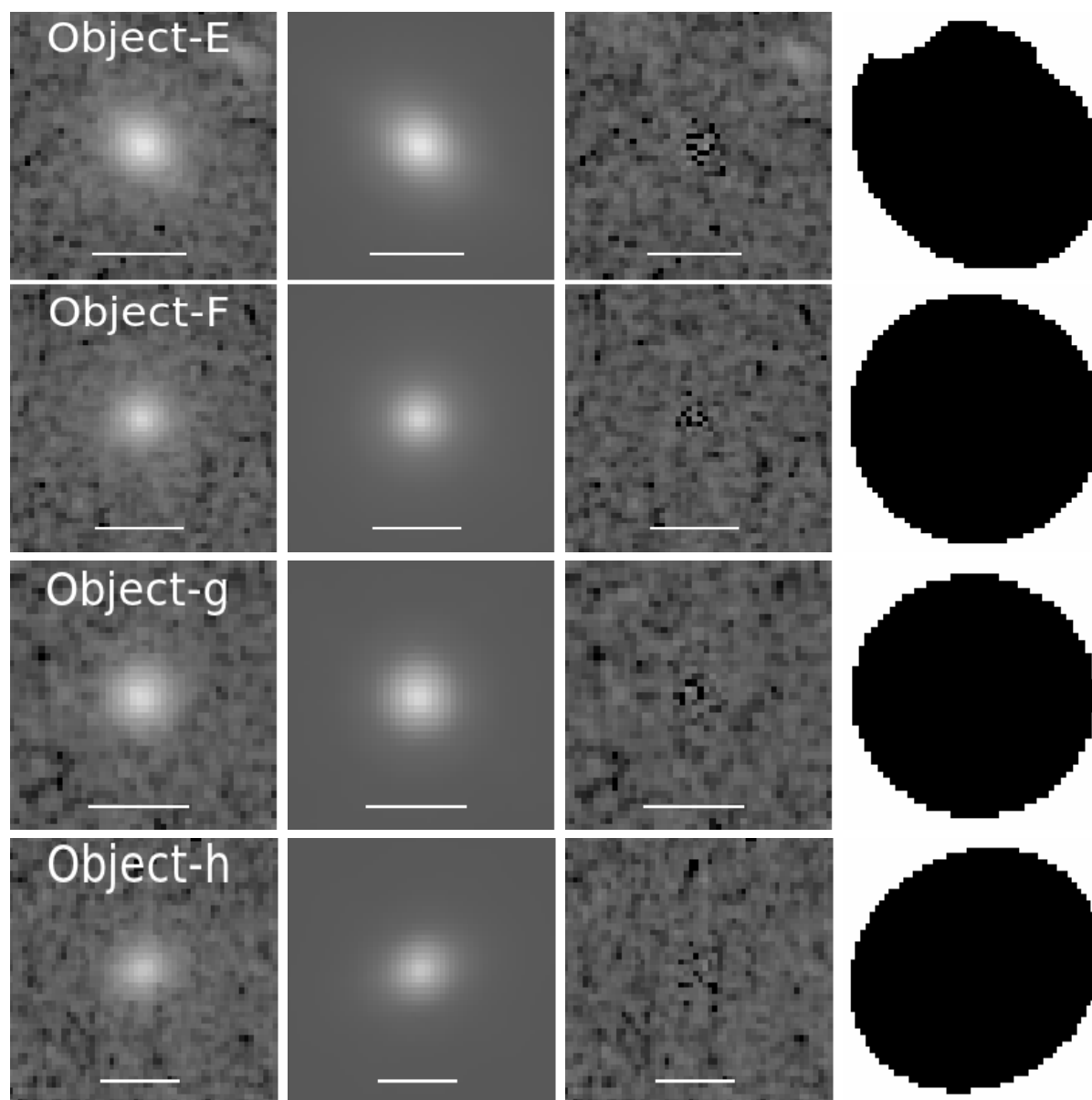


Figure 4.7: As in Figure 4.6 but for object-E to h.



Figure 4.8: Simulated image of the group in WFC3 F160W band. Structural parameters such as Sérsic and r_{50} are fixed to the values derived by fitting procedure. The background is also simulated at the same level as in the real H -band data assuming Gaussian noise.

level as in the real data assuming Gaussian noise and place the group members at the same relative location with the same Sérsic indices and half-light radii as the values measured in the CANDELS image for each galaxy. We exclude object-D because we fail to fit this object and therefore cannot use the fitted parameters for the simulation. We then run GALFIT on a simulated image and store the output parameters. We repeat this procedure on 2000 simulated images and adopt the 68% interval of the output parameters as errors. In the figures, we show this error or the error estimated in the first simulation, whichever is larger. In most cases, the latter error is larger. For systematic offsets, we find that the input parameters and the median of the output parameters agree within 10% for all the galaxies. This is consistent with the systematic offsets estimated in the first simulation and this 10% is a reasonable estimate of the systematics.

As shown in Fig. 4.1, there are a few X-ray point sources among the group member candidates. This X-ray emission is likely due to nuclear activity. To make sure, the presence of AGN does not impact our analysis, we repeat the GALFIT analysis with the central 3

Table 4.2: Structural properties of galaxies. The numbers in the brackets are obtained by applying a circular mask of 3 pixel radius at the center (i.e., $\sim 2 \times \text{FWHM}$ region is masked) to avoid contamination of central point sources. Note that object-D is too close to the BGG and we fail to fit the object. Note as well that the uncertainties quoted here are statistical uncertainties. We expect $\sim 10\%$ systematics on all the parameters.

hline ID	Sérsic index	half-light radius (kpc)	axial ratio
object-A	$2.75^{+0.05}_{-0.01}$ ($2.07^{+0.06}_{-0.01}$)	$8.75^{+0.20}_{-0.04}$ ($7.69^{+0.14}_{-0.03}$)	$0.60^{+0.01}_{-0.01}$ ($0.60^{+0.01}_{-0.01}$)
object-B	$1.93^{+0.04}_{-0.01}$ ($1.52^{+0.06}_{-0.01}$)	$2.60^{+0.03}_{-0.01}$ ($2.66^{+0.03}_{-0.01}$)	$0.58^{+0.01}_{-0.01}$ ($0.58^{+0.01}_{-0.01}$)
object-C	$3.42^{+0.18}_{-0.04}$	$1.42^{+0.05}_{-0.01}$	$0.67^{+0.02}_{-0.01}$
object-D	3.43	21.82	0.28
object-E	$2.99^{+0.29}_{-0.06}$	$1.36^{+0.07}_{-0.01}$	$0.66^{+0.03}_{-0.01}$
object-F	$5.27^{+1.21}_{-0.23}$	$1.53^{+0.37}_{-0.05}$	$0.94^{+0.06}_{-0.01}$
object-g	$2.26^{+0.38}_{-0.07}$ ($1.27^{+0.77}_{-0.12}$)	$0.83^{+0.05}_{-0.01}$ ($1.09^{+0.22}_{-0.05}$)	$0.82^{+0.06}_{-0.01}$ ($0.84^{+0.07}_{-0.01}$)
object-h	$2.27^{+0.47}_{-0.07}$	$1.59^{+0.14}_{-0.03}$	$0.48^{+0.05}_{-0.01}$

pixels in radius masked out. The derived structural parameters are summarized in Table 4.2. We also show axial ratios (b/a) for reference. Note that the structural parameters derived with the central masking do not differ significantly from those derived without it.

4.4.3 Structural properties

Let us now compare the structural parameters of the group galaxies with those measured at $z = 0$ to quantify the morphological evolution. For this comparison, we use data from the Sloan Digital Sky Survey (York et al., 2000). We use galaxies in the Main sample (Strauss et al., 2002) located at $0.05 < z < 0.07$. The F160W filter of WFC3 probes rest-frame $\sim 6000\text{\AA}$ at $z = 1.6$, which is very close to the effective wavelength of the r -band filter in SDSS (Doi et al., 2010). Therefore, the morphological k -correction is negligible. The PSF of the stacked F160W image is 0.2 arcsec, which corresponds to 1.7 kpc at $z = 1.6$. The average seeing in SDSS is 1.5 arcsec, which is also 1.7 kpc at the median redshift of our SDSS sample. The surface brightness limit is much deeper for SDSS than for the $z = 1.6$ galaxies. But, we have performed a Monte-Carlo simulation to quantify uncertainties on our structural parameter estimates at $z = 1.6$ as described above and the shallow limit at $z = 1.6$ is folded into the uncertainty. For the Sérsic index and half-light radius of $z = 0$ galaxies, we use the New-York University Value Added Catalog (Blanton et al., 2005c). The stellar mass for the SDSS sample is taken from Tanaka (2012) who fitted the SDSS spectra with Bruzual & Charlot (2003) model templates assuming the Chabrier IMF. Note that a correction for the fiber loss is applied in a crude way by assuming that the light within a fiber is representative of the light from the entire galaxy.

Fig 4.9 presents the Sérsic index, n , and half-light radius plotted against stellar mass. As can be seen in the left panel, most of the $z = 0$ galaxies have Sérsic index between 1

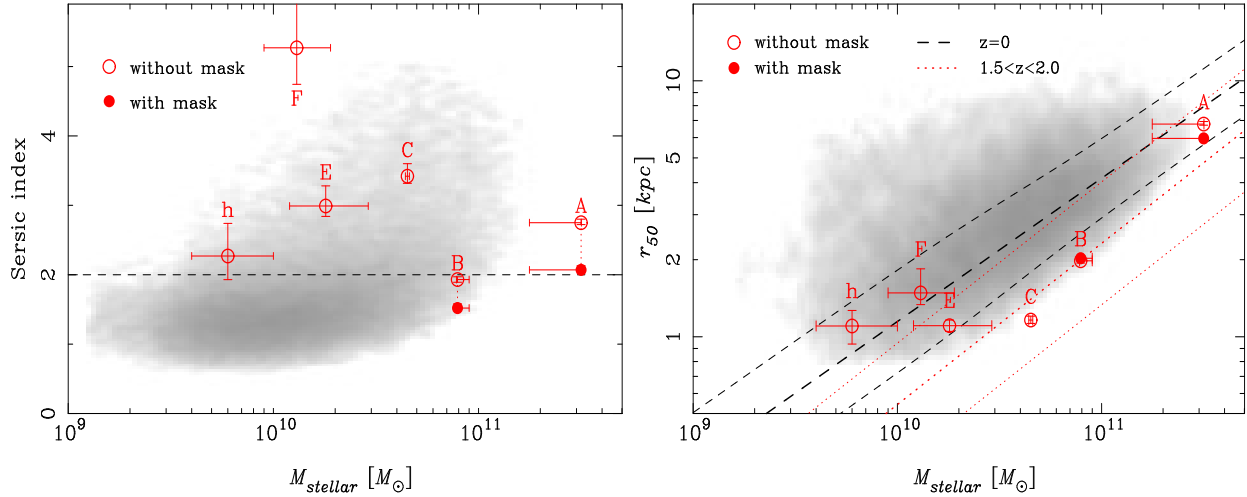


Figure 4.9: **Left:** Sérsic index plotted against stellar mass. The gray scales are galaxies at $0.05 < z < 0.07$ from SDSS. For clarity, only 95% of the galaxies are plotted. The large symbols are the $z = 1.6$ galaxies and the associated error bars show the statistical uncertainty. We recall that we have a $\sim 10\%$ systematic uncertainty on the structural parameters. Object-A and B likely host AGNs and we show the Sérsic index measured both with and without the central mask. Object-g is a moderately strong AGN and is not plotted here because no reliable stellar mass estimate is available, while Object-D is not plotted because we fail to find an adequate fit to this object. The horizontal dashed line shows the rough separation between early-type and late-type galaxies. **Right:** Half-light radius plotted against stellar mass. As in the left panel, the gray scales are for $z = 0$ galaxies, but here we show only early-type galaxies with $n > 2$. The thick dashed line is the size-mass relation of early-type galaxies at $z = 0$ from Shen et al. (2003) and the thin dashed lines show 1σ scatter. The thick dotted line is for $1.5 < z < 2.0$ quiescent early-type galaxies from Newman et al. (2012) and the thin dotted lines show a 1σ scatter in the relation.

and 2. This is the typical range for late-type galaxies. The index shows a tail towards a larger index at high mass, which shows that most massive galaxies tend to be early-type galaxies. We separate early and late-type galaxies at the Sérsic index of $n = 2$ as shown by the horizontal dashed line in the left panel. If we turn our attention to the $z = 1.6$ galaxies shown as the large circles in the left panel, we find that most of them have $n > 2$. In other words, most of the galaxies in the $z = 1.6$ group are early-type galaxies. We know that groups and clusters at $z = 0$ are dominated by early-type galaxies (Dressler, 1980; Postman & Geller, 1984), but it is surprising that a group at such a high redshift is also dominated by early-type galaxies. We have shown in the previous section that these galaxies are mostly quiescent galaxies. Therefore, the group appears fairly similar to groups and clusters in the local universe.

In addition to the Sérsic index, another interesting structural parameter of galaxies is their physical size. The size evolution is particularly interesting given the recent ob-

servations that distant quiescent galaxies are compact compared to $z = 0$ counterparts (e.g., Daddi et al. (2005); Trujillo et al. (2006); Toft et al. (2007)). It would therefore be interesting to study whether the size evolution depends on environment. Rettura et al. (2010) studied a cluster at $z = 1.24$ and suggested that the cluster and field galaxies at the same redshift have similar sizes. The newly confirmed group is one of the highest redshift systems discovered so far where high quality WFC3 images are available, allowing us to investigate galaxy sizes in the group.

We show half-light radius, r_{50} , against stellar mass in the right panel of Fig. 4.9. As a $z = 0$ reference, we show the size-mass distribution of local early-type ($n > 2$) galaxies as well as a size-mass relation of the local early-type galaxies from Shen et al. (2003). We note that Shen et al. (2003) measured sizes in the z -band, while we use the r -band. Therefore, care needs to be taken when comparing these two samples. We also note that the resolution limit of the F160W image is $r_{50} \sim 0.5$ kpc and thus all the $z = 1.6$ galaxies plotted are well resolved. The Figure also shows the size-mass relation for quiescent galaxies from Newman et al. (2012). Their quiescent galaxies typically have early-type morphology with $n \sim 3 - 4$ and their result is directly comparable to ours. They did not characterize the environment of the galaxies. However, most of the galaxies in their sample are likely field galaxies and we refer to their sample as a field sample.

The BGG is within the scatter of the local and $1.5 < z < 2.0$ size-mass relations and it appears that the BGG in the $z = 1.6$ group already has a similar size to local massive galaxies. The low-mass galaxies with $\sim 10^{10} M_{\odot}$ are also consistent with both relations. Only object-B and C are clearly below the local relation, and they are consistent with the $1.5 < z < 2.0$ field relation. Overall, the size-mass relation of the group galaxies seems to fall in between the $1.5 < z < 2.0$ and $z = 0$ relations. Papovich et al. (2012) claimed that galaxies in another $z = 1.6$ group in SXDF exhibit smaller sizes at fixed stellar mass compared to the local galaxies, but they are larger than field galaxies at the same redshift. Our result in Fig. 4.9 may be consistent with their finding. Zirm, Toft & Tanaka (2012) reported on a similar trend in a $z = 2.16$ proto-cluster. However, the statistics in all these studies, including this paper, are not sufficient to allow a clear conclusion.

Lotz et al. (2011) reported on an elevated merger/interaction rate in the $z = 1.62$ system in SXDF. Only one of the 8 group member candidates (object-D) shows a highly distorted morphology and all the other galaxies have well-defined early-type morphologies. We also do not observe a strong elevated rate of nearby companions (see Fig. 4.6). We may tend to miss interacting galaxies due to possibly poor photo- z 's for such objects. To be sure, we visually inspect all the bright galaxies with $H < 24$ located within r_{200} without using photo- z 's. Fore-/background galaxies with secure spec- z 's are excluded from this exercise. We find 3 clear cases for disturbed morphology in addition to object-D. We have carefully examined the SEDs of the 3 objects and find that only one of them is marginally consistent with being at the group redshift. The other SEDs look normal and they are likely at $z \sim 3$. Although the statistics are very poor, it is unlikely that a large fraction of the group galaxies are undergoing interaction. The possible different trend between the two systems might be due to their different dynamical states. That is, the newly confirmed $z = 1.61$ group in this paper is a more relaxed system than the one in SXDF. If the X-ray

emission around object-A is partly due to a cool core, it lends support a relaxed system with no recent merger events. It would then not be a surprise that few group members are undergoing interactions with other galaxies. On the other hand, the group in SXDF shows a somewhat irregular distribution of the members and it potentially has a companion group (but see also the shallow Chandra observations by Pierre et al. (2012)). The possibly different dynamical states could explain the different merger/interaction rates in these two groups at the same redshift.

Finally, we briefly mention the ellipticity of the $z = 1.6$ galaxies. As shown in Table 4.2, most of them have an axis ratio of $b/a \sim 0.6$. By excluding object-D, which we fail to fit, we measure an average axis ratio of 0.68 with a scatter of $\sigma = 0.14$. This axis ratio is consistent with field galaxies at similar redshifts ($\langle b/a \rangle = 0.66$; Newman et al. (2012)). Holden et al. (2009) found that cluster early-type galaxies have the median axis ratio of 0.70 and this does not strongly evolve at $z < 1$. Our finding here may extend the result by Holden et al. (2009) to a redshift of $z = 1.6$, although the cluster mass ranges explored are very different (our group has a much lower mass than those studied by Holden et al. (2009)).

To summarize, we find that most of the galaxies in the $z = 1.6$ group are early-type galaxies with Sérsic index $n > 2$. There are a few galaxies that have smaller physical sizes than their local counterparts, but the overall size-mass relation of the group galaxies does not seem to be significantly different from the local relation. In all of these aspects, the group is strikingly similar to local groups and clusters and the environmental dependence of galaxy properties is clearly in place by $z = 1.6$.

4.4.4 Summary and conclusion

We have discovered an X-ray selected galaxy group at $z = 1.6$ in CDFS. The redshift of the group is determined by three spectroscopic counterparts. We have also shown that the member galaxies form a red sequence corresponding to redshift of 1.6. We calculated the mass of $M_{200} = (3.2 \pm 0.8) \times 10^{13} M_{\odot}$ for the group using the scaling relation between weak lensing mass and X-ray luminosity. Thus, this group is the lowest mass system discovered at redshifts above 1.5.

We studied the properties of member galaxies by estimating the stellar mass and morphological inspection. For estimation of stellar mass of galaxies, we applied the SED fitting method using templates of SEDs. The structural parameters of member galaxies were also calculated for morphological studies. We derived the Sérsic index, r_{50} , and ellipticity of galaxies by fitting Sérsic function on surface brightness profile of the galaxies in H band of CANDELS data. By a set of Monte-Carlo simulation, we also quantified the uncertainties in measurement of structural parameters.

We showed that the member galaxies in this group (except one) have Sérsic index similar to the ones of early-type galaxies in the local universe. They also are located in between of $z = 0$ and $1.5 < z < 2.0$ mass-size relations for early-type galaxies. This indicates that in terms of morphology, the member galaxies of the group are similar to early-type galaxies in the local universe.

We conclude that the group is already dominated by early-type red galaxies at $z = 1.6$. The only possible difference between this group and local groups and clusters consists in a higher fraction of AGN activities since three out of eight member galaxies are X-ray point sources. A simple interpretation of our results is that environmental process or processes, which lead to type transformation of member galaxies in this group, operated before redshift 1.6.

Chapter 5

Conclusion

In this chapter, I summarize the conclusion of all previous chapters. I categorize the results according to their technical and scientific importance.

5.1 Technical results

5.1.1 Red sequence technique

I describe a multi-color red sequence finder and calibrate it for CFHTLS $u^*g'r'i'z'$ filters for the redshift below 1.1. The color evolution model of red sequence galaxies is derived from a large sample of early-type galaxies (up to redshift 0.8). The intrinsic dispersion of red sequence is also modeled by few stellar population models with different metallicities. I show that the derived intrinsic dispersion using metallicities of 1 and 0.75 of solar is large enough to enclose the red galaxies and increasing the width by a factor of 50% does not change the integrated luminosity of galaxies on the red sequence.

I explore a single color and a multi color selection of red sequence galaxies and show that the multi color selection of red galaxies decreases the scatter in the relation between X-ray luminosity and the integrated luminosity of the cluster in z -band. This point is very important for mass estimation of clusters without X-ray or SZ data.

This set of optical methods for cluster finding are particularly useful for providing large samples of X-ray luminous (or massive) clusters (especially for cosmological studies) using shallow X-ray data and wide optical surveys. First, by applying the red sequence finder, we can extract a pure sample of clusters out of a list of X-ray sources. Second, by measuring the optical luminosity of clusters within an appropriate fixed radius we can estimate the cluster total mass, allowing an efficient separation of high X-ray luminous (high-mass) clusters for further studies.

5.1.2 Computing the stellar mass and the stellar mass error

I compute the stellar mass for ~ 5 million galaxies in three fields of CFHTLS using the SED fitting method. The redshift of each galaxy is fixed to the photometric value, unless a

spectroscopic redshift is available. I accurately characterize the photometric redshift error as a function of magnitude of galaxies.

For the very first time, the error in the compute stellar mass is precisely estimate as a function of redshift and magnitude. The total error in the stellar mass is computed by considering the errors induced by lack of near-infrared data, errors in photometry, errors in photometric redshift and internal error in SED fitting method. The uncertainty caused by lack of NIR data and photometric error is calculated by a comparison with stellar mass derived from a deep field of CFHTLS with additional *JHK* bands. I model the stellar mass error induced by photometric redshift error by comparison with stellar masses computed by spectroscopic redshifts. I also adopt a fixed 0.14 dex error for intrinsic SED method error. The derived stellar mass error map shows the minimum and maximum errors of ~ 0.2 to 0.65 dex for brightest galaxies in low redshift and faintest galaxies at high redshift respectively.

5.1.3 Testing the method of mass function computation on mock catalog

I also successfully test the mass function computation method using a mock catalog with induced errors in mass and redshift. I add the noise to the redshifts and the stellar masses in the mock catalog and show that there is no significant difference between two stellar mass functions derived with and without noise. I also introduce a method for selection of member galaxies via photometric redshift. Following my results on the dependence of the photometric redshift errors on magnitude of galaxies, I change the redshift range for selection of galaxies according to their magnitude – larger redshift range for faint galaxies and smaller range for brighter ones.

5.2 Scientific results

5.2.1 X-ray selected clusters in CFHTLS

Using XMM observations, 196 cluster are discovered in three wide fields of CFHTLS with a 100% identification rate achieved for the high-significance sample. The redshifts of clusters are determined via red sequence method and spectroscopic redshifts. The mass of clusters are computed by a scaling relation between the M_{200} and X-ray luminosity. Out of 81 XMM clusters with spectroscopic redshift, 71 of them have at least two spectroscopic redshift. In comparison to other XMM samples, the XMM clusters are typically of $\sim 10^{14} M_{\odot}$ mass, while e.g. COSMOS X-ray selected groups are of an order of magnitude lower mass. This is a result of shallower observations but covering larger area, characteristic of our program.

I also explore the RASS X-ray sources in CFHTLS and identify 27 clusters. Similar to XMM clusters, the velocity dispersion of the RASS clusters is computed for those one with at least 5 spectroscopic members.

5.2.2 Scaling relations

I explore a correlation of integrated optical luminosity and X-ray luminosity. I show that multi-color red sequence reduces the scatter in the relation down to 0.22 dex in X-ray luminosity. This set of optical methods for cluster finding are particularly useful for providing large samples of X-ray luminous (or massive) clusters (especially for cosmological studies) using shallow X-ray data and wide optical surveys. Using this scaling relation, I compute the X-ray luminosity for 27 RASS clusters with shallow X-ray data.

I also calculate the velocity dispersions with an iterative gapper method and derive the scaling relation between velocity dispersion and X-ray luminosity of clusters.

5.2.3 GSMF of X-ray selected clusters

We use the clean cluster sample created on the basis of the multi-color space red sequence finder, in addition to the X-ray detected group sample of Finoguenov et al. (2007); George et al. (2011) of the COSMOS field, to analyse the galaxy stellar mass function (GSMF) as a function of the host halo mass. We show that the characteristic mass of satellite galaxies in groups and clusters is independent of the host halo mass. In addition, it increases by a factor of 0.25-0.3 dex from redshift 0.9 to 0.3. We also show that there is an impressive consistency between the mass evolution of satellite galaxies and their mass growth caused by star-formation history. This would indicate that star formation is the main mechanism for satellite galaxies to accrete their mass. In contrast, the mass of central galaxies is correlated with host halo mass. We do not find any redshift evolution in relation between the mean central galaxy stellar mass and the host halo mass. This suggests that the mass growth of central galaxy is controlled by hierarchical mass growth of the host halo. Thus, in contrast to satellite galaxies, likely merger events play the main role in mass accretion history of central galaxies with respect to the star formation activity. We finally compare the GSMF in the massive halos with the global population GSMF. Although a low fraction of low mass galaxies reside in group and clusters, almost all massive galaxies with masses above $10^{11}M_{\odot}$ are in groups and clusters. The density of cluster galaxies with stellar masses above $10^{11.5}M_{\odot}$, which is described by Gaussian component, is comparable to the density of galaxies with similar mass in the field. This means that strong mass segregation in massive halos is mostly caused by central galaxies.

5.2.4 Morphology of group galaxies at redshift 1.6

We discover an X-ray selected galaxy group at $z = 1.6$ in CDFS. The redshift of the group is determined by three spectroscopic counterparts. We also show that the member galaxies form a red sequence corresponding to a redshift of 1.6. We calculate the mass of $M_{200} = (3.2 \pm 0.8) \times 10^{13}M_{\odot}$ for the group using the scaling relation between weak lensing mass and X-ray luminosity. Thus, this group is the lowest mass system discovered at redshifts above 1.5.

We study the properties of member galaxies by estimating the stellar mass and morphological inspection. For estimation of stellar mass of galaxies, we apply the SED fitting method using templates of SEDs. The structural parameters of member galaxies are also calculated for morphological studies. We derive the Sérsic index, r_{50} , and ellipticity of galaxies by fitting Sérsic function on the surface brightness profile of the galaxies in H band of CANDELS data. By a set of Monte-Carlo simulation, we also quantify the uncertainties in measurement of structural parameters.

We show that the most member galaxies of this group (except one) have Sérsic index similar to the ones of early-type galaxies in the local universe. They are also located in between of $z = 0$ and $1.5 < z < 2.0$ mass-size relations for early-type galaxies. This indicates that in terms of morphology, the member galaxies of the group are similar to early-type galaxies in the local universe.

We conclude that this group is already dominated by early-type red galaxies at $z = 1.6$. The only possible difference between this group and local groups and clusters consists in a higher fraction of AGN activities since three out of eight member galaxies are X-ray point sources. A simple interpretation of our results is that environmental process or processes, which lead to type transformation of member galaxies in this group, operated before redshift 1.6.

Bibliography

- Aihara H. et al., 2011, ApJS, 193, 29
- Akritas M. G., Bershadsky M. A., 1996, ApJ, 470, 706
- Alimi J.-M., Füzfa A., Boucher V., Rasera Y., Courtin J., Corasaniti P.-S., 2010, MNRAS, 401, 775
- Allen S. W., Evrard A. E., Mantz A. B., 2011, ARA&A, 49, 409
- Allevato V. et al., 2012, ApJ, 758, 47
- Allington-Smith J. R., Ellis R., Zirbel E. L., Oemler, Jr. A., 1993, ApJ, 404, 521
- Anderhalden D., Diemand J., 2013, J. Cosmol. Astropat. Phys., 4, 9
- Andreon S., 2012, A&A, 548, A83
- Annis J. et al., 1999, in Bulletin of the American Astronomical Society, Vol. 31, American Astronomical Society Meeting Abstracts, p. 1391
- Arnouts S. et al., 2002, MNRAS, 329, 355
- Arnouts S. et al., 2007, A&A, 476, 137
- Baldry I. K., Glazebrook K., Driver S. P., 2008, MNRAS, 388, 945
- Balestra I. et al., 2010, A&A, 512, A12
- Ball N. M., Loveday J., Brunner R. J., 2008, MNRAS, 383, 907
- Balogh M. L. et al., 2009, MNRAS, 398, 754
- Balogh M. L. et al., 2011, MNRAS, 412, 2303
- Bamford S. P., Rojas A. L., Nichol R. C., Miller C. J., Wasserman L., Genovese C. R., Freeman P. E., 2008, MNRAS, 391, 607
- Bardeen J. M., Bond J. R., Kaiser N., Szalay A. S., 1986, ApJ, 304, 15

- Bardeen J. M., Steinhardt P. J., Turner M. S., 1983, *Phys. Rev. D*, 28, 679
- Bauer A. E., Grützbauch R., Jørgensen I., Varela J., Bergmann M., 2011, *MNRAS*, 411, 2009
- Bauer F. E. et al., 2002, *AJ*, 123, 1163
- Baum W. A., 1959, *PASP*, 71, 106
- Beers T. C., Flynn K., Gebhardt K., 1990, *AJ*, 100, 32
- Bertin E., Arnouts S., 1996, *A&AS*, 117, 393
- Bertschinger E., 1998, *ARA&A*, 36, 599
- Bielby R. et al., 2012, *A&A*, 545, A23
- Bielby R. M. et al., 2010, *A&A*, 523, A66
- Blanton M. R., Eisenstein D., Hogg D. W., Schlegel D. J., Brinkmann J., 2005a, *ApJ*, 629, 143
- Blanton M. R., Lupton R. H., Schlegel D. J., Strauss M. A., Brinkmann J., Fukugita M., Loveday J., 2005b, *ApJ*, 631, 208
- Blanton M. R., Moustakas J., 2009, *ARA&A*, 47, 159
- Blanton M. R. et al., 2005c, *AJ*, 129, 2562
- Bond J. R., Efstathiou G., 1984, *ApJ*, 285, L45
- Bond J. R., Kofman L., Pogosyan D., 1996, *Nat*, 380, 603
- Borgani S., Kravtsov A., 2011, *Advanced Science Letters*, 4, 204
- Borgani S. et al., 2001, *ApJ*, 561, 13
- Boselli A., Gavazzi G., 2006, *PASP*, 118, 517
- Bower R. G., Lucey J. R., Ellis R. S., 1992, *MNRAS*, 254, 601
- Brimouille F., Lerchster M., Seitz S., Bender R., Snigula J., 2008, *ArXiv e-prints*
- Bruzual G., Charlot S., 2003, *MNRAS*, 344, 1000
- Butcher H., Oemler, Jr. A., 1978, *ApJ*, 226, 559
- Butcher H., Oemler, Jr. A., 1984, *ApJ*, 285, 426

- Calzetti D., Armus L., Bohlin R. C., Kinney A. L., Koornneef J., Storchi-Bergmann T., 2000, *ApJ*, 533, 682
- Caon N., Capaccioli M., D'Onofrio M., 1993, *MNRAS*, 265, 1013
- Capak P. et al., 2007, *ApJS*, 172, 99
- Capak P. et al., 2008, *VizieR Online Data Catalog*, 2284, 0
- Cappelluti N. et al., 2007, *ApJS*, 172, 341
- Cardamone C. N. et al., 2010, *ApJS*, 189, 270
- Cavaliere A. G., Gursky H., Tucker W. H., 1971, *Nat*, 231, 437
- Chabrier G., 2003, *PASP*, 115, 763
- Christlein D., Zabludoff A. I., 2005, *ApJ*, 621, 201
- Chwolson O., 1924, *Astronomische Nachrichten*, 221, 329
- Colless M., 1989, *MNRAS*, 237, 799
- Connelly J. L. et al., 2012, *ApJ*, 756, 139
- Cool R. J., Howell S. B., Peña M., Adamson A. J., Thompson R. R., 2005, *PASP*, 117, 462
- Cooper M. C. et al., 2012, *MNRAS*, 419, 3018
- Cooper M. C. et al., 2007, *MNRAS*, 376, 1445
- Coupon J. et al., 2009, *A&A*, 500, 981
- Cristiani S. et al., 2000, *A&A*, 359, 489
- Croom S. M., Smith R. J., Boyle B. J., Shanks T., Loaring N. S., Miller L., Lewis I. J., 2001, *MNRAS*, 322, L29
- Cucciati O. et al., 2010, *A&A*, 524, A2
- Cuesta A. J., Prada F., Klypin A., Moles M., 2008, *MNRAS*, 389, 385
- Daddi E. et al., 2005, *ApJ*, 626, 680
- Dalal N., Doré O., Huterer D., Shirokov A., 2008, *Phys. Rev. D*, 77, 123514
- Damen M. et al., 2011, *ApJ*, 727, 1
- Davis M., Efstathiou G., Frenk C. S., White S. D. M., 1985, *ApJ*, 292, 371
- Davis M., Geller M. J., 1976, *ApJ*, 208, 13

- De Lucia G., Blaizot J., 2007, MNRAS, 375, 2
- De Lucia G., Springel V., White S. D. M., Croton D., Kauffmann G., 2006, MNRAS, 366, 499
- de Vaucouleurs G., 1948, Annales d'Astrophysique, 11, 247
- Doherty M., Bunker A. J., Ellis R. S., McCarthy P. J., 2005, MNRAS, 361, 525
- Doi M. et al., 2010, AJ, 139, 1628
- Dolag K., Bykov A. M., Diaferio A., 2008, Space Science Reviews, 134, 311
- Dressler A., 1980, ApJ, 236, 351
- Efron B., 1982, The Jackknife, the Bootstrap and other resampling plans
- Einasto J., Klypin A. A., Saar E., Shandarin S. F., 1984, MNRAS, 206, 529
- Einstein A., 1936, Science, 84, 506
- Eisenstein D. J. et al., 2001, AJ, 122, 2267
- Eisenstein D. J., Hu W., 1999, ApJ, 511, 5
- Elvis M. et al., 2009, ApJS, 184, 158
- Erfanianfar G. et al., 2013, ApJ, 765, 117
- Fabricant D. et al., 2005, PASP, 117, 1411
- Fassbender R. et al., 2011, A&A, 527, L10
- Feldmann R. et al., 2006, MNRAS, 372, 565
- Finoguenov A. et al., 2009, ApJ, 704, 564
- Finoguenov A. et al., 2007, ApJS, 172, 182
- Finoguenov A., Streblyanska A., Hasinger G., Hashimoto Y., Szokoly G., 2005, Advances in Space Research, 36, 710
- Finoguenov A. et al., 2010, MNRAS, 403, 2063
- Forman W., Kellogg E., Gursky H., Tananbaum H., Giacconi R., 1972, ApJ, 178, 309
- Friedmann A., 1922, Zeitschrift fur Physik, 10, 377
- Gawiser E. et al., 2006, ApJS, 162, 1
- George M. R. et al., 2012, ApJ, 757, 2

- George M. R. et al., 2011, ApJ, 742, 125
- Gerke B. F. et al., 2012, ApJ, 751, 50
- Gerke B. F. et al., 2007, MNRAS, 376, 1425
- Giacconi R. et al., 2002, ApJS, 139, 369
- Giodini S. et al., 2012, A&A, 538, A104
- Giodini S. et al., 2009, ApJ, 703, 982
- Gladders M. D., Yee H. K. C., 2000, AJ, 120, 2148
- Gómez P. L. et al., 2003, ApJ, 584, 210
- Goto T., Yamauchi C., Fujita Y., Okamura S., Sekiguchi M., Smail I., Bernardi M., Gomez P. L., 2003, MNRAS, 346, 601
- Gozaliasl G. et al., 2014, A&A, 566, A140
- Graham A., Lauer T. R., Colless M., Postman M., 1996, ApJ, 465, 534
- Graham A. W., Guzmán R., 2003, AJ, 125, 2936
- Grazian A. et al., 2006, A&A, 449, 951
- Grogin N. A. et al., 2011, ApJS, 197, 35
- Gunn J. E., Gott I. J. R., 1972, ApJ, 176, 1
- Guo Q. et al., 2011, MNRAS, 413, 101
- Gursky H., Kellogg E., Murray S., Leong C., Tananbaum H., Giacconi R., 1971, ApJ, 167, L81
- Guth A. H., Pi S.-Y., 1982, Physical Review Letters, 49, 1110
- Hasinger G. et al., 2007, ApJS, 172, 29
- Hayashi M., Kodama T., Koyama Y., Tanaka I., Shimasaku K., Okamura S., 2010, MNRAS, 402, 1980
- Heath D. J., 1977, MNRAS, 179, 351
- Holden B. P. et al., 2009, ApJ, 693, 617
- Hoyle F., Rojas R. R., Vogeley M. S., Brinkmann J., 2005, ApJ, 620, 618
- Hoyos C. et al., 2011, MNRAS, 411, 2439

- Hubble E., Humason M. L., 1931, ApJ, 74, 43
- Hubble E. P., 1930, ApJ, 71, 231
- Huchra J. P., Geller M. J., 1982, ApJ, 257, 423
- Ilbert O. et al., 2006, A&A, 457, 841
- Ilbert O. et al., 2009, ApJ, 690, 1236
- Ilbert O. et al., 2010, ApJ, 709, 644
- Iovino A. et al., 2010, A&A, 509, A40
- Kauffmann G., White S. D. M., Heckman T. M., Ménard B., Brinchmann J., Charlot S., Tremonti C., Brinkmann J., 2004, MNRAS, 353, 713
- Kellogg E., Schreier E., Tananbaum H., Gursky H., Giacconi R., 1972, in Bulletin of the American Astronomical Society, Vol. 4, Bulletin of the American Astronomical Society, p. 336
- Kitzbichler M. G., White S. D. M., 2007, MNRAS, 376, 2
- Knobel C. et al., 2012, ApJ, 753, 121
- Koekemoer A. M. et al., 2011, ApJS, 197, 36
- Koester B. P. et al., 2007, ApJ, 660, 221
- Komatsu E. et al., 2011, ApJS, 192, 18
- Kravtsov A. V., Borgani S., 2012, ARA&A, 50, 353
- Kravtsov A. V., Vikhlinin A., Nagai D., 2006, ApJ, 650, 128
- Kurk J. et al., 2009, A&A, 504, 331
- Lahav O., Lilje P. B., Primack J. R., Rees M. J., 1991, MNRAS, 251, 128
- Lavery R. J., Henry J. P., 1986, ApJ, 304, L5
- Lavery R. J., Henry J. P., 1988, ApJ, 330, 596
- Le Fèvre O. et al., 2005, A&A, 439, 845
- Leauthaud A. et al., 2010, ApJ, 709, 97
- Lewis I. et al., 2002, MNRAS, 334, 673
- Lidman C. et al., 2008, A&A, 489, 981

- Lilly S. J. et al., 2007, *ApJS*, 172, 70
- Lotz J. M., Jonsson P., Cox T. J., Croton D., Primack J. R., Somerville R. S., Stewart K., 2011, *ApJ*, 742, 103
- Luo B. et al., 2008, *ApJS*, 179, 19
- Maraston C., Strömbäck G., Thomas D., Wake D. A., Nichol R. C., 2009, *MNRAS*, 394, L107
- Marchesini D., van Dokkum P. G., Förster Schreiber N. M., Franx M., Labbé I., Wuyts S., 2009, *ApJ*, 701, 1765
- Margoniner V. E., de Carvalho R. R., Gal R. R., Djorgovski S. G., 2001, *ApJ*, 548, L143
- Markevitch M., 2006, in *ESA Special Publication*, Vol. 604, *The X-ray Universe 2005*, Wilson A., ed., p. 723
- Martin D. C. et al., 2005, *ApJ*, 619, L1
- Mathews W. G., Brighenti F., 2003, *ARA&A*, 41, 191
- Meekins J. F., Fritz G., Chubb T. A., Friedman H., 1971, *Nat*, 231, 107
- Mei S. et al., 2012, *ApJ*, 754, 141
- Menanteau F. et al., 2012, *ApJ*, 748, 7
- Mignoli M. et al., 2005, *A&A*, 437, 883
- Miyazaki S., Hamana T., Ellis R. S., Kashikawa N., Massey R. J., Taylor J., Refregier A., 2007, *ApJ*, 669, 714
- Mo H., van den Bosch F. C., White S., 2010, *Galaxy Formation and Evolution*
- Mullis C. R., Rosati P., Lamer G., Böhringer H., Schwobe A., Schuecker P., Fassbender R., 2005, *ApJ*, 623, L85
- Nagai D., Vikhlinin A., Kravtsov A. V., 2007, *ApJ*, 655, 98
- Nastasi A. et al., 2011, *A&A*, 532, L6
- Nelan J. E., Smith R. J., Hudson M. J., Wegner G. A., Lucey J. R., Moore S. A. W., Quinney S. J., Suntzeff N. B., 2005, *ApJ*, 632, 137
- Newman A. B., Ellis R. S., Bundy K., Treu T., 2012, *ApJ*, 746, 162
- Nonino M. et al., 2009, *ApJS*, 183, 244
- Norberg P. et al., 2002, *MNRAS*, 332, 827

- Norman M. L., 2010, ArXiv e-prints
- Pacaud F. et al., 2007, MNRAS, 382, 1289
- Papovich C. et al., 2012, ApJ, 750, 93
- Papovich C. et al., 2010, ApJ, 716, 1503
- Park C., Choi Y.-Y., Vogeley M. S., Gott, III J. R., Blanton M. R., SDSS Collaboration, 2007, ApJ, 658, 898
- Peebles P. J. E., 1980, The large-scale structure of the universe
- Peebles P. J. E., 1982, ApJ, 263, L1
- Peng C. Y., Ho L. C., Impey C. D., Rix H.-W., 2002, AJ, 124, 266
- Peng C. Y., Ho L. C., Impey C. D., Rix H.-W., 2010, AJ, 139, 2097
- Perlmutter S. et al., 1999, ApJ, 517, 565
- Pierre M., Clerc N., Maughan B., Pacaud F., Papovich C., Willmer C. N. A., 2012, A&A, 540, A4
- Piffaretti R., Arnaud M., Pratt G. W., Pointecouteau E., Melin J.-B., 2011, A&A, 534, A109
- Planck Collaboration et al., 2013, ArXiv e-prints
- Planck Collaboration et al., 2011, A&A, 536, A8
- Poggianti B. M. et al., 2006, ApJ, 642, 188
- Polletta M. et al., 2007, ApJ, 663, 81
- Popesso P., Böhringer H., Brinkmann J., Voges W., York D. G., 2004, A&A, 423, 449
- Popesso P., Böhringer H., Romaniello M., Voges W., 2005, A&A, 433, 415
- Popesso P. et al., 2009, A&A, 494, 443
- Postman M., Geller M. J., 1984, ApJ, 281, 95
- Pozzetti L. et al., 2007, A&A, 474, 443
- Prada F., Klypin A. A., Simonneau E., Betancort-Rijo J., Patiri S., Gottlöber S., Sanchez-Conde M. A., 2006, ApJ, 645, 1001

- Predehl P. et al., 2010, in Society of Photo-Optical Instrumentation Engineers (SPIE) Conference Series, Vol. 7732, Society of Photo-Optical Instrumentation Engineers (SPIE) Conference Series
- Prescott M. K. M., Impey C. D., Cool R. J., Scoville N. Z., 2006, *ApJ*, 644, 100
- Press W. H., Davis M., 1982, *ApJ*, 259, 449
- Press W. H., Schechter P., 1974, *ApJ*, 187, 425
- Prevot M. L., Lequeux J., Prevot L., Maurice E., Rocca-Volmerange B., 1984, *A&A*, 132, 389
- Quintero A. D., Berlind A. A., Blanton M., Hogg D. W., 2006, ArXiv Astrophysics e-prints
- Rafferty D. A., Brandt W. N., Alexander D. M., Xue Y. Q., Bauer F. E., Lehmer B. D., Luo B., Papovich C., 2011, *ApJ*, 742, 3
- Rakos K. D., Schombert J. M., 1995, *ApJ*, 439, 47
- Ravikumar C. D. et al., 2007, *A&A*, 465, 1099
- Reichardt C. L. et al., 2013, *ApJ*, 763, 127
- Rettura A. et al., 2010, *ApJ*, 709, 512
- Reynolds J. H., 1913, *MNRAS*, 74, 132
- Riess A. G. et al., 1998, *AJ*, 116, 1009
- Riess A. G. et al., 2011, *ApJ*, 730, 119
- Robertson H. P., 1935, *ApJ*, 82, 284
- Rosati P., Borgani S., Norman C., 2002, *ARA&A*, 40, 539
- Rosati P., della Ceca R., Norman C., Giacconi R., 1998, *ApJ*, 492, L21
- Rozo E., Bartlett J. G., Evrard A. E., Rykoff E. S., 2014, *MNRAS*, 438, 78
- Ruel J. et al., 2013, ArXiv e-prints
- Rykoff E. S. et al., 2012, *ApJ*, 746, 178
- Rykoff E. S. et al., 2013, ArXiv e-prints
- Salvato M. et al., 2009, *ApJ*, 690, 1250
- Sanders D. B. et al., 2007, *ApJS*, 172, 86

- Santini P. et al., 2009, *A&A*, 504, 751
- Santos J. S. et al., 2011, *A&A*, 531, L15
- Schechter P., 1976, *ApJ*, 203, 297
- Schiminovich D. et al., 2007, *ApJS*, 173, 315
- Schneider P., 2006, *Extragalactic Astronomy and Cosmology*
- Sérsic J. L., 1963, *Boletin de la Asociacion Argentina de Astronomia La Plata Argentina*, 6, 41
- Sérsic J. L., Pastoriza M., 1967, *PASP*, 79, 152
- Shaw L. D., Holder G. P., Bode P., 2008, *ApJ*, 686, 206
- Shen S., Mo H. J., White S. D. M., Blanton M. R., Kauffmann G., Voges W., Brinkmann J., Csabai I., 2003, *MNRAS*, 343, 978
- Silva L., Granato G. L., Bressan A., Danese L., 1998, *ApJ*, 509, 103
- Silverman J. D. et al., 2009, *ApJ*, 695, 171
- Smith S., 1936, *ApJ*, 83, 23
- Spergel D. N. et al., 2003, *ApJS*, 148, 175
- Springel V. et al., 2005, *Nat*, 435, 629
- Springob C. M., Haynes M. P., Giovanelli R., 2005, *ApJ*, 621, 215
- Stanford S. A. et al., 2012, *ApJ*, 753, 164
- Stanford S. A. et al., 2006, *ApJ*, 646, L13
- Strauss M. A. et al., 2002, *AJ*, 124, 1810
- Strolger L.-G. et al., 2004, *ApJ*, 613, 200
- Sunyaev R. A., Zeldovich Y. B., 1970, *Comments on Astrophysics and Space Physics*, 2, 66
- Sunyaev R. A., Zeldovich Y. B., 1972, *Comments on Astrophysics and Space Physics*, 4, 173
- Szokoly G. P. et al., 2004, *ApJS*, 155, 271
- Tanaka M., 2012, *PASJ*, 64, 36

- Tanaka M. et al., 2008, *A&A*, 489, 571
- Tanaka M. et al., 2013, *PASJ*, 65, 17
- Tanaka M., Finoguenov A., Ueda Y., 2010, *ApJ*, 716, L152
- Taniguchi Y. et al., 2007, *ApJS*, 172, 9
- Taylor E. N. et al., 2009, *ApJS*, 183, 295
- Tinker J., Kravtsov A. V., Klypin A., Abazajian K., Warren M., Yepes G., Gottlöber S., Holz D. E., 2008, *ApJ*, 688, 709
- Toft S. et al., 2007, *ApJ*, 671, 285
- Trujillo I. et al., 2006, *ApJ*, 650, 18
- Trump J. R. et al., 2007, *ApJS*, 172, 383
- Vale C., White M., 2006, *New Astronomy*, 11, 207
- van den Bergh S., 2002, *AJ*, 124, 782
- van den Bosch F. C., Aquino D., Yang X., Mo H. J., Pasquali A., McIntosh D. H., Weinmann S. M., Kang X., 2008, *MNRAS*, 387, 79
- van der Burg R. F. J. et al., 2013, *A&A*, 557, A15
- van der Wel A., Franx M., van Dokkum P. G., Rix H.-W., 2004, *ApJ*, 601, L5
- Vanzella E. et al., 2008, *A&A*, 478, 83
- Vikhlinin A. et al., 2009, *ApJ*, 692, 1060
- Vikhlinin A., McNamara B. R., Forman W., Jones C., Quintana H., Hornstrup A., 1998, *ApJ*, 502, 558
- Voges W. et al., 1999, *A&A*, 349, 389
- Vulcani B. et al., 2011, *MNRAS*, 413, 921
- Weinberg D. H., Mortonson M. J., Eisenstein D. J., Hirata C., Riess A. G., Rozo E., 2012, *ArXiv e-prints*
- Williamson R. et al., 2011, *ApJ*, 738, 139
- Wilman D. J., Balogh M. L., Bower R. G., Mulchaey J. S., Oemler A., Carlberg R. G., Morris S. L., Whitaker R. J., 2005, *MNRAS*, 358, 71
- Wilman D. J., Erwin P., 2012, *ApJ*, 746, 160

- Wilman D. J., Oemler J. A., Mulchaey J. S., McGee S. L., Balogh M. L., Bower R. G., 2009, *ApJ*, 692, 298
- Wolf C. et al., 2009, *MNRAS*, 393, 1302
- Wolf C., Hildebrandt H., Taylor E. N., Meisenheimer K., 2008, *A&A*, 492, 933
- Wolf C. et al., 2004, *A&A*, 421, 913
- Wright N. J., Drake J. J., Civano F., 2010, *ApJ*, 725, 480
- Wuyts S. et al., 2011, *ApJ*, 742, 96
- Xue Y. Q. et al., 2011, *ApJS*, 195, 10
- Yang X., Mo H. J., van den Bosch F. C., 2009, *ApJ*, 695, 900
- Yang X., Mo H. J., van den Bosch F. C., Pasquali A., Li C., Barden M., 2007, *ApJ*, 671, 153
- York D. G. et al., 2000, *AJ*, 120, 1579
- Zirm A. W., Toft S., Tanaka M., 2012, *ApJ*, 744, 181
- Zwicky F., 1933, *Helvetica Physica Acta*, 6, 110
- Zwicky F., 1937, *ApJ*, 86, 217

Acknowledgement

In the past three years, I had the chance to attend in one of the best astrophysical institute in the Europe and working with many people who contributed to this thesis either scientifically, financially, or with moral support.

It is my pleasure to thank Paul Nandra for being a superb supervisor for encouraging the projects and spreading a positive attitude. I would like to thank my project supervisors Alexis Finoguenov and Paola Popesso. Thanks Alexis for giving me the chance of studying in PhD program, defining great scientific projects and for his valuable advices. Thanks Paola for her great supervising, for encouraging new projects, and for supporting new ideas and approaches.

I would like to thank Masayuki Tanaka for the useful discussion and enjoyable collaborations. I am also indebted to Mike Lerchster, Mara Salvato, Daniele Pierini, and Felicia Ziparo for sharing their expertise. I wish also to thank Alex for the good chats and all her helps. Very warm thanks go to Birgit Böller for going beyond the call duty of a secretary on more than one occasion.

Very special thanks go to my family. I owe to thank my father, mother, and sister for all their love and encouragement. And finally, I would like to thank my office mate, best friend, and my wife Ghazaleh for the joy and the serenity she gave me.

Cirriculum Vitae

Mohammad Mirkazemi

Departmental Address:

Max Planck Institute for Extraterrestrial Physics
Giessenbachstrasse 1
85748 Garching, Germany
+49-89-30000-3210
erfanian@mpe.mpg.de

Educations:

2011–2014: PhD student of the International Max Planck Research School at the Max-Planck-Institut für extraterrestrische Physik (Garching bei München, Germany).

2010: Master degree in Physics at Sharif university of technology (Tehran, Iran).

2008: Bachelor degree in Physics at Sharif university of technology (Tehran, Iran).

Publicatios:

- **BRIGHTEST X-RAY CLUSTERS OF GALAXIES IN THE CFHTLS WIDE FIELDS**
M. Mirkazemi, A. Finoguenov, M. J. Pereira, M. Tanaka, et al. (submitted to ApJ)
- **STELLAR MASS FUNCTION OF X-RAY SELECTED GALAXY CLUSTERS IN CFHTLS AND COSMOS**
M. Mirkazemi, P. Popesso, A. Finoguenov, et al. (in perp)
- **AN X-RAY DETECTED GROUP OF QUIESCENT EARLY-TYPE GALAXIES AT $z=1.6$ IN THE CHANDRA DEEP FIELD SOUTH**
M. Tanaka, A. Finoguenov, M. Mirkazemi, D. Wilman, et al. (2013, 65, 17, PASJ)

- EVOLUTION OF LUMINOSITY GAP IN X-RAY GALAXY GROUPS IN CFHTLS
G. Gozaliasl, A. Finoguenov, H. G. Khosroshahi, M. Mirkazemi, M. Salvato, et al. (A&A.)
- CFHTLENS: WEAK LENSING CALIBRATED SCALING RELATIONS FOR LOW MASS CLUSTERS OF GALAXIES
K. Kettula, S. Giodini, E. van Uitert, ... ,M.Mirkazemi, et al. (submitted to MNRAS)
- X-RAY GROUPS OF GALAXIES IN THE AEGIS DEEP AND WIDE FIELDS
G. Erfanianfar, A. Finoguenov, M. Tanaka, ..., M. Mirkazemi, et al. (2013, 756, 117 ApJ)
- THE EVOLUTION OF STAR FORMATION ACTIVITY IN X-RAY SELECTED GALAXY GROUPS SINCE $z \sim 1$
G. Erfanianfar, P. Popesso, A. Finoguenov, A. Biviano, D. Wilman, M. Mirkazemi et al. (submitted to MNRAS)

Languages:

Persian : Native Speaker

English : Fluent

German : Basic